

Desulfurization by Metal Oxide/Graphene Composites

by

Hoon Sub Song

A thesis

presented to the University of Waterloo

in fulfillment of the

thesis requirement for the degree of

Doctor of Philosophy

in

Chemical Engineering

Waterloo, Ontario, Canada 2014

© Hoon Sub Song 2014

Author's Declaration

I hereby declare that I am the sole author of this thesis. This is a true copy of the thesis, including any required final revisions, as accepted by my examiners.

I understand that my thesis may be made electronically available to the public.

Abstract

Desulfurization of liquid and gas phase sulfur compounds has been receiving dramatic attention since sulfur compounds cause environmental damages (especially acid rain) and pose industrial challenges (i.e. corrosion of equipment and deactivation of catalysts). This thesis has focused on the removal of liquid phase aromatic sulfur compounds (i.e. thiophene or dibenzothiophene (DBT)), as well as on the removal of gas phase hydrogen sulfide (H_2S) through adsorption method by metal oxide/graphene composites. More specifically, the effects of graphene (or reduced graphite oxide) as a substrate were thoroughly investigated. For liquid phase sulfur removal, graphene which possesses π orbitals can adsorb aromatic sulfur compounds through π - π interactions. In addition, depending on the synthesis methods, higher quality graphene (i.e. thinner or larger graphene) could be obtained; and it improved the amount of DBT adsorption.

For gas phase desulfurization (i.e. H_2S adsorption), zinc oxide (ZnO) and reduced graphite oxide (rGO) composites have been studied. This study highlights the critical role of rGO as a substrate to enhance the H_2S adsorption capacity. The presence of rGO with ZnO increases the surface area compared with pure ZnO since the oxygen functional groups on rGO prevent the aggregation of nano-sized ZnO particles for mid temperature sulfidation processes. The average particle size for pure ZnO was increased from 110 nm to 201 nm during the adsorption process while that for ZnO/rGO was maintained as 95 nm even after adsorption at 300°C. This contributes to explain that the presence of rGO with ZnO can enhance the H_2S adsorption capacity from 31.7 mg S/g ads (for pure ZnO) to 172.6 mg S/g ads (for ZnO/rGO), that is more than a 5-fold increase. Moreover, the presence of rGO with ZnO considerably improves the

stability of the adsorbent; for multiple regeneration cycles at 600°C (in N₂ environment), the adsorption capacity for ZnO/rGO stabilized at 93.1 mg S/g ads after the 8th cycle, while that for pure ZnO was nil after 5 cycles.

The effects of copper (5, 10, 15, 20 and 25 mol%) with zinc oxide (ZnO) and reduced graphite oxide (rGO) composite on the hydrogen sulfide (H₂S) adsorption capacity have also been studied. It was found that depending on the copper loading, the H₂S adsorption capacity has been increased by up to 18 times compared to pure ZnO. In order to investigate the oxidation changes on copper and zinc oxides, crystallite analysis by XRD and chemical state analysis by XPS were performed. It was confirmed that the 2D rGO substrate, containing abundant oxygen functional groups, promoted the metal oxide dispersion and increased the H₂S adsorption efficiency by providing loosely bonded oxygen ions to the sulfur molecules. In addition, it was determined that the optimum content of copper was 15 mol% relative to ZnO for maximizing the H₂S adsorption. The 15% copper with ZnO/rGO led to the highest portion of zinc ions located in the Zn-O lattice; and led to the co-existence of Cu¹⁺ and Cu²⁺ ions with ZnO. The H₂S exposure at 300°C produces metal sulfides (i.e. zinc sulfide and copper sulfide) and sulfate ions.

Acknowledgements

First of all, I have to thank my supervisors, Prof. Eric Croiset and Prof. Zhongwei Chen, who showed great confidence in me, and provided me with a great deal of support. Also, I would like to thank my PhD defense committees composed of Prof. Boxin Zhao, Prof. Vivek Maheshwari, Prof. Aiping Yu and Prof. Hui Wang.

I would like to show my deepest gratitude to my lovely wife Su-jeong Park and family. Without your patience and considerations, it would have been impossible to complete my degree. I also want to show my appreciations to Dr. Sung-chan Nam and Prof. Kwang-bok Yi who gave me valuable supports and guidance for my studies in Korea.

Special thanks to my dear friends and colleagues; Moon-gyu Park, Young-jae Kim, Sung-ho Park, Tae-jung Kwon, Yi-young Choi, Kyung-guk Jo, Min-ho Jung, Sung-nam Lim, Sae-guk Park, Wook Ahn, Soon-jin Kwon, and Larry Liu. You made my life much more enjoyable and unforgettable in Korea and Canada.

Table of Contents

Author's Declaration	ii
Abstract	iii
Acknowledgements	v
List of Figures	x
List of Tables	xv
Nomenclature.....	xvi
Chapter 1. Introduction	1
1.1. Introduction	1
1.2. Motivations.....	3
1.3. Research objectives.....	5
1.4. Thesis outline.....	6
Chapter 2. Background and Literature Reviews	8
2.1. Liquid-phase sulfur compound removal	8
2.1.1. Hydrodesulfurization (HDS)-based process	10
2.1.1.1. Conventional HDS	10
2.1.1.2. Advanced HDS	14
2.1.2. Non-HDS-based process.....	15
2.1.2.1. Shifting the boiling point.....	15
2.1.2.2. Extraction	16
2.1.2.3. Adsorption on a solid sorbent	17
2.2. Gas-phase sulfur removal process	21

2.2.1. <i>In situ</i> sulfur removal method	22
2.2.2. Downstream sulfur removal.....	25
2.2.2.1. Reaction mechanism	25
2.2.2.1. Zinc oxide-based sorbents	29
2.2.2.2. Copper oxide-based sorbent	34
2.3. Graphene-based Adsorbent	36
2.3.1 Graphite oxide.....	37
2.3.2 Graphene.....	40
2.3.3. Metal oxide/reduced graphite oxide (rGO) composite	44
2.3.3.1. Metal oxide and graphene interactions	44
2.3.3.2. ZnO/rGO composite.....	46
2.3.3.3. Cu ₂ O/rGO composite	51
2.3.3.4. Effects of rGO for H ₂ S adsorption efficiency	55
2.4. Research scope	57
Chapter 3. Experimental.....	58
3.1. Adsorbent preparation.....	58
3.1.1. Preparation of graphite oxide (GO).....	58
3.1.2. Preparation of graphene and reduced graphite oxide (rGO).....	59
3.1.3. Preparation of metal oxide/rGO composite	59
3.2. Adsorbent characterizations	61
3.2.1. BET.....	61
3.2.2. XRD.....	63
3.2.3. XPS.....	64

3.2.4. FT-IR.....	66
3.3. Adsorption conditions and tests.....	67
3.3.1. DBT adsorption test.....	67
3.3.2. H ₂ S adsorption tests.....	68
Chapter 4. DBT Adsorption on graphene.....	71
4.1. DBT adsorption capacity on graphene.....	71
4.2. Characterizations of graphene adsorbents.....	74
4.3. Summary	82
Chapter 5: H ₂ S Adsorption on ZnO/rGO Composite.....	83
5.1. Characterizations of fresh ZnO/rGO adsorbents	83
5.2. H ₂ S breakthrough tests at room temperature.....	98
5.3. H ₂ S breakthrough tests at mid temperature.....	100
5.4. Characterizations of spent ZnO/rGO adsorbents.....	104
5.5. Summary	112
Chapter 6. H ₂ S adsorption on Cu ₂ O-ZnO/rGO composites	114
6.1. H ₂ S breakthrough tests at mid temperature.....	114
6.2. Characterizations of fresh Cu ₂ O-ZnO/rGO adsorbents	116
6.3. Characterizations of spent Cu ₂ O-ZnO/rGO adsorbents.....	128
6.4. Summary	132
Chapter 7. Regeneration of ZnO/rGO composites.....	133
7.1. H ₂ S adsorption capacity through regeneration cycles	133
7.2. Characterizations of fresh and spent adsorbents after regeneration	135
7.3. Summary	146

Chapter 8. Conclusions and Recommendations	147
8.1. Conclusions	147
8.2. Recommendations.....	149
References	152
Appendix I: Sample calculations	176
Appendix II: Crystal Size Calculation	178
Appendix III: Mass Flow Controller Calibration	180
Appendix IV: Raw Data.....	185
1. DBT adsorption data.....	186
2. H ₂ S adsorption data on ZnO and ZnO/rGO composite	187

List of Figures

Figure 2.1: Classification of desulfurization technologies by nature of a key process for sulfur removal [14]	9
Figure 2.2: Alkylation of thiophene via reaction with olefin [14]	16
Figure 2.3: General process flow of extractive desulfurization [19]	17
Figure 2.4: Adsorptive desulfurization IRVAD process [21]	18
Figure 2.5: General reactive adsorption desulfurization [23]	19
Figure 2.6: Sulfur breakthrough curves for adsorption desulfurization of DBT over differently treated activated carbons [24]	20
Figure 2.7: Mechanism of surface reaction of H ₂ S with metal oxide (Me) [41]	26
Figure 2.8: Sulfur coverage as a function of the amount of H ₂ S exposure to metal oxides at 300K with the band gap of each oxide [45]	28
Figure 2.9: Breakthrough curves of H ₂ S (4000 ppmv) using YL and AC supported ZnFe ₂ O ₄ at 500°C (R-1,2,3 and 4 indicate the number of regeneration) [51]	31
Figure 2.10: H ₂ S removal reactivity (at 450 °C) of 50 mol% ZnO with various TiO ₂ and ZrO ₂ composition [55]	33
Figure 2.11: Product gas compositions of H ₂ S, H ₂ O and SO ₂ for H ₂ S sulfidation on CuO in presence (A) and absence of H ₂ (B) at 600 °C and 1% of H ₂ S/He [61]	35
Figure 2.12: Schematic of graphene synthesis through chemical reduction method [66]	37
Figure 2.13: XRD patterns of graphite, graphite oxide and graphene [67]	38
Figure 2.14: C1s XPS spectra of (a) graphite oxide and (b) reduced graphite oxide [69]	39
Figure 2.15: Raman spectrum of graphite, graphite oxide, and graphene [70]	40

Figure 2.16: (a) Raman spectra of graphene and graphite measured at 514.5 nm; (b) Comparison of the 2D peaks in graphene and graphite [68].....	42
Figure 2.17: Evolution of (a) G peak and (b) 2D peak as function of number of layers at 514.5 nm [70]	43
Figure 2.18: TEM images of ZnO/graphene composite [93]	49
Figure 2.19: Raman spectrum of the ZnO/graphene composite [96].....	50
Figure 2.20: FT-IR spectra of graphite oxide and ZnO/graphene composite [100]	51
Figure 2.21: XRD of (a) graphite oxide, (b) graphene, and (c) Cu ₂ O/graphene composite [104] ..	52
Figure 2.22: FT-IR spectra of (a) graphite oxide, (b) Cu(Ac) ₂ , (c) Cu(Ac) ₂ /graphite oxide composite [99]	54
Figure 2.23: (a) TEM; (b) SEM images of Cu ₂ O/graphene composites [109].....	55
Figure 3.1: Illustration of the synthesis of metal oxide/rGO composite	60
Figure 3.2: Schematic illustration of XPS [118].....	65
Figure 3.3: H ₂ S adsorption experiment setup	69
Figure 4.1: Schematic illustration of the adsorption of DBT on graphene	72
Figure 4.2: DBT adsorption on graphene using a modeled diesel solution	73
Figure 4.3: XRD for graphite oxide and interlayer <i>d</i> -spacing: (A) GOH and (B) GOP	75
Figure 4.4: XRD of graphene and interlayer <i>d</i> -spacing: (A) GPH and (B) GPP.....	76
Figure 4.5: XPS of graphite oxide; (A) GOH and (B) GOP	78
Figure 4.6: XPS of graphene; (A) GPH and (B) GPP.....	80
Figure 4.7: Raman spectroscopy of graphite oxide and graphene	81
Figure 5.1: XRD patterns of (A): GO, (B): rGO-R, (C): rGO-M, (D): ZnO/rGO-R, (E): ZnO/rGO-M.....	85

Figure 5.2: XRD patterns of (A): ZnO/rGO-M, (B): ZnO/rGO-M-W, (C): ZnO/rGO-M-H ₂ S	86
Figure 5.3: FT-IR spectra of (A): ZnO, (B): rGO-R, (C): rGO-M, (D): ZnO/rGO-R, (E): ZnO/rGO-M.....	88
Figure 5.4: XPS analysis for (A) ZnO/rGO-R and (B) ZnO/rGO-M (C-OH/C-C: 0.19 / 0.35)....	89
Figure 5.5: FT-IR spectra of (A): ZnO/rGO-M, (B): ZnO/rGO-M-W, (C): ZnO/rGO-M-H ₂ S	90
Figure 5.6: Raman spectra of rGO-R, rGO-M, ZnO/rGO-R and ZnO/rGO-M.....	91
Figure 5.7: SEM images of (A) ZnO/rGO-R and (B): ZnO/rGO-M	92
Figure 5.8: Zn 2p XPS for (a) pure ZnO and (b) ZnO/rGO composite	93
Figure 5.9: Zn2p _{3/2} spectrum for (a) pure ZnO and (b) ZnO/rGO composite	95
Figure 5.10: O1s XPS for (a) pure ZnO and (b) ZnO/rGO composite	96
Figure 5.11: C1s XPS for ZnO/rGO composite.....	97
Figure 5.12: TEM of ZnO/rGO composite with particle size measurement	98
Figure 5.13: H ₂ S adsorption tests at ambient conditions after 1 h of moisturizing pretreatment ..	99
Figure 5.14: Dynamic H ₂ S breakthrough tests for ZnO and ZnO/rGO composite at 300°C in presence of different gases	101
Figure 5.15: SEM images for fresh and spent samples at 300°C in N ₂ for 2h: (A) ZnO fresh, (B) ZnO spent, (C) ZnO/rGO fresh and (D) ZnO/rGO spent.....	104
Figure 5.16: After H ₂ S exposure Zn 2p _{3/2} XPS for (a) ZnO and (b) ZnO/rGO composite	107
Figure 5.17: After H ₂ S exposure O1s XPS for (a) ZnO and (b) ZnO/rGO composite	108
Figure 5.18: After H ₂ S exposure S1s XPS for (a) ZnO and (b) ZnO/rGO composite.....	111
Figure 5.19: After H ₂ S exposure C1s XPS for ZnO/rGO composite	112
Figure 6.1: H ₂ S adsorption breakthrough tests at 300°C depending on Cu/Zn ratios	115

Figure 6.2: XRD for fresh Cu ₂ O/ZnO/rGO composites: (A) ZnO/rGO, (B) Cu ₅ Zn ₉₅ /rGO, (C) Cu ₁₀ Zn ₉₀ /rGO, (D) Cu ₁₅ Zn ₈₅ /rGO, (E) Cu ₂₀ Zn ₈₀ /rGO, (F) Cu ₂₅ Zn ₇₅ /rGO and (G) Cu ₃₅ Zn ₆₅ /rGO.....	117
Figure 6.3: Detail XRD peak analysis depending on the fraction of Cu ₂ O (111) and ZnO (101): (A) Cu ₁₀ Zn ₉₀ /rGO, (B) Cu ₁₅ Zn ₈₅ /rGO, (C) Cu ₂₀ Zn ₈₀ /rGO and (D) Cu ₂₅ Zn ₇₅ /rGO ..	121
Figure 6.4: Cu _{2p} XPS analysis: (a) Cu _{2p} survey (b) Cu ₅ Zn ₉₅ /rGO, (c) Cu ₁₀ Zn ₉₀ /rGO, (d) Cu ₁₅ Zn ₈₅ /rGO, (e) Cu ₂₀ Zn ₈₀ /rGO and (f) Cu ₂₅ Zn ₇₅ /rGO	123
Figure 6.5: Zn _{2p} XPS analysis: (a) Zn _{2p} survey (b) Cu ₅ Zn ₉₅ /rGO, (c) Cu ₁₀ Zn ₉₀ /rGO, (d) Cu ₁₅ Zn ₈₅ /rGO, (e) Cu ₂₀ Zn ₈₀ /rGO and (f) Cu ₂₅ Zn ₇₅ /rGO	125
Figure 6.6: O _{1s} XPS analysis: (A) Cu ₅ Zn ₉₅ /rGO, (B) Cu ₁₀ Zn ₉₀ /rGO, (C) Cu ₁₅ Zn ₈₅ /rGO, (D) Cu ₂₀ Zn ₈₀ /rGO and (E) Cu ₂₅ Zn ₇₅ /rGO	127
Figure 6.7: (A) Overall XRD analysis and (B) detail XRD diffractions for spent Cu ₁₅ Zn ₈₅ /rGO composite.....	129
Figure 6.8: XRD for ZnO/Cu ₂ O area ratio for spent Cu ₁₅ Zn ₈₅ /rGO composite	130
Figure 6.9: S _{2p} XPS analysis for Cu ₁₅ Zn ₈₅ /rGO composite after H ₂ S exposure	131
Figure 7.1: H ₂ S adsorption capacities on ZnO and ZnO/rGO composite at 300 °C sulfidation with 600 °C regeneration in N ₂	134
Figure 7.2: Morphology changes during the regeneration cycles: (a) fresh ZnO, (b) ZnO after 5 cycles, (c) fresh ZnO/rGO and (d) ZnO/rGO after 8 cycles.....	137
Figure 7.3: XRD patterns for ZnO/rGO: (a) fresh, (b) after 1 st sulfidation, (c) after 1 st regeneration, (d) after 8 th sulfidation and (e) after 8 th regeneration.....	139

Figure 7.4: Zn2p _{3/2} spectra for ZnO (a) fresh, (b) after 1 st regeneration and (c) after 5 th regeneration; and ZnO/rGO (d) fresh, (e) after 1 st regeneration and (f) after 8 th regeneration	143
Figure 7.5: O1s spectra for ZnO (a) fresh, (b) after 1 st regeneration and (c) after 5 th regeneration; and ZnO/rGO (d) fresh, (e) after 1 st regeneration and (f) after 8 th regeneration	145
Figure I: Repeated results for H ₂ S adsorption in different conditions	177
Figure II: ZnO lattice parameter calculation	179

List of Tables

Table 2.1: Organosulfur compounds and their hydrotreating pathway [15]	12
Table 2.2: Allowable sulfur levels for synthesis gas applications [29].....	22
Table 2.3: Thermodynamic data for the reaction of various metal oxides with H ₂ S [45]	29
Table 3.1: Characteristics of IR spectra [120]	67
Table 4.1: Surface area and overall crystallite size (L _a and L _c) analysis	77
Table 4.2: XPS fitting analysis for graphite oxide and graphene	79
Table 5.1: Comparison of H ₂ S adsorption capacity and utilization.....	102
Table 5.2: XRD for ZnO after H ₂ S exposure	105
Table 5.3: XRD for ZnO/rGO composite after H ₂ S exposure.....	105
Table 5.4: XPS fitting area portion for pure ZnO and ZnO/rGO composite.....	109
Table 6.1: XRD crystallite analysis for ZnO/Cu ₂ O/rGO composite.....	119
Table 7.1: Crystallite size changes over regeneration cycles	141
Table 7.2: Ratios of Zn ^I /Zn ^{II} for ZnO and ZnO/rGO composite during regeneration cycles	141

Nomenclature

AC	activated carbon
N_{AV}	Avogadro's number
β	full width height maximum
C	BET constant
T (nm)	crystal size (nm)
K	crystal shape factor
C_o	concentration of DBT after reaction (ppm)
C_i	initial concentration of DBT (ppm)
ΔH_a	enthalpy change of adsorption
ΔG	free energy change
E_b	binding energy
E_f	energy of the ionized atom
E_i	initial state of the target energy
n_m	number of moles
$h\nu$	photoelectron energy
P_0	vapor pressure of the adsorbing gas at a given temperature
S	surface area (m^2/g)
$d(hkl)$	spacing between planes with hkl reflection
t	experimental breakthrough time (min/g of adsorbent)
T_t	theoretical breakthrough time
V_{sol}	volume of DBT solution tested (mL)
V_m	maximum volume of gas adsorbed in the monolayer ($2.8619 \text{ cm}^3/g$)
λ	wavelength of X-ray (\AA)

Chapter 1. Introduction

1.1. Introduction

Refineries convert crude oil to higher value products (i.e. liquid petroleum gas, gasoline, jet fuel and diesel) by employing various technologies such as distillation, extraction, reforming, hydrogenation and cracking [1]. Currently, about 2.2 million barrels of diesel fuel are consumed daily in the US road transportation [2]. Therefore, increasing attention is being paid to the chemistry of diesel fuel processing. However, refineries are challenged by the harmful sulfur oxides releases into the air from the combustion of high sulfur content fossil fuels. Therefore, environmental restrictions regarding the quality of fuels produced and the emissions from refinery have received dramatic attentions recently. There are extensive efforts to decrease the sulfur content in the fossil fuels [3]. Transportation fuels (i.e. gasoline and diesel) and non-transportation fuels are about 80% of the total refinery products [2].

In terms of technology availability, sulfur content in gasoline can be reduced to less than 30 ppmw by current hydrotreating process [4]. The major problem for deep desulfurization of gasoline is that the conventional hydrotreating technology results in a significant reduction of octane number. For diesel fuel, with the current hydrotreating technology it is difficult to reduce the sulfur compounds in current diesel below 500 ppmw S level because of refractory sulfur compounds [5]. These refractory sulfur compounds are the alkyl dibenzothiophene (DBTs) with one or two alkyl groups at 4- and/or 6-positions (4,6-dimethyldibenzothiophene, 4,6-DMDBT), which strongly inhibit hydrodesulfurization of the compounds [6]. A kinetic study shows that in order to reduce the sulfur content of the diesel fuel from 500 to less than 15ppmw using the

current hydrotreating technology, the reactor volume or the catalyst activity must be at least three times larger than those currently used in refineries [5].

Besides liquid sulfur content, gas-phase sulfur contents (i.e. hydrogen sulfide and sulfur dioxide) cause serious environmental issues [7]. The sulfur present in the fuels generates SO_x , known air pollutants. It is expected that sulfur emission levels will be further restricted in the future. Therefore, improving current refinery technologies and developing advanced materials is necessary for a minimum sulfur emission environment. Hydrogen sulfide (H_2S) is one of the most common sulfur components and is considered as an undesirable component in most industrial applications since sulfur impurities rapidly deactivate or poison catalysts, which are widely used in the chemical or petrochemical industries [8]. Therefore, the removal of sulfur-containing gases (i.e. SO_2 , H_2S etc.) has become a critical issue. Various approaches to remove H_2S , such as sorption, catalysis or condensation, have been applied [9]. Among those approaches, different adsorbents, such as activated carbon, zeolites [10], [11], modified alumina [12] or metal oxides [13], [14], have been investigated. Zinc oxide (ZnO) has been widely used as an adsorbent for removal of H_2S from hot gas streams (in range of 500-800°C) with the formation of zinc sulfide (ZnS) through the following reaction ($\text{ZnO}_{(s)} + \text{H}_2\text{S}_{(g)} \rightarrow \text{ZnS}_{(s)} + \text{H}_2\text{O}_{(g)}$) [15]. There is a critical drawback, however, to use ZnO for hot-gas H_2S removal process. Due to its thermal instability, the ZnO adsorbent has a risk of evaporating as volatile metallic zinc [16]. For lower temperature applications, the thermal stability is not an issue and ZnO can be converted to ZnS at even ambient condition [17].

Graphene (2 dimensional, mono-atomic thick sp^2 -carbon structure) has recently received increasing attention as a material of interest due to its high electronic conductivity, large surface area and high mechanical strength [18], [19]. Because of those benefits, most of the graphene-

based material studies focused on the electrochemistry field, such as battery [20], [21] or super-capacitors [19], [22]. More recently, graphite oxide (GO) with metal oxide composites have been extensively studied as adsorbents [23]–[25]. Graphite oxide-based or graphene-based materials are known to be useful for water purification, toxic gas removal and ammonia adsorption applications [26]–[28]. Graphite oxide, which possesses oxygen functional groups attached on both sides of the surface, received attention due to its ability to modify the physical properties and surface chemistry in order to enhance the interactions with target molecules [29]. The presence of oxygen groups on the surface of GO makes (or anchors) bonds with active metal oxides. Therefore, those oxygen functional groups are able to modify the availability of active sites on the surface of adsorbents depending on the dispersion of those active metal oxides and their chemical heterogeneity with GO [24].

1.2. Motivations

Desulfurization of fuels has received worldwide attention. The conventional desulfurization method in refineries is hydrodesulfurization (HDS) process. However, in conventional HDS, it is difficult to remove aromatic sulfur compounds, such as dibenzothiophene (DBT). A non-HDS technique, such as adsorptive desulfurization, relying on π -complexation bonding, is promising since the adsorption process could be accomplished at ambient temperature and pressure. Carbon materials (e.g. activated carbon, carbon nanotubes) have been widely investigated to adsorb thiophene compounds. Carbon based materials have also been investigated because of their high surface area.

It can be expected that an adsorbent possessing high surface area coupled with active sites (e.g. π orbitals) should present excellent adsorption performance. Reduced graphite oxide, (rGO), where the amounts and types of oxygen functional groups could be adjusted, possesses the characteristics mentioned above. When all oxygen functional groups are eliminated, then the rGO becomes graphene, which also possesses properties to generate a good sorbent (e.g. high surface area). To our knowledge, removal of bulky thiophene compound (e.g. DBT) using graphene as adsorbents has not been investigated.

In addition, metal oxides (e.g. ZnO, CuO) are used for H₂S removal from natural gas or syngas. For H₂S desulphurization it is proposed to use a substrate that contains oxygen functional groups capable of anchoring metal ions on the surface. This idea led the author to apply the unique characteristics of rGO for hydrogen sulfide gas adsorption. It was expected that the rGO substrate should be able to load more active and more evenly distributed metal oxides, which should improve the adsorption performance.

There are several metal oxides candidates, the mostly commonly encountered being ZnO. To further improve the adsorption capacity, it may be advantageous to take advantage of bi-metal oxide composites on the rGO substrate. In this study, another widely proposed active metal oxide, copper oxide, was chosen as a guest element. The author decided to also investigate the effects of the presence of various amounts copper oxide with zinc oxide.

Finally, from an industrial point of view, it is critical to be able to regenerate the spent sorbent, which is usually done at elevated temperature (500-600 °C). For high desulfurization efficiency the sorbents developed in this work are characterized by the presence of nano-sized metal oxide sorbents which can provide high surface area to the target molecules. Regeneration at elevated temperature could cause some sintering effects which can lead to reduced

performance and to shorten the life time of adsorbents. Investigation of sorbent regeneration is, therefore, also necessary, which was done for a 2D rGO substrates with nano-sized metal oxide.

1.3. Research objectives

The goal of this research is to develop appropriate graphene/rGO-based adsorbents which can achieve deep desulfurization level from liquid and gas-phase sulfur compounds. The target sulfur compounds were dibenzothiophene (DBT) for liquid fuels (i.e. gasoline and diesel) and hydrogen sulfide (H₂S) for gaseous streams. The following tasks were considered to achieve the research objectives:

- Understanding the mechanism of the exfoliation from 3D graphite powder to 2D rGO and then to 2D graphene in order to apply unique characteristics of each material to sulfur compound adsorption.
- Investigating the interactions between metal oxide and rGO in order to control the degree of dispersion and particle size of metal oxide on the surface of rGO.
- Evaluating the sulfur adsorption capacity of the synthesized metal oxide/rGO composites.
- Analyzing the sulfur adsorption mechanism and determining the roles of rGO on the adsorption capacity.
- Evaluating the regeneration of metal oxide/rGO composites.

1.4. Thesis outline

This thesis consists of 8 chapters and it is organized as follows:

- Chapter 1 introduces the present work, its motivation and research objectives.
- Chapter 2 provides the background on desulfurization by adsorption. This chapter also gives the necessary background on graphene and reduced graphite oxide (rGO).
- Chapter 3 provides descriptions of experimental details including the synthesis methods of the adsorbents, adsorption test equipment set-up, operational procedures and characterization methods.
- Chapter 4 presents the experimental results and discussion for dibenzothiophene (DBT) adsorption on synthesized graphene.
- Chapter 5 presents the experimental results and discussion for H₂S adsorption on zinc oxide/reduced graphite oxide (rGO) composites. In this chapter, different temperatures (25 and 300 °C) were applied and the critical roles of rGO as a substrate on the adsorption capacity are described.
- Chapter 6 presents the effects of the presence of additional copper oxide to ZnO/rGO composites for H₂S adsorption. The effects of presence of various portions (in mol%) of copper oxide with ZnO/rGO composite are described.
- Chapter 7 presents the regeneration ability of ZnO/rGO composite at 300°C for H₂S adsorption. In this chapter, the critical functionality of rGO for sulfidation-regeneration cycles is discussed.

- Chapter 8 gives the main conclusions of this research work and proposes recommendations for further studies.

Chapter 2. Background and Literature Reviews

2.1. Liquid-phase sulfur compound removal

Desulfurization methods can be categorized according to several aspects, such as the fate of the organosulfur compounds, the role of hydrogen and the nature of the processes (i.e. chemical or physical). In addition, based on the treatment method of the organosulfur compounds (decomposed, separated without decomposition or both separated then decomposed), the processes can be divided into three groups. The conventional hydrodesulfurization (HDS) method uses the decomposition of the sulfur compounds where gaseous or solid sulfur products are formed while the hydrocarbon is recovered in the refinery streams. A second method (different from decomposition) first transforms the sulfur compounds into other easily separated compounds from the refinery stream. A third method separates organosulfur compounds from the streams first and simultaneously decomposes them in a single reactor unit [30].

Depending on the role of the hydrogen stream, the desulfurization processes can be classified into two groups (i.e. HDS-based and non-HDS-based), as indicated in Figure 2.1.

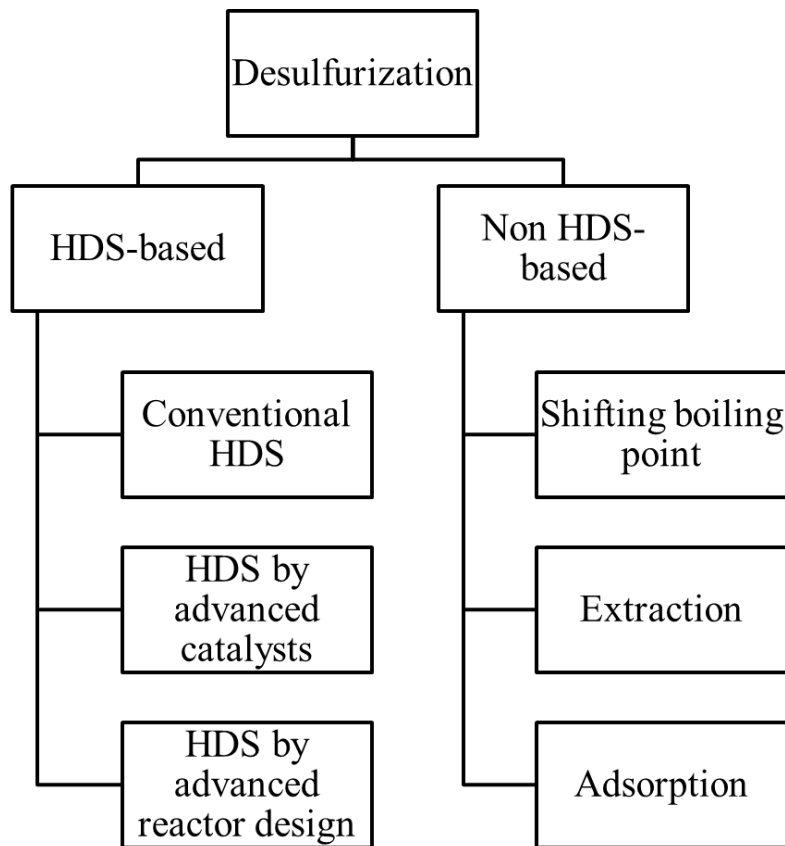


Figure 2.1: Classification of desulfurization technologies by nature of a key process for sulfur removal [30]

The HDS-based process requires hydrogen for the decomposition of the organosulfur compounds and the elimination of sulfur from the refinery stream while the non-HDS-based method does not require a hydrogen stream. The most common sulfur elimination process is the HDS method (catalytic transformation); however the sulfur compound separation process is usually a non-HDS process (physic-chemical separation) [30].

2.1.1. Hydrodesulfurization (HDS)-based process

2.1.1.1. Conventional HDS

Hydrodesulfurization (HDS) is historically a conventional method to remove sulfur compounds from the fuel feedstock and in natural gas purification process. It is the most typical method to reduce the sulfur content in commercial gasoline, diesel or jet fuel. The HDS reaction takes place in a fixed-bed reactor at elevated temperatures (i.e. 300-400°C) and pressures (i.e. 30-130 atm) [30], [31]. The conventional HDS process is usually conducted over sulfide CoMo/Al₂O₃ and NiMo/Al₂O₃ catalysts [30], [32]. Their catalytic performances (i.e. desulfurization level, activity and selectivity) depends on a few important factors, such as the properties of the catalyst (i.e. active species concentration, support properties, synthesis route), the reaction conditions (i.e. sulfiding protocol, reaction temperature, and hydrogen and H₂S partial pressures) and the nature and concentration of the sulfur compounds present in the feed stream [30].

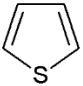
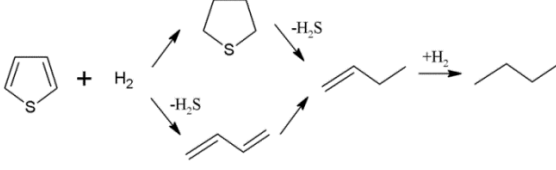
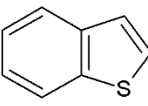
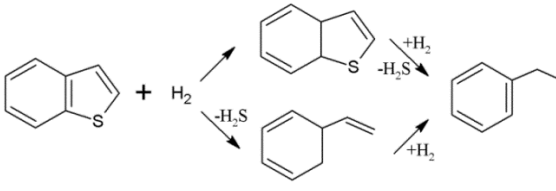
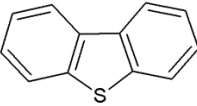
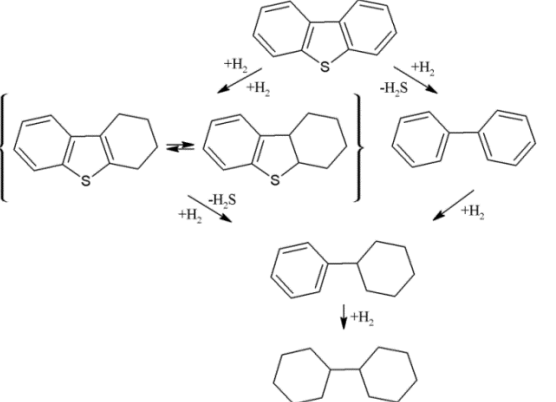
From crude oil distillation, a wide spectrum of sulfur-containing compounds is present. It is widely reported that most of the crude oil contains abundant amounts of organosulfur compounds which can be classified into two categories depending on their boiling point (i.e. low-boiling crude oil and high-boiling crude oil) [2]. The reactivity of those organosulfur compounds depends on their structure and local sulfur atom environment. The low-boiling crude oil mainly consists of the aliphatic organosulfur compounds, such as mercaptans, sulfides and disulfides; and those sulfur compounds are relatively easy to be removed by the conventional hydrotreating process. The high-boiling crude oil, however, consisting of heavy run naphtha, and

light FCC naphtha contains thiophenic rings [30]. Generally, higher boiling point fractions contain relatively higher concentration of sulfur and have higher molecular weight.

Depending on the number of aromatic rings attached with thiophene, benzothiophene and dibenzothiophene, those sulfur compounds containing thiophenic compounds are more difficult to be removed by a hydrotreating method. The reactivity is significantly affected by the degree of substitution of the thiophenic ring. The substitution of these compounds by ring alkylation further affects the reactivity. The reactivities of the 1 to 3 ring sulfur compounds decreases in the following order : thiophene (T) > benzothiophene (BT) > dibenzothiophene (DBT) > 4,6-dimethyldibenzothiophene (4,6-DMDBT) [2], [31].

Two reaction pathways are typically occurring during the HDS process of thiophenic compounds, as listed in Table 2.1. The first pathway is to directly remove the sulfur atom from the thiophenic compounds (hydrogenolysis pathway); and in the second pathway, the aromatic rings are hydrogenated first then the sulfur atom is subsequently removed (hydrogenation pathway). Depending on the nature of sulfur compounds and reaction conditions, those reaction pathways can occur simultaneously or one reaction pathway dominate. For example, the DBT is preferably removed through the hydrogenolysis pathway, but the 4,6-DMDBT is removed through simultaneous hydrogenation and hydrogenolysis pathways [31].

Table 2.1: Organosulfur compounds and their hydrotreating pathway [31]

Type of organic sulfur compound	Chemical structure	Mechanism of hydrotreating reaction
Mercaptanes	$R-S-H$	$R-S-H + H_2 \rightarrow R-H + H_2S$
Sulfides	R^1-S-R^2	$R^1-S-R^2 + H_2 \rightarrow R^1-H + R^2-H + H_2S$
Disulfides	$R^1-S-S-R^2$	$R^1-S-S-R^2 + H_2 \rightarrow R^1-H + R^2-H + H_2S$
Thiophene		
Benzothiophene		
Dibenzothiophene		

For the conventional HDS process, cobalt and nickel catalysts supported on cobalt (or nickel)/molybdenum/alumina ($\text{CoMo}/\text{Al}_2\text{O}_3$ and $\text{NiMo}/\text{Al}_2\text{O}_3$) are widely used [32]. Characteristics of catalysts (i.e. concentration of active species and support properties), the reaction conditions (i.e. temperature and partial pressure of hydrogen) and the reactor design (i.e. continuous or batch and co-current or counter-current) should be considered in order to choose appropriate catalysts.

The HDS reactions *via* hydrogenolysis and hydrogenation for the removal of sulfur atoms selectively occur depending on the nature of the sulfur compounds and the reaction conditions; also different active components of catalysts are used. It is reported that $\text{CoMo}/\text{Al}_2\text{O}_3$ catalyst prefers the hydrogenolysis pathway (requiring relatively little hydrogen); but the $\text{NiMo}/\text{Al}_2\text{O}_3$ catalyst possesses high hydrogenation activity [30]. In term of the nature of sulfur compound, 4,6-DMDBT compound which is considered as the least reactive thiophenic compound is more easily desulfurized on $\text{NiMo}/\text{Al}_2\text{O}_3$ than on $\text{CoMo}/\text{Al}_2\text{O}_3$ in a continuous flow reactor [33]. However, it was reported that $\text{CoMo}/\text{Al}_2\text{O}_3$ is properly reactive in a batch reactor [34]. Depending on the feedstock composition, those NiMo and CoMo catalysts show their preferences. The CoMo catalysts are preferable for relatively high sulfur level (100 – 500 ppm) at low temperature. The NiMo catalysts are especially suitable for low sulfur level fuels (< 100 ppm) at high pressure. Those catalysts show stable performance for long-term run of 400 days on stream [32].

2.1.1.2. Advanced HDS

Most of the sulfur compounds in gasoline come from fluid catalytic cracking (FCC). In order to obtain gasoline which should contain less than 30 ppm S, treatment of FCC gasoline is essential. By using CoMo and NiMo catalysts, a relatively high degree of desulfurization can be achieved. However, it is critical to minimize the hydrogenation of olefins since it causes reduction in the octane number of the gasoline because of the removal of aromatics from the gasoline product. In addition, when desulfurization of FCC gasoline is conducted at high temperature, it can increase coke formation and subsequent catalyst deactivation. Therefore, instead of applying severe HDS conditions, development of HDS catalysts for improved activity and selectivity are an ideal option. In order to achieve advanced catalysts, there are many key points (i.e. precursor of the active species, support selection, synthesis procedure and post-treatment) that should be taken in account. Song proposed a new concept of HDS catalyst, bifunctional catalyst [35]. The author proposed bifunctional catalysts combining catalyst supports with bimodal pore size distribution (i.e. zeolites) and two types of sulfur resistant active sites. The first active sites are placed in large pores and are accessible for larger organosulfur compounds. The second active sites are located in small pores. Therefore, these are not accessible for large organosulfur compounds, and thus are stable against poisoning by H₂S. This novel method uses the concept that hydrogen can easily access the sites placed in the small pores and could be adsorbed and transported to regenerate the poisoned metal sites of the first active sites, named as auto-regeneration.

There is another attempt using new types of supports (i.e. amorphous silica-alumina, ASA) for active species. The active catalytic species (Pt, PtPd and NiW catalysts) are capable of

reducing sulfur content down to 6 ppm while 75 % of aromatics are simultaneously reduced. Especially, the PtPd/ASA catalysts are suitable for low sulfur level and low aromatics; but the Pt/ASA catalysts show better performance for high level of aromatics. However, those two Pt and PtPd catalysts are deactivated or poisoned by high sulfur level stream. Nonetheless, a NiW/ASA catalyst is a suitable choice for deep desulfurization [36].

2.1.2. Non-HDS-based process

Non-HDS processes imply that the desulfurization does not require a hydrogen feed for catalytic decomposition of organosulfur compounds.

2.1.2.1. Shifting the boiling point

Shifting (or increasing) the boiling point of organosulfur compounds allows the removal of sulfur-containing compounds by distillation method from light fractions of FCC. This shifting of the boiling point method was developed by British Petroleum and applied to desulfurize the thiophenic sulfur elements by alkylation in FCC gasoline stream [30] to increase the boiling temperature of the sulfur-containing hydrocarbon compounds (Figure 2.2).

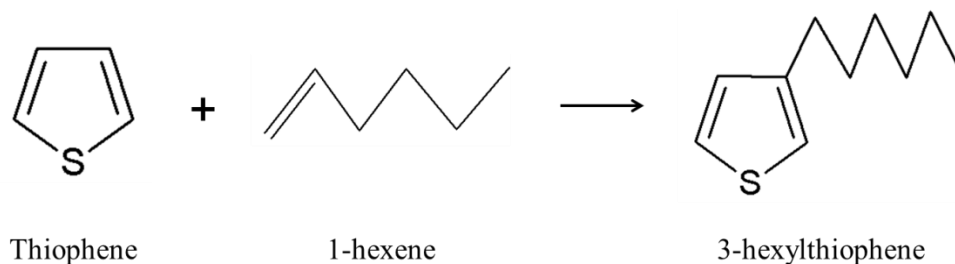


Figure 2.2: Alkylation of thiophene via reaction with olefin [30]

To remove a thiophene (boiling point around 85°C), the alkylation of thiophene with olefins (e.g. 3-hexylthiophene) can increase the boiling point to 221°C, which enables them to be separated from the gasoline easily by distillation [30].

2.1.2.2. Extraction

Desulfurization by extraction is based on the fact that organosulfur compounds are more stable than hydrocarbons in a solvent. One of the most attractive features of the extraction method is its applicability at low temperature and pressure. In addition, the extraction method does not affect the chemical structure of the fuel oil components. A critical requirement for this method is to carefully select appropriate solvents. First, the organosulfur compounds should be highly soluble in the solvent. Second, the boiling temperature of the solvent should be different than that of the sulfur compounds. Last, the solvent should be inexpensive for economic feasibility [30]. The diagram of the extraction process is shown in Figure 2.3.

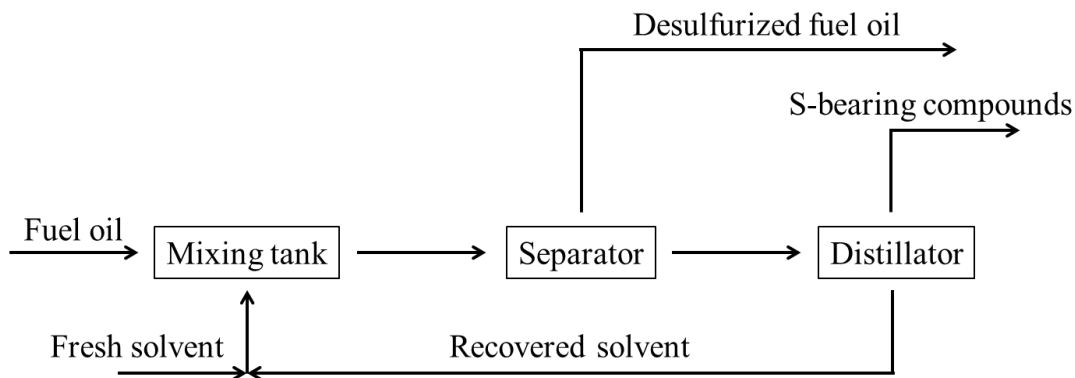


Figure 2.3: General process flow of extractive desulfurization [35]

The sulfur compounds from the fuel oil are mixed with the solvent in the mixing tank. The hydrocarbons are separated from the solvent-fuel oil mixture in a separator. The desulfurized hydrocarbons can be used as a component to be blended into the final products. Besides, the organosulfur compounds are separated by distillation and the solvent is recycled back to the mixing tank [30].

2.1.2.3. Adsorption on a solid sorbent

Desulfurization by adsorption (DAS) is based on the ability of a solid sorbent to selectively adsorb organosulfur compounds from refinery streams [30]. Depending on the interaction mechanism between the sulfur compounds and sorbents, the DAS process could be classified into two groups: (i) adsorptive desulfurization and (ii) reactive adsorption. The adsorptive desulfurization is based on the physical adsorption of sulfur compounds onto the surface of the solid sorbents while the reactive adsorption involves chemical interaction between

the sulfur compounds and the sorbent. The desulfurization efficiency is mainly determined by the properties of the sorbents (i.e. adsorption capacity, selectivity, durability and regenerability).

There is a conventional adsorptive desulfurization technology called IRVAD [37] and it was proposed to remove a wide spectrum of organosulfur compounds from refinery (FCC gasoline). A simplified process diagram is shown in Figure 2.4.

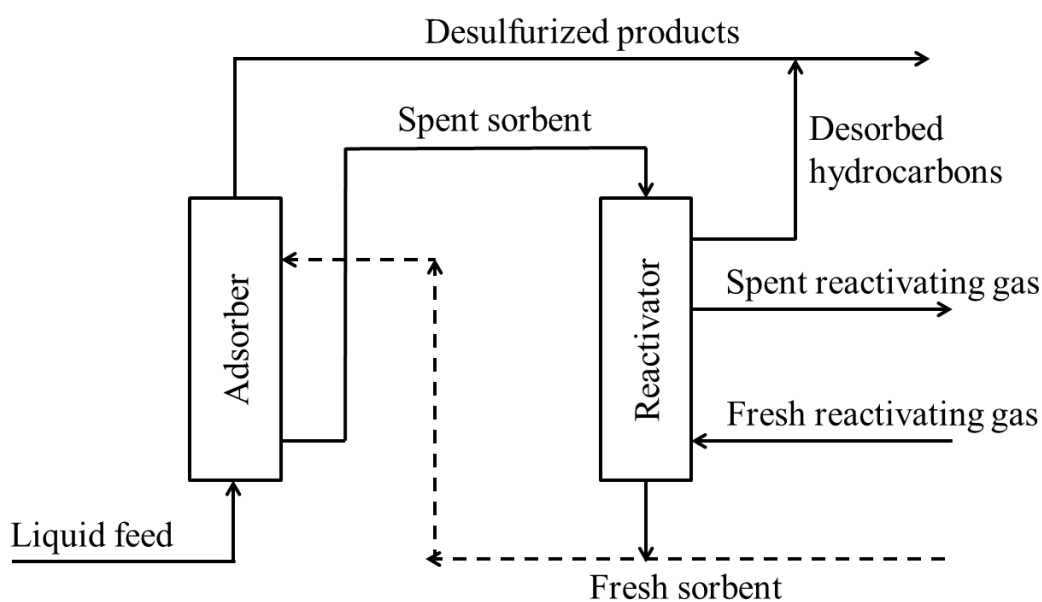


Figure 2.4: Adsorptive desulfurization IRVAD process [37]

The desulfurized hydrocarbon stream could be obtained from the top of the adsorber whereas the spent sorbents are withdrawn from the bottom. The spent sorbents are transferred to the bed for recirculation to the adsorber. The operating temperature for IRVAD is about 240°C. Since hydrogen is not required for this process, the sulfur removal is not accompanied by undesired olefin saturation. Typical desulfurization levels are claimed to be about 90% reduction of sulfur. Salem and Hamid [38] studied the adsorptive desulfurization for removing sulfur

compounds from naphtha using activated carbon and zeolite 13X as sorbents. The authors found that activated carbon showed high capacity but a low desulfurization level; but Zeolite 13X had excellent performance for low sulfur streams at room temperature. Therefore, the authors proposed a two-bed combination for industrial application. Activated carbon was placed in the first bed and removed about 65% of sulfur at 80°C. Then, the second bed was filled up with Zeolite 13X. This combination could achieve almost 100% of desulfurization efficiency even at low temperature.

The general reactive adsorption process is illustrated in Figure 2.5. The sulfur atom is removed from the molecule and is bound by the sorbent. The hydrocarbon part is returned to the final product without any structural changes [30].

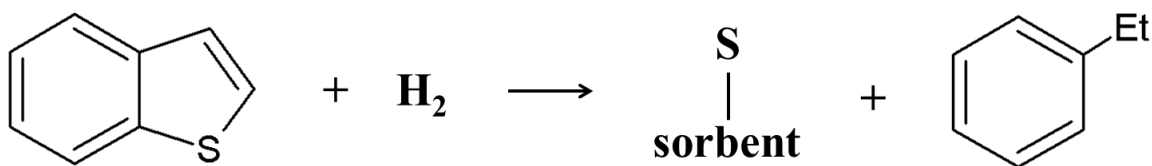


Figure 2.5: General reactive adsorption desulfurization [39]

Reactive adsorption technology has been developed by Phillips Petroleum Co., USA and called Phillips S Zorb technology [39]. This process is similar to the IRVAD technology but the operating conditions are more severe (i.e. temperature range between 340 and 410°C and pressure range between 2 and 20 bar). The S Zorb technology is able to remove about 98% of sulfur compounds from gasoline.

Thiophene, dibenzothiophene (DBT) and its alkyl derivatives are the most common sulfur containing organic molecules existing in the petroleum-derived feedstocks. The difficulty

in removing the sulfur from DBT is derived from the strong stability of the aromatic ring [40]. Thus, the key point in the reaction would be the weakening of the aromatic π bonding upon adsorption on the metal surface on the catalyst support (alumina, activated carbon, zeolites) [41]. Recently, numerous studies have focused on applications of activated carbons for ultra-deep desulfurization. The adsorbents reported were highly selective toward aromatic sulfur compounds, which are not efficiently removed by HDS [42]–[44].

The DBT breakthrough curves for the activated carbons which were oxidized at different temperatures (i.e. AC₄₇₃ at 473 K, AC₅₇₃ at 573 K and AC₆₇₃ at 673 K) were obtained at 298 K with a feed containing 320 mgS/L of DBT, as shown in Figure 2.6.

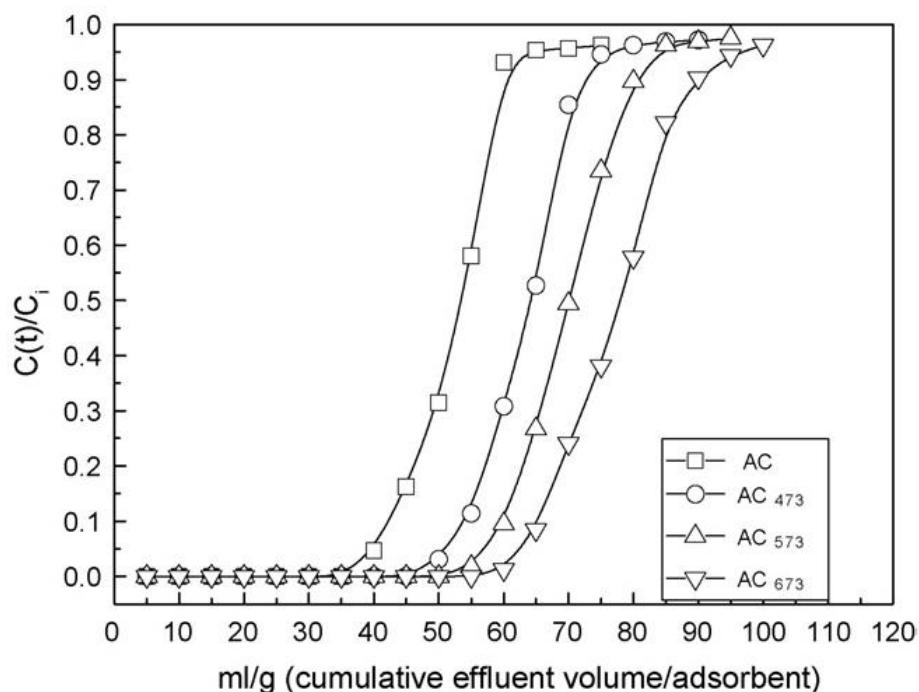


Figure 2.6: Sulfur breakthrough curves for adsorption desulfurization of DBT over differently treated activated carbons [40]

It can be seen that the cumulative effluent volume per adsorbent at breakthrough of DBT in the fixed beds packed with AC₆₇₃ was the highest, AC₅₇₃ being the next higher and AC₄₇₃ being the third higher, while that in the fixed beds packed with the original AC was the lowest.

2.2. Gas-phase sulfur removal process

Synthesis gas (i.e. mixture of H₂ and CO) can be obtained from the reforming of natural gas and is commonly used to produce pure hydrogen. However, contaminants in the natural gas are a major concern for the synthesis gas applications since those contaminants damage downstream process equipment and catalysts. Sulfur-containing compounds which are considered as the major contaminants can be produced during the combustion and gasification process. The sulfur-containing contaminants are easily converted to hydrogen sulfide (H₂S), sulfur dioxide (SO₂), carbon disulfide (CS₂), mercaptans (CH₃SH and CH₃CH₂SH), carbonyl sulfide (COS) and thiophene (C₄H₄S) [45].

Generally, a concentration of about 100 ppmv of H₂S is produced from the gasification of biomass fuels; but occasionally the gasification of the pulp and paper manufacturing process produces about 2000 to 3000 ppmv of sulfur species [45]. However, there are certain standards of sulfur contents for applications which require more stringent requirements (listed in Table 2.2).

Table 2.2: Allowable sulfur levels for synthesis gas applications [45]

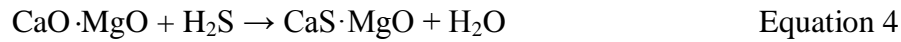
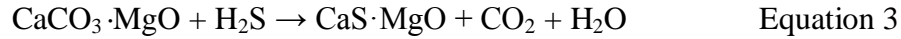
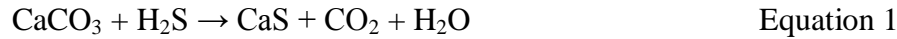
Applications	Allowable sulfur level (ppmv)	References
Ammonia production	< 0.1	[46]
Methanol synthesis	< 0.5	
Solid oxide fuel cell	< 1	
Fischer-Tropsch process	< 1	[47]
Gas turbines	< 100	

There are various methods and pathways to remove sulfur from gasification processes. In general, they are categorized into two categories: *in situ* sulfur removal and downstream sulfur removal.

2.2.1. *In situ* sulfur removal method

Typically, calcium-based sorbents (i.e. limestone or dolomite) are generally used; and commercial calcium-based sorbents, such as calcium acetate or calcium magnesium acetate, are extensively studied for *in situ* sulfur removal processes [48]. As briefly described above, the *in situ* (or in bed) desulfurization process typically uses the calcium-based sorbents; and the general sulfidation reactions for calcium-based sorbents are proposed below:

Sulfidation reactions



Side reaction



A relatively unstable product, CaS, is likely to react with oxygen through a side reaction (Eq. 5). This side reaction generates an unwanted product (CaSO₄) which can cover the surface of the sorbents and negatively affect the sulfidation reactions [45]. Therefore, sorbents' calcination (or regeneration) conditions where sintering of the oxides are avoided, are considered as the most critical factors in order to achieve sufficient sulfur removal efficiency; and extensive studies have been conducted over the past decades to find an optimum environment for extending the lifetime and efficiency of the calcium-based sorbents. Squires et al. [49] and Borgwardt and Roache [50] proposed optimum sulfidation temperatures for dolomites and limestone. They found that the dolomite and limestone can be used at high temperature (about 750°C) for fuel gas cleaning since the side reaction of CaS formation on limestone and dolomite could be prevented above 750°C. Abbasian et al. [51] further demonstrated that in the temperature range between 650 and 1050°C the sulfur removal efficiency was not affected by the sulfidation temperature for dolomite and limestone. However, dolomite was able to remove sulfur almost twice as rapidly as limestone due to its porous matrix; but the product CaS also reacted with oxygen to generate CaSO₄. Furthermore, Heesink and Swaij [52] found that high

oxygen content caused a decrease in the sulfidation rate due to the formation of CaSO_4 ; but small oxygen supply led to an increase in the sulfidation process. In addition, it was also found that the presence of COS , H_2 or CO with H_2S inhibited the sulfidation on CaO sorbents since it induced the rate determining layer diffusion by the formation of CaCO_3 on the surface. Yrjas et al. suggested that calcined dolomite and limestone had a significantly higher H_2S absorption capacity than uncalcined sorbents since the calcination process caused to produce high porosity sorbents [53].

As introduced above, commercially available calcium-based sorbents, such as calcium acetate (CA) and calcium magnesium acetate (CMA), show high efficiency in heavy duty gasoline (HDG) processes. Garcia-Labiano et al. [48] compared the performance of H_2S removal for different calcium-based sorbents. They found that the order, in term of H_2S sulfidation performance, was: $\text{CA} > \text{CMA} > \text{dolomite} > \text{limestone}$ at 1000°C with 5000 ppmv of H_2S feed concentration. Adanez et al. [54] also presented similar results for CA (90%) and CMA (60%) at 1000°C with 500 ppmv H_2S . Yang et al. [55] prepared calcium silicates and silica supported limestone for sulfidation-regeneration tests. It was found that the silica supported calcium oxide sorbents were very reactive for sulfidation; and their regeneration rates were substantially higher than that of pure calcium oxide sorbents with several successful sorption and regeneration cycles. Even though the calcium-based sorbents were able to be regenerated, there are some limitations. Dolomite and limestone are quite soft materials and easily broken up; and a stable sulfate surface layers are formed, thus reducing the active surface [45]. Therefore, more stable materials (i.e. metal oxides) for regeneration should be applied in order to achieve deep desulfurization (< 100 ppmv) in downstream processes.

2.2.2. Downstream sulfur removal

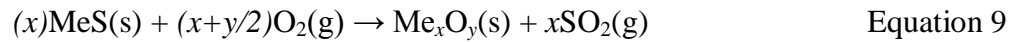
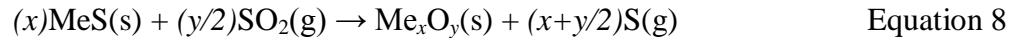
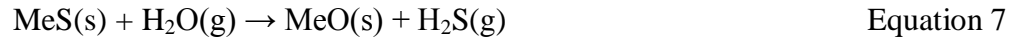
2.2.2.1. Reaction mechanism

Various types of metal oxides are mainly used for downstream hot-gas desulfurization (HGD) process. In order to apply metal oxides for the HDG process, there are some general requirements for the sorbents [56]: (1) The metal oxide should possess a high equilibrium constant and fast kinetics; (2) It should have high selectivity towards sulfur removal and avoid side reactions; (3) It should have high mechanical stability to minimize mass loss; and (4) It should be able to be regenerated easily.

General metal oxide-H₂S sulfidation



Hot-gas desulfurization (HDG)



Side reaction



The general sulfidation reaction between metal oxide and H₂S can be written in Eq. 6; and HDG reactions can be illustrated in Eq. 7 to Eq. 9. It can be noticed that the regeneration of metal sulfide oxides depends on the partial pressures of oxygen contents (Eq. 8 and 9); but

excess of oxygen can form the by-product metal sulfate (Eq. 10) which would decrease the activity of the materials.

H₂S molecules mainly interact with the metal sites of the oxides; the interactions of H₂S with O sites of the oxide surfaces are negligible (Figure 2.7).

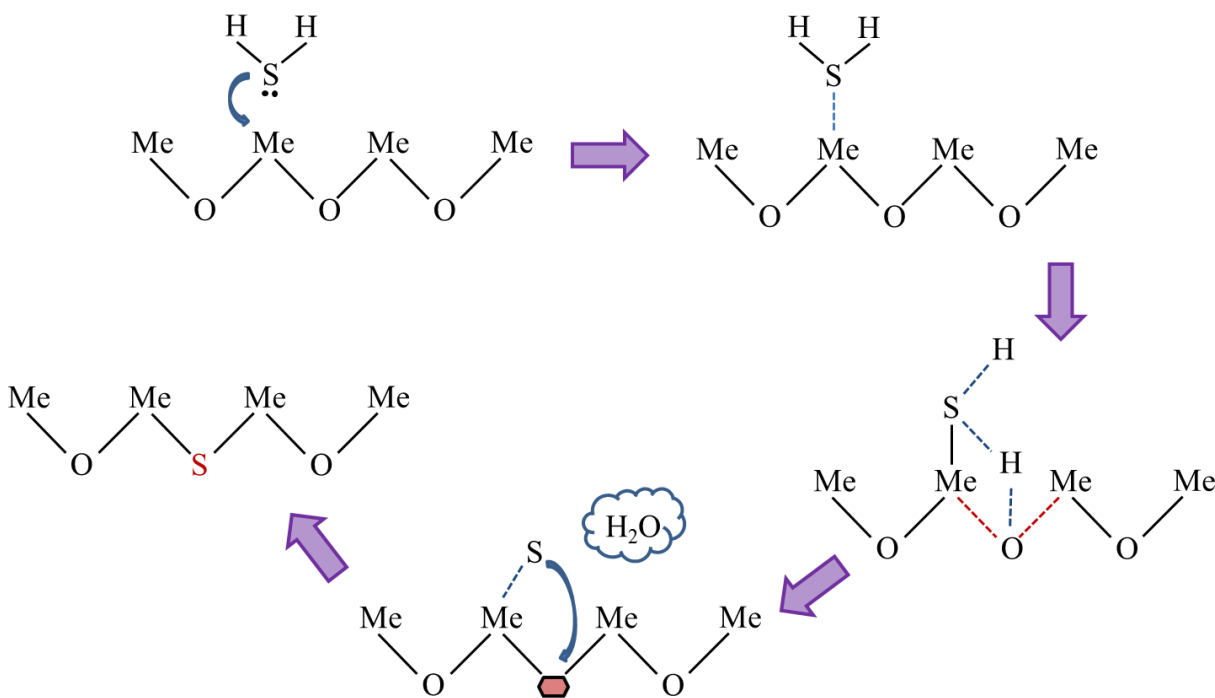


Figure 2.7: Mechanism of surface reaction of H₂S with metal oxide (Me) [57]

- (1) H₂S is approaching to the surface adsorption site of the metal oxide
- (2) The H₂S is chemisorbed onto the surface, followed by the formation of a chemical bonding with a metal cation
- (3) One of hydrogen from H₂S is interacting with the surface oxygen atom from metal oxide
- (4) Water molecules are formed with the subsequent formation of an oxygen vacant site

- (5) Sulfur atom is incorporated in the previously formed oxygen vacant site to form a surface metal sulfide

The mechanism of H₂S adsorption on an ionic solid has been introduced in previous studies starting with the dissociation of H₂S into H⁺ and HS⁻, followed by diffusion of HS⁻ into the oxide lattice and migration of oxide and water to the surface [9], [58]. Therefore, the diffusion of S²⁻ and HS⁻ ions into the metal oxide is required in order to convert MeO to MeS by proton transfers from H₂S to the chemisorbed OH groups on the Me-O surface [57]. The overall dissociative H₂S adsorption on MeO can be represented by the Eq. 6 above.

There are trials to investigate the H₂S adsorption efficiency on different types of metal oxides (i.e. Fe, Zn, Mn, V, Ca, Sr, Ba, Co and Cu) [8], [59]. It is proposed that the band gap energy of each metal oxide is a parameter to determine the appropriate metal oxides for H₂S adsorption process (Figure 2.8).

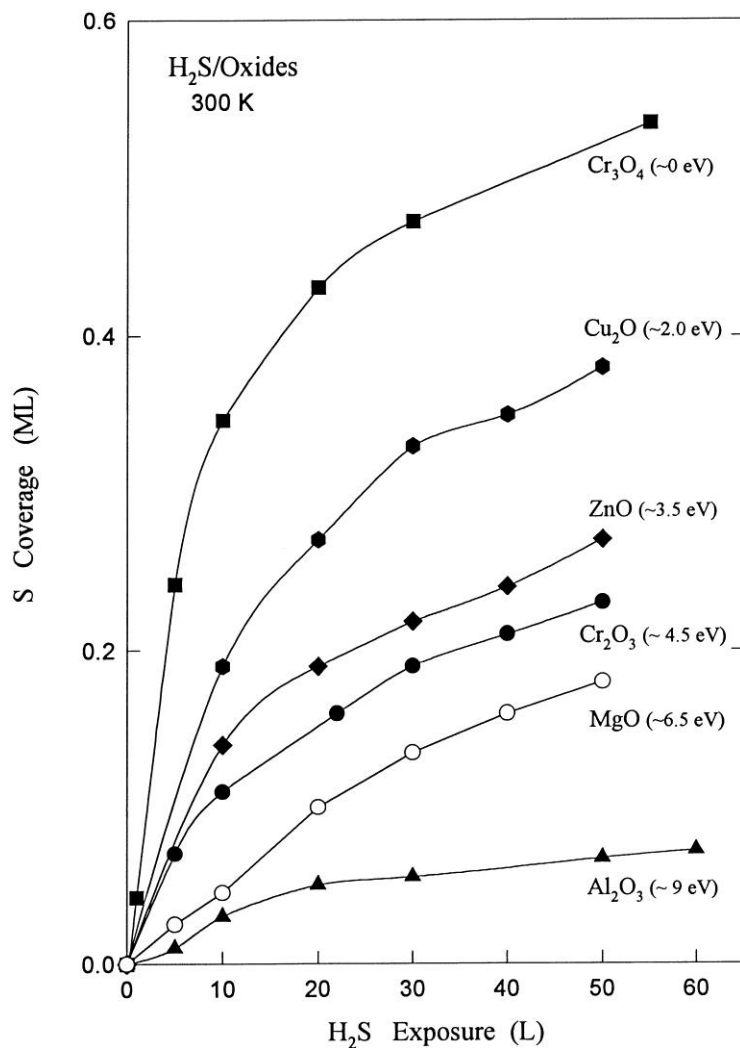


Figure 2.8: Sulfur coverage as a function of the amount of H₂S exposure to metal oxides at 300K with the band gap of each oxide [60]

When the size of the band gap follows the following order: Al₂O₃ (~ 9 eV) > ZnO (3.4 eV) > Cu₂O (2.2 eV) > Cr₃O₄ (0 eV), the adsorption abilities on the metal oxide follows the order: Al₂O₃ < ZnO < Cu₂O < Cr₃O₄. Therefore, there is an agreement that the lower the band gap energy, the more H₂S is adsorbed [60].

Thermodynamics (Table 2.3) of the reaction for H₂S and the selected metal oxides indicate a negative free-energy change (ΔG), implying that those are spontaneous reactions.

Table 2.3: Thermodynamic data for the reaction of various metal oxides with H₂S [60]

Reaction	ΔG (kJ/mol) at 298K
$\text{Cu}_2\text{O} + \text{H}_2\text{S} \rightarrow \text{Cu}_2\text{S} + \text{H}_2\text{O}$	-137
$\text{ZnO} + \text{H}_2\text{S} \rightarrow \text{ZnS} + \text{H}_2\text{O}$	-76
$\text{CuO} + \text{H}_2\text{S} \rightarrow \text{CuS} + \text{H}_2\text{O}$	-126
$\text{Fe}_2\text{O}_3 + 3\text{H}_2\text{S} \rightarrow \text{FeS} + \text{FeS}_2 + 3\text{H}_2\text{O}$	-136
$\text{Co}_3\text{O}_4 + 4\text{H}_2\text{S} \rightarrow \text{CoS} + \text{Co}_2\text{S}_3 + 4\text{H}_2\text{O}$	-251

The more negative ΔG represents a greater reactivity for H₂S adsorption. Therefore, based on free-energy change calculation, the reactivity order for H₂S removal increased with the following order: $\text{Co}_3\text{O}_4 > \text{Cu}_2\text{O} \approx \text{Fe}_2\text{O}_3 > \text{CuO} > \text{ZnO}$.

2.2.2.1. Zinc oxide-based sorbents

Zinc-based sorbents are widely used in H₂S desulfurization sorbents due to favorable thermodynamics [9]. Zinc oxide (ZnO) is considered as one of the effective sorbents for removal of H₂S from hot gas steams, from a thermodynamic point of view, with the formation of zinc sulfide (ZnS) [15] (Eq. 11). An important drawback when using ZnO for hot-gas H₂S removal process is its thermal instability to volatile metallic zinc [16]. However, for lower temperature

applications (below 600 °C), thermal stability is no longer an issue and ZnO can be converted to ZnS at ambient condition [17].



Although Zinc oxide (ZnO) has high H₂S removal efficiency, the vaporization of elemental Zn above 600 °C can cause serious problems. Zinc ferrite (ZnFe₂O₄, ZF) has been prepared using different methods, such as spray drying, impregnation, crushing and screening; and tested over a total of 175 sulfidation-regeneration cycles [61]. In order to enhance the stability of ZnO at high temperatures, Pineda et al. [62] proposed the addition of other metals (i.e. Cu or titanium oxide) to ZnO and ZF samples. The authors found that up to an atomic ratio of Ti/Zn = 0.5 the stability of ZnO increased due to the formation of Zn₂TiO₄; and the addition of Cu to ZF samples enhanced the sorbent performance by the formation of ferrite. In addition, the addition of Ti to ZF was able to prevent its decomposition leading to a stable structure by intercalating Ti atoms in the ferrite lattice. Besides improving the ZnO stability for desulfurization, there have been attempts to enhance the H₂S removal capacity.

Ikenaga et al. [63] used carbon-based materials (i.e. activated carbon, AC, and Yallourn coal, YL) as a support for ZF (ZnFe₂O₄) sorbents at 500°C to achieve deep desulfurization level (Figure 2.9). The authors found that the degree of H₂S removal had been reached to nearly 100% from the stoichiometric amount.

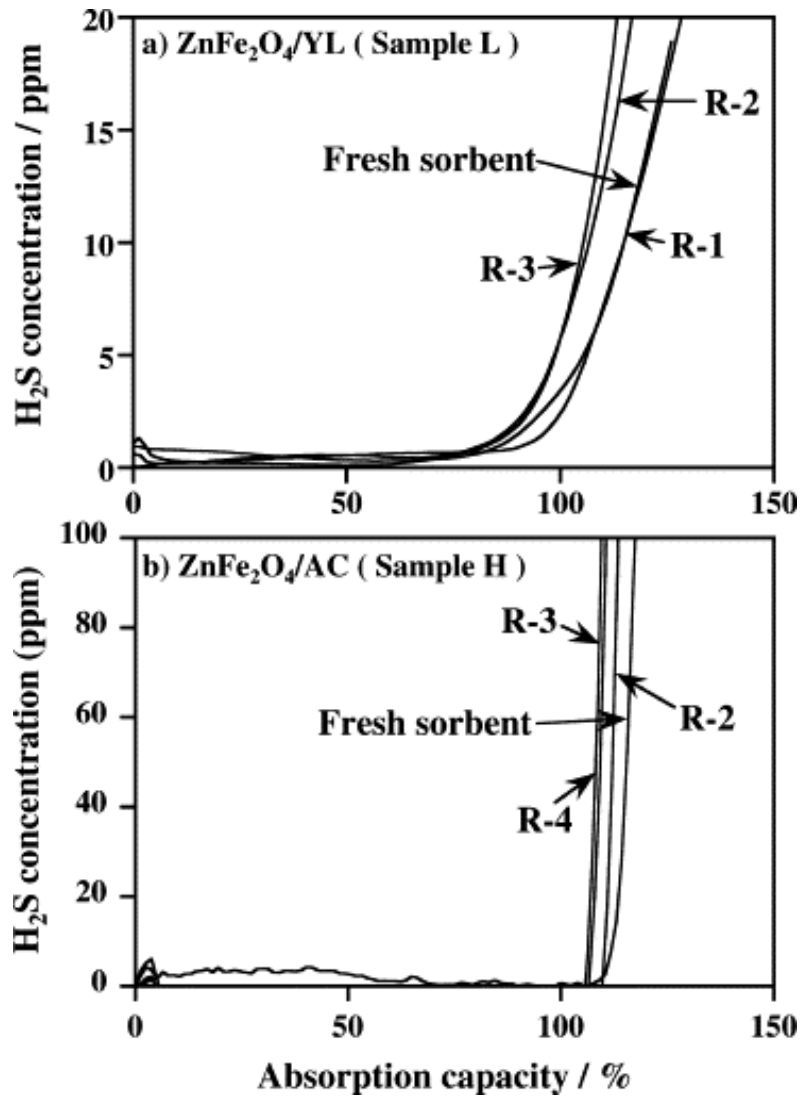


Figure 2.9: Breakthrough curves of H₂S (4000 ppmv) using YL and AC supported ZnFe₂O₄ at 500°C (R-1,2,3 and 4 indicate the number of regeneration) [63]

In addition, the authors insisted that the activated carbon supported ZF sorbents were able to be regenerated from ZnS and FeS in argon environment at 450°C. Liang et al. [64] have prepared various ZF sorbents using different binders (i.e. bentonite, mixed clay, fire clay and kaolinite); and conducted desulfurization reactions in the temperature range of 350 to 400°C. The

authors found that the addition of kaolinite as a binder showed the best performance toward H₂S removal among others; and successful sulfidation-regeneration cycles.

Although ZF sorbents show substantial improvements over pure ZnO, vaporization of Zn at high temperature and regeneration issues still need to be overcome. Previous studies proposed that addition of Ti to zinc oxide sorbents (named as ZT) could be an attractive method to deal with the limitations of ZF. Lew et al. [65] prepared various compositions of Zn and Ti oxides (Zn-Ti-O crystalline phases) within the temperature range of 400 to 800°C. The authors found that the initial sulfidation rate of Zn-Ti-O sorbents was about two times slower than that of ZnO. However, the formation of cracks was significantly reduced by prohibiting the reduction of Zn. Therefore, the Zn-Ti-O sorbents allowed an increase in the operating temperature for the HGD process; especially, when the Zn/Ti ratio was 2/3. The Zn reduction rate for the Zn-Ti-O sorbent was reduced about 9 fold compared to that of pure ZnO. Elseviers and Verelst [66] prepared a new composition of ZT, ZnO dispersed on TiO₂ matrix (ZnO(TiO₂)_{2.6}). This sorbent was able to achieve deep desulfurization (from 3250 ppmv H₂S level to the thermodynamic equilibrium level); and it could be almost completely regenerated at 600°C in argon environment.

Sasaoka et al. [67] tried to modify ZnO-TiO₂ by the addition of various compositions of ZrO₂ (Figure 2.10). The authors proposed that the addition of ZrO₂ improved the reactivity for H₂S removal and regenerability of the sorbents; however, due to sintering effects during the regeneration procedure, the surface area of the sorbents was decreased.

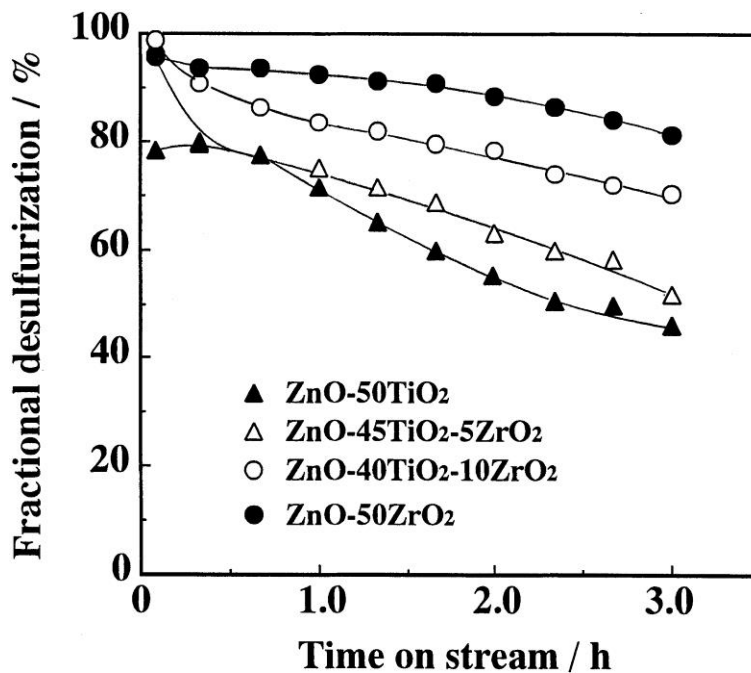


Figure 2.10: H₂S removal reactivity (at 450 °C) of 50 mol% ZnO with various TiO₂ and ZrO₂ composition [67]

Jun et al. [68] added about 25 wt% of Co₃O₄ into the ZT sorbents to increase the reactivity and stability. The authors confirmed that the addition of Co₃O₄ promoted the sulfur capture efficiency; and it allowed 10 cycles of sulfidation-regeneration with no deactivation within the temperature range of 480 to 650°C due to the formation of a spinel phase, ZnCoTiO₄ which could work not only as an active sites but also as a support for preventing zinc migration. Bu et al. [69] have applied addition of Cu and Mn oxides (1 to 2 wt%) to ZT sorbents by changing the Zn/Ti ratios from 2/3 to 1/1; and these additions enhanced the sulfidation efficiency in the temperature range of 600 to 700°C, even after 17 cycles of regenerations. Recently Lee et al. [70] investigated the effect of the surface area to the H₂S removal level. The authors found that depending on the zinc precursors, such as zinc acetate, zinc nitrate and zinc chloride, the

surface area of ZnO has been measured as 38.8, 40.7 and 24.2 m²/g, respectively. The levels of H₂S removal tests at 500°C indicated that the larger surface area showed higher sulfidation rates due to larger contact areas.

2.2.2.2. Copper oxide-based sorbent

Copper oxide-based sorbents are also considered as one of the most typical sorbents for HGD since they possess favorable thermodynamics and high sorption rate. However, rapid reducibility of uncombined CuO form to metallic copper in reducing environment (i.e. H₂ and CO in synthesis gas) causes to lower the sulfidation efficiency. In addition, the formation of a sulfide layer on the surface of CuO limits the utilization of active copper [45]. Therefore, similar to ZnO, there are many studies preparing mixed and dispersed copper oxide sorbents in order to overcome those weakness of CuO for sulfur removal.

A combination of active CuO with supports, such as SiO₂ and zeolite was able to enhance the utilization of CuO almost completely since the composites could provide dispersed copper species on the supports ensuring an unhindered contact with H₂S [71]. Li et al. [72] added Cr₂O₃ to CuO with various ratios (CuO : Cr₂O₃) of 3:1, 1:1 and 1:3. The authors found that the CuO-Cr₂O₃ composite could remove H₂S from coal-derived fuel gas down to 5 ppmv within the temperature range of 650 to 850°C. The formation of stable CuCr₂O₄ in the CuO-Cr₂O₃ composite was able to preserve the oxidation state of copper oxide as Cu²⁺ or Cu¹⁺ which are requirement for high H₂S removal.

Yasyerli et al. [73] tested H₂S sorption efficiency for CuO, Cu-V and Cu-Mo mixed oxides to investigate the effects of the presence of H₂ at 600°C. The authors found that only CuO

did not generate SO_2 when H_2 was not applied, but all samples formed SO_2 in the presence of H_2 with H_2S (Figure 2.11).

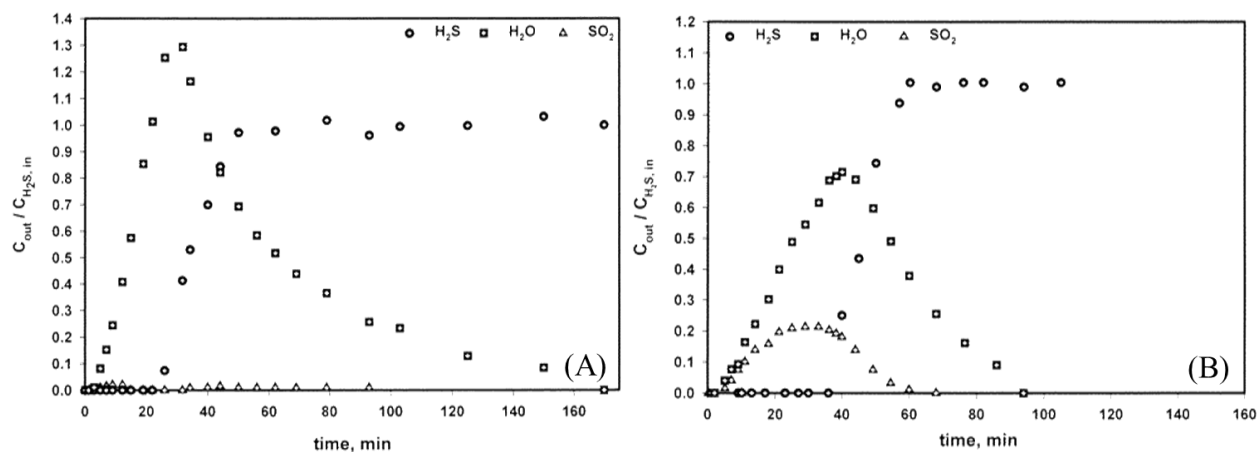


Figure 2.11: Product gas compositions of H_2S , H_2O and SO_2 for H_2S sulfidation on CuO in presence (A) and absence of H_2 (B) at 600°C and 1% of $\text{H}_2\text{S}/\text{He}$ [73]

Recently, Karvan et al. [74] prepared $\text{CuO}/\text{mesoporous silica (SBA-15)}$ with different ratios of Cu contents (i.e. 22 and 40 wt% Cu); and tested them for H_2S removal-regeneration cycles at 515°C . The authors found that the H_2S removal efficiency was affected by the content of Cu ; and the higher content of Cu (i.e. 40 wt% $\text{Cu}/\text{SBA-15}$) showed higher H_2S sulfidation capacity than that of the 22 wt% $\text{Cu}/\text{SBA-15}$ sample. However, the sample with 22 wt% Cu retained its sulfidation efficiency over the three cycle tests; but the sample with 40 wt% Cu decreased its efficiency by 19% after three cycles.

2.3. Graphene-based Adsorbent

Graphene, a single atomic sheet of bulk graphite, was first discovered in 2004 [75]. Graphene shows extreme physical strength and high electron mobility resulting from extensive π electron conjugation and delocalization [76], [77]. It has a large theoretical specific surface area (2630 m²/g), high Young's modulus (~ 1.0 TPa) and high thermal conductivity (~ 5000 W/m/K). Graphene can be produced by four different methods, including chemical vapor deposition (CVD), chemical exfoliation of graphite, epitaxial growth on electrically insulating surface and creation of colloidal suspensions by chemical reduction [78].

Exfoliated individual graphene sheets are obtained following a chemical reduction process (Figure 2.12): (i) transition from graphite to graphite oxide (GO); (ii) exfoliation with conversion of GO into graphene. Graphite oxide (GO) can be reduced to graphene either chemically by exposing GO to hydrazine or by rapid heating to high temperature or, alternatively, a combination of both [78], [79].

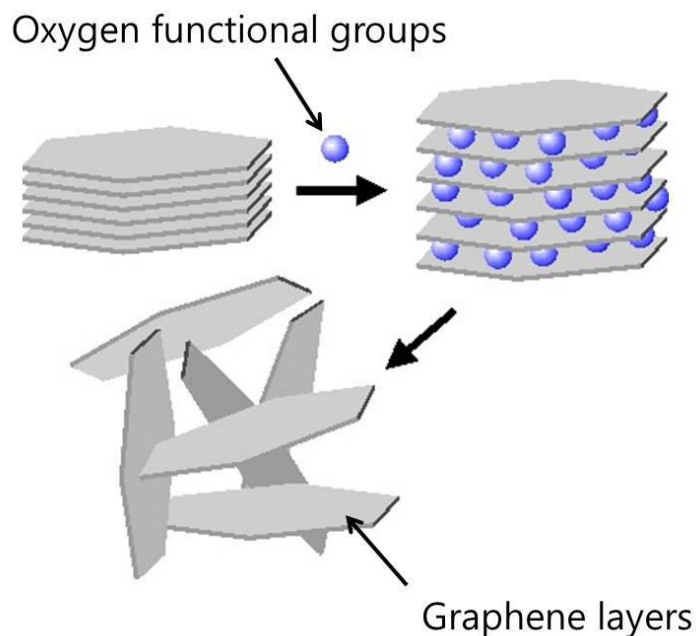


Figure 2.12: Schematic of graphene synthesis through chemical reduction method [78]

2.3.1 Graphite oxide

Graphite oxide (GO) is the product of the oxidation of graphite layers. Figure 2.13 shows the XRD patterns for graphite, graphite oxide and graphene. After chemical oxidation, the C(002) peak of graphite ($2\theta = 26.5^\circ$, corresponding to $d_{0001} = 0.34$ nm spacing between atomic planes in graphite) shifts by $10\text{-}12^\circ$ (d-spacing: $\sim 0.6\text{-}0.7$ nm). This implies that a layer expanded GO phase was produced along with the introduction of oxygenated functional groups (e.g. hydroxyl, epoxy and carboxyl) [79], [80].

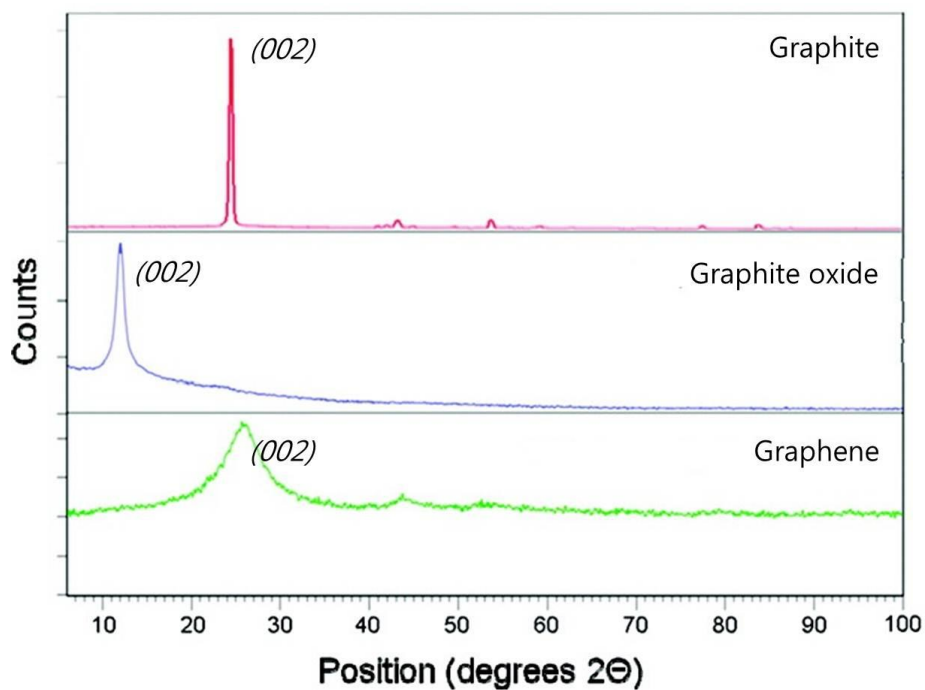


Figure 2.13: XRD patterns of graphite, graphite oxide and graphene [67]

X-ray photoelectron spectroscopy (XPS) shows the formation of surface functional groups on the obtained materials (Figure 2.14) [81]. The C^{1s} spectrum is a superposition of two strong peaks at 286.2 and 284.4 eV that are fingerprints of C-O (including epoxy and hydroxyl groups) and C-C bonds, respectively [78], [79]. Some C=O and C(=O)-(OH) bonds (with corresponding peaks at 287.5 and 289.2 eV) are also expected to be present [79]. The relative C-C peak area in the GO was significantly reduced, while the peaks associated with oxidized carbon increased, implying that a chemical oxidation process of graphite occurred [80].

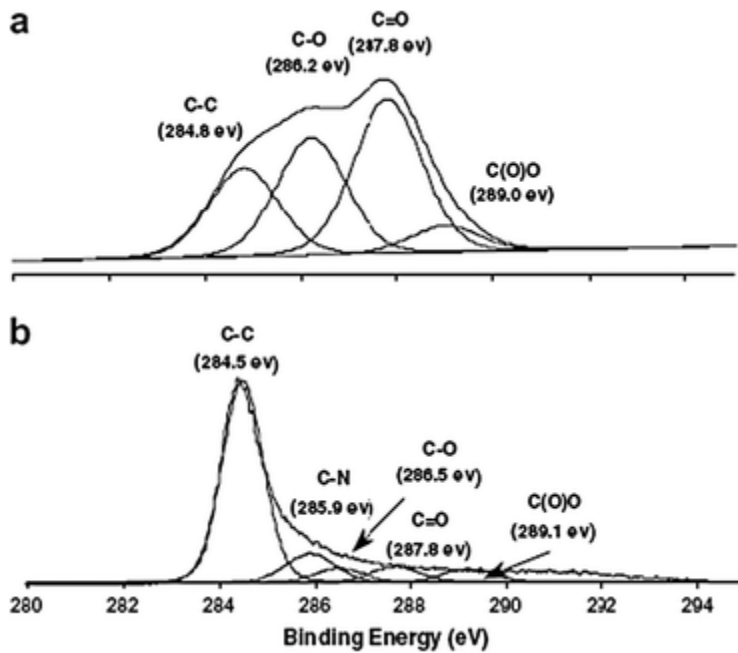


Figure 2.14: C1s XPS spectra of (a) graphite oxide and (b) reduced graphite oxide [81]

Raman spectroscopy has been used extensively to investigate the graphene chemistry. Raman spectra consist of three major peaks (i.e. G, D and 2D bands). The G-band ($\sim 1580 \text{ cm}^{-1}$) is due to the bond stretching of all pairs of sp^2 carbon atoms in both rings and chains [82]; the D peak ($1350\text{-}1370 \text{ cm}^{-1}$) is from the disorder-induced phonon mode due to defects [83]; as well as the stacking order (2D band at $\sim 2700 \text{ cm}^{-1}$), as shown in Figure 2.15 [84].

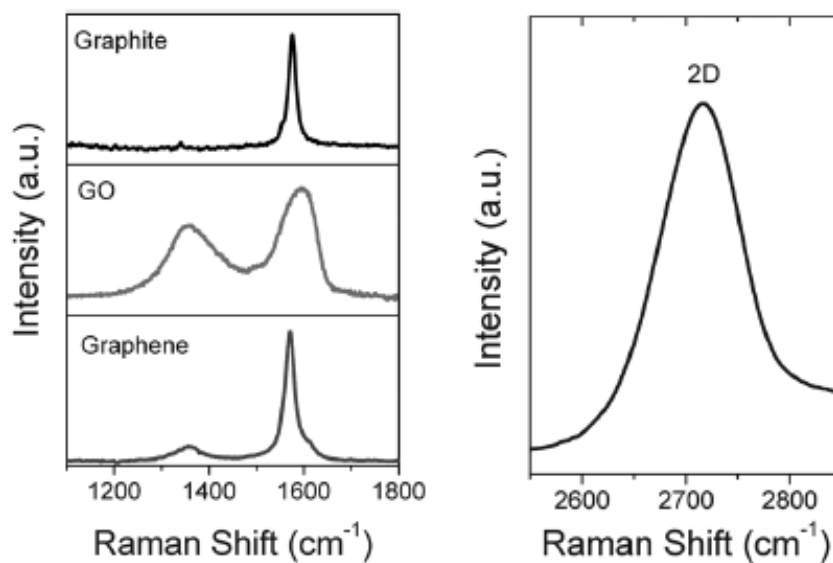


Figure 2.15: Raman spectrum of graphite, graphite oxide, and graphene [82]

The assignment of the G and D peaks is straightforward in the “molecular” picture of carbon materials [82]. The 2D band has been widely used as a simple and efficient way to confirm the number of graphene layers [75]. Along with the graphite to GO path, the G and D bands of the GO were broadened, and the G band was shifted to a higher frequency (to 1572 cm⁻¹) compared to that of graphite due to the formation of sp³ carbon by functionalization [78], [80].

2.3.2 Graphene

The disappearance of the crystalline (002) peak in the XRD pattern suggests that graphene is formed from GO through the separation of each layer [80]. The oxygen reduction and simultaneous transformation of the carbon sp³ bonds into sp² can be explained by dehydration of GO. If hydroxyl groups and hydrogen atoms are attached to two neighboring

carbons, in an acidic environment they can combine through dehydration reaction, resulting in H₂O and graphene with sp²-bonded carbon atoms. For epoxy groups, the reduction is a two-step process. If an epoxy group is attached to carbon atoms of graphene with two hydrogen atoms attached to the neighboring carbons, in an acidic environment the system first hydrates, transforming the epoxy group (-O-) to two hydroxyl groups (-OH), which then reduces to H₂O and graphene with sp²-bonded carbon atoms. Since the presence of hydrogen atoms next to the hydroxyl groups is needed for oxygen reduction, their availability will set the limit of oxygen reduction in the GO to graphene transformation, which can explain the presence of residual oxygen in the graphene [79].

Raman spectroscopy has been utilized as a powerful tool for the characterization of graphene, as it can identify the number of layers, the edge structure and any defects in graphene [75], [85]. After exfoliation, the G and D bands appeared in these spectra due to the in-phase vibration of the graphite lattice and the disorder of the graphite edges, respectively [80]. After the exfoliation of the GO to graphene, the G band shifted to lower values, indicating that graphene was produced [80]. For a single-layer graphene, a single G and 2D peak are apparent, as seen in Figure 2.16.

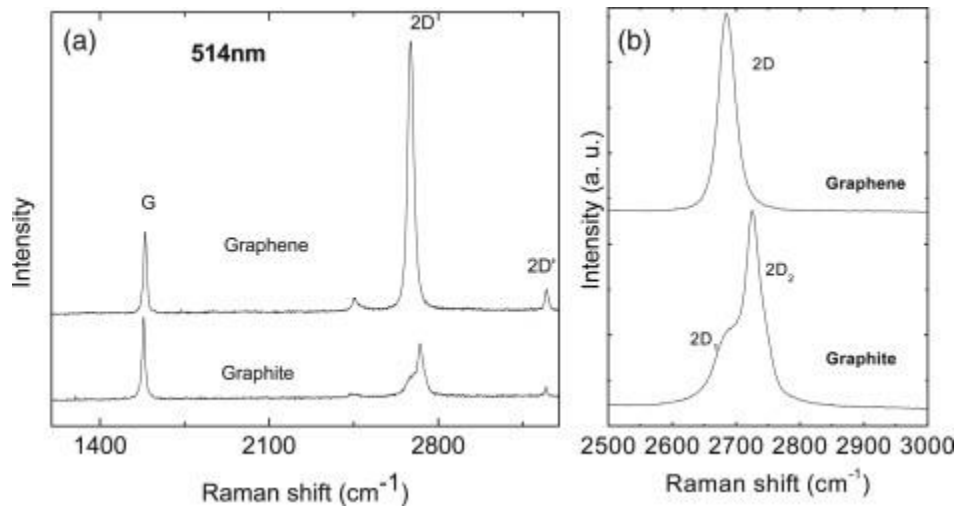


Figure 2.16: (a) Raman spectra of graphene and graphite measured at 514.5 nm; (b) Comparison of the 2D peaks in graphene and graphite [80]

From Figure 2.17 it is also seen that the 2D peak is roughly four times more intense than the G peak [82]. When the number of graphene layer increases, a much broader and upshifted 2D band is shown.

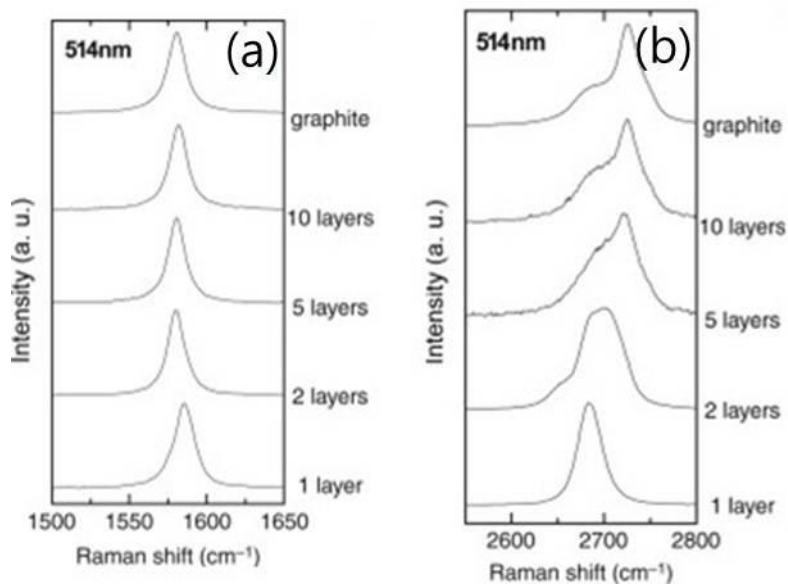


Figure 2.17: Evolution of (a) G peak and (b) 2D peak as function of number of layers at 514.5 nm [82]

For more than five layers, the Raman spectrum becomes hardly distinguishable from that of bulk graphite [82], [86]. The intensity ratio of the D-band against the G-band ($R = I_D/I_G$) is widely used to evaluate the quality of graphene materials. It shows the dependence both on the degree of graphitization and the orientation of graphite plan in the surface of graphene materials [83]. The intensity ratio can be used to determine the chemical reactivity of graphene [85] since it implies that at higher intensity ratio the skeleton structure of carbon atoms becomes more regular, and its lamellar spacing is more complete and compact [83]. The I_D/I_G values decreased in order of single-, bi-, and tri-layer graphene [85].

2.3.3. Metal oxide/reduced graphite oxide (rGO) composite

One possible way to utilize the unique properties of graphene is its incorporation in a composite material. In this regard, graphene-containing composite materials have attracted much attention [87]. Fabrication of such composites requires not only high quality production of graphene sheets but also their effective incorporation in various and desirable matrices. A method to obtain graphene as individual sheets and to maintain it in the reduced form in a suspension is the development of graphene-based composite systems. Concerning this, composition of metal [88] or metal oxide [89] nano-particles with graphene sheets have been reported. As recently demonstrated, graphene can be obtained in bulk by chemical reduction of graphene oxide (e.g. using thylene glycol as reductant [90]). Attachment of additions, such as polar molecules and polymers, on graphene oxide during the reduction process can reduce the aggregation of these graphene sheets [91].

2.3.3.1. Metal oxide and graphene interactions

It is widely known that graphite oxide (GO) obtained from the oxidation of graphite possesses various oxygen functional groups, such as hydroxides, epoxides, and carboxylic groups on the surface of GO planes [92], [93]. Because of those functional groups, GO can be dispersed in polar solvents to form a colloidal dispersion. In addition, the oxygen functional groups attached on the surface of GO play an important role in anchoring and site-nucleation of metal nanoparticles to the basal plane. The fabrication of metal oxide/graphene composite is initiated by electrostatic interaction [92]. Hydrogen bonds from the functional groups (i.e. $-OH$, -

COOH) are formed with other molecules for a hybrid composite synthesis [94]. The negatively charged GO sheets due to the oxygen functional groups have a high capability of absorbing positively charged metal ions (i.e. Co^{2+} , Zn^{2+} , Pt^{4+} or Cu^+) *via* electrostatic interactions; and act as nucleation sites [92], [93], [95]–[97]. The metal ions anchored at the nucleation sites (e.g. carboxyl, hydroxyl or epoxide groups on the GO surface) form metal clusters acting as nuclei for particle growth in later heat treatment [92], [95], [97]. The polarized metal clusters are anchored onto the GO surface by the electron transfer of conduction band electrons from the metal oxide to the rGO sheet [93], [98]. Therefore, the larger amount of functional groups acting as an electron-donating source provides a larger amount and smaller nanoparticles on the rGO sheet [95], [99]. A study proposed that, depending on the metal to be anchored, a different location of the atoms on graphene layer is predicted [77]. For example, alkaline metals (e.g. K, Na, Ti and Fe) are preferentially located at the center of the hexagon (H sites); Au, Cu, Ni, and Sn metals are expected to be placed at the top of the carbon atom (T sites); and Pt, Cr, Cl and P ions are expected to bind on top of a carbon-carbon bond (B sites). In order to promote the dispersion of metal salt ions through the GO suspension, additives (e.g. urea [100] or Na_2S [96]) have been applied since those additives release hydroxyl ions during the hydrolysis and they promote the formation of metal hydroxide which is an electrochemically active material from the metal salts ions.

The metal salt (or metal hydroxide) and GO suspension mixture is reduced to metal oxide/graphene (or graphene oxide) composite by various reduction processes, such as hydrothermal (i.e. reflux, autoclave, or microwave-assisted [101], [102]), chemical [103] and photo-catalytic method, [93]. Graphite oxide (GO) is regarded as a single layer of graphite sheet containing different hydrophilic oxygen-containing functional groups at the edge (or surface) of

the sheet [94]. After the reduction process, significant amount of C=O and C-O is removed [101], [103]; and a partial restoration of the π - π network happens. In addition, the metal particles intercalated between the GO layers lead to the exfoliation of GO [92]. From an electrochemistry point of view, electrons obtained from ethylene glycol (EG) in GO suspension are consumed during the reduction of GO; and some of them are restored in the rGO [93]. It has been proposed that about 16% of the restored electrons in the rGO network is transferred to metal ions attached on the rGO surface (i.e. Ag^+) to form metal nanocrystals (Ag^0) [93]. Metal nanoparticle (or metal oxide) and graphene (or graphene oxide) composites have been extensively studied for various applications (in particular as electrode [103]). The enhancement of electron transfer by the graphene could be attributed to their unique characteristics for the nanosheet structure and high electrical conductivity [103].

2.3.3.2. ZnO/rGO composite

Graphite oxide (GO) is negatively charged due to the functional groups attached to the sheet surface [104]. When Zinc acetate is mixed with GO, these positive Zn^{2+} ions would adsorb onto the surface of GO sheets owing to electrostatic attraction, and then in site react with NaOH to form small ZnO clusters [105]. In addition, GO is simultaneously reduced to graphene by ethylene glycol at high temperature during the formation of ZnO nanoparticles with graphene composite.

It is known that GO sheets have their basal planes decorated mostly with epoxy and hydroxyl groups, while carboxyl groups are located at the edges [106]. These functional groups, acting as anchor sites, enable the subsequent formation of nanostructures attachment on the

surfaces and edges of GO sheets [92]. At the initial stage of the reaction, zinc ions are adsorbed on graphite oxide sheets through coordination interactions of the C-O-C and -OH, or through ion-exchange with H⁺ from carboxyl. Usually, there are two interactions between GO sheets: electrostatic interactions and van der Waals interactions. If the electrostatic repulsion is dominant, then graphene oxides could be well dispersed. On the contrary, if the van der Waals interaction dominates, aggregation of exfoliated GO layers occurs during the reaction process. Consequently, there should be a critical ratio of zinc ions to GO to form well-dispersed colloids of GO sheets. When the ratio of zinc ions is lower than the critical ratio, coagulation of GO occurs during the reaction process because negative charges on reduced GO are partially or fully neutralized by zinc ions, and thus there are fewer graphene sheets in the resulting composites. With the continuous increase of the ratio of the zinc ions to GO, the electrostatic repulsion interaction between the charged GO gradually reaches and finally exceeds the van der Waals interactions because of excess sorption of zinc ion.

The characteristic peak at around a scattering angle of 10.6° corresponding to the (001) crystalline plane of GO, and the interlayer spacing of GO is 0.83 nm. In the XRD patterns of the ZnO/graphene, there are nine main peaks at $2\theta = 31.7^\circ, 34.4^\circ, 36.2^\circ, 47.5^\circ, 56.6^\circ, 62.8^\circ, 66.3^\circ, 67.9^\circ$ and 69.1° , which correspond to the (100), (002), (101), (102), (110), (103), (200), (112) and (201) crystalline planes of ZnO, respectively. This result indicates that the ZnO nanoparticles on the graphene sheets are of a wurtzite [107] structure and with a size of 16-20 nm according to the Scherrer equation (Eq. 12).

$$T(\text{nm}) = K\lambda\beta\cos\theta \quad \text{Equation 12}$$

where T is the crystal size (nm), K is the crystal shape factor, λ is the wavelength of the X-ray for the Cu target (1.542 Å), θ is the Bragg's angle and β is the full width height maximum (fwhm). However, no characteristic peaks assigned to graphene oxide or graphite is found in ZnO/graphene because the regular stacks of graphene oxide or graphite are destroyed by exfoliation. If there are no reflection peaks for graphene at $2\theta = 24.6^\circ$ and 43.3° , it indicates that the surfaces of graphene are fully covered by ZnO.

The direct evidence of the formation of ZnO nanoparticles on the plane and edges of graphene sheets is given by TEM (Figure 2.18). It can be observed that the graphene sheets are decorated by ZnO nanoparticles with an average size of 20 nm, which is consistent with the Scherrer equation analysis. The ZnO nanoparticles are well separated from each other and distributed randomly on the graphene sheets. Additionally, the shapes of the ZnO particles strictly depend on the preparation route [105]. The ZnO nanoparticles in the graphene-ZnO nanocomposites have a spherical shape; this is possible because the addition of OH⁻ caused fast reaction rate, which might cause more nuclei to form in a short time. As a result, spherical ZnO nanocrystals are obtained.

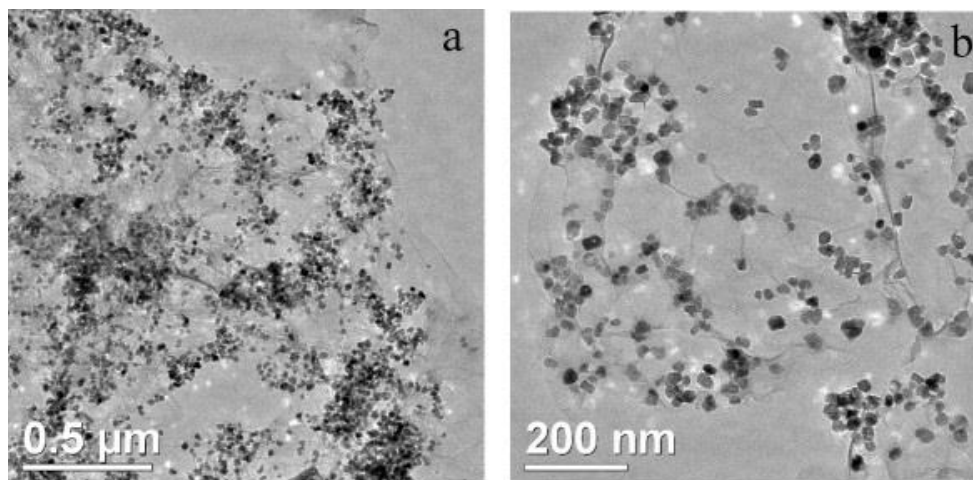


Figure 2.18: TEM images of ZnO/graphene composite [105]

The Raman spectrum of GO displays prominent peaks at $\sim 1350\text{ cm}^{-1}$ (D band), at $\sim 1580\text{ cm}^{-1}$ (G band) and at $\sim 2680\text{ cm}^{-1}$ (2D band), as shown in Figure 2.19 [108]. The Raman spectrum of ZnO/graphene also contains the D bands and G bands, but the intensity of D/G is increased, indicating the existence of a reduction procedure of GO [109]. Moreover, it has been reported that the shape and position of the overtone of the D band (2D band at $\sim 2700\text{ cm}^{-1}$) are a significant fingerprint which can be related to the formation and the number of layers of graphene sheets. The 2D peak position of the single-layer graphene sheets is observed at 2679 cm^{-1} , while the 2D band of multilayer shifts to higher frequencies by 19 cm^{-1} [110].

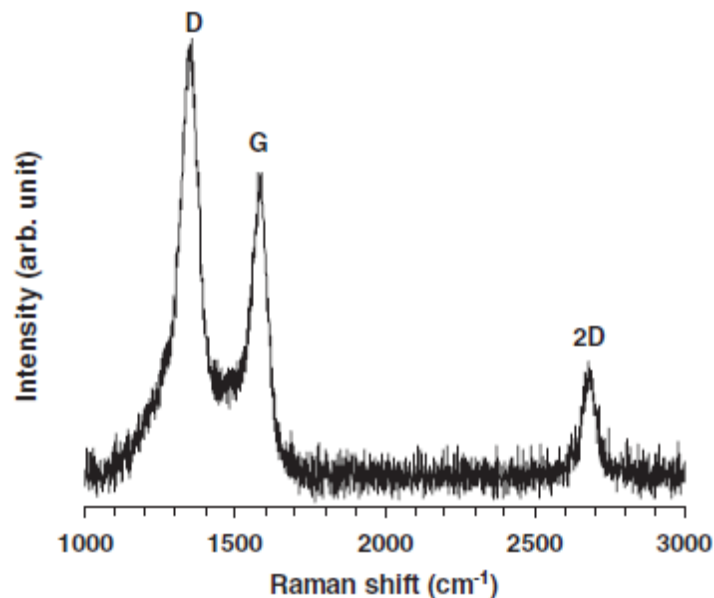


Figure 2.19: Raman spectrum of the ZnO/graphene composite [108]

Fourier transformed infrared (FT-IR) spectroscopy can also be used to characterize ZnO/graphene nanocomposites. The representative FT-IR peaks of GO at 1620 cm⁻¹ corresponding to the remaining sp² character [111]; the absorption peak at 1726 cm⁻¹, 1390 cm⁻¹ and 1223 cm⁻¹ are ascribed to C=O stretching of COOH groups, tertiary C-OH groups vibrations and epoxy symmetrical ring deformation vibrations, respectively (Figure 2.20) [112]. Furthermore, the band at 1064 cm⁻¹ is assigned to C-O stretching vibrations mixed with C-OH bending. In the FT-IR spectrum of ZnO/graphene, the absorption peak around 1210 cm⁻¹ is attributed to C-OH; the characteristic features of GO almost disappeared, indicating the reduction of GO to graphene [112].

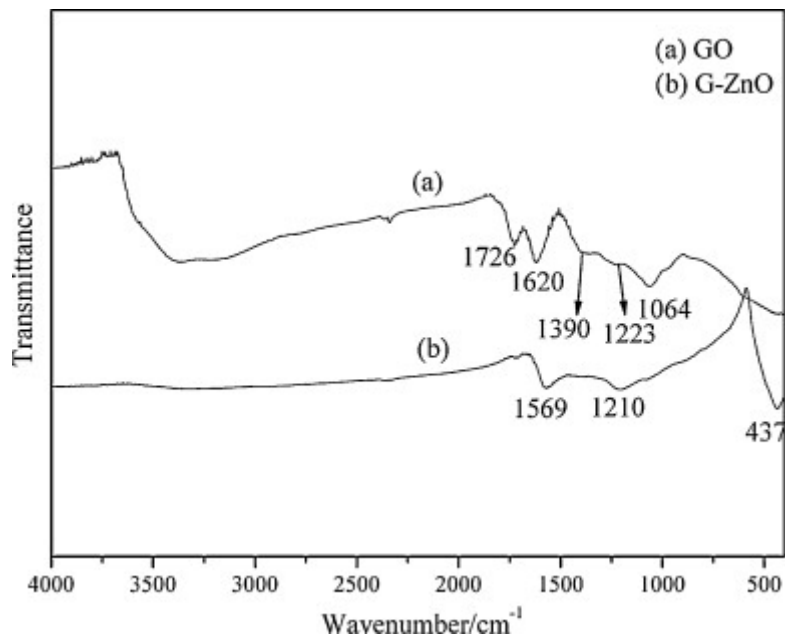


Figure 2.20: FT-IR spectra of graphite oxide and ZnO/graphene composite [112]

Additionally, the new absorption band at 1569 cm^{-1} is attributed to the skeletal vibration of the graphene sheets. The absorption band at 437 cm^{-1} is owing to stretching mode of Zn-O [113], and no characteristic absorbance of CH_3COO^- assigned to raw material zinc acetate is detected, which can confirm that the ZnO/graphene nanocomposites have been successfully prepared.

2.3.3.3. $\text{Cu}_2\text{O}/\text{rGO}$ composite

Copper oxide (Cu_2O) is attracting more research attention for its potential applications in hydrogen production, solar energy, and catalysis as well as in energy storage application [114]. Several studies have been performed regarding the integration of Cu_2O on carbonaceous materials to obtain enhanced properties for applications, such as stable catalytic activity of

carbon nanotubes-Cu₂O cathodes in water treatment [115]. Figure 2.21 shows the XRD patterns of GO, graphene and Cu₂O/graphene. The pattern of GO reveals an intense, sharp peak at $2\theta = 10.6^\circ$, corresponding to the (002) interplanar spacing of 0.749 nm [116]. This could be ascribed to the introduction of various oxygenic functional groups (epoxy, hydroxyl, carboxyl and carbonyl) attached on both sides and edges of carbon sheets. These oxygen-containing functional groups will subsequently serve to locate sites for metal complexes [117]. No peaks for graphite ($2\theta = 26.6^\circ$) could be observed, suggesting no further agglomeration of a few layer of graphene sheets which are hindered by Cu₂O.

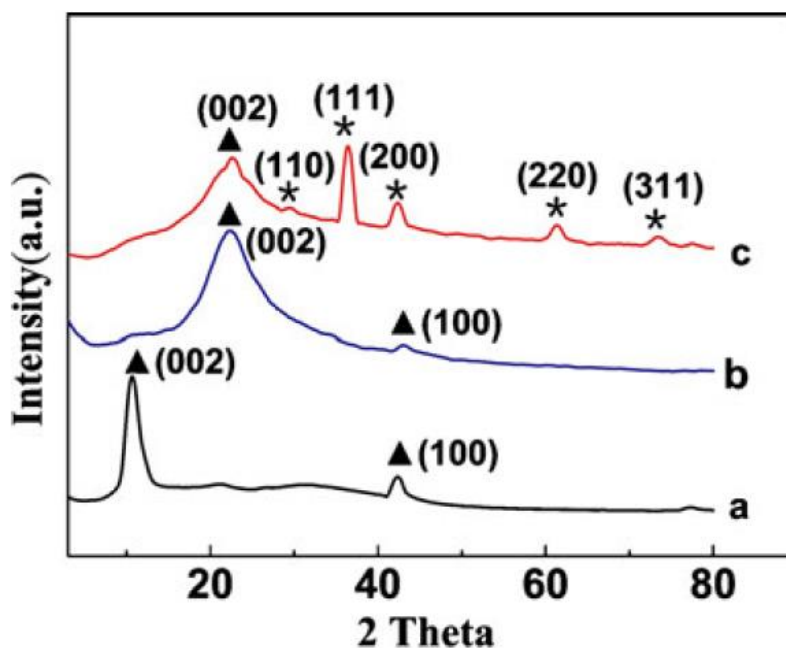


Figure 2.21: XRD of (a) graphite oxide, (b) graphene, and (c) Cu₂O/graphene composite [116]

The diffraction peak of GO ($2\theta = 10.6^\circ$) could no longer be observed, which demonstrates the reduction of GO. The strong diffraction peaks at $2\theta = 29.6^\circ, 36.5^\circ, 42.5^\circ, 61.8^\circ$

and 73.6° are in good agreement with the (110), (111), (200), (220) and (311) crystal planes of pure Cu_2O with cubic phase, respectively. The position of the (002) diffraction peak (d-space 0.39 nm at 22.6°) moved slightly to higher angle after deposition of Cu_2O nanoparticles on graphene, which indicates that GO was further converted to crystalline graphene, and the conjugated graphene network (sp^2 carbon) has been reestablished due to the reduction process.

As a result of the introduction of oxygen-containing functional groups (hydroxyl, carboxyl, and epoxy groups) on graphene nanosheets, GO could easily adsorb polar molecules or polymers via the functional groups as anchors [111]. The characteristic features in the FT-IR spectrum of GO are the absorption bands corresponding to the C=O carbonyl stretching at 1720 cm^{-1} , the C-OH stretching at 1224 cm^{-1} , the C-O stretching at 1050 cm^{-1} , and the remaining sp^2 character at 1620 cm^{-1} (Figure 2.22) [111]. A composite of copper and graphene can be identified by FT-IR. After mixing the two components of GO and copper acetate ($\text{Cu}(\text{Ac})$), the FT-IR spectrum of the hybrid becomes a combination of the absorption bands of GO and $\text{Cu}(\text{Ac})_2$ [118]. Apart from the signal of $\text{Cu}(\text{Ac})_2$, the absorption bands at 1720 and 1620 cm^{-1} (a shoulder peak) are attributed to GO [119]. Additionally, the absorption band of carbonyl of the copper acetate shifting from 1600 to 1560 cm^{-1} and the broadened peaks appearing around 1100 cm^{-1} both indicate that there is a strong interaction between copper acetate and GO. After adsorption of $\text{Cu}(\text{Ac})_2$ molecules on graphite oxide sheets, the interlayer spacing of the dried GO broadened [120].

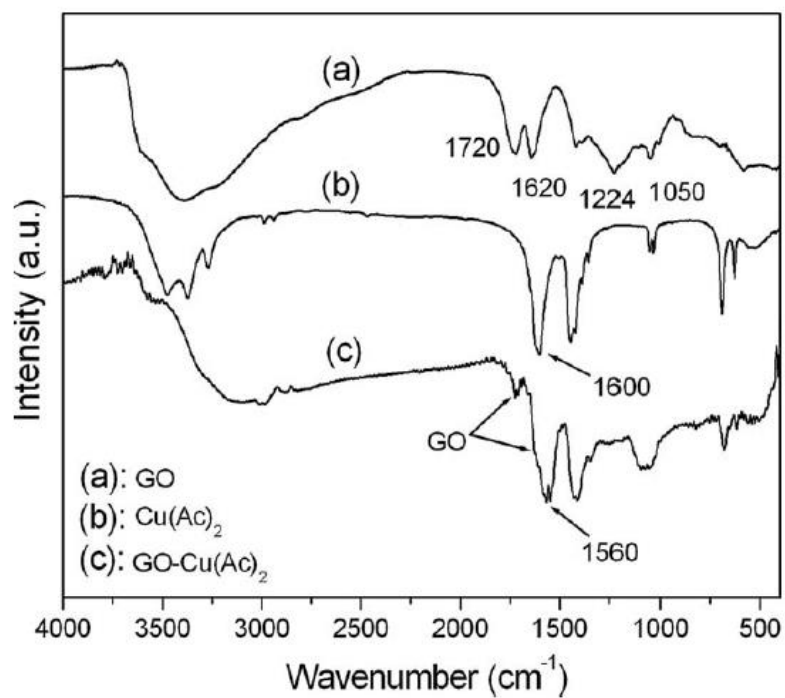


Figure 2.22: FT-IR spectra of (a) graphite oxide, (b) $\text{Cu}(\text{Ac})_2$, (c) $\text{Cu}(\text{Ac})_2$ /graphite oxide composite [111]

Morphology of Cu_2O /graphene nanocomposites has been characterized by TEM and SEM (Figure 2.23) [121].

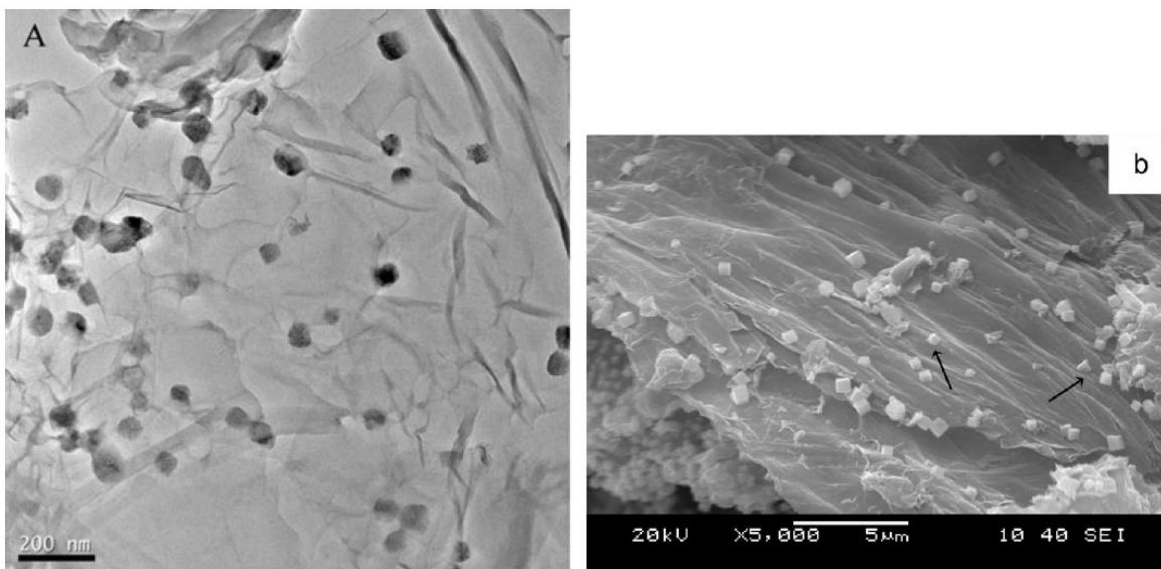


Figure 2.23: (a) TEM; (b) SEM images of Cu₂O/graphene composites [121]

The Cu₂O particles were uniformly distributed on transparent graphene and no particles scattered out of the supports, indicating a strong interaction between graphene and the particles. Some Cu₂O nanoparticles were slightly aggregated due to the loading level close to saturation. Highly dispersed Cu₂O on the support with larger surface areas have advantages for catalytic activity.

2.3.3.4. Effects of rGO for H₂S adsorption efficiency

The oxygen functional groups attached on the surface of GO play a critical role for H₂S adsorption. It has been widely announced that GO consists of graphene layers connected with various oxygen-containing functional groups, such as hydroxyl, epoxy and carboxyl, on the basal planes and at the edges of these layers [23], [122]–[124]. Those oxygen-containing functional groups provide potential sites to load nanoparticles (i.e. Cu(OH)₂ [29], MOF [123], Cu₂O [124]).

The metal oxide and GO are linked by hydrogen bonding which are generated during the composite synthesis procedure [23]. The hydrogen and oxygen bonding are connecting the metal oxide (or hydroxide) to the epoxy and hydroxyl groups existing on the basal GO planes [24]. Those new linkage groups result in the change of the surface chemistry (i.e. pK_a distribution of the bridging and terminal hydroxides) of the composite; thus increasing the surface basicity of the composite [24], [125]. It promotes H_2S dissociation to HS^- [23]. The dissociated HS^- is associated with the $-OH$ terminal groups on GO and metal hydroxide; and replace each other. This activation of oxygen by the carbonaceous component causes the formation of sulfide (or sulfites) [29]. Involvement of these hydroxyl groups in the reactive adsorption process could be confirmed using FT-IR and potentiometric titration analysis since most of the terminal $-OH$ groups disappeared after H_2S exposure [24], [29]. As metal oxide (or hydroxide) and GO are sharing the hydroxyl groups, this leads to an increase in surface basicity. According to those phenomena, metal oxide/GO composite generally possesses a higher H_2S adsorption capacity than metal oxide/graphene composite [125].

For H_2S adsorption, several studies have been conducted under moist and dry conditions [24]. For moist condition, the water is apparently a critical factor since it dissociates H_2S ; and the dissociated HS^- ions are adsorbed on the surface [29], [125]. This explains why the H_2S adsorption capacity under moist condition was observed to be much higher than that under dry condition [125]. The chemisorbed oxygen on the surface is consumed for the adsorption. It was confirmed that the carboxylate groups on composite (located at 1400 and 1500 cm^{-1} FTIR spectra) significantly decreased after H_2S exposure [125]. For dry condition, different mechanisms govern the adsorption. Direct replacement of the dissociated HS^- ions with $-OH$ groups on oxide particles are the dominant mechanism [29] for sulfide formation due to the limitation of the

hydroxyl groups. After H₂S exposure, the appearance of water has been found as a product from the sulfidation reaction using FTIR analysis (~ 3500 cm⁻¹ band) [29]. Therefore, even without moisture during H₂S adsorption experiments, hydroxyl groups existing on the basal of GO planes are promoting the adsorption capacity.

2.4. Research scope

As described in this chapter, adsorptive desulfurization method from liquid and gas phase sulfur compounds has been extensively studied; and various carbon adsorbents have been used in order to achieve deep desulfurization levels. Several challenges (e.g. providing high surface area and preventing sintering of nano-sized metal oxides) for room temperature and high temperature processes should be solved. A novel approach to overcome those challenges is proposed in this work where 2-dimensional carbon material (graphene-related) has been investigated since its unique characteristics, such as sp² carbon configuration for graphene and oxygen functional groups on reduced graphite oxide (rGO), could be an answer to solve those challenges. Therefore, the synthesis methods of graphene, rGO and metal oxide/rGO composites are introduced. Results and discussion for DBT adsorption on graphene, H₂S adsorption on ZnO/rGO composite, H₂S adsorption on Cu₂O-ZnO/rGO composite and regeneration ability on ZnO/rGO composite are presented in the following chapters.

Chapter 3. Experimental

3.1. Adsorbent preparation

3.1.1. Preparation of graphite oxide (GO)

Graphite oxide was synthesized using a mixture of 360 mL of sulfuric acid (Sigma-Aldrich, ACS reagent, 95.0-98.0%), 40 mL of phosphoric acid (Sigma-Aldrich, ACS reagent, $\geq 85\text{wt}\%$ in H_2O), and 3.0 g of graphite powder (Sigma-Aldrich, $<45\mu\text{m}$, $\geq 99.99\%$). This mixture was placed in an ice bath and when the temperature reached below 5°C , 18.0 g of KMnO_4 (Samchun Chemical, 99.3%) was added drop-wise. The mixture was stirred for 1 h and then transferred to a heating mantle to provide isothermal conditions at 50°C . The oxidation process was conducted for 18 h. The system was then cooled to room temperature naturally, and then placed in an ice bath again. 400 mL of de-ionized water and 15 mL of 30% H_2O_2 (OCI Company Ltd, 30wt% in H_2O) were added gradually. The mixture turned bright yellow and generated copious bubbles. The mixture was stirred for 1 h and then centrifuged at 3500 rpm for 3 min. The remaining solid paste was washed with a mixture of 100 mL of de-ionized water and 100 mL of 30% HCl (Sigma-Aldrich, ACS reagent, 37%) twice. The product was then rinsed twice again with 200 mL of de-ionized water. After the washing steps, the paste was freeze- and vacuum-dried overnight [126].

3.1.2. Preparation of graphene and reduced graphite oxide (rGO)

Graphene samples were prepared using the following procedure. One gram of each GO was dissolved in a solution of 500 mL of de-ionized H₂O and 1.5 mL of aqueous ammonia solution and then ultra-sonicated for 1 h in order to prepare a well-dissolved GO aqueous suspension. Then 500 µL of hydrazine solution (35 wt% in H₂O, Sigma-Aldrich) was added. The mixture was then boiled at 100 °C overnight. The mixture was cooled to room temperature, and then filtered through a 0.22 µm membrane filter (GVWP type, Millipore). The product was washed with 500 mL of de-ionized water for 1 hr and then filtered again. The graphene powder was dried overnight in a vacuum chamber at room temperature.

Reduced graphite oxide (rGO) samples were prepared by the following method. 400 mg of GO was dissolved in 200 mL of ethylene glycol and 200 mL of 1M NaOH aqueous solution. Then the GO mixture was ultra-sonicated for 30 min. 300 µL of hydrazine solution (Sigma-Aldrich, 35wt% in H₂O) was added before the reduction process. Then the ultra-sonicated mixture was reduced by microwave irradiation for 3 min (1 min irradiation with 1 min break, 3 times). After cooling down, the mixture was filtered and washed with DI-water three times using centrifuge. Finally, the paste was freeze- and vacuum-dried overnight.

3.1.3. Preparation of metal oxide/rGO composite

For ZnO/rGO composite, 400 mg of GO was dissolved in 200 mL of ethylene glycol (Sigma-Aldrich, ReagentPlus[®], ≥99%) and then underwent ultra-sonication for 30 min. 100 mL of 0.1 M aqueous NaOH (Sigma-Aldrich, ACS reagent, ≥97.0%) solution was added, and the

mixture was sonicated for an additional 30 min. Then, 100 mL of 0.07 M aqueous zinc acetate (Sigma-Aldrich, ACS reagent, $\geq 98\%$) solution was added into the mixture drop-wise (2.0 mL/min) for 50 min. 300 μL of hydrazine solution (Sigma-Aldrich, 35wt% in H_2O) was added before the reduction process. The zinc acetate/GO (ZnAc/GO) mixture was reduced by microwave irradiation for 3 min (1 min irradiation with 1 min break, 3 times). This reduction process produces ZnO/rGO composite. After cooling down, the ZnO/rGO mixture was filtered and washed with DI-water three times until the pH reached around 7.0. Finally, the paste was freeze- and vacuum-dried overnight. For reference, ZnO powder was also prepared. The synthesis of metal oxide/rGO composite is illustrated as Figure 3.1 [126].

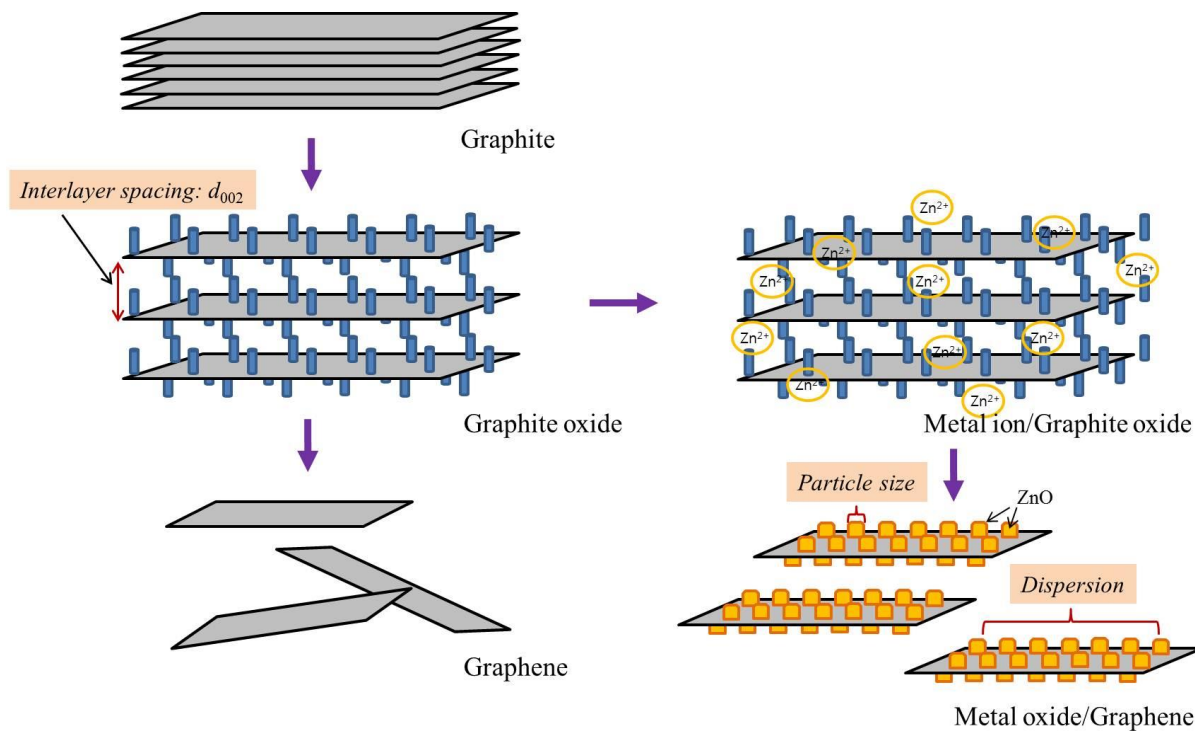


Figure 3.1: Illustration of the synthesis of metal oxide/rGO composite

For Cu₂O-ZnO/rGO composites, 0.07 M aqueous zinc and copper acetate (Sigma-Aldrich, ACS reagent, ≥98%) solutions were prepared. Then, 100 mL of 0.07 M metal acetate solutions were prepared depending on the Cu/Zn ratios (0/100, 2/98, 5/95, 10/90, 15/85, 20/80, 25/75 and 35/65 vol%, respectively). Those prepared metal solutions were mixed with GO solutions; then sonicated another 30 min. 300 μL of hydrazine solution (Sigma-Aldrich, 35wt% in H₂O) was added before the reduction process. The Cu/Zn/GO mixture was reduced by microwave irradiation for 3 min (1 min irradiation with 1 min break, 3 times). After cooling down, the mixture was filtered and washed with DI-water three times using centrifuge. Finally, the paste was freeze- and vacuum-dried overnight [126].

3.2. Adsorbent characterizations

3.2.1. BET

The Langmuir isotherm theory widely used for monolayer adsorption can also be applied to model multi-layer adsorption *via* the method invented by Brunauer, Emmett and Teller in 1938 (BET method) with a few assumptions: (i) the adsorbate is typically adsorbed in a monolayer (ii) one species is adsorbed per site (iii) ΔH_a (enthalpy of adsorption) is independent of θ (coverage) and (iv) equilibrium exists between adsorption and desorption. Based on the assumptions listed above, the coverage for multilayer adsorption, θ, can be derived by Equation 13:

$$\theta = \frac{V}{V_m} = \frac{cx}{(1-x)[1+(c-1)x]} \quad \text{Equation 13}$$

where $x = P/P_0$, P_0 = vapor pressure of the adsorbing gas at a given temperature, and V_m is the maximum volume of gas adsorbed in the monolayer. The values of c and V_m can be obtained by experimental data. Eq. 13 can be linearized and rearranged to Equation 14.

$$\frac{1}{V[(P_0/P)-1]} = \frac{1}{V_m c} + \frac{c-1}{V_m c} \left(\frac{P}{P_0}\right) \quad \text{Equation 14}$$

V = amount of gas adsorbed (cm^3/g)

P = gas pressure

P_0 = equilibrium vapor pressure at the test temperature

V_m = amount of adsorbate as monolayer (cm^3/g) (= 2.8619 cm^3/g)

C = BET constant

Volume adsorbed versus P/P_0 experimental data are collected at the boiling point of the adsorbate, normally N_2 at -196°C . When the vapor pressure (P) is low compared to P_0 ($0.05 < P/P_0 < 0.3$), the plot of $1/[V*((P_0/P)-1)]$ vs. (P/P_0) is linear and the plot yields the magnitudes of C and W_m . The surface area S per unit mass (m) of the sample is computed by the following Equation 15 using the cross-sectional area of the adsorbed gas molecules

$$S = n_m N_{AV} \alpha \quad (\text{m}^2/\text{g}) \quad \text{Equation 15}$$

where S = surface area (m^2/g), n_m = number of mole, N_{AV} = Avogadro's number and $\alpha = 1.62 * 10^{-20} \text{ m}^2/\text{molecule}$ for N_2 .

For this study, the BET measurements for pure ZnO and ZnO/rGO composites were conducted using a Micromeritics Gemini 3 2375. Nitrogen gas was used as the adsorbate. Around 100 mg of the pelletized catalysts were loaded and pre-treated at 200°C in vacuum overnight to remove any impurities and moisture on the surface. The surface area was measured at 77 K which is the boiling point of nitrogen within a P/P₀ range between 0.05 to 0.3.

3.2.2. XRD

XRD is widely used to characterize and identify catalysts. An X-ray beam is scattered when it hits the atoms in a crystal. XRD patterns are generated using a stationary X-ray source (usually Cu K α), and the scattered X-rays are detected by a movable detector. Since crystals consist of regular, repeated arrays of atoms, the X-ray beam diffracted by the atoms has a regular array of waves. The detector scans the intensity of the diffracted radiation as a function of 2 θ between the initial and the diffracted radiation. The 2 θ angle value from XRD provides the corresponding lattice spacing which is characteristic of a certain crystal (Equation 16).

$$n\lambda = 2d\sin\theta$$

Equation 16

λ : Wavelength of the X-ray

d : Distance between two lattice planes

θ : Angle between the incoming x-ray and the normal to the reflecting lattice plane

n : Integer called the order of the reflection

The width of the diffraction peaks provides information about the dimensions of the reflecting phases (Equation 17). The shape, intensity and position of the diffraction peaks can provide information about the crystallinity.

$$\langle L \rangle = \frac{K\lambda}{\beta \cos\theta} \quad \text{Equation 17}$$

$\langle L \rangle$: A measure for the dimension of the particle in the direction perpendicular to the reflecting plane

β : Peak width

λ : X-ray wavelength

K : A constant (~ 1)

θ : Angle between the beam and the normal on the reflecting plane

For this research, powder X-ray diffraction patterns were measured on a Rigaku D/Max-III C using standard Bragg-Brentano geometry with Ni-filtered Cu K α radiation ($\lambda_1 = 1.5406\text{\AA}$, $\lambda_2 = 1.5444\text{\AA}$) and 40 kV/100 mA X-ray radiation. The spectra were collected for a 2θ range of 5 to 80° using a step size of 0.01 and a count time of 1s.

3.2.3. XPS

X-ray photoelectron spectroscopy (XPS) is a technique to investigate the chemical composition of surfaces. The low energy (~ 1.5 keV) X-ray irradiates the surface to provoke the photoelectric effect. A high resolution electron spectrometer determines the energy spectrum of

the emitted photoelectrons. The specific *quantitative* information of the surface functional groups can be measured. The initial total energy state of the system when the emission of the photoelectron is applied is the sum of the applied photoelectron energy ($h\nu$) and the initial state of the target energy (E_i). After the X-ray hits the surface, the total energy of the final stage is the sum of the kinetic energy of the photoelectron ($E_k(e^-)$) and the energy of the ionized atom (E_f) as illustrated in Figure 3.2 and balanced by the following equations 18 and 19.

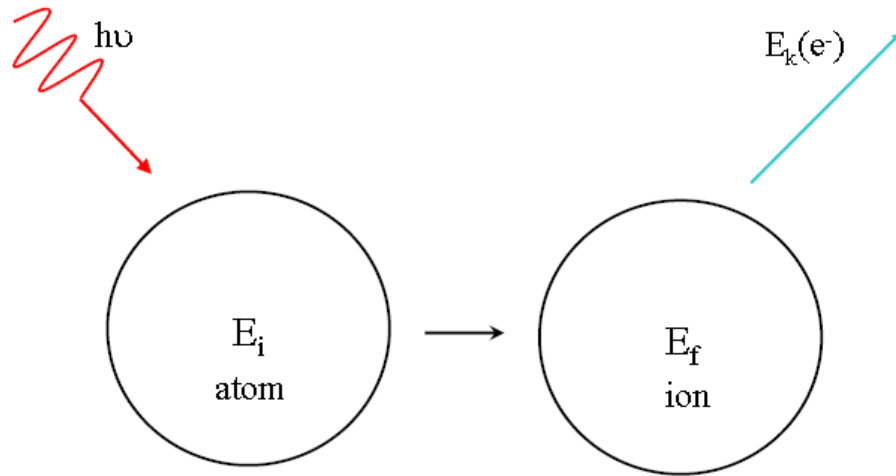


Figure 3.2: Schematic illustration of XPS [127]

$$h\nu + E_i = E_k(e^-) + E_f \quad \text{Equation 18}$$

$$h\nu - E_k(e^-) = E_f - E_i = E_b \quad \text{Equation 19}$$

By equating the total energies of the initial and final stages, the “binding energy” (E_b) of the electron can be obtained from the difference between the final and initial state energies. The binding energies are characteristics of specific electron orbitals in specific atom [127].

For this study, the x-ray photoelectron spectroscopy (XPS, AXIS Ultra DLD, KRATOS Inc.) was used with Mono chromatic Al Ka (1486.6 eV) for X-ray source, 0.05 eV/step; and no surface treatment were used.

3.2.4. FT-IR

Infrared (IR) spectroscopy is widely known for its uniqueness to identify vibrational structure of various materials since the spectra is able to measure complex molecular vibrational modes. IR radiations are the electromagnetic waves in the range of 100 cm^{-1} to 14285 cm^{-1} microns (longer than the red of visible light and shorter than microwaves) [128]. When chemical bonds absorb IR radiation, the bonds vibrate and the intermolecular distance of two or more atoms changes. There are two general types of vibrations: stretching and bending. Stretching is a symmetric or asymmetric rhythmical movement while bending vibration implies the changes of the bonding angles of atoms. Therefore, the specific information of the functional groups can be identified due to the correlation between the wavenumbers at which a molecule absorbs IR radiation and its structure. When the beam passes through the sample, the sample adsorbs all the different wavelengths characteristics of its spectrum. From FT-IR measurement, the difference in the surface chemistry, depending on the synthesis methods, could be distinguished (Table 3.1) [129].

Table 3.1: Characteristics of IR spectra [129]

Chemical structure	IR frequency (cm ⁻¹)
O-H	3440
C=O	1741
C=C	1623
C-O	1398, 1288, 1076
C-H	2881

For this study, fourier-transform infrared (FT-IR) spectroscopy was carried out using a Nicolet 6700 (Thermo Scientific) with KBr dilution at 1:1200 weight ratio.

3.3. Adsorption conditions and tests

3.3.1. DBT adsorption test

For the dibenzothiophene (DBT) adsorption reaction, 25 mg of graphene material was loaded into vials. Two mL of a diesel modeled solution (initial sulfur concentration of 377.1 ppm in *n*-tetradecane) and modified commercial diesel (SK Energy, South Korea, initial sulfur level: 8.99 ppmw) solution with initial sulfur concentration of 376.1 ppmw were loaded into the vials. The reactions were conducted in ultra-sonication (Model: Branson 5510) for 1 hr. After the reaction was complete, the product mixture was filtered through a syringe filter (Puradisc 25 PP filter, Whatman[®], diameter: 25 mm, pore size: 0.2 μm) to collect the liquid product only. The product samples were analyzed in a trace sulfur analyzer [Model: TS-100V; Mitsubishi Chemical;

Analytical method: oxidative pyrolysis-ultraviolet fluorescence method; Furnace temperature: 900-1000°C; Gas flow: O₂ (391 mL/min), AUX (177 mL/min), Ar (351 mL/min)]. The quantitative adsorption amount of DBT can be measured using Eq. 20.

$$\frac{g \text{ of } S}{g \text{ of ads}} = \frac{(C_{o,DBT} - C_{i,DBT}) \times V_{sol} \times \rho_{n-tetradecane}}{g \text{ of ads}} \quad \text{Equation 20}$$

where C_{o,DBT} is the concentration of DBT after reaction (ppm), C_{i,DBT} is the initial concentration of DBT (ppm) and V_{sol} is the volume of DBT solution tested (mL).

3.3.2. H₂S adsorption tests

Dynamic breakthrough tests were conducted at 300°C. 0.5 cm³ of the adsorbents diluted with 1.0 cm³ of Al₂O₃ (Sigma-Aldrich, ~ 150 mesh) for a total of 1.5 cm³ of bed were packed into a quartz tube (internal diameter 10 mm). In a typical test, as illustrated in Figure 3.3, a flow of H₂S (5 mL/min, 3.01 vol% of H₂S balanced with N₂) was mixed with 195 mL/min of N₂ gas before passing through the adsorbent bed.

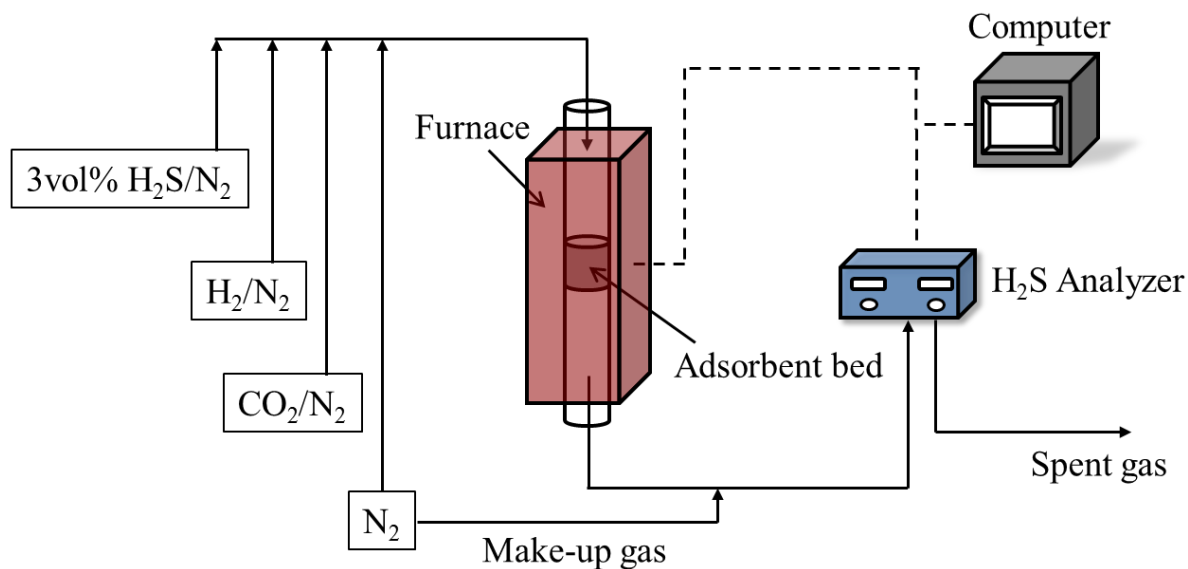


Figure 3.3: H₂S adsorption experiment setup

The feed H₂S concentration was 750 ppm with a total flow rate of 200 mL/min. The product stream was further diluted with 1800.0 mL of N₂ before injection to the H₂S analyzer (approximately 10 times dilution) since the limitation of the H₂S analyzer detectable range is only up to 20 ppm (Fluorescence H₂S Analyzer, Model 101E, Teledyne). The experiments were carried out until the output H₂S concentration reached ~ 5 ppm from the analyzer reading (the actual concentration leaving the bed being then ~ 50 ppm). The experimental breakthrough time is determined when the outlet H₂S concentration reaches 1 ppm. For regeneration tests, the spent adsorbent was heated to 600°C in N₂ environment for 1 hr. After the hydrothermal decomposition, the adsorbent was cooled down to the reaction temperature (i.e. 200 or 300 °C) in N₂ for another sulfidation reaction.

In order to quantify the reactivity of adsorbents with H₂S, sorbent utilizations were calculated as follows (Eq. 21) with a initial H₂S flow rate of 0.15 mL H₂S/min.

$$\text{Sorbent utilization (\%)} = t / T_t * 100\% \quad \text{Equation 21}$$

$$T_t = \frac{1 \text{ mol ZnO}}{81.4 \text{ g ZnO}} \times \frac{22400 \text{ mL H}_2\text{S}}{1 \text{ mol H}_2\text{S}} \times \frac{\text{min}}{0.15 \text{ mL H}_2\text{S}} = 1834 \text{ min/g ZnO} \quad \text{Equation 22}$$

$$\frac{\text{g of S}}{\text{g of Ads.}} = \frac{0.15 \text{ mL H}_2\text{S}}{\text{min}} \times \frac{1 \text{ mol H}_2\text{S}}{22400 \text{ mL H}_2\text{S}} \times \frac{34.08 \text{ g H}_2\text{S}}{1 \text{ mol H}_2\text{S}} \times \frac{32.06 \text{ g S}}{34.08 \text{ g H}_2\text{S}} \times t \left(\frac{\text{min}}{\text{g Ads.}} \right) \quad \text{Equation 23}$$

$$\text{Efficiency (\%)} = \left(\frac{t}{T_t} \right) \times \left(\frac{1}{\text{wt\% ZnO}} \right) \quad \text{Equation 24}$$

where t is the experimental breakthrough time (min/g of adsorbent), and T_t is the theoretical breakthrough time (min/g of ZnO). The experimental breakthrough time (t) is determined when the outlet H_2S concentration reaches 0.1 ppm. The quantitative amount of sulfur adsorbed per gram of adsorbent (i.e. ZnO or ZnO/rGO) can be calculated using Eq. 23. The ZnO utilization efficiency (%) can be calculated based on the ZnO weight percentage of 62.3% in the adsorbent using Eq. 24.

Chapter 4. DBT Adsorption on graphene

This chapter presents DBT adsorption experimental results and discussions with characterizations of graphene adsorbent. As listed in Chapter 2, the conventional hydrodesulfurization (HDS) process is widely used for most fuels currently. However, the HDS process possesses an important drawback in that bulky thiophene compounds (e.g. dibenzothiophene, DBT) are known to be the most difficult sulfur compound to be removed from the conventional HDS process. Therefore, a non-HDS technique (i.e. adsorptive desulfurization) is required in order to achieve deep desulfurization level, including DBT. Chapter 2 introduced several metal oxide adsorbents which can remove DBT compounds relying on the π - π interaction mechanism since DBT possesses two benzene rings with thiophene. Using this concept, a novel method using 2D carbon material, graphene, which possess sp^2 carbon configuration (free π orbitals on both side of graphene layer) has been applied in order to achieve deep desulfurization efficiency of DBT.

4.1. DBT adsorption capacity on graphene

Given the characterizations described, GOP, which has the larger interlayer d -spacing, should be more easily reduced than GOH. GPP has fewer defects (larger L_a) and thinner (smaller L_c) resulting in a higher specific surface area than GPH. It can be concluded therefore that GPP should have a better structural integrity for sp^2 configuration (possessing π -bonds) than GPH. In other words, for an identical mass of graphene, GPP should have a greater density of π -bonds than GPH. Since π - π interaction is important for adsorbing bulky thiophenes [130], [131], it was

decided to characterize further both GPP and GPH through their capacity to adsorb dibenzothiophene (Figure 4.1).

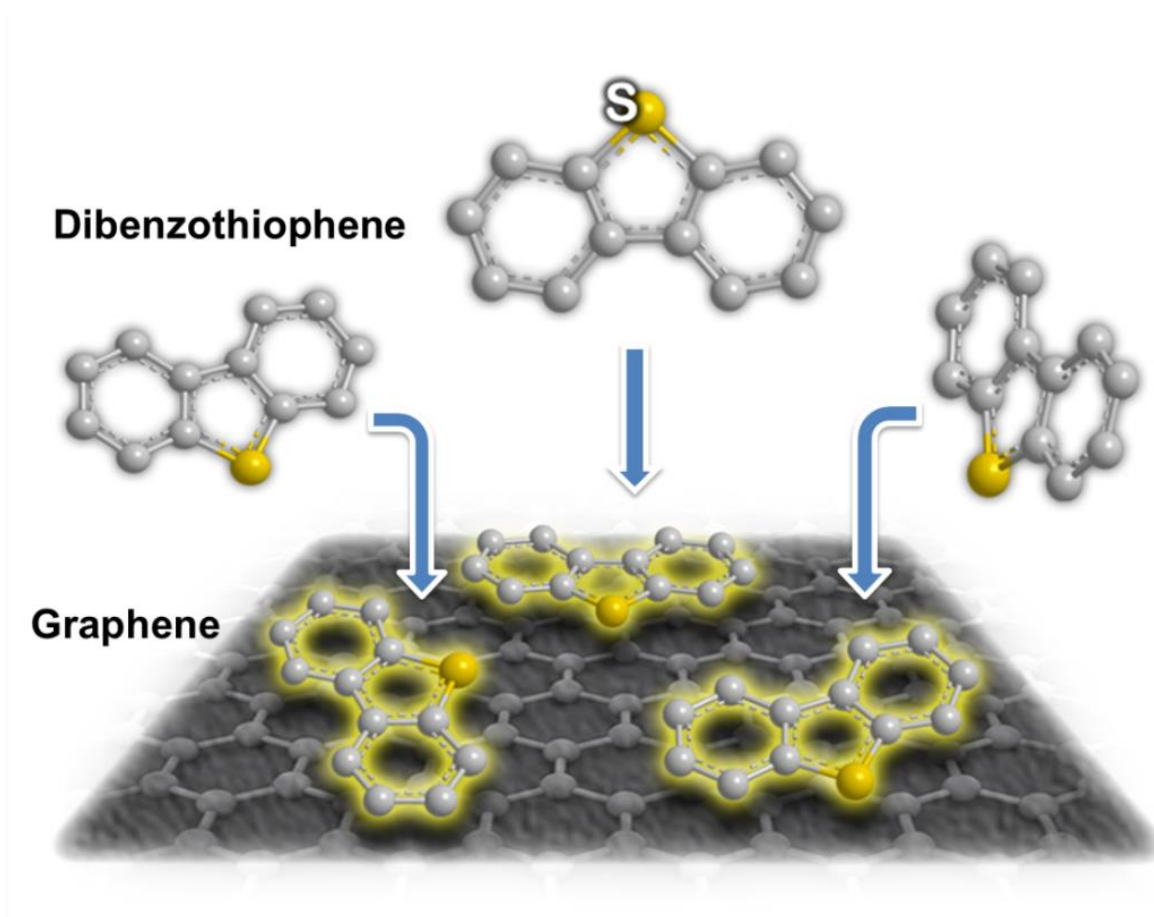


Figure 4.1: Schematic illustration of the adsorption of DBT on graphene

Dibenzothiophene (DBT), which has two aromatic rings with thiophene, can be adsorbed via π - π interaction [120], [132]. Our results suggest that GPP has more available π -bonds than GPH. Figure 4.2 shows DBT adsorption results obtained using commercial diesel and model diesel solutions. The initial sulfur concentration for the model solution was set at 377.1 ppmw. Because graphite oxide has a sp^3 configuration (no available π -bonds for the adsorption),

the raw graphite and graphite oxides cannot adsorb DBT, even though DBT has π -bonds from both aromatic rings. However, the DBT compounds were adsorbed on the surface of graphene, a fact that confirms that π -bonds (sp^2 carbon configuration) are needed for the adsorption of DBT compounds. It was found that, depending on the synthesis methods of the graphite oxide, the adsorption capacity of DBT on graphene is affected. Our results indicate that the adsorption capacity of GPP (10.6 ± 0.5 mg S/g Ads.) is almost twice that of GPH (5.5 ± 0.6 mg S/g Ads.), with an initial sulfur concentration of 377.1 ppm.

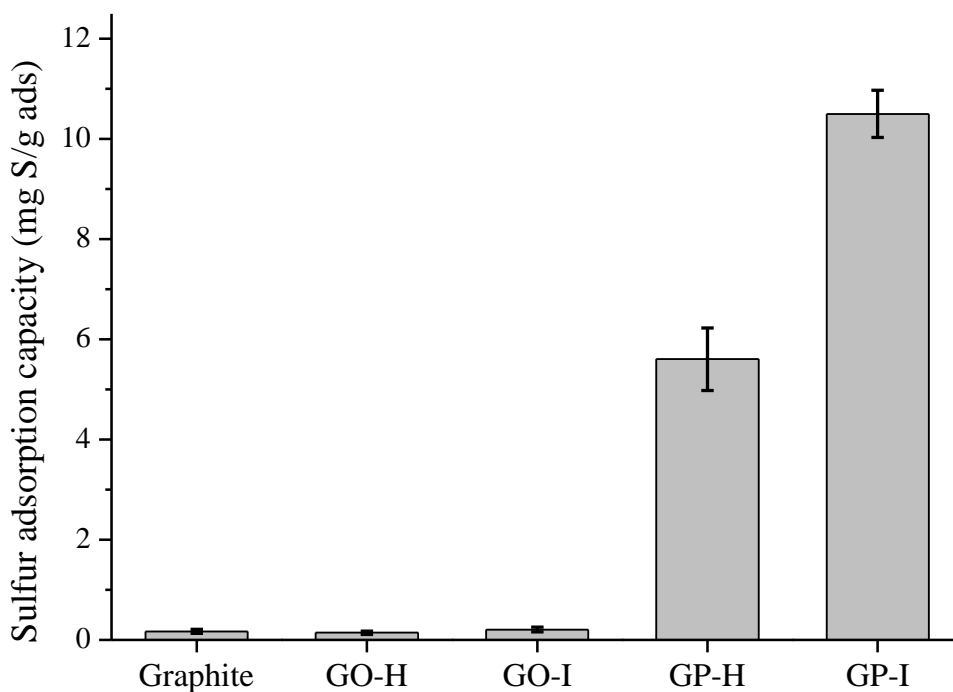


Figure 4.2: DBT adsorption on graphene using a modeled diesel solution

Since a commercial diesel fuel contains only 8.99 ppm sulfur, extra DBT was added for the adsorption tests, resulting in a total initial sulfur concentration of 376.1 ppm. Since commercial diesel contains many aromatic compounds, it is anticipated that the DBT adsorption capacity obtained with commercial diesel will be lower than that with a model diesel. Using commercial diesel, GPH and GPP showed an adsorption capacity of 1.85 and 3.31 mg S/g adsorbent, respectively. Even in a very severe environment (a commercial diesel fuel), graphene shows a sulfur adsorption capacity even though the amount of sulfur adsorbed is much less than when using the model diesel. To investigate the selectivity of DBT, the effect of toluene (aromatic compound) was tested by adding different concentrations of toluene – 9 and 36 wt% of toluene in *n*-tetradecane solvent. The addition of aromatic component, toluene, decreased the DBT adsorption capacity for both graphene samples, GPH and GPP, since the graphene and toluene also form π - π interaction between them.

4.2. Characterizations of graphene adsorbents

Figures 4.3 and 4.4 show the XRD patterns for graphite oxide and graphene, respectively. The interlayer *d*-spacing between the graphitic layers should be an indicator of the degree of oxidation of graphite oxide. Oxygen-containing functional groups, such as hydroxyl, epoxy or carboxyl groups, on and between graphite layers enlarge the interlayer spacing of the graphite layers [133] and turn the graphite oxide to an sp^3 configuration. A larger interlayer spacing should therefore indicate a higher degree of oxidation of the graphite oxide.

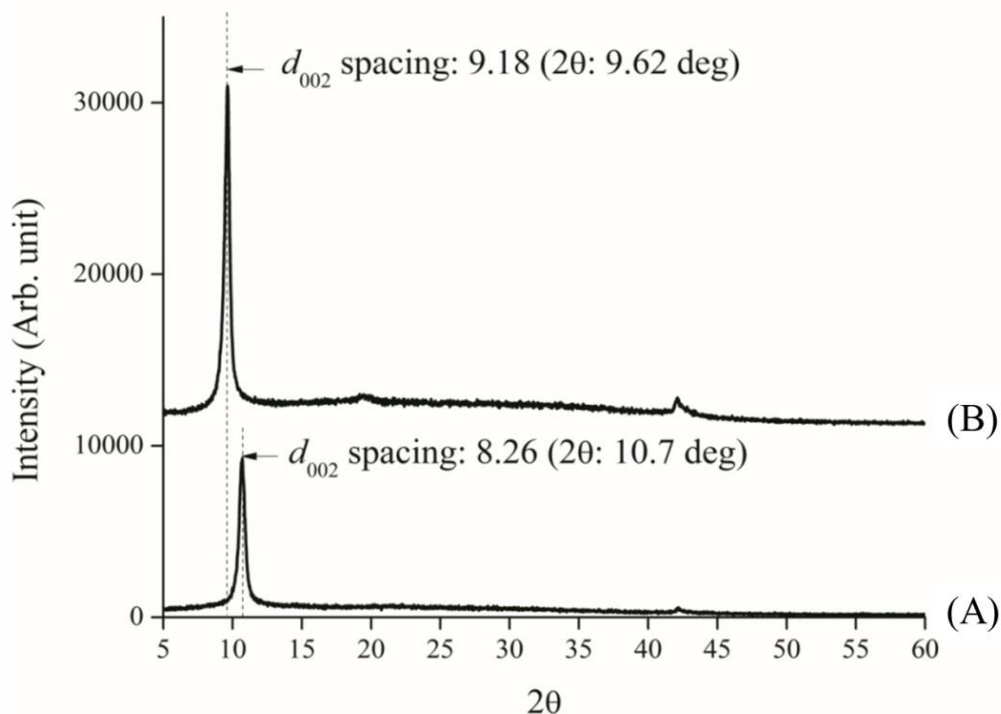


Figure 4.3: XRD for graphite oxide and interlayer d -spacing: (A) GOH and (B) GOP

The interlayer spacing (d -spacing) has been calculated from the Bragg's Law. A typical interlayer spacing for GO has been reported as 7~8 Å [133]–[135]. An earlier study [136] confirmed that the d -spacing for the graphite oxide produced with H_3PO_4 has a larger d -spacing than for that synthesized using the Hummers' method. In this study, the (002) peak [137] for GOH and GOP was located at 10.7° and 9.6° , corresponding to an interlayer d -spacing of 8.2 Å and 9.2 Å, respectively. Since the typical spacing between the graphite layers is known to be 3.4 Å [138], the larger d -spacing for the graphite oxides implies that the oxygen-containing functional groups occur between the graphite oxide layers. It can also be seen that the graphite oxides with H_3PO_4 (GOP) have a larger interlayer spacing than that of the graphite oxide obtained from the Hummers' method (GOH). Once the graphite oxide layers are exfoliated and

reduced, they return to a sp^2 layer structure. Therefore, the intensity of the graphite oxide peak completely disappeared in the XRD pattern of graphene, characterized by a broad peak centered around 24° and corresponding to an interlayer d -spacing of 3.69 \AA with (002) structure [139], [140]. This result could indicate the recovery of graphitic crystal structure [134].

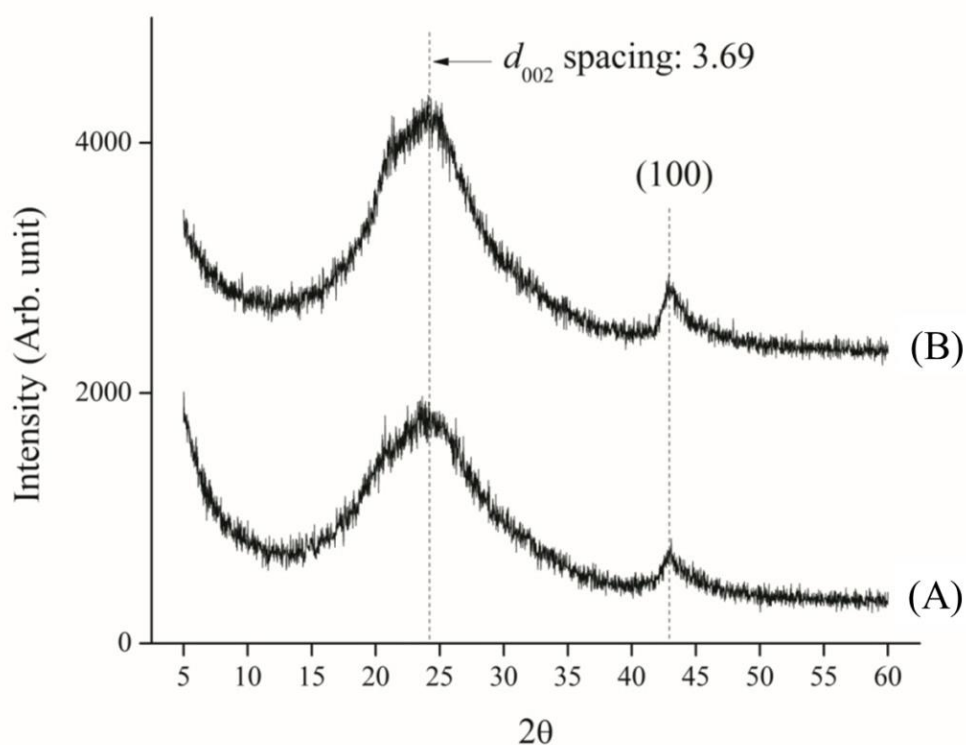


Figure 4.4: XRD of graphene and interlayer d -spacing: (A) GPH and (B) GPP

Table 4.1 shows the overall crystallite size (L_a) and thickness (L_c) of graphite oxide and graphene calculated from the Scherrer equation: For the graphite oxides, the overall size (L_a) is larger and thicker (L_c) than for graphene. It can be concluded that the oxygen-containing functional groups on the surface of the graphite oxide are removed; then the graphene layers are

exfoliated from each other, leading to a smaller number of graphene layers. It is also supported from BET analysis since GPP which has a fewer number of layers possesses a higher specific surface area of 853.9 m²/g than GPH (394.9 m²/g).

Table 4.1: Surface area and overall crystallite size (L_a and L_c) analysis

	BET	XRD							
	Surface area	(002) plane					(100) plane		
	(m ² /g)	2 θ (°)	Width (°)	L_c (nm)	d -spacing (Å)	Number of layers	2 θ (°)	Width (°)	L_a (nm)
GOH	-	10.7	0.5	35	8.3	42	42.2	0.2	163.5
GOP	-	9.6	0.4	39	9.2	43	42.1	0.3	141.7
GPH	394.9	24.1	7.4	2.3	3.7	6	42.9	0.9	40.0
GPP	853.9	23.6	11.6	1.5	3.8	4	43.1	0.7	50.1

The binding energies of the C 1s level of the graphite oxides were determined by XPS, and are shown in Figure 4.5. The degree of oxidation of graphite oxide can be determined from the ratio of the areas under the curve for C-C and C-O (including epoxy and hydroxyl groups) located at 284.4 and 286.2 eV, respectively [79].

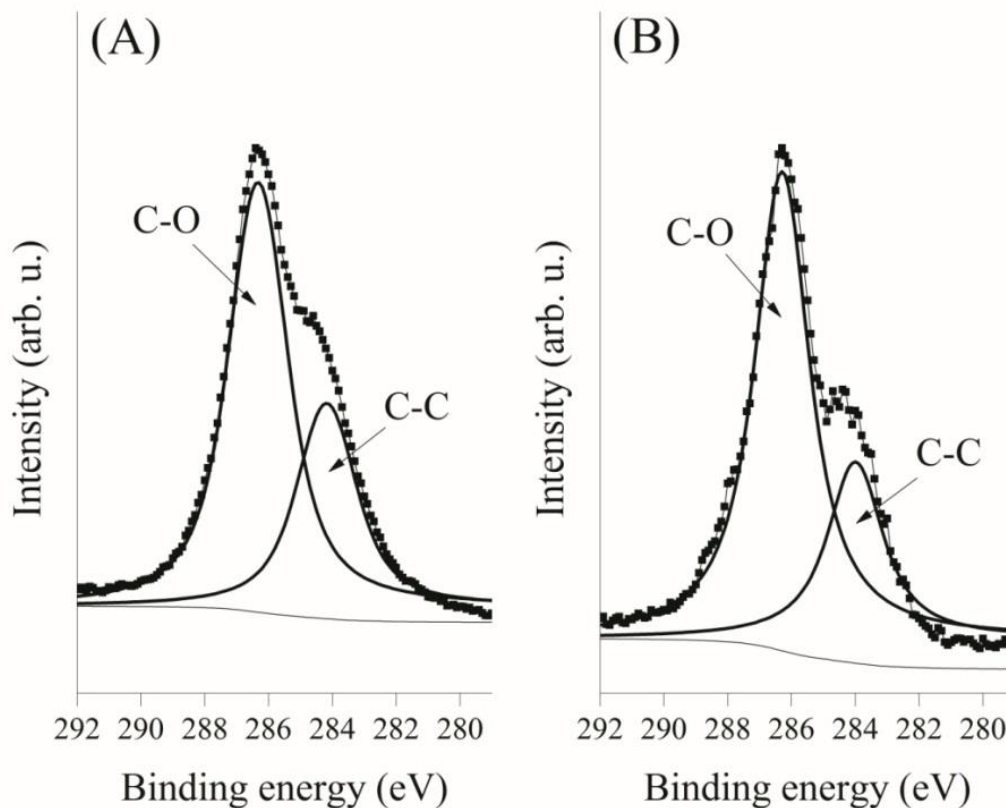


Figure 4.5: XPS of graphite oxide; (A) GOH and (B) GOP

Depending on the synthesis methods, the ratio of oxygen to carbon varies, as shown in Table 4.2. The quantitative fractions, C-O bonds to C-C bonds ratio, of the GOH and GOP are 2.08 and 2.69, respectively. This confirms that GOP has a higher degree of oxidation than the graphite oxide obtained from the Hummers' method (GOH). To obtain graphene, the oxygen-containing functional groups attached to two neighboring graphene layers are reduced in a hydrazine aqueous solution environment, a process that transforms the sp^3 bonds to sp^2 bonds. The graphene layers are then detached from each other. As a result, two types of graphenes, GPH, obtained from GOH, and GPP, reduced from GOP, were obtained.

Table 4.2: XPS fitting analysis for graphite oxide and graphene

	Binding energy (eV)	GOH (area)	GOP (area)	GPH (area)	GPP (area)
C-C	284.18	57507	3328	361316	205309
C-O	286.33	119609	8939	54129	30325
Ratio of C-O/C-C		2.08	2.69	0.15	0.15

The XPS analysis, Figure 4.6, confirmed that the degree of oxidation of GPH and GPP decreased from ~2 to 0.15. It is difficult to distinguish the quantitative difference between GPH and GPP from XPS analysis since most of the oxygen-containing functional groups between the layers were removed by the reduction process.

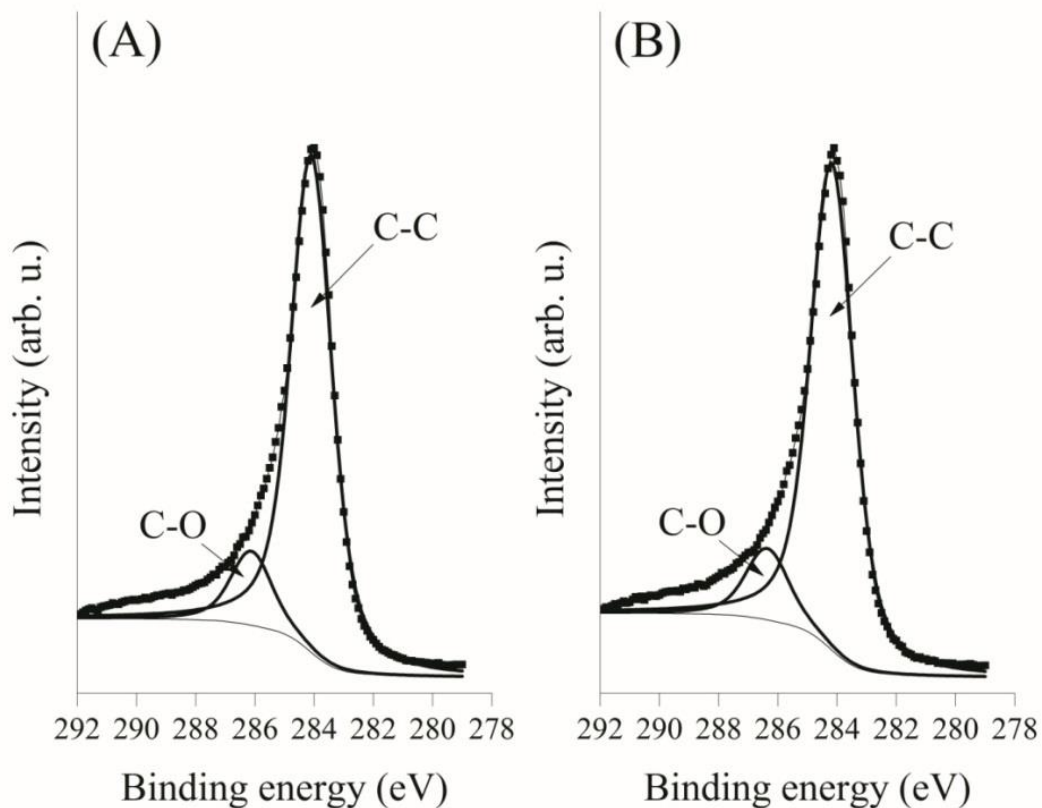


Figure 4.6: XPS of graphene; (A) GPH and (B) GPP

Raman spectroscopy analysis has been chosen to probe the structural and electronic characteristics of graphitic materials [75] because it provides information on in-plane bond stretching of sp^2 carbon atoms in both rings and chains (G band in the range of $1500-1600\text{ cm}^{-1}$), information on the defects from the breathing modes of sp^2 atoms in hexagonal rings (D band in the range of $1200-1500\text{ cm}^{-1}$), and information on the stacking order (2D band) [82]. Raman G band can be attributed therefore to graphitic sp^2 bonded carbon, and D band is also widely used for determining the thickness of graphene materials [141]. Figure 4.7 shows Raman spectroscopy results obtained with an excitation wavelength of 514.5 nm for graphite oxide and graphene.

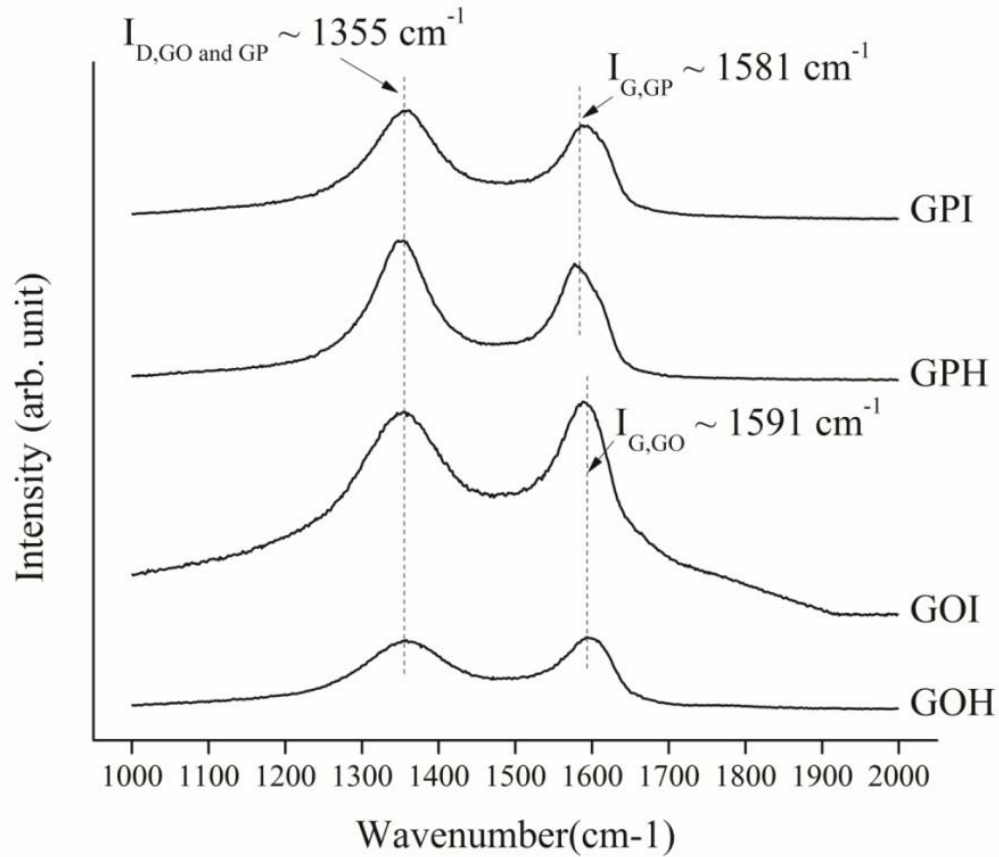


Figure 4.7: Raman spectroscopy of graphite oxide and graphene

All samples were deposited on silicon wafers in powder form without the use of a solvent. Graphite has a single G band at 1580 cm^{-1} [133]. When graphite was oxidized to graphite oxide, the G band peak shifted from 1580 to 1591 cm^{-1} , and the D band intensity at 1355 cm^{-1} increased due to the resonance of isolated double bonds on graphite oxide [80]. After the graphite oxide was reduced to a 2D graphene layer, the G band returned from 1591 to 1581 cm^{-1} . The structural changes from graphite oxide to graphene (i.e., the graphitization degree of carbonaceous materials and the defect density [142]) could be observed by comparing the intensity ratio of the D and G bands (I_D/I_G). I_D/I_G ratios for GOH and GPI were 0.94 and 0.95, respectively. In

addition, I_D/I_G ratios for GPH and GPP were 1.25 and 1.12, respectively. In agreement with previous reports for graphite oxides and graphene, the ratio of I_D/I_G increases when the graphite oxide is reduced to graphene [143], [144]. This result indicates that the chemical reduction of graphite oxide increases the number of small regions of aromatic compounds that can be detected from the D band. Also, the ratio I_D/I_G , for GPP is lower than for GPH, implying, perhaps, that GPP has fewer defects than GPH and/or larger overall size. This hypothesis is supported by the L_a and L_c results (Table 4.1) calculated from the Scherrer equation [144].

4.3. Summary

Graphite oxide (GO) synthesized with phosphoric acid, labeled GOP, shows a higher degree of oxidation, and has a larger interlayer spacing, than the oxide prepared using the conventional Hummers' method, referred to as GOH, as confirmed by X-Ray photoelectron spectroscopy and X-Ray diffraction analyses. This study was performed under the assumption that the oxygen-containing functional groups between the GOP layers are more easily reduced than those between the GOH layers. Raman analysis supported this assumption in that the reduced graphene from GOP has a larger number of sp^2 carbons and fewer defects than the graphene obtained from GOH. The relative extent of defects in graphene can be investigated by dibenzothiophene (DBT) adsorption, which requires π - π interactions between the free π -bonds of sp^2 atoms from graphene and those from the aromatic ring of DBT. The graphene obtained from GOP showed higher DBT adsorption capacity than that synthesized from GOH. In addition, the DBT adsorption capacity on graphene decreased as the concentration of other aromatic compounds increases.

Chapter 5: H₂S Adsorption on ZnO/rGO Composite

This chapter presents the H₂S adsorption capacity on ZnO/rGO composite at room temperature and 300 °C in dry and wet conditions. Chapter 2 introduced various metal oxides that are active for H₂S adsorption; ZnO is one of the preferred metal oxides since ZnO is thermodynamically favorable for H₂S adsorption at low temperature due to the negative ΔG . Among various metal oxides, it is known that ZnO has very high equilibrium constant for sulfidation which yield high efficiency of H₂S removal. Therefore, this study considered 2D reduced graphite oxide (rGO) as substrate for active ZnO deposition. rGO possesses abundant amount of oxygen-containing functional groups on its surface. In this chapter, a novel approach to use those functional groups acting as anchor to hold metal ions (and metal oxide) on the surface is presented. Various characterization techniques have been used to investigate in details the chemical and physical properties of the adsorbents for fresh and spent samples.

5.1. Characterizations of fresh ZnO/rGO adsorbents

The crystal structures of the graphite oxide (GO), reduced graphite oxide (rGO), and zinc oxide/rGO composites were characterized using XRD (Figure 5.1). The 2θ of GO is located at 9.62° . The interlayer spacing of GO ($d_{002} = 9.18 \text{ \AA}$) is larger than graphite (3.4 \AA) implying that oxygen containing functional groups, such as hydroxyl, epoxy and carboxyl, are intercalated between the graphite layers [145]. Since the surface functional groups on the surface of rGO act as active sites for guest materials [20], [146], the rGO is considered as an attractive substrate for nano-metal oxide composites. Due to its surface functional groups, GO is negatively charged.

Therefore, positively charged Zn^{2+} ions in zinc salt solution are able to be adsorbed on the surface of GO from negatively charged oxygen functional groups and form ZnO clusters which may act as nuclei for the particle growth in subsequent heat treatment [97]. After reduction by reflux and microwave, the characteristic peak of GO disappeared by removing the oxygen functional groups which link the GO layers indicating that the structure of GO vanished. After the deposition of nano-ZnO particles on rGO, XRD peaks of ZnO appeared at 2θ of 31.64, 34.28, 36.12, 47.36 and 56.38°; and those peaks matched other references [147], [148]. It was also confirmed that the structure of rGO was not destroyed even after the deposition of ZnO; and the strong peaks of ZnO imply that ZnO attached on rGO is highly crystalline.

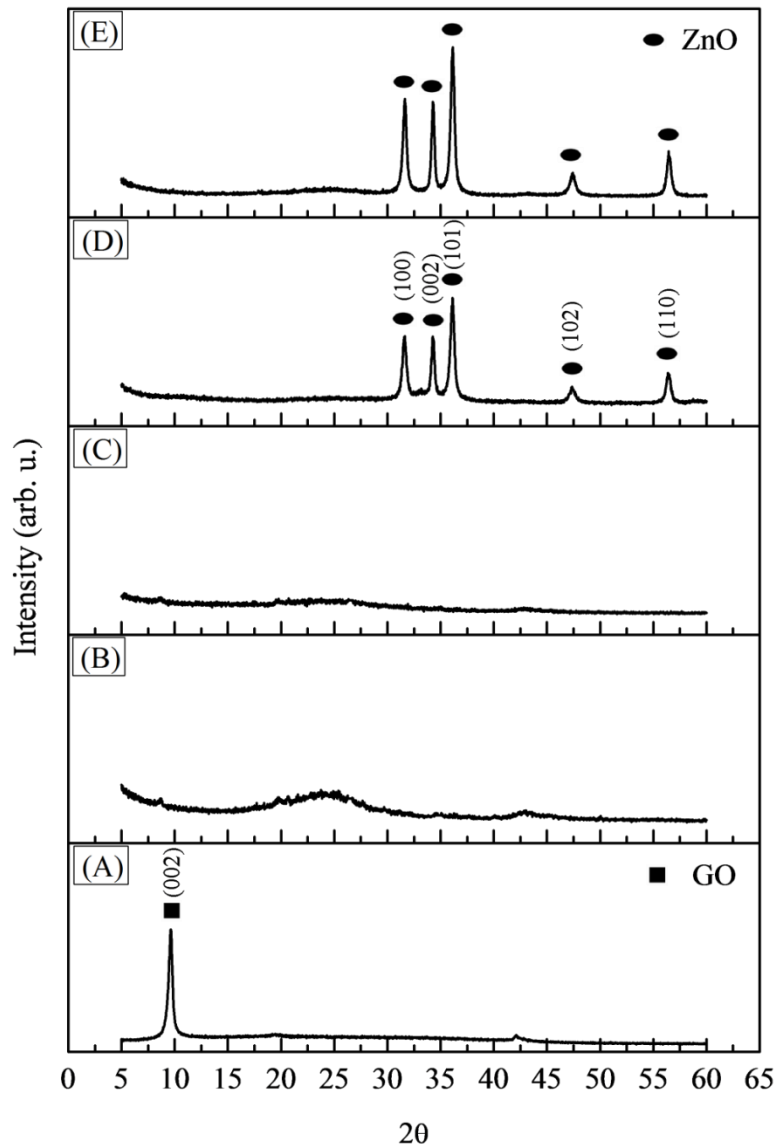


Figure 5.1: XRD patterns of (A): GO, (B): rGO-R, (C): rGO-M, (D): ZnO/rGO-R, (E): ZnO/rGO-M

Figure 5.2 shows the crystal structure changes of ZnO/rGO composites during the pre-treatment with moisturizing and H₂S adsorption process at ambient condition. It was confirmed

that during humidification and H₂S adsorption, the crystal structures of ZnO/rGO composite were not changed; but ZnS peaks appeared after the adsorption process. The intensity of ZnO peaks decreased after the H₂S adsorption test, but the ZnS peak intensity increased. This indicates that the H₂S adsorption tests did not modify the crystal structure of the composite; but a portion of ZnO crystal changed to ZnS. However,

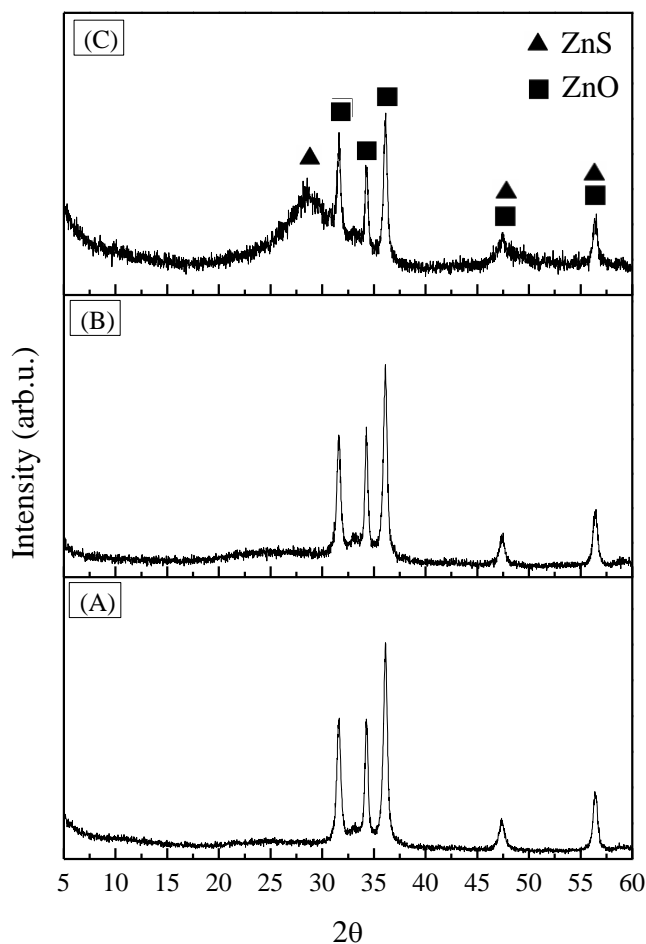


Figure 5.2: XRD patterns of (A): ZnO/rGO-M, (B): ZnO/rGO-M-W, (C): ZnO/rGO-M-H₂S

Figure 5.3 shows the FT-IR spectra of GO, rGO and ZnO/rGO composite. The broad absorptions at about 3425 and 1551 cm^{-1} are assigned to the hydroxyl groups. The absorption band at 1041 cm^{-1} can be assigned to the stretching vibration of C-O. In addition, the strong absorption band at 443 cm^{-1} corresponds to the vibrations of Zn-O bonds [146]. The composites from the microwave method (rGO-M and ZnO/rGO-M) possess stronger peaks of hydroxyl groups than that those obtained from the reflux method (rGO-R and ZnO/rGO-R). It implies that the 3 min (six times of 30 sec irradiation with 30 sec interval) of microwave reduction provides a milder reduction environment than the 18 h of reflux reaction, even though the microwave provides rapid heating of the solution.

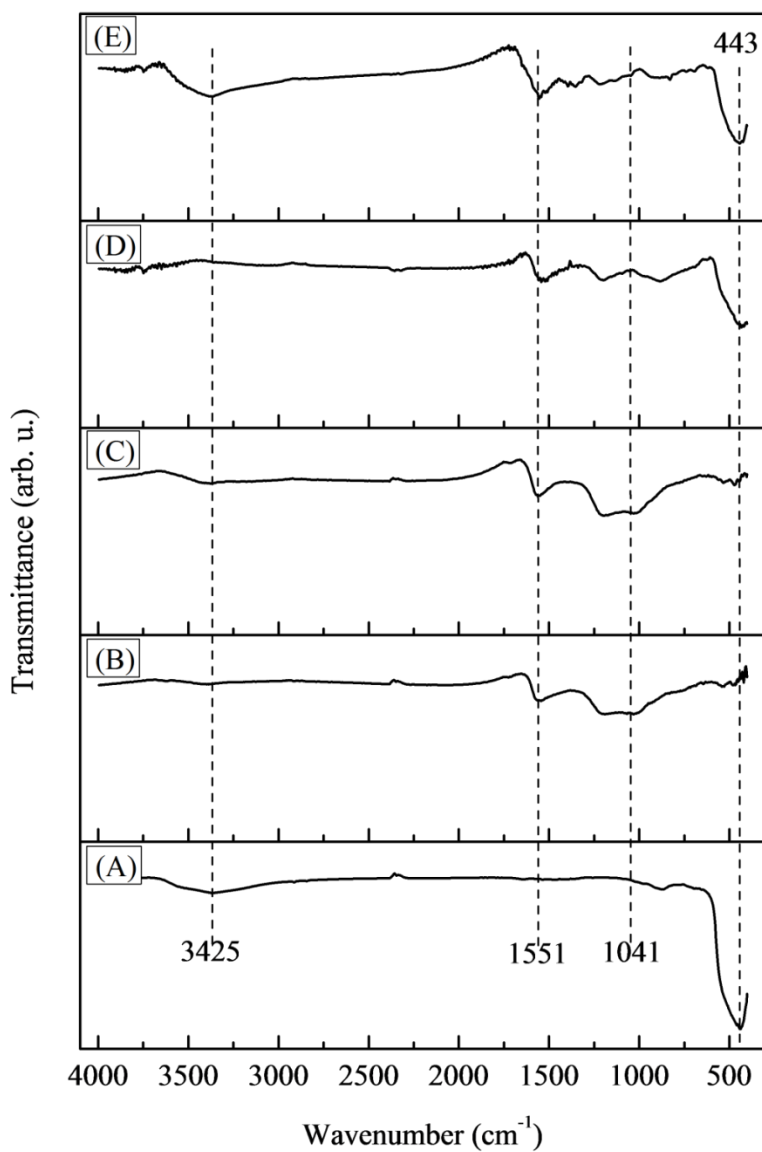


Figure 5.3: FT-IR spectra of (A): ZnO, (B): rGO-R, (C): rGO-M, (D): ZnO/rGO-R, (E): ZnO/rGO-M

XPS analysis (Figure 5.4) confirms that the microwaved rGO (rGO-M) possesses a larger amount of oxygen-containing functional groups, such as hydroxyl, epoxy, carbonyl and

carboxyl, than the refluxed rGO (rGO-R) since the XPS area ratios of the carbon-oxygen to carbon-carbon for rGO-R and rGO-M are 0.38 and 0.51, respectively.

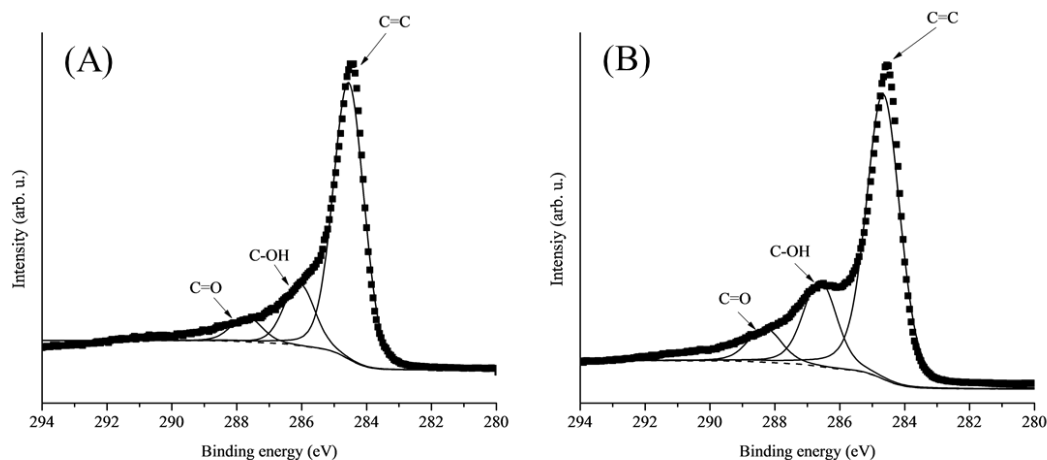


Figure 5.4: XPS analysis for (A) ZnO/rGO-R and (B) ZnO/rGO-M (C-OH/C-C: 0.19 / 0.35)

Figure 5.5 shows the FT-IR pattern changes of ZnO/rGO-M sample after H₂S exposure. After the moisturizing process, the amount of hydroxyl group (at 3425 cm⁻¹) on ZnO surface increased compared to that of the fresh sample. It implies that the moist air provides -OH groups to the ZnO/rGO surface. However, after the H₂S adsorption test, the amount of the hydroxyl groups decreased. It indicates that the hydroxyl groups, which are attached on the ZnO surface, play a critical role for the H₂S adsorption. In addition, the intensity of Zn-O bond also decreased after the adsorption test. It also confirms that a portion of Zn-O bond reacted with H₂S and changed to ZnS.

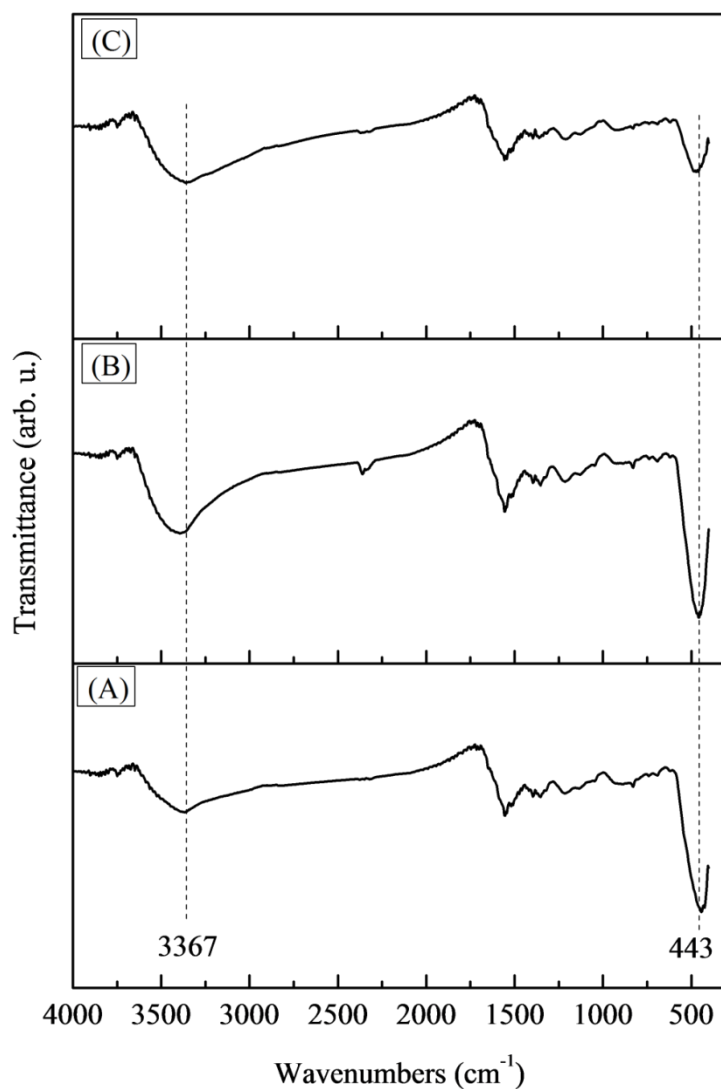


Figure 5.5: FT-IR spectra of (A): ZnO/rGO-M, (B): ZnO/rGO-M-W, (C): ZnO/rGO-M-H₂S

In order to characterize the carbon materials, Raman analysis was conducted. It is well known that the Raman spectra bands of graphene have two typical bands (G and D band at ~ 1580 and ~ 1350 cm^{-1} , respectively). Those bands represent the in-phase vibration of graphite lattice (G band) and the disorder in the hexagonal graphitic lattice (D band), respectively [97],

[133], [142]. For the characterizations, the intensity ratios of I_D/I_G for samples were compared in Figure 5.6.

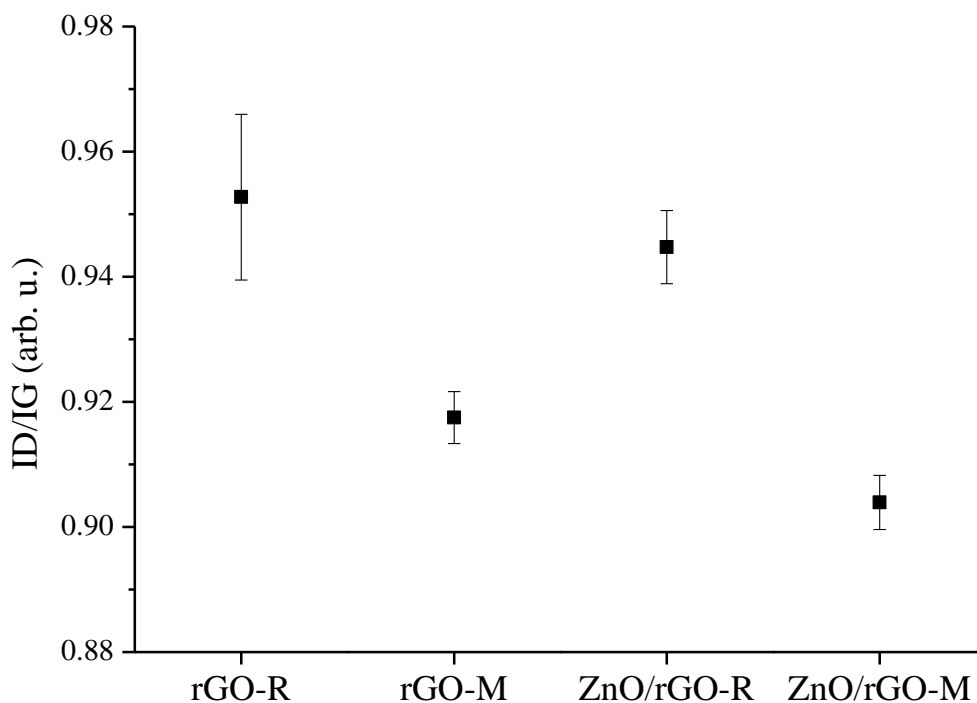


Figure 5.6: Raman spectra of rGO-R, rGO-M, ZnO/rGO-R and ZnO/rGO-M

The intensity ratios for rGO-R and ZnO/rGO-R are higher than those for rGO-M and ZnO/rGO-M. It can be determined that the microwaved-assisted samples (rGO-M and ZnO/rGO-M) possess less defects which are normally caused from the reduction of graphite oxide to graphene [107], [146]. Therefore, it is reasonable to use the intensity ratio of two peaks (I_D/I_G) in order to determine the degree of reduction of the composites. This further supports that the short-

time microwave treatment would provide a milder reduction environment than the long-term reflux treatment.

Based on the above analysis, the short-term microwave treatment provides a milder reducing environment than the reflux method. In addition, it is known that the functional groups on rGO play critical roles to anchor the Zn^{2+} ions on the surface [20], [146]. Therefore, the aggregation of the nano-sized ZnO particles can be avoided since the remaining functional groups on 2D rGO sheets are acting as active sites for the Zn ions. SEM analysis (Figure 5.7) clearly shows the difference that the ZnO particles from microwave-assisted method are more widely dispersed and have a smaller particle size than that from reflux method in the role of anchor sites for the Zn ions on rGO sheets.

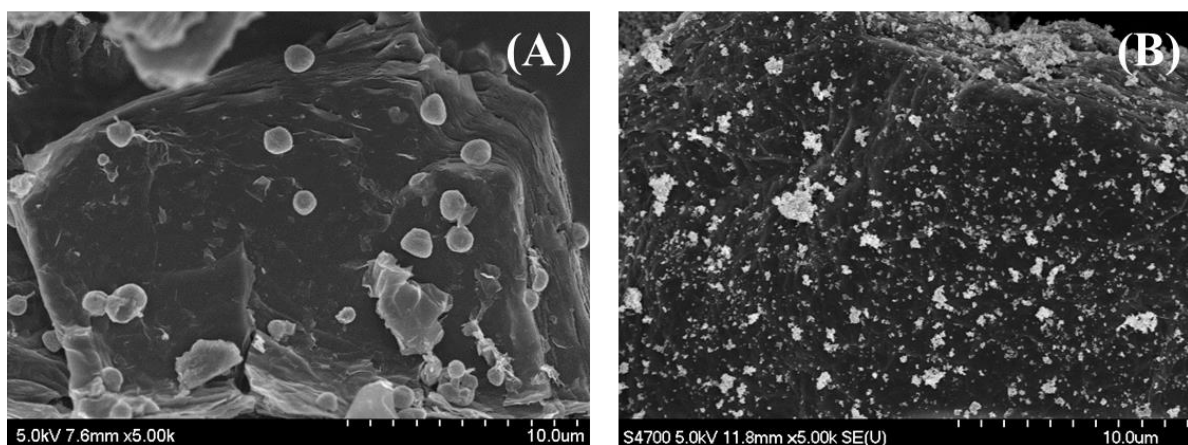


Figure 5.7: SEM images of (A) ZnO/rGO-R and (B): ZnO/rGO-M

Beside the metal oxide dispersion effect, the change of chemical oxidation states also would cause an increase in H_2S adsorption capacity for the ZnO/rGO composite. In order to investigate the detailed electrochemical states for Zinc, Zn 2p_{3/2} peaks for pure and rGO composite were compared (Figure 5.8). From the Zn 2p XPS, the binding energy (BE) difference

between the Zn 2p_{1/2} (1045.53 eV) and Zn 2p_{3/2} (1022.37 eV) was 23.16 eV for pure ZnO. The BE difference for ZnO/rGO was identical as 23.16 eV (1048.01 eV for Zn 2p_{1/2} and 1024.85 eV for Zn 2p_{3/2}). This implies that the oxidation state of ZnO deposited on rGO surface is +2. In addition, a slight shift of BEs toward higher BE has been observed when ZnO particles were loaded onto the rGO surface. This indicates that the interaction between ZnO and rGO is not only physically but also chemically bonded.

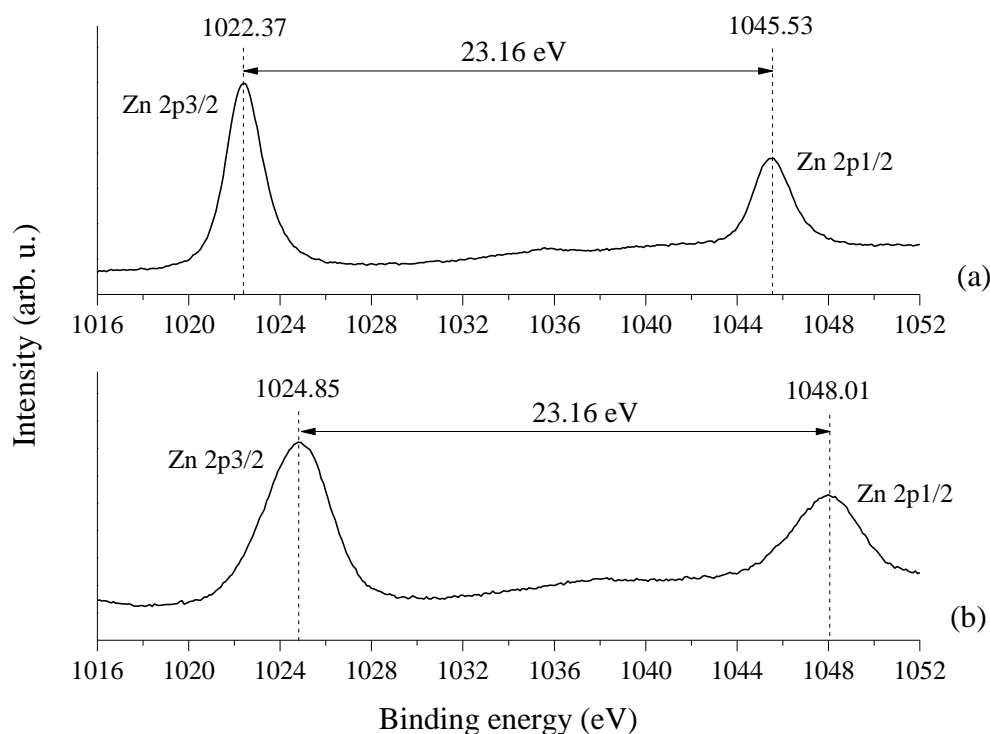


Figure 5.8: Zn 2p XPS for (a) pure ZnO and (b) ZnO/rGO composite

The Zn 2p_{3/2} peak could be fitted by two major Zn peaks in the binding energy of ~ 1022 (Zn^I) and ~ 1023 eV (Zn^{II}) shown in Figure 5.9. The Zn^I phase represents the characteristic of Zn atoms in Zn-O bonds; the Zn^{II} phase is assigned to the Zn in the Zn-O bonds surrounded

by oxygen vacancies implying that Zn atoms are not exactly occupied in the ZnO lattice [149], [150]. It is clearly observed that the pure ZnO and ZnO/rGO composite possess different oxidation states. The difference could be caused by the interaction between the ZnO and the oxygen-containing functional groups attached on the rGO surface. For pure ZnO, the ratio of Zn^I to Zn^{II} is 2.2; and it becomes 1.1 for the ZnO/rGO composite. This suggests that for pure ZnO, Zn atoms are dominantly occupied in the ZnO lattice. However, when ZnO particles are attached onto the rGO surface, the chemical state of ZnO is modified due to the oxygen functional groups attached on the rGO surface. It could thus be inferred that when the oxygen functional groups are anchoring the metal ions during the synthesis process, the abundant amount of Zn ions are located at the oxygen vacancy sites. It is widely proposed that the dissociated H₂S ions (i.e. HS⁻ and S²⁻) should be bonded with Zn²⁺ ions [9], [151] for the adsorption process. The above XPS analysis suggests that the Zn^{II} phase (Zn ions which are not exactly located in the Zn-O lattice) is a preferred state than the Zn^I phase for H₂S adsorption. Therefore, critical roles of rGO for H₂S adsorption are not only dispersion of ZnO but also modifying the Zn oxidation states to a more preferable state. In addition, it indicates that Zn atoms at the oxygen vacancy sites play important roles for the H₂S adsorption.

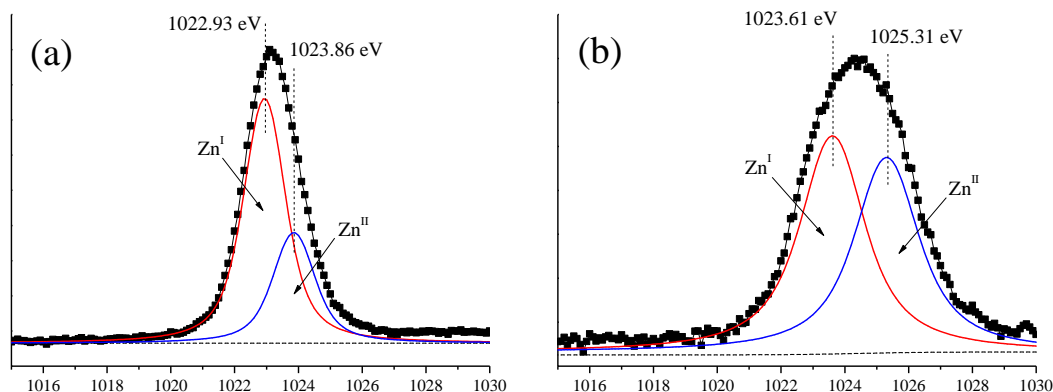


Figure 5.9: Zn2p3/2 spectrum for (a) pure ZnO and (b) ZnO/rGO composite

The oxidation state changes of O1s for pure ZnO and ZnO/rGO composite are shown in Figure 5.10. Similar to the Zn 2p spectrum, the O1s spectrum is able to be sub-divided into three phases (O^I , O^{II} and O^{III}). O^I (~ 531 eV) peak indicates the O^{2-} ion in the wurtzite Zn-O lattice; O^{II} (~ 532 eV) represents the oxygen in the deficient region and surrounded by the oxygen vacancies; and O^{III} (~ 534 eV) implies the chemisorbed oxygen or moisture on the surface [152]. The quantitative portions of $O^I/O^{II}/O^{III}$ for pure ZnO and ZnO/rGO composite are 59.1/26.7/14.2 % and 14.4/39.3/46.3 %, respectively. A slight BE shift toward higher BE ($\sim +1$ eV) for ZnO/rGO composite was observed. This means that for pure ZnO, dominant oxygen (O^{2-}) ions are located in the wurtzite structure of ZnO lattice. However, when ZnO particles are loaded onto the rGO surface, the chemical status of oxygen is changed. The portion of oxygen in the Zn-O lattice (O^I) decreased, with significant increase in the amount of oxygen ions located on the oxygen vacancy sites (O^{II}) or on the surface (O^{III}). This suggests that the oxygen ions at O^{II} and O^{III} sites play a critical role to enhance H_2S adsorption by providing a more favorable environment for H_2S surface dissociation to HS^- or S^{2-} which are bonding with Zn^{2+} .

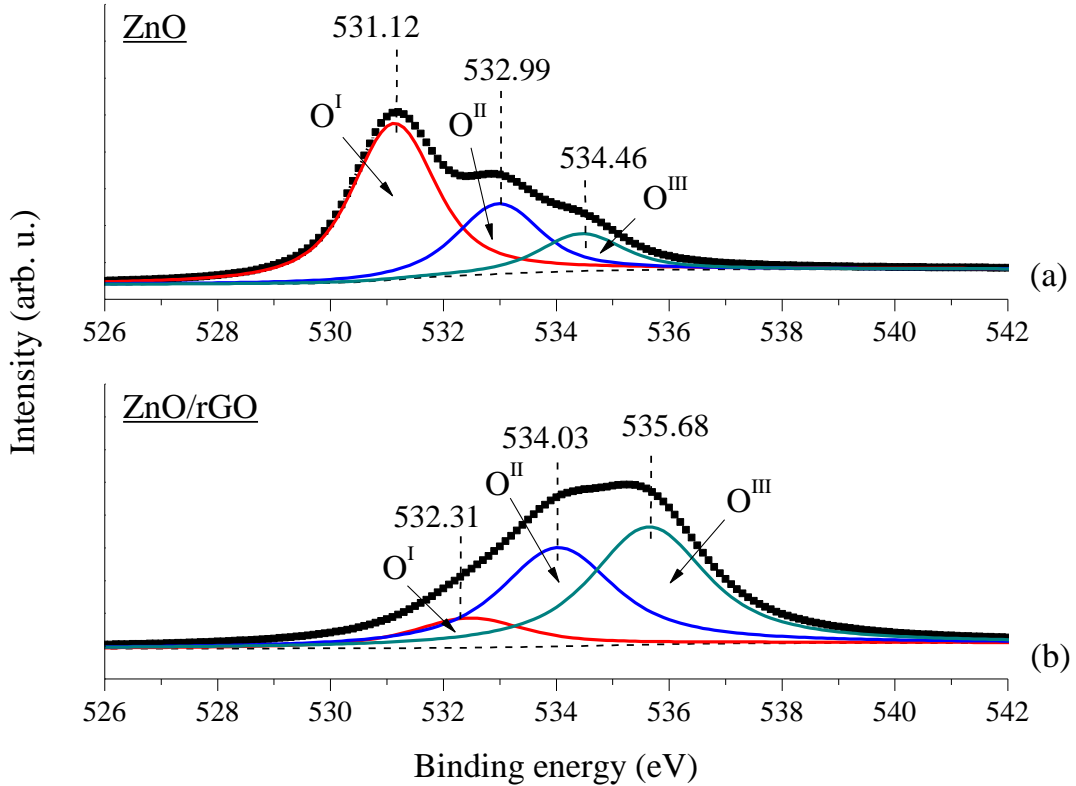


Figure 5.10: O1s XPS for (a) pure ZnO and (b) ZnO/rGO composite

From Figure 5.11, representing C1s XPS data for ZnO/rGO composite, it is possible to determine the oxygen functional groups attached on the surface of rGO generally in agreement with previous studies [153], [154]. The C1s spectra for ZnO/rGO composite can be fitted into four peaks for four different carbons: sp^2 carbon (284.6 eV), carbon in C-O bonds (286.3 eV), carbonyl carbon C=O (287.8 eV) and carboxylate carbon O-C=O (289.5 eV).

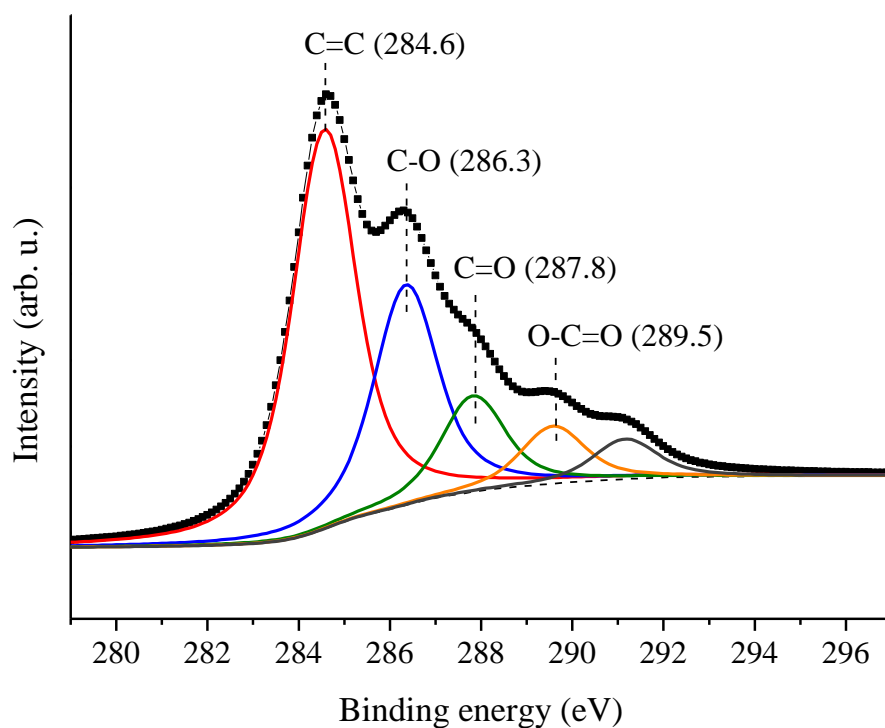


Figure 5.11: C1s XPS for ZnO/rGO composite

The ratio of sp^2 carbon to carbon-oxygen groups is 1.1. This suggests that the rGO surface possesses significant amount of oxygen functional groups. As discussed above, those oxygen functional groups are chemically bonded with ZnO particles and modify the electrochemistry of ZnO. It provides a preferred status of ZnO to help dissociating H_2S molecules on the surface of ZnO, leading to enhance H_2S adsorption capacity about 10 times than that of pure ZnO.

The direct evidence of the formation of nano-sized ZnO deposited on the surface of rGO is provided by TEM/EDS analysis (Figure 5.12) since TEM analysis is an ideal method of proving the particle size of ZnO deposited on the rGO surface. It is observed that nano-size ZnO

particles were deposited on the surface of rGO. Those ZnO particles are well dispersed and separated from each other on the rGO surface which displays a good combination between rGO sheet and ZnO nanoparticles. Based on the TEM image, the average ZnO particle size was measured as $35.7 (\pm 4.4)$ nm.

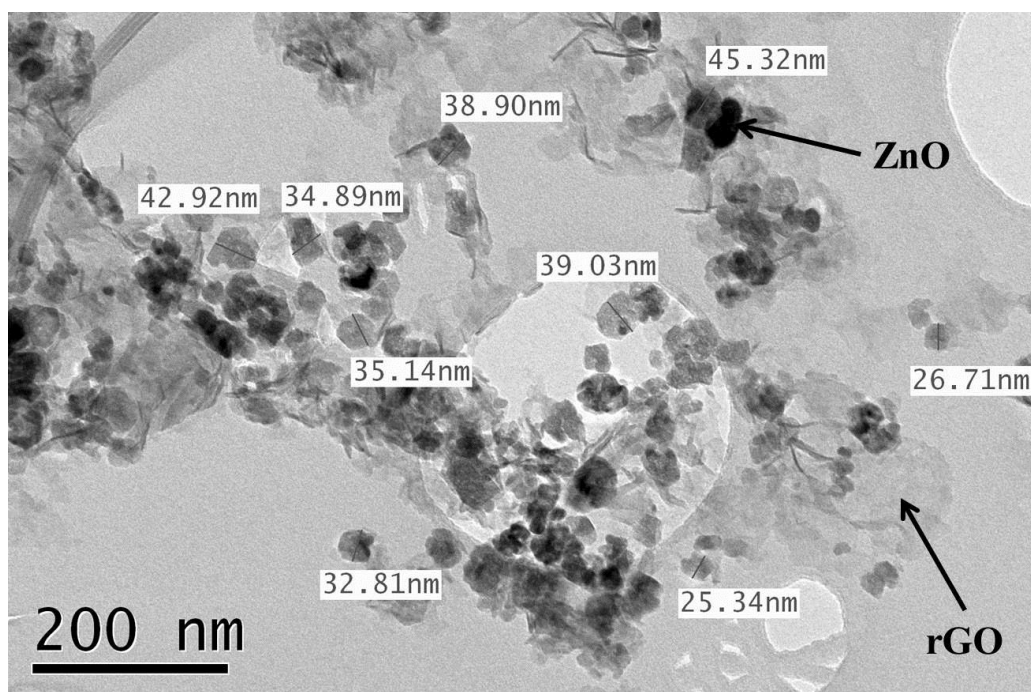


Figure 5.12: TEM of ZnO/rGO composite with particle size measurement

5.2. H₂S breakthrough tests at room temperature

In order to investigate the characteristics of ZnO/rGO composites, H₂S adsorption tests at ambient conditions were conducted. Comparing the breakthrough time of the samples should be an ideal method to determine the adsorption capacity from the samples. The breakthrough test results are shown in Figure 5.13. Carbon nanotube (CNT), which has similar property as that of

graphene, but not 2-D shape, was selected as a reference. First, it was observed that CNT and rGO were not able to adsorb any H₂S. This was expected since CNTs and rGO do not possess any active sites for the adsorption. The breakthrough time for the ZnO itself showed 77 (± 2) min/gram of adsorbent.

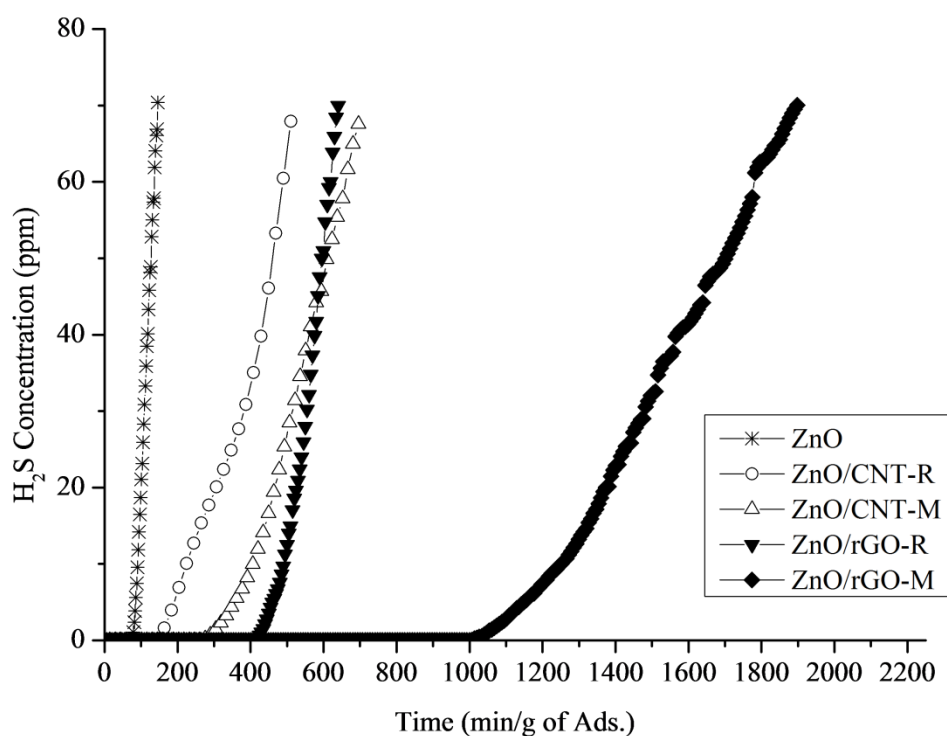


Figure 5.13: H₂S adsorption tests at ambient conditions after 1 h of moisturizing pretreatment

This supports the important role of the 2D rGO sheet for the distribution of active ZnO particles. Still, the ZnO/CNT-M composite showed a longer breakthrough time than the ZnO/CNT-R composite. One possible reason is that the rapid and short heating process by microwave decreases the particle size of ZnO. Therefore, the surface area of ZnO for the H₂S

adsorption has increased. These phenomena were also shown for the ZnO/rGO composites. However, the increase of the breakthrough time for the ZnO/rGO was 576 (\pm 6) min/g of adsorbent (increasing from 410 to 986 min/gram of adsorbent for ZnO/rGO-R to ZnO/rGO-M, respectively). It is almost five-fold than the breakthrough time for ZnO/CNT (increasing 142 (\pm 5) to 260 (\pm 2) min/gram of adsorbent for ZnO/CNT-R to ZnO/CNT-M, respectively). In addition, the 2-D rGO sheets played a critical role for the uniform distribution of active ZnO particles.

5.3. H₂S breakthrough tests at mid temperature

As described above, it was confirmed that a mildly reduced graphite oxide (rGO) could be obtained from a microwave-assisted reduction process. This mildly reduced rGO allows for some amount of oxygen-containing functional groups to remain on the rGO surface. The presence of those functional groups was confirmed from FTIR and XPS analysis. It was already proposed that oxygen functional groups are anchoring metal ions on the surface and help the dispersion of metal ions [157]. From an application point of view, those uniformly distributed ZnO particles should be able to promote H₂S adsorption capacity. From our preliminary experiments, it was found that reduced graphite oxide (rGO) itself did not adsorb any H₂S. It implies that breakthrough experiments should be able to determine the functionality of active ZnO for H₂S adsorption. Those phenomena have been confirmed by the H₂S breakthrough adsorption tests (Figure 5.14) and quantitative data are shown in Table 5.1. For the breakthrough tests, beds of 150 mg of ZnO/rGO composite and 350 mg of ZnO were fed with a nitrogen stream containing 750 ppm of H₂S.

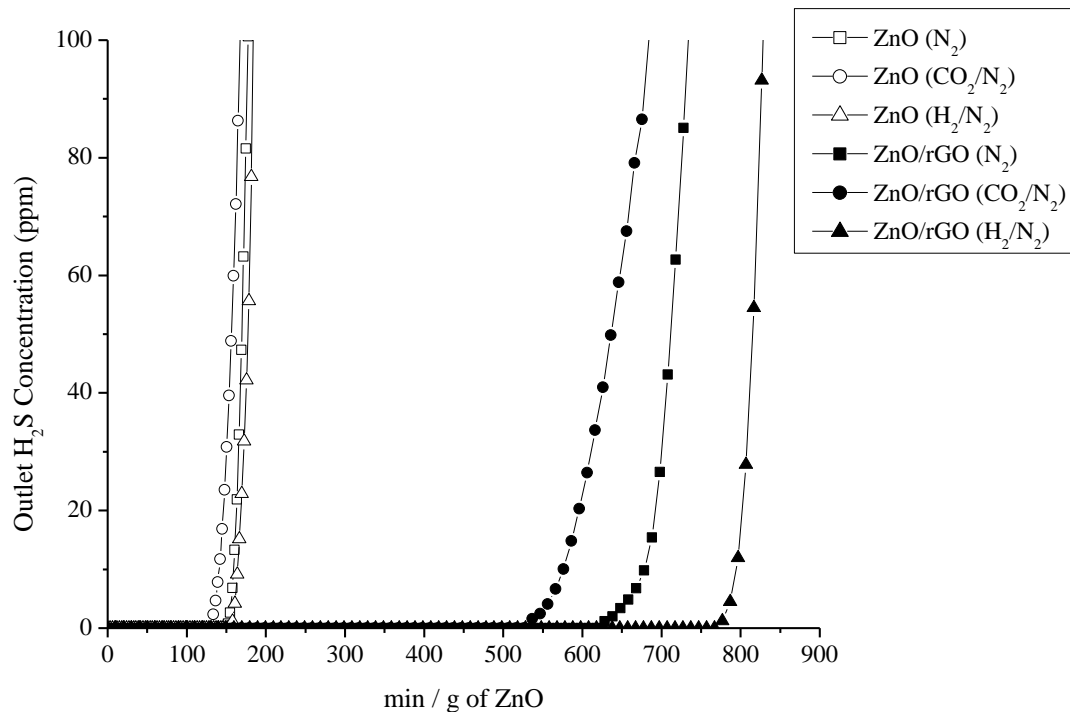


Figure 5.14: Dynamic H₂S breakthrough tests for ZnO and ZnO/rGO composite at 300°C in presence of different gases

The low ZnO utilization efficiency could be caused by the aggregation effect on ZnO particles. However, with the help of rGO, the ZnO/rGO composite showed 60.3 (\pm 1.5) % of ZnO utilization efficiency. About 4 times higher ZnO utilization efficiency has been observed. Those critical functionality of rGO as a substrate for gas adsorption has been proposed in previous studies [23]–[25].

Table 5.1: Comparison of H₂S adsorption capacity and utilization

	ZnO			ZnO/rGO		
	N ₂	N ₂ /CO ₂	N ₂ /H ₂	N ₂	N ₂ /CO ₂	N ₂ /H ₂
Breakthrough time (min/g ZnO)	155 (± 6)	134 (± 8)	158 (± 6)	628 (± 10)	537 (± 6)	777 (± 12)
Total sulfur adsorbed (mg of S/g of ZnO)	70.9 (± 2.7)	61.3 (± 3.6)	72.2 (± 2.9)	305.7 (± 4.5)	245.5 (± 2.9)	355.2 (± 5.5)
Utilization (%)	17.4 (± 1.4)	15.0 (± 1.9)	17.7 (± 1.6)	70.6 (± 2.4)	60.3 (± 1.5)	87.3 (± 3.0)

* Confidence interval: 95%

The effect of the presence of carbon dioxide (CO₂) and hydrogen (H₂) has been investigated as well (Figure 5.14 and Table 5.1). In this study, 2.8 vol% of H₂ with 3 vol% of H₂S/N₂ was passed through the adsorbent bed. Overall, for H₂S adsorption onto ZnO, H₂S should be dissociated into H⁺ and HS⁻ followed by the diffusion of the sulfur into the oxide lattice [158], [159]. The additional supply of hydrogen at 300°C might promote the reducibility of ZnO; simultaneously decomposing ZnS [160], [161]. It should be able to provide more active Zn²⁺ for sulfur molecules. However, it was seen that the reaction temperature of 300°C was relatively low for pure ZnO particles from the H₂S breakthrough experiments. Therefore, at 300°C, the increase of H₂S adsorption capacity on the pure ZnO particles was almost negligible since the 17.4 (± 1.4) % of the ZnO utilization efficiency (in H₂S/N₂) was just increased to 17.7 (± 1.6) % (in H₂S/H₂/N₂ environment). However, from the ZnO/rGO composite, the effects of H₂ were clearly shown. The H₂S breakthrough time in H₂S/N₂ was 400 min; however, in H₂S/H₂/N₂, it increased to 494 min. Accordingly, ZnO utilization efficiency was increased from 70.6 (± 2.4) % in H₂S/N₂

to 87.3 (\pm 3.0) % in H₂S/H₂/N₂. From a qualitative evaluation based on the data obtained in this work, it was found that the presence of CO₂ leads to lower H₂S adsorption capacity of ZnO than in its absence. The H₂S breakthrough time has been decreased from 628 min (in N₂) to 537 min (in CO₂/N₂). In addition, the ZnO utilization efficiencies accordingly decreased from 70.6 (\pm 2.4) % (in N₂) to 60.3 (\pm 1.5) % (in CO₂/N₂). It implies that CO₂ showed an inhibiting effect on H₂S adsorption by ZnO. This could be explained by two possible reasons. First, as mentioned above, in order to adsorb H₂S onto ZnO, the decomposition products of H₂S (i.e. HS⁻ and S²⁻) should be substituted for oxygen atoms in the lattice of ZnO [160]. However, supplying CO₂ reduces the reducing effect of Zn-O which hinders providing active Zn²⁺ states to the sulfur elements. Second, since both H₂S and CO₂ are classified as acidic gases, those gases may strongly interact with the sorbents which have a basic character [162]. Therefore, competitive adsorption between H₂S and CO₂ could happen [160]. The competitive adsorption of CO₂ on ZnO limits the diffusion of HS⁻ and S²⁻ into the bulk of unreacted ZnO.

For pure ZnO particles, at 300°C, aggregations of the nano-particles were observed. However, as previously proposed in this study, for ZnO/rGO composite, the critical functionality of rGO anchoring metal oxide has been observed (Figure 5.15). After 300°C calcination in N₂ environment for 2 h, the morphology of the samples changed dramatically. It was clearly observed that the average ZnO particle size of the pure ZnO sample was increased. However, for the ZnO/rGO composite, the average particle size change was almost negligible. Therefore, it could be confirmed that the rGO plays a critical role in the dispersion of the active ZnO particles for H₂S adsorption by avoiding aggregation of ZnO at 300°C, thus providing constant higher specific surface area of ZnO to the reactant H₂S gas.

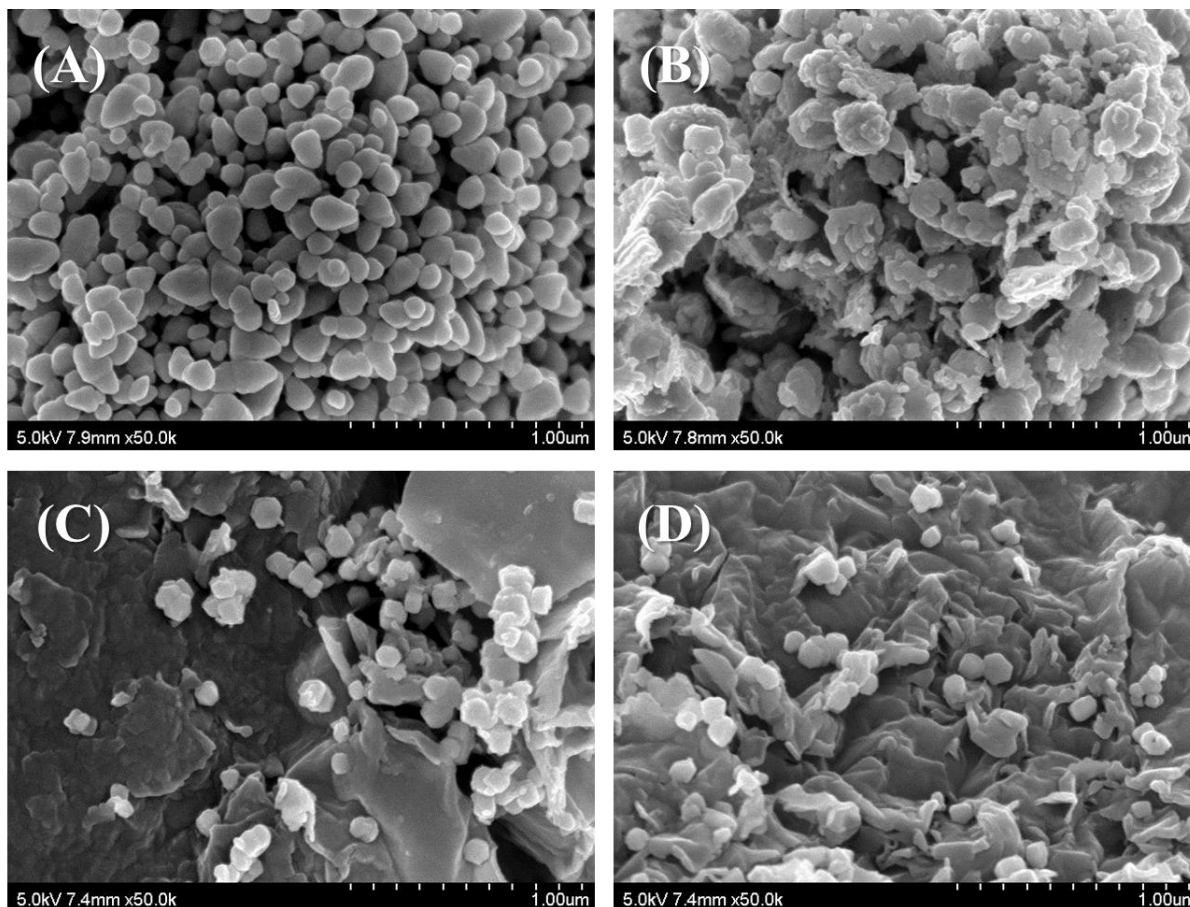


Figure 5.15 SEM images for fresh and spent samples at 300°C in N₂ for 2h: (A) ZnO fresh, (B) ZnO spent, (C) ZnO/rGO fresh and (D) ZnO/rGO spent

5.4. Characterizations of spent ZnO/rGO adsorbents

In this session, the characterizations of the spent (after H₂S adsorption) samples are described in order to determine the chemistry changes from the adsorption. The exposure to H₂S created new ZnS peaks located at $2\theta = 28.55$ (*111*), 47.44 (*220*) and 56.39° (*311*) which are matched with JCPDS 77-2100 [163]. This confirms that ZnS is the product of the H₂S adsorption on ZnO. The intensity of the ZnS peak for pure ZnO is much weaker than other ZnO peaks.

However, for the ZnO/rGO composite, the ZnS peak is clearly visible. This indicates that the ZnO/rGO composite is more active for the H₂S adsorption than ZnO. For both ZnO and ZnO/rGO composite, the ZnO peaks were still present, even after H₂S exposure. Detailed crystal structure analysis for ZnO and ZnO/rGO composite are listed in Tables 5.2 and 5.3.

Table 5.2: XRD for ZnO after H₂S exposure

ZnO						
2θ (°)	(hkl)	FWHM (°)	a (nm)	c (nm)	crystallite (nm)	d (Å)
31.76	(100)	0.286	0.325		30.19	2.82
34.42	(002)	0.294		0.521	29.49	2.60
36.26	(101)	0.303			28.74	2.48
47.54	(102)	0.371			24.41	1.91
56.60	(110)	0.369			25.54	1.62

Table 5.3: XRD for ZnO/rGO composite after H₂S exposure

ZnO/rGO						
2θ (°)	(hkl)	FWHM (°)	a (nm)	c (nm)	crystallite (nm)	d (Å)
31.62	100	0.374	0.327		23.08	2.82
34.26	002	0.338		0.523	25.66	2.61
36.12	101	0.422			20.69	2.48
47.46	102	0.820			11.05	1.91
56.38	110	0.520			18.12	1.63

The characteristic peaks of ZnO are maintained for both samples after H₂S exposure. This suggests that the adsorption process did not change the crystal structure of ZnO. The lattice constants a and c for the remained ZnO were calculated as 0.3251 and 0.5207 nm, respectively for pure ZnO; and as 0.3265 and 0.5231 nm, respectively for the ZnO/rGO composite. Those lattice constants are almost identical to that of the fresh samples. In addition, d -spacing for ZnO and ZnO/rGO composite did not change either after the exposure. The FWHM value at (002) plane was 0.312° for fresh ZnO; and after the exposure was 0.295° for spent ZnO. However, for ZnO/rGO composite, the FWHM value was 0.247° for fresh and 0.338° for spent sample. This indicates that for pure ZnO, the FWHM values were not changed significantly; but, for ZnO/rGO composite, the FWHM values increased, implying that the crystallite size decreased. The grain sizes of pure ZnO at (002) plane were 27.825 nm (fresh) and 29.486 nm (spent); but for ZnO/rGO composite, the grain sizes were changed from 35.211 nm (fresh) to 25.664 nm (spent). In summary, for both ZnO and ZnO/rGO composite, the characteristics of ZnO particles were not affected even after H₂S exposure since the lattice constants (a and c) and d -spacing remained unchanged. However, the crystallite sizes (or grain size) were affected. For pure ZnO, the crystallite sizes did not change significantly, but for the ZnO/rGO composite, the crystallite sizes clearly decreased after H₂S exposure.

Figure 5.16 shows the Zn 2p_{3/2} XPS data after H₂S exposure, and Table 5.4 presents the corresponding fractions of Zn, O and S in their various phases. After H₂S exposure, the fraction of Zn^{II} phase for pure ZnO decreased significantly (from 56.7 to 36.7%) implying that the zinc ions at the oxygen vacancy sites (Zn^{II}) had been participated during the adsorption process. For the ZnO/rGO composite, it was observed from the fresh sample that Zn²⁺ ions located near the

oxygen vacancy sites were dominant (61.4%) because the rGO contains abundant oxygen functional groups on the surface.

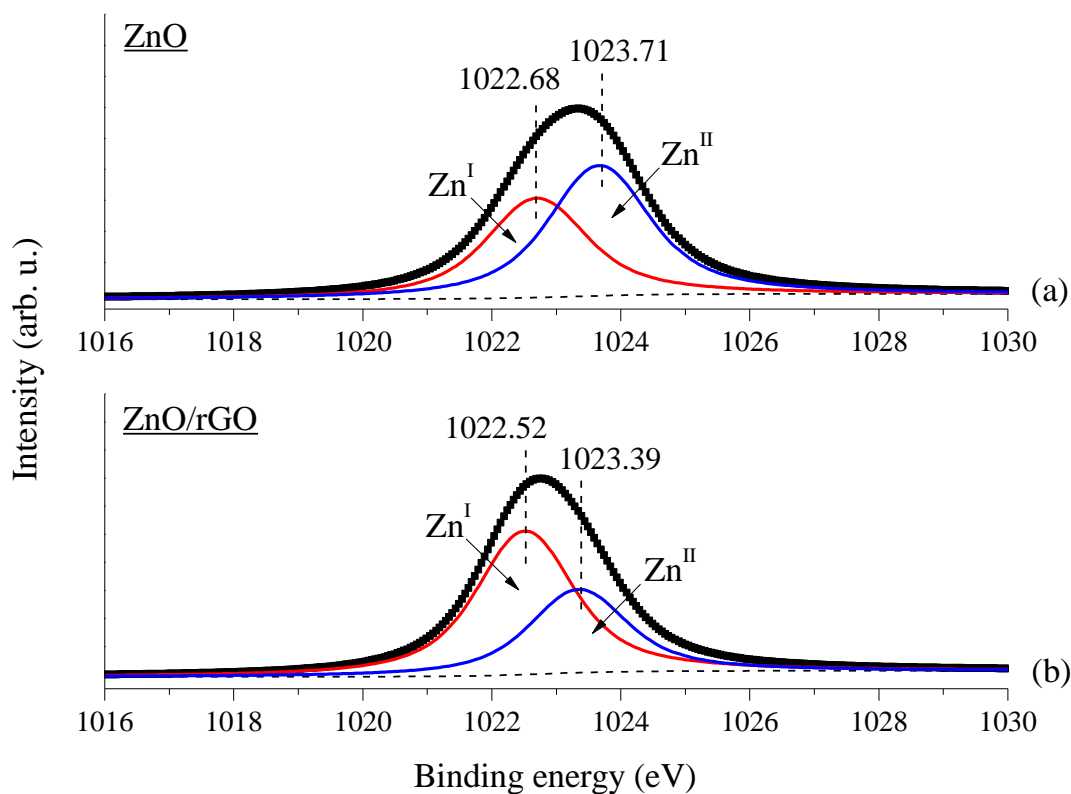


Figure 5.16: After H₂S exposure Zn 2p_{3/2} XPS for (a) ZnO and (b) ZnO/rGO composite

After the H₂S exposure, the fraction of Zn²⁺ ions classified as Zn^{II} decreased to 36.7%. This suggests that the oxygen functional groups from the rGO provides Zn ions which are loosely bonded in Zn-O and located near the oxygen vacancy sites (Zn^{II}) for HS⁻ and S²⁻ ions. Therefore, those Zn²⁺ ions preferably reacted with sulfur ions and turned to ZnS.

As mentioned earlier, abundant O^{II} and O^{III} phases in ZnO/rGO composite had a critical role to enhance the H₂S adsorption capacity since those phases provide surface oxygen to H₂S

molecules which can promote the dissociation of H_2S into HS^- and S^{2-} . Three major sub-peaks were also founded after H_2S exposure (Figure 5.17).

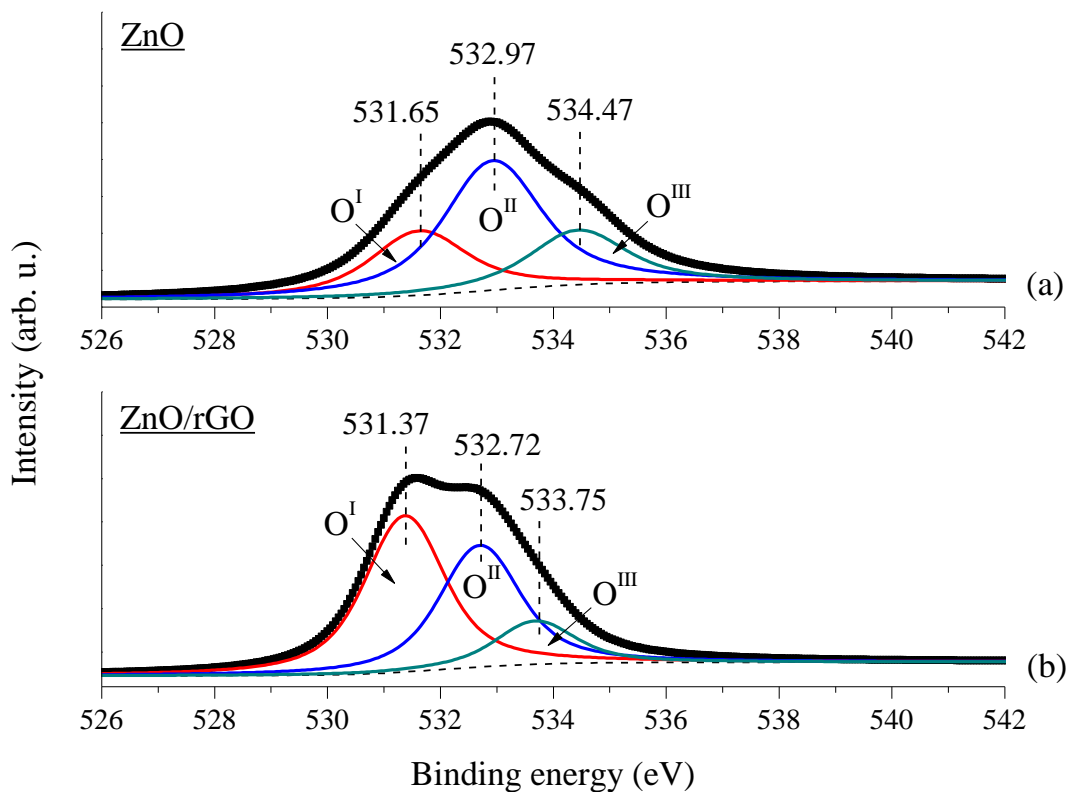


Figure 5.17: After H_2S exposure O1s XPS for (a) ZnO and (b) ZnO/rGO composite

For pure ZnO, O^{I} at 531.65 eV, O^{II} at 532.97 eV and O^{III} at 534.47 eV; for ZnO/rGO composite, O^{I} at 531.37 eV, O^{II} at 532.72 eV and O^{III} at 533.75 eV were observed. The slight BE shift toward higher range from the fresh samples disappeared. The quantitative fraction for O^{I} , O^{II} , and O^{III} also changed (Table 5.4).

Table 5.4: XPS fitting area portion for pure ZnO and ZnO/rGO composite

Elements	Phases	Fresh		After H ₂ S exposure	
		ZnO	ZnO/rGO	ZnO	ZnO/rGO
Zn	I	84.5%	38.6%	43.3%	63.3%
	II	15.5%	61.4%	56.7%	36.7%
O	I	59.1%	14.4%	25.8%	48.5%
	II	26.7%	39.3%	52.1%	38.0%
	III	14.2%	46.3%	22.0%	13.5%
S	I			35.0%	28.0%
	II			65.0%	35.7%
	III				36.3%

For pure ZnO, the O^I phase (59.1% for fresh sample) decreased to 25.8% implying that oxygen in Zn-O lattice had participated dominantly in the adsorption process. After the adsorption process, most of the oxygen ions were in phase II (52.1% for O^{II}). However, oxygen ions in ZnO/rGO composite behaved differently. Most of oxygen ions located on the surface and oxygen vacancy sites participated in the adsorption. The portion of O^{III} from the fresh sample (46.3%) decreased to 13.5%. The O^{III} phase is also considered as oxygen ions originated from the oxygen functional groups on the rGO surface. This suggests that the rGO composite could provide chemically adsorbed moisture or loosely bonded oxygen ions to ZnO which are preferentially active with sulfur containing ions (HS⁻ and S²⁻) for the adsorption.

From the H₂S adsorption process, a new product element was created, Zinc sulfide (ZnS), and it was confirmed from the XRD data. Figure 5.18 shows the XPS S2p spectra. For pure ZnO, one S2p peak was observed which could be sub-divided into two phases (S^I and S^{II}). The S^I and

S^{II} phases were located at 163.06 and 164.41 eV, respectively. The S^I and S^{II} phases are assigned to S 2p_{3/2} and S 2p_{1/2}, respectively [164], and those phases represent the monosulfide S²⁻ ions in Zn-S [165], [166]. The quantitative fractions for S^I and S^{II} were calculated as 35.0% and 65.0%, respectively. For ZnO/rGO composite, one additional S2p peak, assigned to S^{III} phase, and located at 170.19 eV was observed. The S^{III} phase represents sulfate (SO₄²⁻) [167], [168]. 36.3% of S^{III} phase was observed for the spent ZnO/rGO composite. The sulfate could originate from the loosely bonded oxygen ions (O^{II} and O^{III}) which are not located in the Zn-O lattice. Those oxygen ions located at the vacancy sites or surface should be able to contact with HS⁻ and S²⁻ ions easily and turn to sulfate. However, the pure ZnO possesses only oxygen ions in Zn-O lattice. Therefore, in order to react with sulfur ions, the Zn-O lattice should be destroyed to provide available Zn²⁺ and O²⁻ ions. This supports the fact that ZnO/rGO composite showed about 10-fold higher H₂S adsorption capacity than that of pure ZnO.

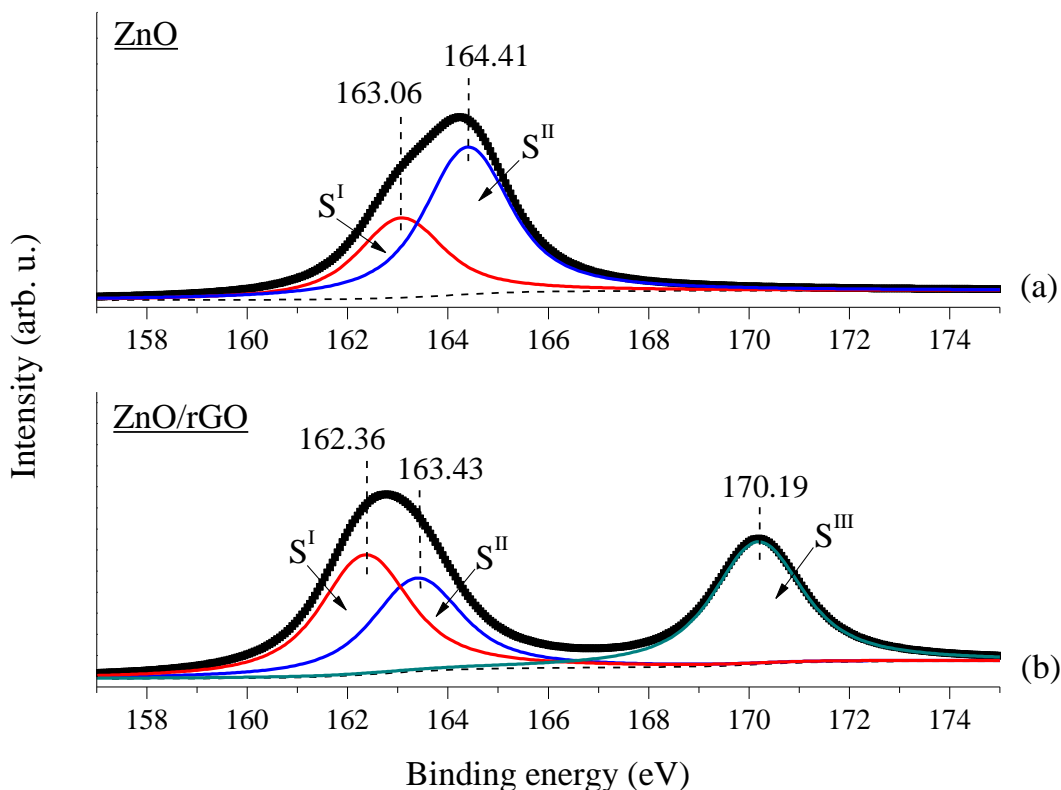


Figure 5.18: After H₂S exposure S1s XPS for (a) ZnO and (b) ZnO/rGO composite

Figure 5.19 shows the C1s XPS spectrum for ZnO/rGO after H₂S exposure. The C1s spectrum was fitted into four peaks like the fresh sample: sp² carbon (284.6 eV), carbon in C-O bonds (286.0 eV), carbonyl carbon C=O (287.5 eV) and carboxylate carbon O-C=O (289.4 eV). From the fresh ZnO/rGO composite, the ratio of carbon-carbon sp² carbon to carbon-oxygen bonds was 0.96. However, after H₂S exposure, the ratio increased to 1.21 implying that the quantity of carbon-oxygen bonds decreased. This further supports the hypothesis that the oxygen groups placed between the ZnO particle and the rGO surface are used during the adsorption process (i.e. H₂O and sulfate).

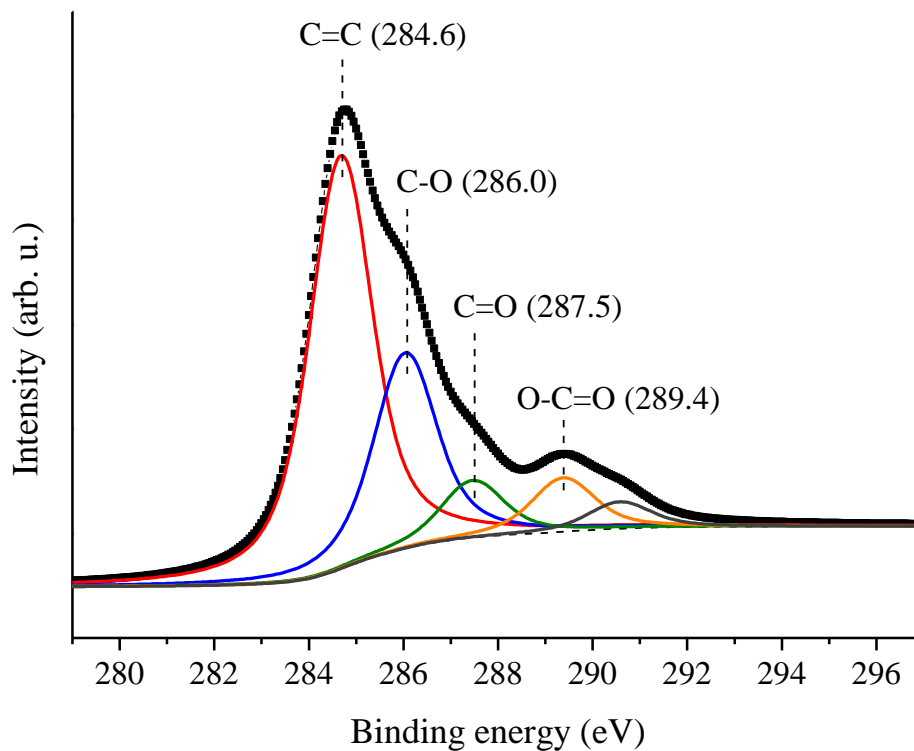


Figure 5.19: After H₂S exposure C1s XPS for ZnO/rGO composite

5.5. Summary

This chapter presents insights on the synthesis of nano-ZnO on reduced graphite oxide (rGO) composite *via* a microwave-assisted route and its use as a potential sorbent to adsorb hydrogen sulfide (H₂S) at ambient conditions and at 300°C. Various characterization methods (TGA, XRD, FT-IR, TEM and XPS) were performed in order to link their H₂S adsorption performance to the properties of the adsorbent's surface. Depending on the synthesis methods, the nano-sized ZnO on rGO presents different characteristics, in particular the degree of nano-

ZnO dispersion on the surface of the rGO. Microwave-assisted reduction was able to offer a mild reduction to the oxygen-containing functional groups attached on the surface of graphite oxide (GO). Those oxygen-containing functional groups provide the bridge and the terminal groups between zinc oxide and the rGO surface. Because those functional groups act as anchor sites for metal ions, it was possible to achieve uniformly distributed nano-sized ZnO particles on the surface of the rGO sheets. It also was confirmed that for the ZnO/rGO synthesized using the microwave method, the ZnO particle size and the degree of ZnO dispersion remained stable over time at 300°C, which was not the case for only the ZnO particles themselves. The effects of the different synthesis methods (microwave vs. reflux) were evaluated for H₂S adsorption. The adsorption capacity increased dramatically for the microwave-assisted composite compared to the composite manufactured using the reflux method.

This stable and highly dispersed feature of the ZnO/rGO composite allows for sustained high surface area over time. This was confirmed through breakthrough experiments for H₂S adsorption where it was found that the ZnO/rGO composite showed almost four times higher ZnO utilization efficiency than ZnO itself at 300 °C. The effect of the H₂ and CO₂ on H₂S adsorption was also investigated. The presence of hydrogen in the H₂S stream had a positive effect on the removal of H₂S since it allows a reducing environment for Zn-O and Zn-S bonds, leading to more active sites (Zn²⁺) to sulfur molecules. On the other hand, the presence of carbon dioxide (CO₂) showed the opposite trend, likely due to the oxidation environment and also due to possible competitive adsorption between H₂S and CO₂.

Chapter 6. H₂S adsorption on Cu₂O-ZnO/rGO composites

This chapter presents the H₂S adsorption capacity on copper oxide/zinc oxide with reduced graphite oxide (rGO) composite at 300 °C in dry condition. From Chapter 5, the ZnO/rGO composite has showed higher H₂S adsorption ability than pure ZnO. Chapter 2 introduced the H₂S adsorption ability for different metal oxides. Copper oxide has been chosen for this study since it is also one of the widely used sorbents for desulfurization processes. This study is investigating the synergetic effect of using bi-metal oxides (copper oxide and zinc oxide) and rGO composite with various amounts of copper oxide. A number of characterization techniques of fresh and spent samples has been used for investigating the chemical state changes of metal oxides while different portions of copper oxide were added. Those analyses indicated that the H₂S adsorption capacity changes depending on the different ratios of Cu₂O/ZnO with rGO composites.

6.1. H₂S breakthrough tests at mid temperature

H₂S adsorption breakthrough times (minute per gram of adsorbent) depending on the Cu/Zn ratios (100 mg of adsorbents were loaded) are presented in Fig. 6.1. It is clear that pure ZnO showed the lowest H₂S adsorption capacity. However, when ZnO nano-sized particles were deposited on a 2D rGO surface, the H₂S adsorption capacity had increased by a factor of more than three. Previous studies [126], [168] have proposed that the rGO containing oxygen functional groups (i.e. hydroxyl, carboxyl and epoxy) are anchoring the metal oxide on the surface, and those functional groups play a critical role in promoting the H₂S adsorption capacity.

One of the major roles is to help dispersing the nano-sized metal oxides on both sides of the rGO surface, preventing an aggregation effect at 300°C [169]. In addition, the oxygen functional groups are activating the oxygen in the lattice structure and graphene-based material (rGO) helps transferring electrons during H₂S adsorption [125]. In order to improve the H₂S adsorption capacity further, another well-known active metal oxide (i.e. copper oxide) has been added with various ratio of Cu/Zn. Clearly, the addition of copper to zinc oxide promoted the H₂S adsorption capacity. However, the degree of H₂S adsorption depended on the ratio of copper to zinc oxide (Figure 6.1).

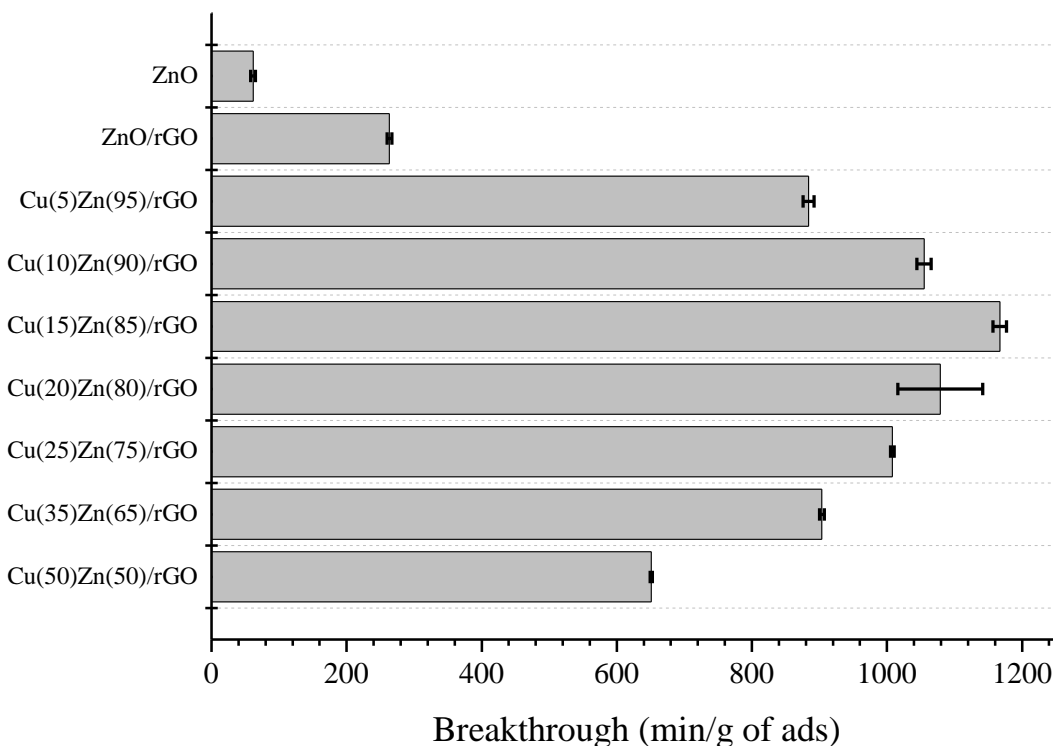


Figure 6.1: H₂S adsorption breakthrough tests at 300°C depending on Cu/Zn ratios

At 300°C in dry condition with 762 ppm of H₂S, the ZnO/rGO composite showed about 4 times higher adsorption capacity (261.9 min/g ads.) than that of pure ZnO (65.3 min/g ads.). When 5 mol% copper oxides (Cu₂O) were added to the ZnO/rGO composite, about 3.4 times increase of H₂S adsorption capacity compared to the ZnO/rGO composite was observed. Figure 6.1 shows that there is an optimum value for the Cu/Zn ratio that maximizes the H₂S adsorption capacity (1162.4 min/g of ads.), which was found for the Cu₁₅Zn₈₅/rGO adsorbent. The amount of H₂S adsorption capacity for Cu₁₅Zn₈₅/rGO composite is about 4.5 times higher than that of ZnO/rGO composite and about 18 times higher than pure ZnO. However, for Cu contents higher than 15 vol% (i.e. 20, 25, 35 and 50 vol% Cu), the H₂S adsorption capacities decreased. This implies that the content of Cu changed the chemistry in the Cu/Zn/rGO composites.

6.2. Characterizations of fresh Cu₂O-ZnO/rGO adsorbents

To shed more light on the H₂S adsorption capacities on various Cu/Zn ratio/rGO composites, analysis of crystal structure changes by XRD was performed (Figure 6.2). This figure confirms that the characteristic peak of graphite oxide (GO) located around 9-10° disappeared from all Cu/Zn/rGO composites when the microwave-assisted reduction process has been applied. This implies that the substrate (rGO) was turned to a 2D structure where both sides of the rGO could be used for metal oxide deposition. After the deposition of ZnO on the rGO surface, the ZnO peaks were shown at $2\theta = 31.7, 34.3, 36.2, 47.4$ and 56.4° which are in agreement with JCPDS 36-1451. When copper components were added into the ZnO/rGO composite, both ZnO and Cu₂O peaks ($2\theta = 36.4$ and 42.4°), corresponding to JCPDS 05-0667, were observed; but still without GO peak.

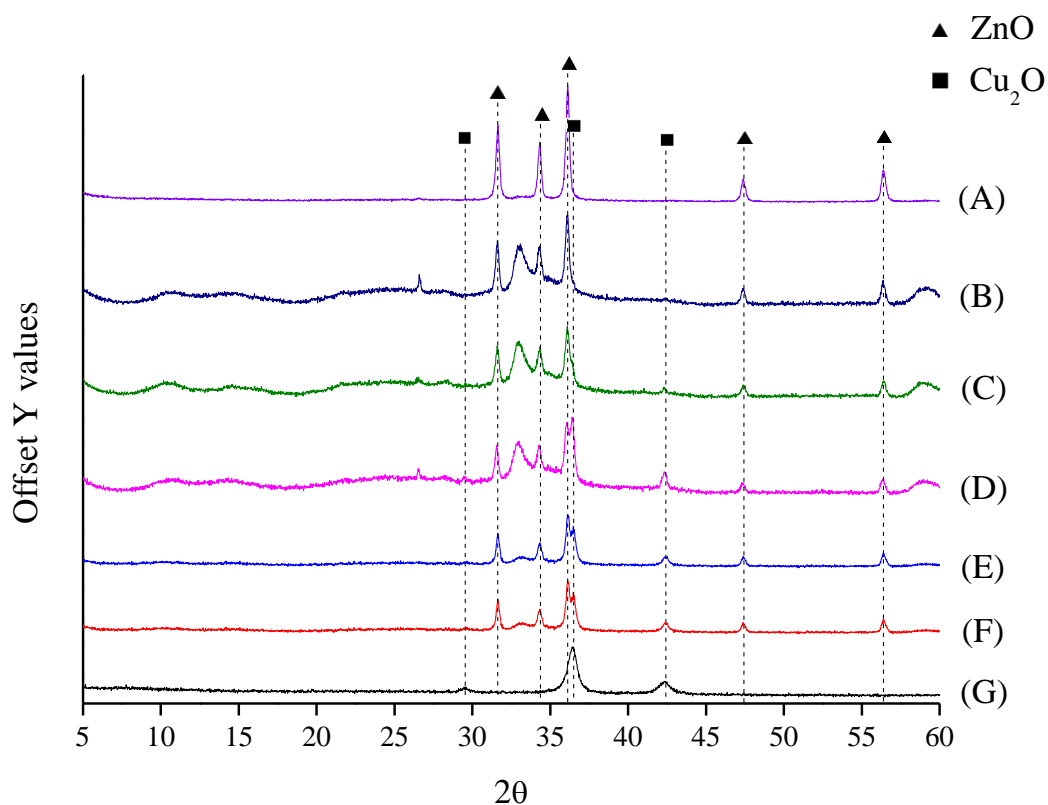


Figure 6.2: XRD for fresh $\text{Cu}_2\text{O}/\text{ZnO}/\text{rGO}$ composites: (A) ZnO/rGO , (B) $\text{Cu}_5\text{Zn}_{95}/\text{rGO}$, (C) $\text{Cu}_{10}\text{Zn}_{90}/\text{rGO}$, (D) $\text{Cu}_{15}\text{Zn}_{85}/\text{rGO}$, (E) $\text{Cu}_{20}\text{Zn}_{80}/\text{rGO}$, (F) $\text{Cu}_{25}\text{Zn}_{75}/\text{rGO}$ and (G) $\text{Cu}_{35}\text{Zn}_{65}/\text{rGO}$

In addition to structural changes, depending on the degree of Cu content in the ZnO/rGO composite, the crystallinity of the $\text{ZnO}/\text{Cu}_2\text{O}$ composites changed. It is reported that the availability of oxide ions on both ZnO and Cu_2O surfaces is a critical factor for H_2S chemisorption since those oxide ions act as Brønsted basic centers [170]. For the $\text{Cu}_5\text{Zn}_{95}/\text{rGO}$, the copper peaks were not observed since the content of Cu was small enough not to be seen compared to the peak ZnO . However, when the content of Cu is larger than 5%, the characteristic peaks of Cu_2O appeared. In addition, the intensity of Cu peaks varied when changing the Cu content, but no significant changes for the ZnO peaks were observed. This

indicates that the ZnO crystallinity is retained even when increasing the concentration of Cu. However, when the Cu content was larger than 25% ($\text{Cu}_{25}\text{Zn}_{85}/\text{rGO}$), the ZnO peaks were about to disappear. It was observed that when the ratios of Cu/Zn ranged from 10% ($\text{Cu}_{10}\text{Zn}_{90}/\text{rGO}$) to 25% ($\text{Cu}_{25}\text{Zn}_{85}/\text{rGO}$), the characteristic peaks of Cu_2O and ZnO were visible together. The detailed crystalline analysis for Cu_2O and ZnO is summarized in Table 6.1. The average ZnO lattice constants of $a (=b)$ and c were 3.26 and 5.22 Å, respectively; the Cu_2O lattice constant of $c (=a =b)$ was 4.258 Å for all samples. Those values are in good agreement with other references [171], [172]. This implies that the deposition of ZnO and Cu_2O particles on the surface of rGO did not change the original structure of the ZnO and Cu_2O .

Table 6.1: XRD crystallite analysis for ZnO/Cu₂O/rGO composite

	ZnO								Cu ₂ O							
	(100)				(002)				(101)		(111)		(200)			
	2θ	FWHM	crystallite size	a=b	2θ	FWHM	c	TC	2θ	FWHM	2θ	FWHM	2θ	FWHM	a=b=c	crystallite size
	(°)	(°)	(nm)	(nm)	(°)	(°)	(nm)		(°)	(°)	(°)	(°)	(°)	(°)	(nm)	(nm)
ZnO	31.7	0.300	28.792	3.255	34.3	0.312	5.219	0.862	36.2	0.319						
ZnO/rGO	31.6	0.266	32.447	3.263	34.3	0.247	5.222	0.219	36.1	0.259						
Cu ₅ Zn ₉₅ /rGO	31.6	0.238	36.280	3.263	34.3	0.281	5.222	0.120	36.1	0.275						
Cu ₁₀ Zn ₉₀ /rGO	31.6	0.251	34.327	3.269	34.3	0.262	5.219	0.100	36.1	0.344	36.4	0.266	42.3	0.163	4.266	54.423
Cu ₁₅ Zn ₈₅ /rGO	31.6	0.252	34.235	3.271	34.3	0.256	5.228	0.092	36.0	0.293	36.4	0.332	42.3	0.359	4.268	24.786
Cu ₂₀ Zn ₈₀ /rGO	31.6	0.232	37.173	3.265	34.3	0.276	5.222	0.066	36.1	0.314	36.5	0.370	42.5	0.362	4.249	24.617
Cu ₂₅ Zn ₇₅ /rGO	31.6	0.234	36.854	3.265	34.3	0.282	5.222	0.068	36.1	0.302	36.5	0.374	42.5	0.363	4.249	24.526
Cu ₃₅ Zn ₆₅ /rGO											36.4	0.676	42.4	0.616	4.262	14.445

Figure 6.3 shows detailed XRD patterns for Cu₂O (110) and ZnO (101) in the 2θ range of 35-38° for Cu (since in this range the peaks for ZnO and Cu₂O overlapped) content between 10 and 25% where clear ZnO and Cu₂O characteristic peaks were observed. In general, in this range, it was confirmed that the nanocrystalline Cu₂O and ZnO particles were well developed with different ratios. The relative amount of ZnO and Cu₂O could be determined by comparing the area ratios of ZnO and Cu₂O. The ZnO/Cu₂O area ratios were calculated as 4.51, 0.81, 1.22 and 1.15 for Cu₁₀Zn₉₀/rGO, Cu₁₅Zn₈₅/rGO, Cu₂₀Zn₈₀/rGO and Cu₂₅Zn₇₅/rGO composites, respectively. Except for 15% Cu addition, deposition of ZnO on the rGO surface was more preferential than that of Cu₂O.

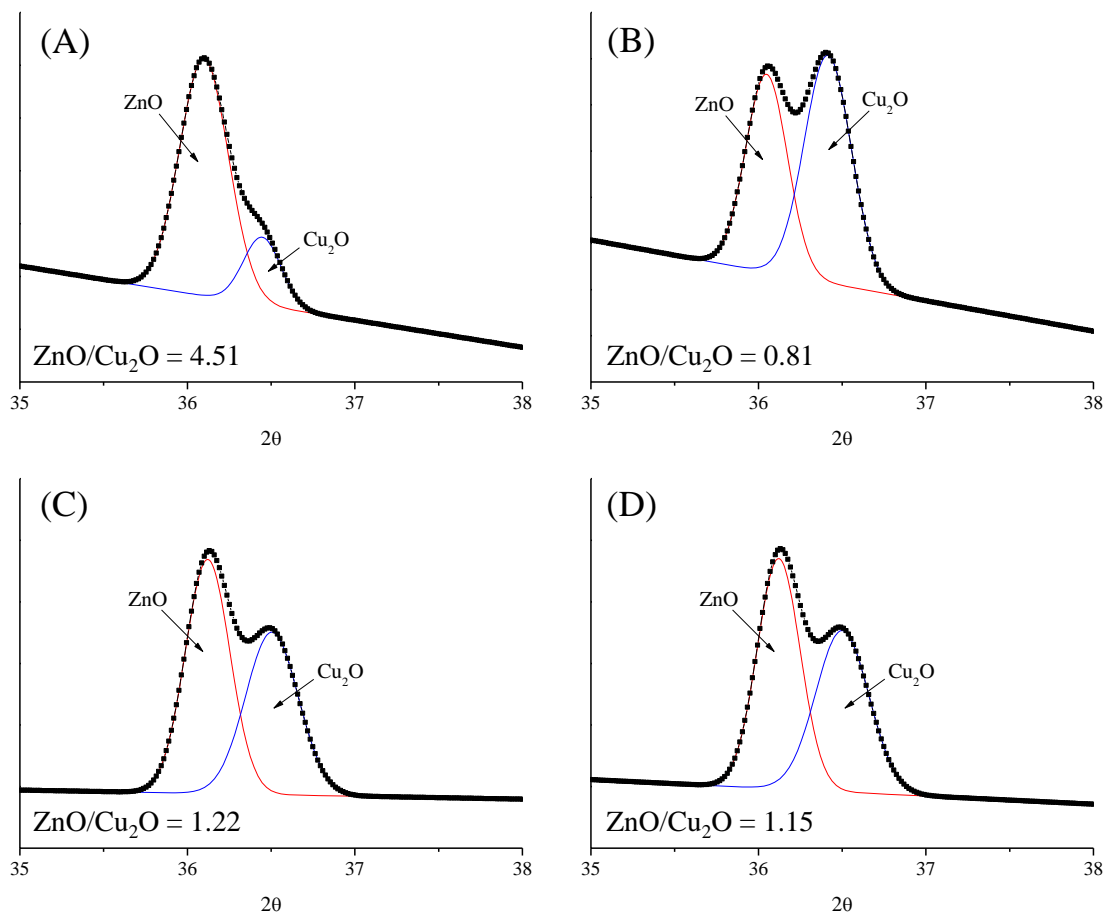


Figure 6.3: Detail XRD peak analysis depending on the fraction of Cu₂O (111) and ZnO (101):

(A) Cu₁₀Zn₉₀/rGO, (B) Cu₁₅Zn₈₅/rGO, (C) Cu₂₀Zn₈₀/rGO and (D) Cu₂₅Zn₇₅/rGO

As described above, the addition of copper ions affected the chemical state of the ZnO. Figure 6.4 presents the XPS survey spectrum of copper in Cu/Zn/rGO composites. Cu 2p_{1/2} (~954.9 eV), Cu 2p_{3/2} (~934.9 eV) and shake-up (~943 eV) peaks were observed. The appearance of the shake-up peak (or satellite peak) represents the presence of Cu²⁺ phase among the copper ions [173]. Similar to zinc ions, the oxidation states of copper also could be divided into two phases (Cu^I and Cu^{II} phases). The Cu^I phase, placed at ~ 933.2 eV, represents the

copper ions of Cu^{1+} ; the Cu^{II} phase located at ~ 934.8 eV indicates Cu^{2+} [174], [175]. As shown in Figure 6.4 (b)-(f), the area portions of $\text{Cu}^{\text{I}}/\text{Cu}^{\text{II}}$ were affected by the ratios of Cu/Zn. The area ratios of Cu^{I} and Cu^{II} phases were 48.4/51.6%, 50.7/49.3%, 55.0/45.0%, 53.7/46.3% and 47.8/52.2% for $\text{Cu}_5\text{Zn}_{95}/\text{rGO}$, $\text{Cu}_{10}\text{Zn}_{90}/\text{rGO}$, $\text{Cu}_{15}\text{Zn}_{85}/\text{rGO}$, $\text{Cu}_{20}\text{Zn}_{80}/\text{rGO}$ and $\text{Cu}_{25}\text{Zn}_{75}/\text{rGO}$, respectively. This confirms that the Cu^{1+} and Cu^{2+} oxidation states of copper ions co-existed and that the ratios of $\text{Cu}^{1+}/\text{Cu}^{2+}$ depended on the amount of copper. Among those composites, $\text{Cu}_{15}\text{Zn}_{85}/\text{rGO}$ composite which had the highest H_2S adsorption capacity possessed the highest portion of Cu^{1+} (55.0%). It is reasonable since it is widely known that Cu^{1+} (i.e. Cu_2O) is more reactive toward H_2S than Cu^{2+} (i.e. CuO) due to the smaller band gap [176].

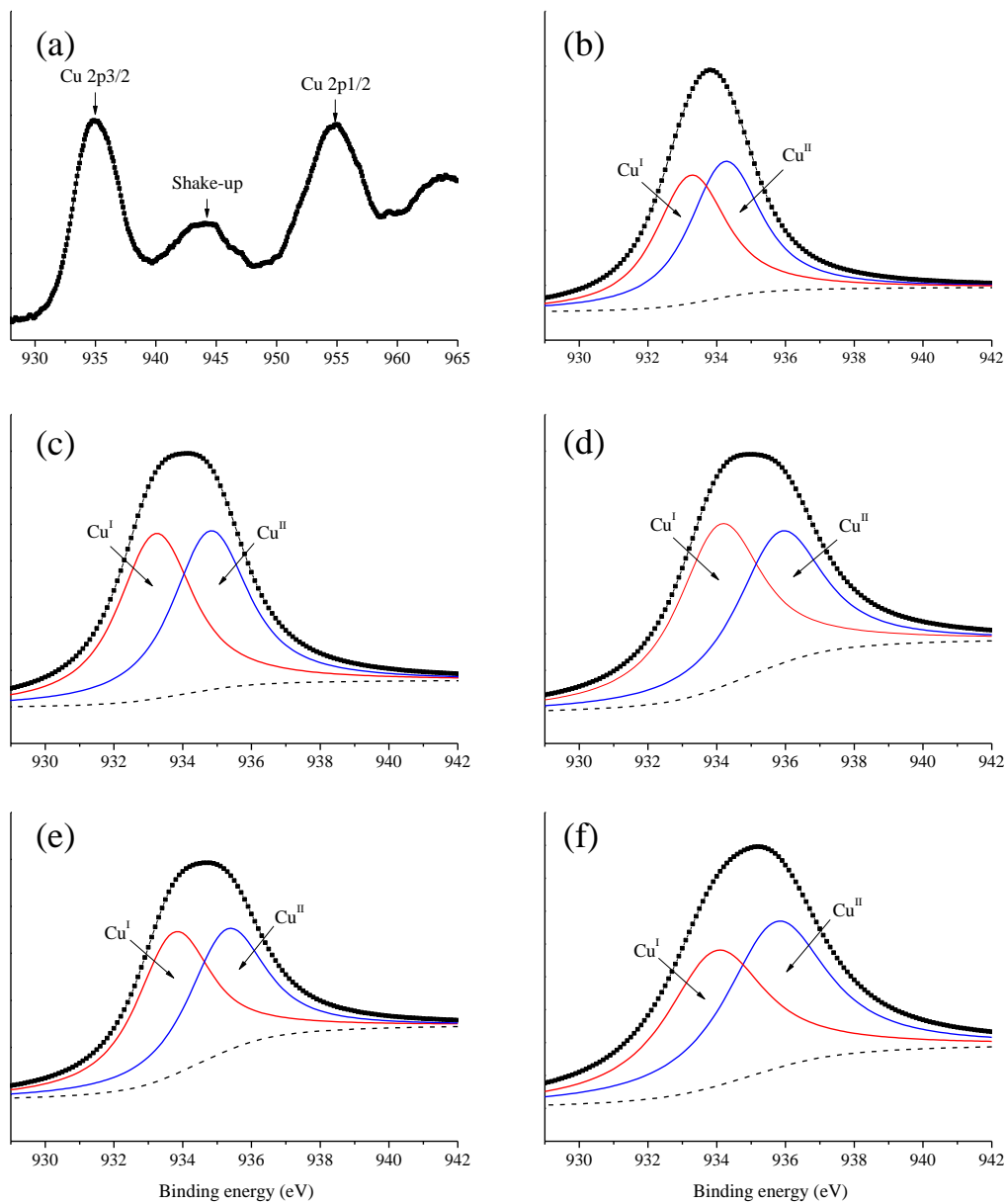


Figure 6.4: Cu_{2p} XPS analysis: (a) Cu_{2p} survey (b) Cu₅Zn₉₅/rGO, (c) Cu₁₀Zn₉₀/rGO, (d) Cu₁₅Zn₈₅/rGO, (e) Cu₂₀Zn₈₀/rGO and (f) Cu₂₅Zn₇₅/rGO

Beside the effect of metal oxide dispersion, the change in chemical oxidation states also would cause a change in H₂S adsorption capacity. Figure 6.5 (a) shows the Zn XPS survey and it

confirmed that the oxidation state of Zn in the Zn/Cu/rGO composite was Zn^{2+} since the binding energy (BE) difference between the Zn 2p_{1/2} (1045.9 eV) and Zn 2p_{3/2} (1022.7 eV) was 23.2 eV [152]. In order to evaluate the effects of copper on the oxidation state change of the ZnO, the Zn 2p_{3/2} peak was divided into two major Zn phases in the binding energy of ~ 1021.1 (Zn^I) and ~ 1022.3 eV (Zn^{II}). The Zn^I phase represents the characteristic of Zn atoms in Zn-O bonds; the Zn^{II} phase is assigned to the Zn in the Zn-O bonds surrounded by oxygen vacancies implying that Zn atoms are not exactly occupied in the ZnO lattice [149], [150]. Depending on the Cu ratios (Figure 6.5 (b)-(f)), the area ratios of Zn^I and Zn^{II} phases were 64.4/35.4%, 66.7/33.3%, 71.4/28.6%, 60.8/39.2% and 50.7/49.3% for Cu_5Zn_{95}/rGO , $Cu_{10}Zn_{90}/rGO$, $Cu_{15}Zn_{85}/rGO$, $Cu_{20}Zn_{80}/rGO$ and $Cu_{25}Zn_{75}/rGO$, respectively. This suggests that the content of Cu in ZnO/rGO modified the chemistry of zinc ions in the ZnO lattice. For $Cu_{15}Zn_{85}/rGO$ composite, the portion of Zn^I phase was highest than for other composites. It implies that when 15% of copper co-existed with ZnO, a higher amount of zinc ions (71.4%) were located in the Zn-O bond lattice; and smaller amount of zinc ions (28.6%) were located at the oxygen vacancy sites (not in the Zn-O lattice). As a result, the larger amount of zinc ions placed in the Zn-O lattice, the higher the H_2S adsorption capacity.

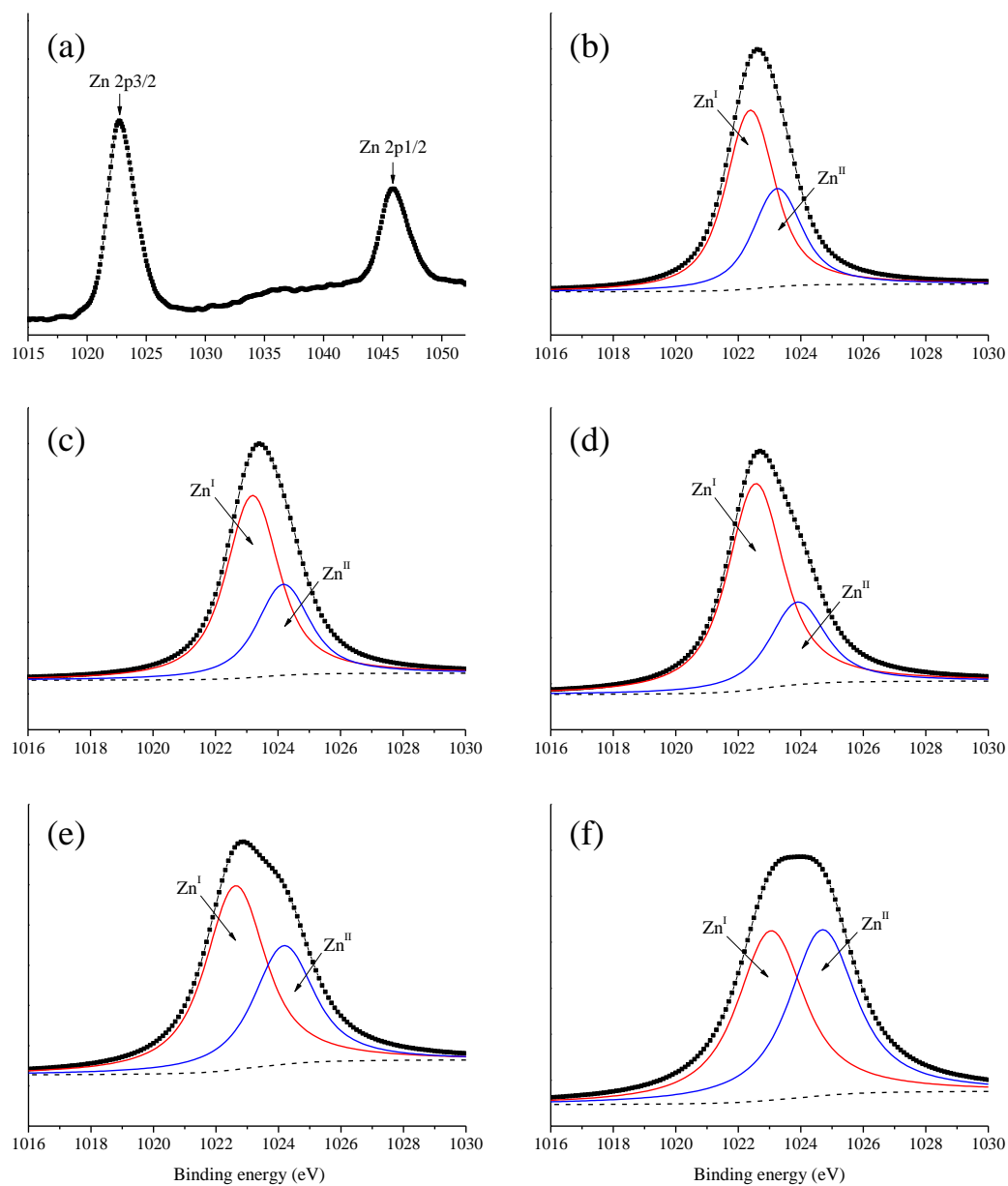


Figure 6.5: Zn 2p XPS analysis: (a) Zn2p survey (b) $\text{Cu}_5\text{Zn}_{95}/\text{rGO}$, (c) $\text{Cu}_{10}\text{Zn}_{90}/\text{rGO}$, (d) $\text{Cu}_{15}\text{Zn}_{85}/\text{rGO}$, (e) $\text{Cu}_{20}\text{Zn}_{80}/\text{rGO}$ and (f) $\text{Cu}_{25}\text{Zn}_{75}/\text{rGO}$

It is necessary to investigate the oxidation states of the oxygen ions since those oxygen sources could be provided from ZnO , Cu_2O , CuO and oxygen functional groups on the rGO

surface. The oxidation states of oxygen ions could be divided into three phases (O^I , O^{II} and O^{III}) depending on the BE (Figure 6.6). The O^I phase (~ 531.3 eV) represents the oxygen ions located in the metal oxide lattice (i.e. ZnO, Cu_2O or CuO); the O^{II} phase (~ 533.0 eV) represents the oxygen ions at the oxygen deficient region; and the O^{III} phase (~ 534.5 eV) indicates the chemisorbed oxygen or adsorbed moisture [174], [177], [178]. The area ratios of $O^I/O^{II}/O^{III}$ phases were 28.8/44.0/27.2%, 22.1/54.5/23.4%, 20.8/48.3/31.0%, 22.1/45.4/32.5% and 24.9/39.9/35.2% for Cu_5Zn_{95}/rGO , $Cu_{10}Zn_{90}/rGO$, $Cu_{15}Zn_{85}/rGO$, $Cu_{20}Zn_{80}/rGO$ and $Cu_{25}Zn_{75}/rGO$, respectively. It is observed that depending on the copper content, the oxygen oxidation states were modified. In addition, the O^{II} and O^{III} phases were dominant in all samples (i.e. $> 60\%$).

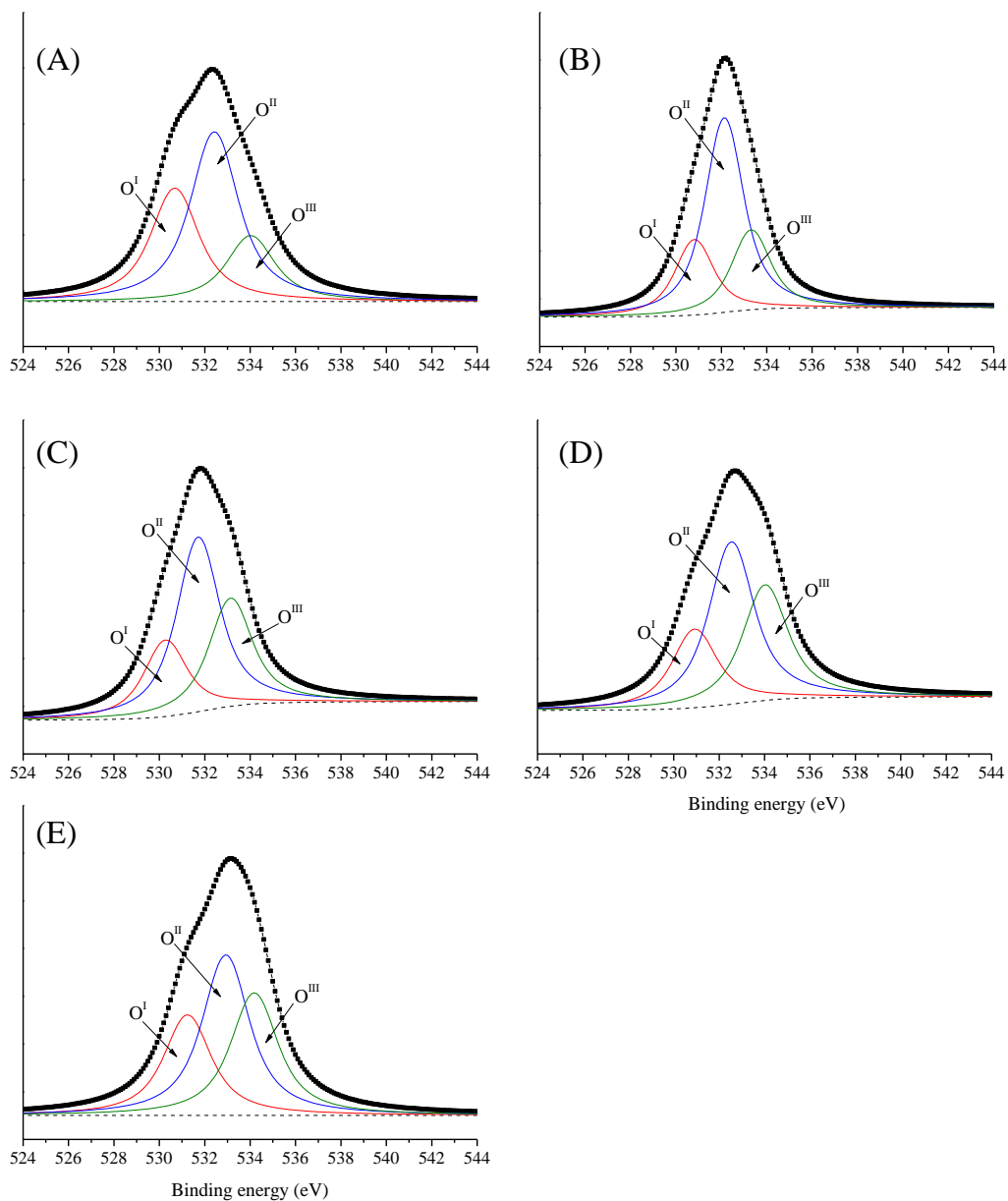


Figure 6.6: O_{1s} XPS analysis: (A) Cu_5Zn_{95}/rGO , (B) $Cu_{10}Zn_{90}/rGO$, (C) $Cu_{15}Zn_{85}/rGO$, (D) $Cu_{20}Zn_{80}/rGO$ and (E) $Cu_{25}Zn_{75}/rGO$

It can, therefore, be concluded that there is an abundant amount of oxygen ions that were not located in the metal oxide lattice, and most of the oxygen ions were from the adsorbed

moisture and located near the metal oxide lattice (i.e. deficient region). Among all composites, the Cu₁₅Zn₈₅/rGO showing the highest H₂S adsorption capacity possessed the largest portion of oxygen from phase O^{II} and O^{III} (i.e. lowest O^I phase). This further confirms that the oxygen functional groups play a critical role for the H₂S adsorption.

6.3. Characterizations of spent Cu₂O-ZnO/rGO adsorbents

As described above, depending on the Cu content, the chemistry of zinc oxide, copper oxide and oxygen has been modified, which in turn affected the H₂S adsorption capacity. After exposure to H₂S at 300°C in 762 ppm of H₂S environment, the characteristics of the crystalline structure changed (Figure 6.7). The Cu₁₅Zn₈₅/rGO composite was chosen for the spent analysis due to its highest H₂S adsorption capacity. First of all, a strong ZnS peak located at 2θ of 28.5° and CuS (2θ of 26.5, 29.4, 32.9, 48.4 and 59.1° corresponding to JCPDS 06-0464) were clearly found (Figure 6.6 (a), (b)).

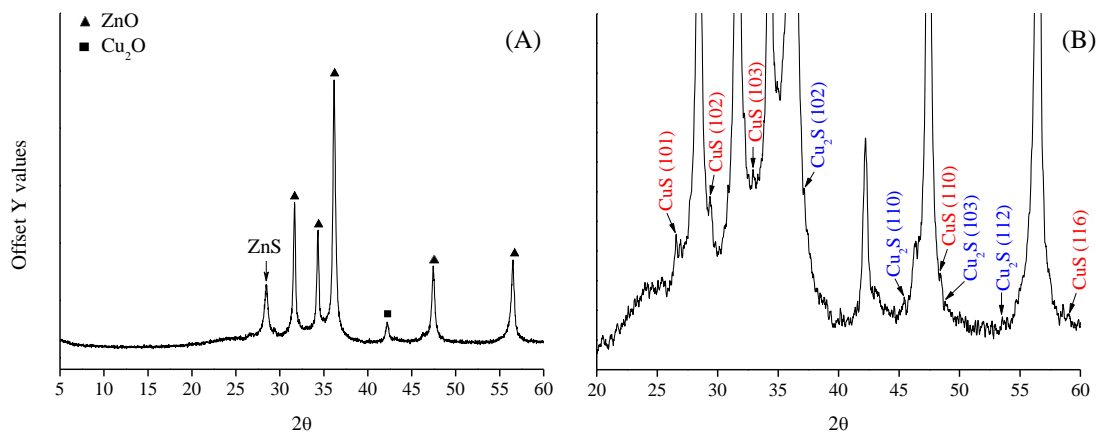


Figure 6.7: (A) Overall XRD analysis and (B) detail XRD diffractions for spent $\text{Cu}_{15}\text{Zn}_{85}/\text{rGO}$ composite

Although, not as obvious, peaks for Cu_2S (2θ of 37.1, 45.4, 48.8 and 53.5° corresponding to JCPDS 26-1116) were also detected. This could support the presence of co-existing Cu^{1+} and Cu^{2+} from the fresh $\text{Cu}_{15}\text{Zn}_{85}/\text{rGO}$ composite. After H_2S adsorption, the $\text{ZnO}/\text{Cu}_2\text{O}$ ratio was increased to 11.21 which represented a dramatic decrease of Cu_2O to CuS or Cu_2S (Figure 6.8). This implies that the copper oxide is more reactive than the zinc oxide for the H_2S adsorption since it is known that each adsorbed H_2S would produce one proton on ZnO while producing two protons on Cu_2O [170].

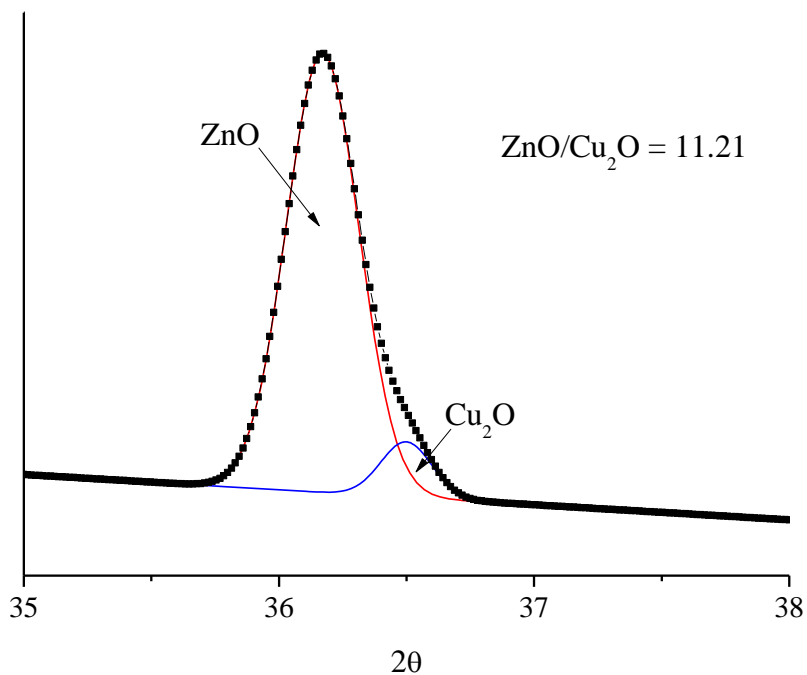


Figure 6.8: XRD for ZnO/Cu₂O area ratio for spent Cu₁₅Zn₈₅/rGO composite

Figure 6.9 shows the new generated S2p spectrum from the Cu₁₅Zn₈₅/rGO composite after exposure to H₂S. The S2p spectrum could be divided into three phases (S^I, S^{II} and S^{III}) located at 162.4, 163.4 and 170.2 eV, respectively. The S^I and S^{II} phases could be assigned to S 2p_{3/2} and S 2p_{1/2}, respectively [164]. Those phases represent the sulfide S²⁻ ions in zinc sulfide or copper sulfide, although they are not clearly classified [165], [166].

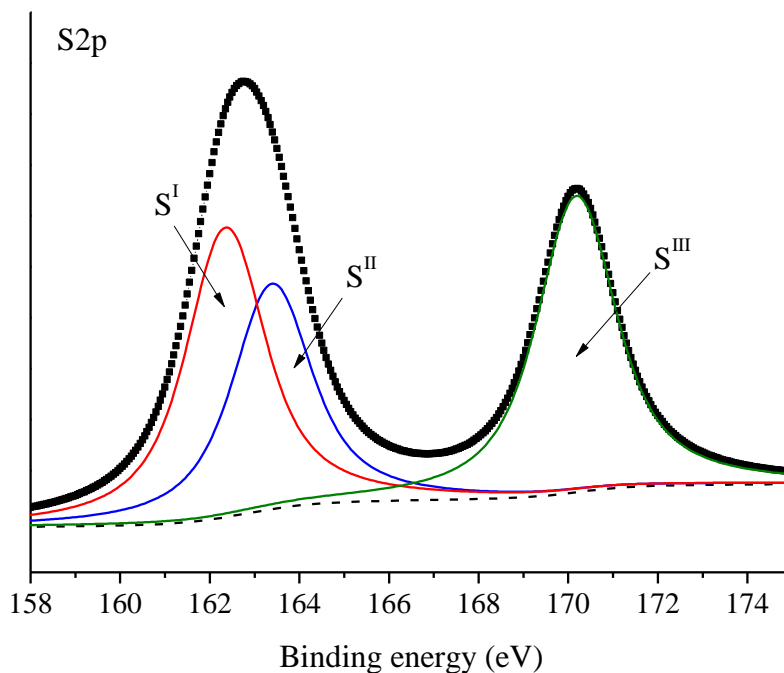


Figure 6.9: S2p XPS analysis for Cu₁₅Zn₈₅/rGO composite after H₂S exposure

The quantitative portions for S^I and S^{II} were calculated as 37.3% and 23.8%, respectively. There was one more S2p peak, assigned to S^{III} phase (38.9%) and representing sulfate (SO₄²⁻) [167], [168]. It can be expected that those sulfate ions originated from the loosely bonded oxygen ions (O^{II} and O^{III}) which were not located in the oxide lattice. Those oxygen ions located at the vacancy sites or at the surface were readily contacted with HS⁻ and S²⁻ ions and turned to sulfate.

6.4. Summary

In this chapter, the effects of copper with zinc oxide (ZnO) and reduced graphite oxide (rGO) composite on the hydrogen sulfide (H₂S) adsorption capacity have been studied. It was found that depending on the copper loading, the H₂S adsorption capacity has been increased by up to 18 times compared to pure ZnO. In order to investigate the oxidation changes on copper and zinc oxides, crystallite analysis by XRD and chemical state analysis by XPS were performed. It was confirmed that the 2D rGO substrate, containing abundant oxygen functional groups, promoted the metal oxide dispersion and increased the H₂S adsorption efficiency by providing loosely bonded oxygen ions to the sulfur molecules. In addition, it was determined that the optimum content of copper was 15% related to the ZnO for maximizing the H₂S adsorption. The 15% copper with ZnO/rGO led to the highest portion of zinc ions located in Zn-O lattice; and to the co-existence of Cu¹⁺ and Cu²⁺ ions with ZnO. The H₂S exposure at 300°C produces metal sulfides (i.e. zinc sulfide and copper sulfide) and sulfate ions.

Chapter 7. Regeneration of ZnO/rGO composites

This chapter presents the H₂S adsorption capacity with regeneration ability for ZnO/reduced graphite oxide (rGO) composite at 300 °C. From an industrial point of view, life time of adsorbents is a critical factor. Therefore, the recycle ability of adsorbents should be considered. From Chapter 5, the ZnO/rGO composite demonstrated considerable improvement in H₂S adsorption capacity compared to pure ZnO particles at 300 °C. However, in industrial point of view, the regeneration ability is considered as one of the most critical factors to choose a right adsorbent. Therefore, it was decided to investigate the regeneration ability of ZnO/rGO composite. This chapter mainly focuses on the chemical state changes in ZnO/rGO composites during recycles. This chapter also sheds light on the critical functionality of rGO as a substrate in order to enhance and maintain the H₂S adsorption capacity and regeneration ability.

7.1. H₂S adsorption capacity through regeneration cycles

From an industrial point of view, regeneration of the adsorbent is critical. Multiple regeneration cycles for pure ZnO and ZnO/rGO composite were then studied. Identical sulfidation conditions (300 °C and 750 ppm H₂S) as in the previous experiments were used; and a temperature of 600 °C (in N₂ only) was used for regeneration. Figure 7.1 shows the regeneration capacities (mg of sulfur adsorbed per gram of adsorbent) for pure ZnO (up to 5 cycles) and ZnO/rGO samples (up to 8 cycles). The initial sulfur adsorption capacity for pure ZnO (31.7 mg S/g ads) is corresponded with ZnO from references; but higher than a commercial BASF ZnO sorbent (19 mg S/g ads) [14], [150]. From previous Chapter, the initial sulfur

adsorption capacity for ZnO/rGO composite (172.6 mg S/g ads) was higher than that from pure ZnO. The rGO which has sp^2 carbon configuration possesses a free π orbital on the surface [179]; therefore, the presence of rGO with ZnO promotes the electron transfer between the H_2S and surface of metal due to the free π orbitals. The formation of ZnO/rGO composite involves the link between the $-OH$ groups on the rGO surface and ZnO lattice, as well as the reactions of zinc ions with acidic groups presented on the edge of the rGO layers [122].

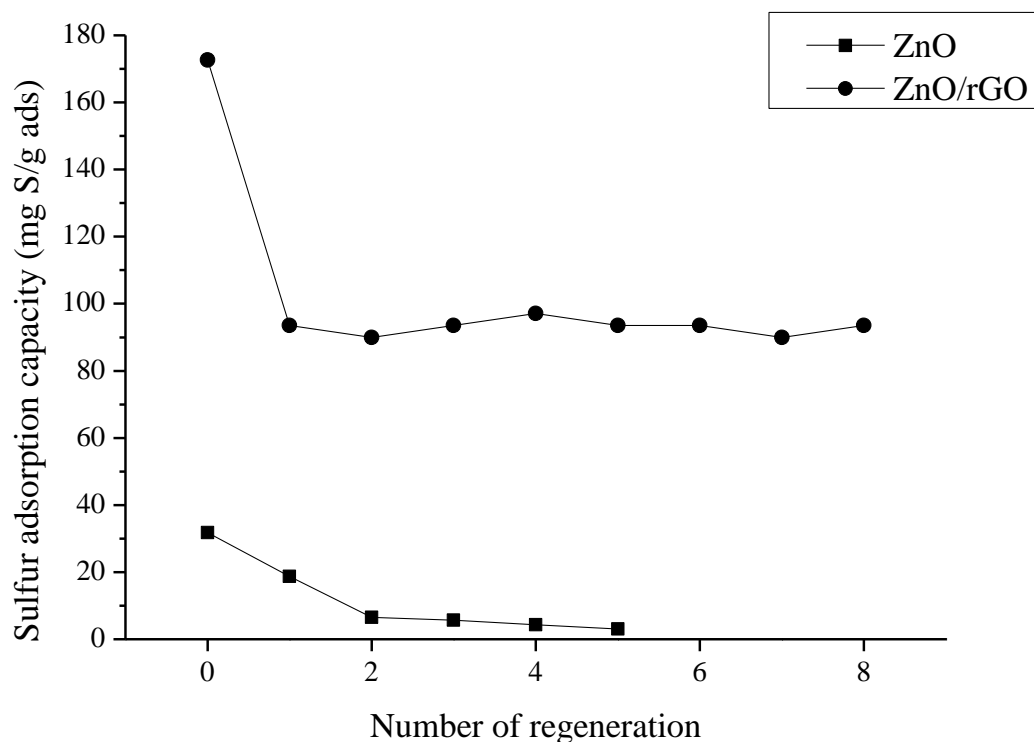


Figure 7.1: H_2S adsorption capacities on ZnO and ZnO/rGO composite at 300 °C sulfidation with 600 °C regeneration in N_2

After the first regeneration, the decrease in sulfur capacity for both samples were observed as 93.5 mg S/g ads for ZnO/rGO and 18.6 mg S/g ads for pure ZnO. It is clear that pure ZnO does not retain its sulfur adsorption capacity, which is nearly zero (3.1 mg S/g ads) after only 5 cycles. On the other hand, although the sulfur adsorption capacity decreases significantly after the first cycle (from ~170 down to ~94 mg S/g ads), this adsorption capacity remains constant, at least over 8 cycles. This supports that the functionality of rGO as a substrate plays a critical role to enhance and maintain the sulfur adsorption capacity over multiple regeneration cycles.

7.2. Characterizations of fresh and spent adsorbents after regeneration

There are several aspects determining the adsorption capacity of the adsorbents. Surface area is an important a factor affecting the adsorption capacity. The initial surface areas of ZnO and ZnO/rGO composite were 68.4 and 265.6 m²/g, respectively. The higher surface area of ZnO/rGO composite was from the 2D rGO substrate since the rGO surface containing oxygen functional groups is able to disperse the nano-sized ZnO particles onto the surface. It would lead to increase the contact area of the active ZnO particles to the target molecules (i.e. HS⁻ and S²⁻). After the first regeneration at 600 °C, the surface areas of ZnO and ZnO/rGO became 25.2 and 178.8 m²/g, respectively. It can be observed that the surface area of ZnO was dramatically decreased after the high temperature annealing. This phenomenon could support the large drop in adsorption capacity after the first regeneration. After further regenerations, the surface area of ZnO was reduced to 15.2 m²/g (after 5th cycles); but that of ZnO/rGO composite was maintained

as 163.1 m²/g (after 8th cycles). Clearly, the pattern for the change in surface area correlates somewhat with that for the change in adsorption performance for both ZnO and ZnO/rGO.

Morphology changes over regeneration cycles were observed through SEM analysis (Figure 7.2). For pure ZnO sample, it was observed that the surface of ZnO shows some aggregation, as well as some cracks (Figure 7.2-(b)). The cracks could be generated due to the multiple sulfidation-regeneration cycles of ZnO since the lattice structure of ZnO was partially destroyed over several cycles. On the other hand, the average surface morphology of ZnO/rGO composite was maintained over 8 cycles. This supports the idea that the presence of rGO as a substrate could distribute the nano-sized ZnO over the surface since it has been known that the oxygen functional groups on rGO surface are anchoring metal ions (Figure 7.2 (c)-(d)). This could explain the stable sulfur adsorption performance over 8 cycles.

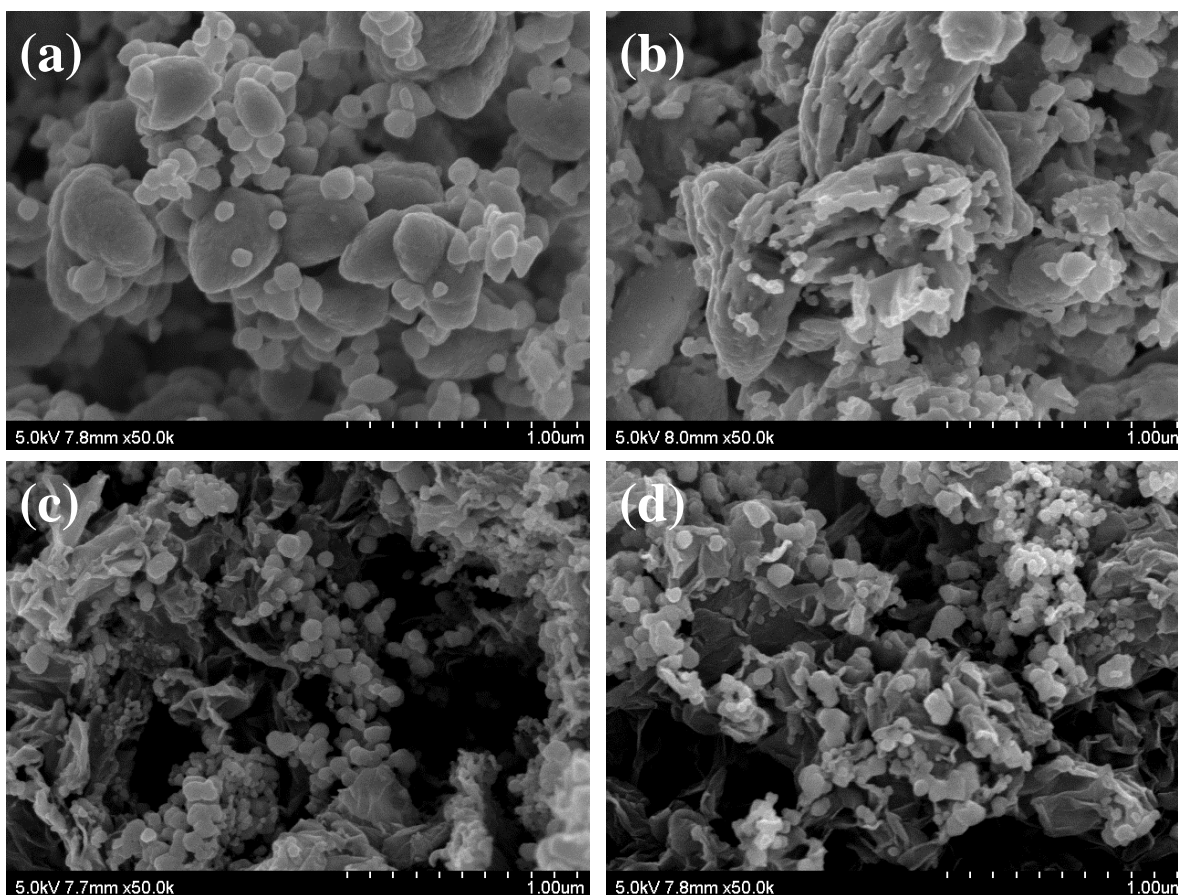


Figure 7.2: Morphology changes during the regeneration cycles: (a) fresh ZnO, (b) ZnO after 5 cycles, (c) fresh ZnO/rGO and (d) ZnO/rGO after 8 cycles

The change in the crystal structure of ZnO/rGO over sulfidation-regeneration cycles is presented in Figure 7.3. It is shown that the XRD patterns of pure ZnO at 2θ of 31.62, 34.30, 36.16, 47.41 and 56.41 corresponding to the crystal planes of (100), (002), (101), (102) and (110), respectively were observed from the fresh ZnO/rGO composite (Figure 7.3-(a)). Those patterns are indexed to be wurtzite ZnO and matched with JCPDS 36-1451. No other characteristic peaks from impurities were detected. After the first H_2S adsorption (Figure 7.3-(b)), other characteristic peaks of wurtzite-structured ZnS were shown at 2θ of 26.46 (100), 47.46 (110) and 56.46 (112)

(matched with JCPDS 75-1547) as well as peaks of pure ZnO simultaneously. It is suggested that Zn-O (wurtzite) crystal structure was converted to Zn-S (wurtzite) from the first H₂S adsorption. However, after the first regeneration (Figure 7.3-(c)), the intensity of (100) ZnS peak was lowered. This implies that the Zn-S structure was destroyed and the sulfur atoms were detached from the zinc atom during the regeneration process. After the 8th H₂S adsorption (Figure 7.3-(d)), another ZnS peaks were observed at 2θ of 28.43, 47.43 and 56.50; and those peaks were identified as cubic (or sphalerite) ZnS corresponding to (111), (220) and (311) planes, respectively (matched with JCPDS 77-2100). Like the first regeneration, after the 8th regeneration (Figure 7.3-(e)), the wurtzite and cubic structured ZnS peaks were weakened, but still present due to the limited regeneration efficiency. However, in general, the overall shape and location of the peaks were very similar during the multiple cycles. The results presented here suggest that the ZnO/rGO composite possesses a stable crystal structure of ZnO and ZnS over cycles; and it supports the stable H₂S adsorption efficiency over eight sulfidation-regeneration cycles.

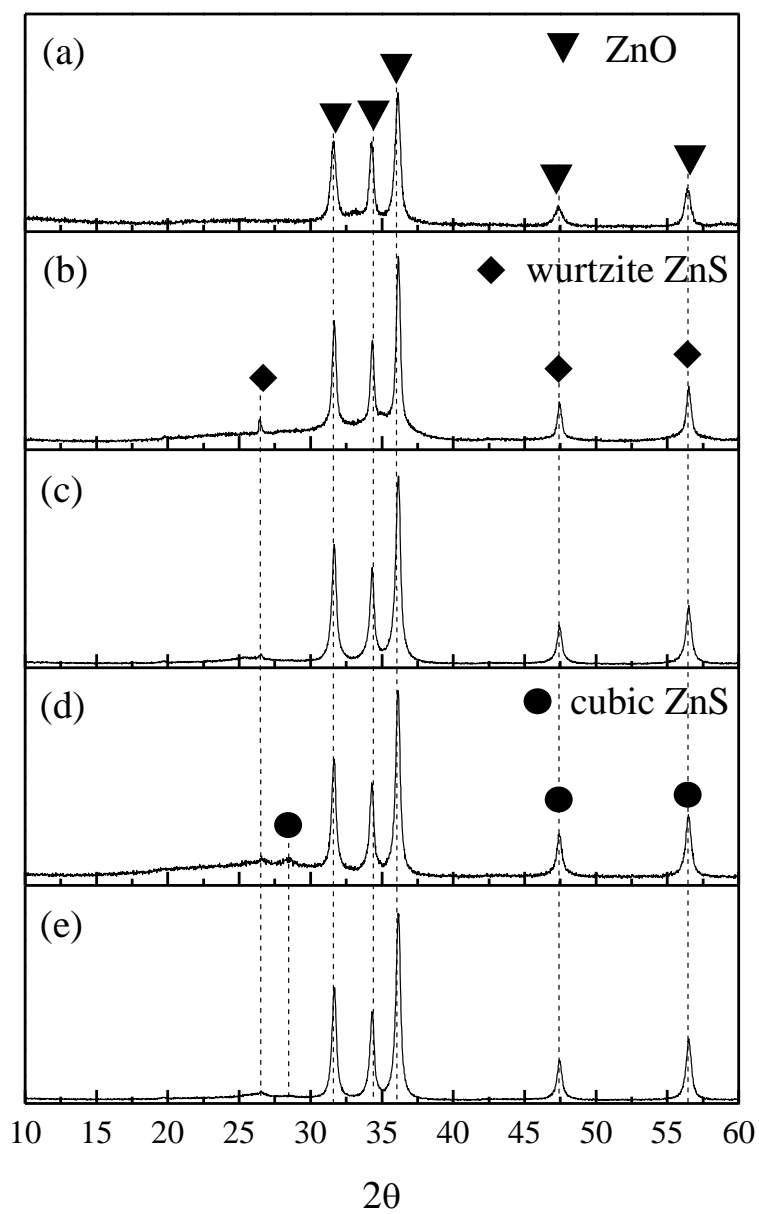


Figure 7.3: XRD patterns for ZnO/rGO: (a) fresh, (b) after 1st sulfidation, (c) after 1st regeneration, (d) after 8th sulfidation and (e) after 8th regeneration

Based on the XRD results from Figure 7.3, the average crystallite sizes for ZnO and ZnO/rGO composite over regeneration cycles were calculated; and listed in Table 7.1 below. The lattice parameter “*a*” from ZnO and ZnO/rGO remained constant, even after recycles, as 0.325 (\pm 0.001) nm. This indicates that the zinc oxide lattice structure is maintained over several cycles. The crystallite sizes of ZnO were smaller than that of ZnO/rGO. In addition, it was found that over regeneration cycles, the crystallite size of ZnO increased. However, the crystallite size on ZnO/rGO remained constant after the first regeneration.

Table 7.1: Crystallite size changes over regeneration cycles

	# of regeneration	2θ ($^\circ$)	FWHM ($^\circ$)	<i>a</i> (nm)	crystallite (nm)
ZnO	Fresh	31.72	0.515	0.325	16.74
	1	31.70	0.483	0.326	17.84
	5	31.72	0.461	0.325	18.69
ZnO/rGO	Fresh	31.64	0.409	0.326	21.07
	1	31.66	0.372	0.326	23.21
	4	31.68	0.361	0.326	23.86
	8	31.64	0.365	0.326	23.61

Beside of the morphology changes, the chemical state of Zn and O in the ZnO matrix was also modified during the H₂S sulfidation-regeneration cycles; and it caused a decrease in adsorption capacity over multiple cycles. Figure 7.4 summarizes the chemical state change of Zn in ZnO and ZnO/rGO composite over several cycles. As previously reported, the various ratios of the zinc chemical states (i.e. Zn^I and Zn^{II}) were observed. Figure 7.4 (a)-(c) presents the

chemical state of Zn in the case of pure ZnO for fresh, after 1st regeneration and after 5th regeneration, respectively. The ratios of Zn^I/Zn^{II} over the cycles were calculated as 2.21, 1.96 and 0.12, respectively (Table 7.2). This implies that the Zn-O lattice matrix (representing Zn^I) was destroyed over the cycles since the dissociated HS⁻ or S²⁻ ions reacted with the zinc ions from the Zn-O lattice. In addition, the defects of ZnO (implying oxygen vacancy sites in ZnO lattice) increase the portion of heterogeneity of ZnO, and the oxygen vacancy is able to hinder the electron-hole recombination [180], which can increase the reactivity of H₂S adsorption. In this study, an oxygen source was not used for the regeneration process to prevent gasification of carbon support (rGO). Therefore, over the cycles, the Zn-O lattice structure was destroyed to produce ZnS structure, but no ZnO regeneration due to the lack of oxygen source. As a result, the Zn^I/Zn^{II} ratios for pure ZnO adsorbent decrease over the cycles. In addition to other critical factors determining the adsorption capacity (i.e. larger ZnO particle size and lower specific surface area), the chemical state changes of Zn in ZnO support the decrease of the H₂S adsorption capacities over the regeneration process.

Table 7.2: Ratios of Zn^I/Zn^{II} for ZnO and ZnO/rGO composite during regeneration cycles

	Initial	1st	Final
Pure ZnO	2.21	1.96	0.12 (5 cycle)
ZnO/rGO	1.13	0.44	0.45 (8 cycle)

Figure 7.4 (d)-(f) show the zinc chemical state changes over regeneration cycles for the ZnO/rGO composite sorbent. To compare with pure ZnO, the ratios of Zn^I/Zn^{II} were obtained (the comparisons of the area fitted as Zn^I and Zn^{II}). The initial ratio for ZnO/rGO was 1.13; after

the first regeneration, the ratio decreased to 0.44; and after the 8th cycle, the ratio was 0.45 (Table 7.1). After the first regeneration, the ratio was decreased since it could be expected that the Zn-O lattice structure was destroyed during the sulfidation process. However, interestingly, the Zn^I/Zn^{II} ratio after the first cycle and 8th cycle were similar. It implies that the chemical state of Zn in ZnO/rGO composite was not affected by high temperature regeneration condition (600 °C). It might explain the critical role of the rGO. The stable chemical states of Zn over cycles can explain in part the stable adsorption capacity.

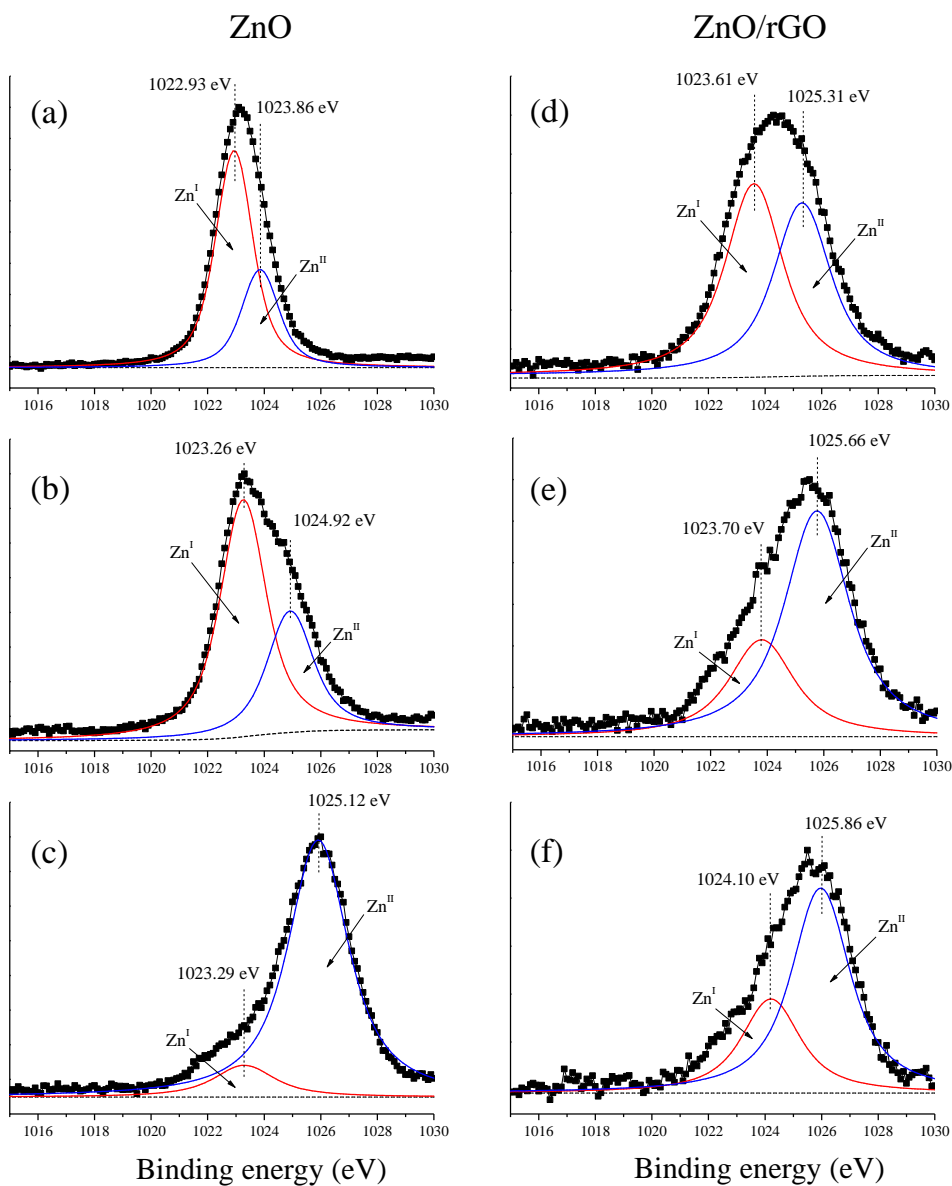


Figure 7.4: Zn_{2p3/2} spectra for ZnO (a) fresh, (b) after 1st regeneration and (c) after 5th regeneration; and ZnO/rGO (d) fresh, (e) after 1st regeneration and (f) after 8th regeneration

In order to support the relationship between the lattice structure of ZnO and the H₂S adsorption capacity, the O1s XPS spectra is provided. It has been observed that the binding energy of O1s for ZnO/rGO was shifted toward higher binding energy than that of ZnO. This

implies that the chemical bondings between the zinc and oxygen in ZnO/rGO were affected by the rGO which contains abundant oxygen functional groups [165], [181]. The O1s peak can be divided into three groups as O^I, O^{II} and O^{III} [180]. Figure 7.5 (a)-(f) show the oxygen chemical state changes over the regeneration cycles. The low binding energy peak (O^I) is attributed to the O²⁻ ions on the wurtzite ZnO lattice; the middle binding energy (O^{II}) is associated with O²⁻ ions in oxygen-deficient regions within the ZnO matrix; and the high binding energy (O^{III}) represents the loosely bound oxygen on the surface of ZnO [152], [182].

Figure 7.5 (a)-(c) show the changes of O1s sub-divided peaks from the fresh to 5th regenerations for pure ZnO. The ratio of O^I/O^{II} can represent the oxygen structure in the ZnO lattice. For the fresh ZnO, the ratio was 1.49 implying that most of oxygen O²⁻ ions are predominantly located in the Zn-O lattice. After the first sulfidation-regeneration cycle, the ratio decreased to 0.97; and further cycles (after 5th cycles) led to further decrease of this ratio to 0.32. These results support the fact that the sulfur ions (i.e. HS⁻ and S²⁻) replace the oxygen ions in the Zn-O lattice; and produce Zn-S. In addition, over the cycles, the oxygen deficient sites were increased due to the lack of oxygen supplies during the regenerations.

Figure 7.5 (d)-(f) show that the oxygen chemical states in the Zn-O lattice in the ZnO/rGO composite had been modified due to the presence of rGO. The ratio of O^I/O^{II} for fresh ZnO/rGO sample was lower (0.92) than that for pure ZnO. It can be expected that the increase of the O^{II} portion was caused by the oxygen functional groups on rGO surface. The oxygen functional groups which are attached to the Zn-O lattice modified the oxygen chemical state in ZnO. After the first regeneration, the ratio was decreased to 0.43; and after the 8th cycle, the ratio was further decreased to 0.39. However, it can be noticed that the decrease of the ratio for ZnO/rGO was smaller from the first regeneration cycle to 8th cycle compared than that for pure

ZnO. It is proposed that the presence of rGO with ZnO could maintain the oxygen chemical states during the regeneration cycles. This also contributes to explain the stability of the H₂S adsorption performance for ZnO/rGO composites over several cycles.

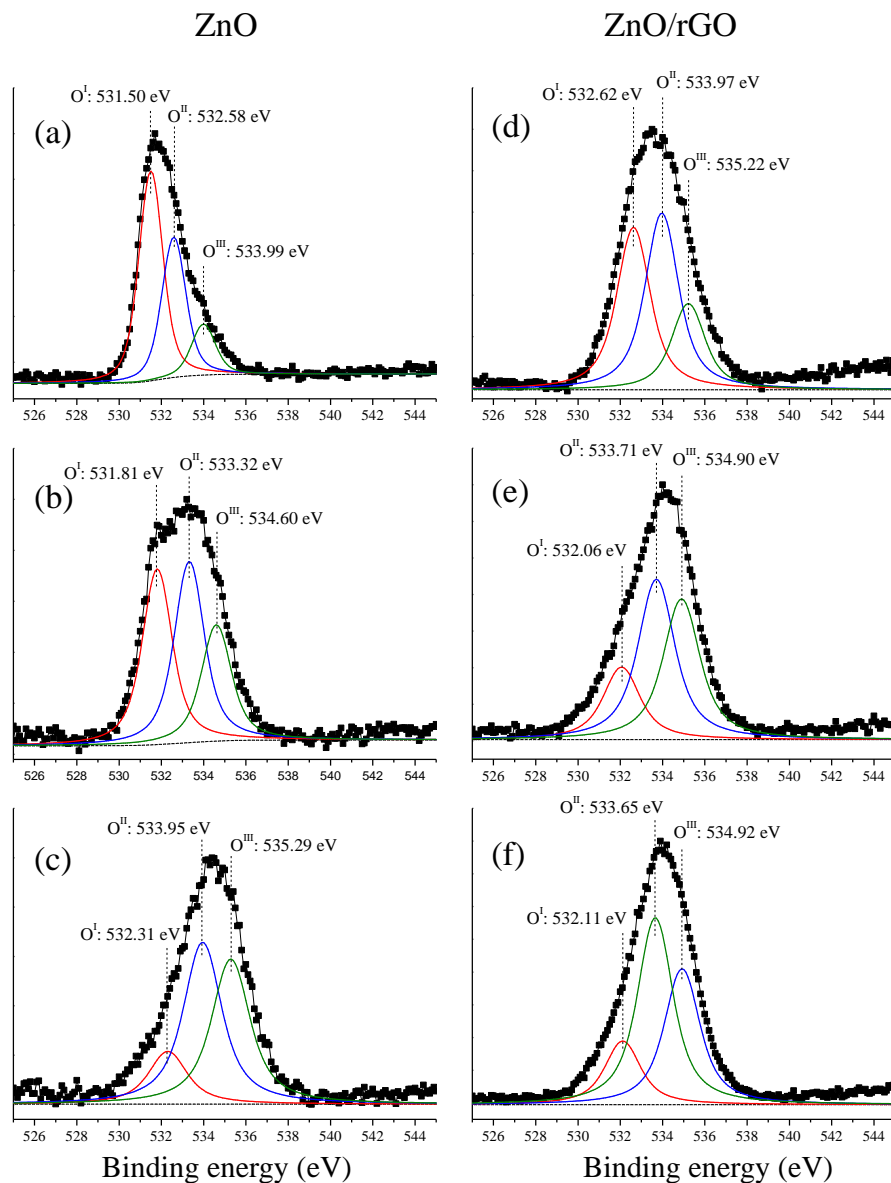


Figure 7.5: O_{1s} spectra for ZnO (a) fresh, (b) after 1st regeneration and (c) after 5th regeneration; and ZnO/rGO (d) fresh, (e) after 1st regeneration and (f) after 8th regeneration

7.3. Summary

This chapter investigated the critical functionalities of rGO for enhancing H₂S adsorption and regeneration ability. The abundant oxygen functional groups attached on the surface of rGO promoted the dispersion of nano-sized ZnO, which leads to a higher surface area of active adsorbent sites. In addition, those oxygen functional groups prevented the aggregation of ZnO particles at the regeneration temperature of 600 °C. Beside those physical property changes, the presence of rGO modified the chemical properties of ZnO due to the oxygen functional groups, as confirmed by XPS analysis. The amount of zinc ions (Zn²⁺) is placed at the oxygen vacant sites, but not only in the Zn-O lattice. For the oxygen side, the amount of oxygen ions in the Zn-O lattice decreased; and loosely bonded oxygen ions near the Zn-O lattice and on the surface were generated. Therefore, it was found that the presence of rGO plays a critical role to provide appropriate conditions for H₂S adsorption, which was confirmed through H₂S adsorption breakthrough and regeneration tests. The ZnO/rGO composite showed about five-fold higher adsorption capacity than pure ZnO; and this capacity was maintained over 8 recycles while that on ZnO decreased dramatically.

Chapter 8. Conclusions and Recommendations

8.1. Conclusions

In this study, liquid and gas phase sulfur compounds were removed by adsorption method using graphene-based materials. For liquid phase dibenzothiophene (DBT) compound removal, the characteristics of graphite oxide and graphene were modified depending on the preparation method used. The interlayer *d*-spacing for graphite oxide was especially controlled by the synthesis method. Synthesizing the graphite oxide with H₃PO₄ led to a higher degree of oxidation than synthesizing it by the Hummers' method, as confirmed by XPS analysis; and it led to a larger crystallite size and thinner graphene than that from Hummers' method. Therefore, it has been confirmed that graphite oxide which has a larger interlayer spacing is able to produce a higher quality graphene possessing a higher surface area, larger overall size and thinner thickness. DBT adsorption tests were carried out for a model diesel compound and a commercial diesel. The graphite oxide (a sp³ configuration) did not adsorb DBT compounds. However, graphene materials, which have a sp² configuration, were able to adsorb DBT compounds *via* π-π interactions. Graphene which has a higher surface area and thinner thickness showed a higher DBT adsorption capacity. The graphene adsorption capacity was lower for the commercial diesel than for the modeled diesel compound, a fact attributed to the presence of many other aromatic compounds in commercial diesel. The reduced DBT adsorption selectivity in the presence of aromatic compounds was confirmed by performing DBT adsorption tests in the presence of different toluene concentrations.

For gas phase hydrogen sulfide (H_2S) removal, the critical role of the reduced graphite oxide (rGO) for active ZnO nano-particle dispersion has been investigated. XPS and FT-IR analysis confirmed that the microwave-assisted reduction process provided a mild reduction environment to GO. Therefore, the oxygen functional groups remained attached on the rGO surface. Those oxygen functional groups were anchoring metal oxide, thus helping the dispersion of the active ZnO particles on the surface. From calcination experiments, it was shown that ZnO/rGO prevented the aggregation effect on ZnO at 300°C which could allow for higher specific surface area of the active ZnO to H_2S gas. From H_2S breakthrough tests, it was confirmed that the ZnO/rGO composite showed almost 4 times higher ZnO utilization efficiency than the pure ZnO particle at 300°C . In addition, it also showed that the presence of H_2 in $\text{H}_2\text{S}/\text{N}_2$ environment, the H_2S breakthrough time had been increased since the hydrogen molecules provided the reducing environment to the product Zn-S. The presence of H_2 led to the decomposition of the Zn-S and provided active Zn^{2+} for sulfur molecules. On the other hand, the presence of CO_2 inhibited the H_2S adsorption. This could be explained by the competitive adsorption between H_2S and CO_2 .

From the regeneration studies (at 600°C in N_2 environment), it was found that the presence of rGO played critical roles to maintain the H_2S adsorption capacity over cycles. The H_2S adsorption capacity for pure ZnO decreased to almost zero after 5th cycles while that of nO/rGO composite maintained a capacity of 93.1 mg S/g ads (about 54% efficiency) over 8 cycles. Interestingly, the adsorption capacity decreased to about half from the first regeneration; then it was stable over cycles. It can propose that the rGO possessing abundant amount of oxygen functional groups resisted the destruction of the ZnO lattice matrix over cycles.

Another metal oxide, copper oxide, which has been known as active metal oxide was added to the ZnO/rGO composite in order to enhance the H₂S adsorption capacity further. Depending on the copper content, the H₂S adsorption capacity has been increased by up to 18 times for Cu₁₅Zn₈₅/rGO compared to pure ZnO. As increasing the Cu mol% to ZnO, the H₂S adsorption capacity increased until the 15 mol% Cu addition showed the highest H₂S adsorption capacity. With higher than 15 mol% Cu, the H₂S adsorption capacity had been decreased. The 2D rGO substrate which contains abundant oxygen functional groups promoted the metal oxide dispersion and increased the H₂S adsorption efficiency. In addition, it was found that the optimum content of copper was 15% in order to maximize the adsorption. 15% of copper corresponded to the highest portion of zinc ions located in the Zn-O lattice. The Cu¹⁺ and Cu²⁺ ions co-existed with ZnO. Due to the oxygen containing functional groups from rGO, the majority of the oxygen ions were located at the oxygen deficient region and on the surface of the oxide. After exposure to H₂S, not only zinc sulfide and copper sulfide were produced, but also sulfate because of the loosely bonded oxygen ions from the rGO surface.

8.2. Recommendations

In this study, the H₂S adsorption on different metal oxides (i.e. zinc oxide and copper oxide) was investigated and the effects of rGO as a substrate to enhance the H₂S adsorption capacity were examined. Several recommended works are proposed below for future studies.

1. Synthesis of well dispersed metal oxide/graphene composite

In order to maximize the H₂S adsorption capacity, well dispersed metal oxide on the rGO surface is necessary. In general, deep understanding of metal oxide/graphene interaction is required to produce an appropriate adsorbent. Essentially, the graphite oxide (GO) possessing a larger interlayer spacing is required to provide easier exfoliation which can produce a thinner layered rGO. The exfoliation of GO to rGO can be controlled depending on the reduction methods. It can be expected that a thinner layered rGO sheet increases the larger surface area for metal oxide deposition. Several recommendations could be proposed.

- The GO having a larger interlayer spacing can be prepared by varying the oxidation conditions of graphite powder.
 - An optimum period of oxidation of graphite powder needs to be determined while the graphite powder is oxidized in H₂SO₄ at 50 °C.
- A thinner rGO prepared by modifying the reduction conditions
 - Dry condition (through microwave irradiation) in nitrogen or argon gas environment with small amount of conductive material (i.e. carbon black or graphene)
- Maximum loading of metal oxide on rGO surface
 - An optimum period of reduction using reducing agent (i.e. hydrazine) needs to be determined while the metal oxide/GO solution is reduced by microwave irradiation.

2. Enhancement of H₂S adsorption capacity and regeneration ability

In this study, ZnO and CuO which are considered as one of the most typical metal oxide sorbents for H₂S removal were deposited on the rGO surface. In this study, it has found that after the first recycle, about 50% of the adsorption capacity has been decreased; but maintained after that. In order to enhance the regeneration ability, the regeneration conditions would be modified.

- Finding an optimum regeneration temperatures (i.e. 300, 400, 500°C)
- Finding an appropriate regeneration period
- Providing different regeneration environments (i.e. applying very small amount of moisture and/or hydrogen)

Besides metal oxides, different adsorbents (i.e. nano-sized zeolite, mesoporous silica or MOF) could be deposited on rGO since ion-exchanged zeolite, mesoporous silica and MOF are widely used as supporters for H₂S adsorption.

References

- [1] J. R. Katzer, M. P. Ramage, and A. V. Sapre, "Petroleum refining: Poised for profound changes," *Chem. Eng. Prog.*, vol. 6, pp. 41–51, 2000.
- [2] C. Song and X. Ma, "New design approaches to ultra-clean diesel fuels by deep desulfurization and deep dearomatization," *Appl. Catal. B*, pp. 207–238, 2003.
- [3] V. Lam, G. Li, C. Song, J. Chen, C. Fairbridge, R. Hui, and J. Zhang, "A review of electrochemical desulfurization technologies for fossil fuels," *Fuel Process. Technol.*, vol. 98, pp. 30–38, Jun. 2012.
- [4] X. Ma, L. Sun, and C. Song, "A new approach to deep desulfurization of gasoline, diesel fuel and jet fuel by selective adsorption for ultra-clean fuels and for fuel cell applications," *Catal. Today*, vol. 77, pp. 107–116, 2002.
- [5] K. G. Knudsen, B. H. Cooper, and H. Topsøe, "Catalyst and process technologies for ultra low sulfur diesel," *Appl. Catal. A Gen.*, vol. 189, no. 2, pp. 205–215, 2005.
- [6] X. Ma, K. Sakanishi, T. Isoda, and I. Mochida, "Quantum chemical calculation on the desulfurization reactivities of heterocyclic sulfur compounds," *Energy & Fuels*, vol. 9, no. 1, pp. 33–37, 1995.
- [7] A. Bagreev and T. J. Bandosz, "On the mechanism of hydrogen sulfide removal from moist air on catalytic carbonaceous adsorbents," *Ind. Eng. Chem. Res.*, vol. 44, pp. 530–538, 2005.
- [8] J. A. Rodriguez and A. Maiti, "Adsorption and decomposition of H₂S on MgO (100), NiMgO (100), and ZnO (0001) surfaces: A first-principles density functional study," *J. Phys. Chem. B*, vol. 104, pp. 3630–3638, 2000.

- [9] A. Samokhvalov and B. J. Tatarchuk, "Characterization of active sites, determination of mechanisms of H₂S, COS and CS₂ sorption and regeneration of ZnO low-temperature sorbents: Past, current and perspectives," *Phys. Chem. Chem. Phys.*, vol. 13, pp. 3197–3209, Feb. 2011.
- [10] C. L. Garcia and J. a. Lercher, "Adsorption of hydrogen sulfide on ZSM 5 zeolites," *J. Phys. Chem.*, vol. 96, no. 5, pp. 2230–2235, Mar. 1992.
- [11] H. G. Karge and R. János, "Hydrogen sulfide adsorption on faujasite-type zeolites with systematically varied Si-Al ratios," *J. Colloid Interface Sci.*, vol. 64, no. 3, pp. 522–532, 1978.
- [12] J. P. Wakker, A. W. Gerritsen, and J. A. Moulijn, "High Temperature H₂S and COS Removal with MnO and FeO on γ -Al₂O₃ Acceptors," *Ind. Eng. Chem. Res.*, vol. 32, pp. 139–149, 1993.
- [13] T.-H. Ko, H. Chu, and L.-K. Chaung, "The sorption of hydrogen sulfide from hot syngas by metal oxides over supports.," *Chemosphere*, vol. 58, no. 4, pp. 467–74, Jan. 2005.
- [14] P. Dhage, A. Samokhvalov, D. Repala, E. C. Duin, M. Bowman, and B. J. Tatarchuk, "Copper-promoted ZnO/SiO₂ regenerable sorbents for the room temperature removal of H₂S from reformat gas streams," *Ind. Eng. Chem. Res.*, vol. 49, pp. 8388–8396, 2010.
- [15] M. V Twigg and M. S. Spencer, "Deactivation of copper metal catalysts for methanol decomposition , methanol steam reforming and methanol synthesis," *Top. Catal.*, vol. 22, no. 3–4, pp. 191–203, 2003.
- [16] S. Lew, K. Jothimurugesan, and M. Flytzani-Stephanopoulos, "High-temperature H₂S removal from fuel gases by regenerable Zinc Oxide-Titanium dioxide sorbents," *Ind. Eng. Chem. Res.*, vol. 28, pp. 535–541, 1989.

- [17] X. Y. Kong, Y. Ding, and Z. L. Wang, "Metal-semiconductor Zn-ZnO core-shell nanobelts and nanotubes," *J. Phys. Chem. B*, vol. 108, pp. 570–574, 2004.
- [18] S. Park, J. An, I. Jung, R. D. Piner, S. J. An, X. Li, A. Velamakanni, and R. S. Ruoff, "Colloidal suspensions of highly reduced graphene oxide in a wide variety of organic solvents.," *Nano Lett.*, vol. 9, no. 4, pp. 1593–7, Apr. 2009.
- [19] M. D. Stoller, S. Park, Y. Zhu, J. An, and R. S. Ruoff, "Graphene-based ultracapacitors," *Nano Lett.*, vol. 8, no. 10, pp. 3498–3502, Oct. 2008.
- [20] N. Li, G. Liu, C. Zhen, F. Li, L. Zhang, and H.-M. Cheng, "Battery Performance and Photocatalytic Activity of Mesoporous Anatase TiO₂ Nanospheres/Graphene Composites by Template-Free Self-Assembly," *Adv. Funct. Mater.*, vol. 21, no. 9, pp. 1717–1722, May 2011.
- [21] J. K. Lee, K. B. Smith, C. M. Hayner, and H. H. Kung, "Silicon nanoparticles-graphene paper composites for Li ion battery anodes," *Chem. Commun.*, vol. 46, pp. 2025–2027, Mar. 2010.
- [22] Y. Zhu, S. Murali, M. D. Stoller, K. J. Ganesh, W. Cai, P. J. Ferreira, A. Pirkle, R. M. Wallace, K. a Cychosz, M. Thommes, D. Su, E. a Stach, and R. S. Ruoff, "Carbon-based supercapacitors produced by activation of graphene.," *Science*, vol. 332, no. 6037, pp. 1537–41, Jun. 2011.
- [23] M. Seredych and T. J. Bandosz, "Reactive adsorption of hydrogen sulfide on graphite oxide/Zr(OH)₄ composites," *Chem. Eng. J.*, vol. 166, no. 3, pp. 1032–1038, Feb. 2011.
- [24] M. Seredych, O. Mabayoje, and T. J. Bandosz, "Visible-Light-Enhanced Interactions of Hydrogen Sulfide with Composites of Zinc (Oxy)hydroxide with Graphite Oxide and Graphene.," *Langmuir*, vol. 28, no. 2, pp. 1337–1346, Jan. 2012.

- [25] M. Seredych, O. Mabayoje, M. M. Koleśnik, V. Krstić, and T. J. Bandoz, “Zinc (hydr)oxide/graphite based-phase composites: effect of the carbonaceous phase on surface properties and enhancement in electrical conductivity,” *J. Mater. Chem.*, vol. 22, pp. 7970–7978, 2012.
- [26] S.-T. Yang, Y. Chang, H. Wang, G. Liu, S. Chen, Y. Wang, Y. Liu, and A. Cao, “Folding/aggregation of graphene oxide and its application in Cu²⁺ removal,” *J. Colloid Interface Sci.*, vol. 351, no. 1, pp. 122–7, Nov. 2010.
- [27] V. Chandra, J. Park, Y. Chun, J. W. Lee, I. Hwang, and K. S. Kim, “Water-Dispersible Magnetite-Reduced Graphene Oxide Composites for Arsenic Removal,” *ACS Nano*, vol. 4, no. 7, pp. 3979–3986, 2010.
- [28] C. Petit, M. Seredych, and T. J. Bandoz, “Revisiting the chemistry of graphite oxides and its effect on ammonia adsorption,” *J. Mater. Chem.*, vol. 19, no. 48, p. 9176, 2009.
- [29] O. Mabayoje, M. Seredych, and T. J. Bandoz, “Enhanced reactive adsorption of hydrogen sulfide on the composites of graphene/graphite oxide with Copper (Hydr)oxychlorides,” *ACS Appl. Mater. Interfaces*, vol. 4, no. 6, p. 3316–3324, 2012.
- [30] I. V. Babich and J. A. Moulijn, “Science and technology of novel processes for deep desulfurization of oil refinery streams: A review,” *Fuel*, vol. 82, pp. 607–631, 2003.
- [31] R. Shafi and G. J. Hutchings, “Hydrodesulfurization of hindered dibenzothiophenes: An overview,” *Catal. Today*, vol. 59, pp. 423–442, 2000.
- [32] E. Furimsky and F. E. Massoth, “Deactivation of hydroprocessing catalysts,” *Catal. Today*, vol. 52, pp. 381–495, 1999.

- [33] F. Bataille, J.-L. Lemberon, P. Michaud, G. Perot, M. Vrinat, M. Lemaire, E. Schulz, M. Breysse, and S. Kasztelan, "Alkyldibenzothiophenes hydrodesulfurization-promoter effect, reactivity and reaction mechanism," *J. Catal.*, vol. 191, pp. 409–422, Apr. 2000.
- [34] E. Lecrenay, K. Sakanishi, and I. Mochida, "Catalytic hydrodesulfurization of gas oil and model sulfur compounds over commercial and laboratory-made CoMo and NiMo catalysts: Activity and reaction scheme," *Catal. Today*, vol. 39, pp. 13–20, 1997.
- [35] C. Song, "Designing sulfur-resistant, noble-metal hydrotreating catalysts," *Chemtech*, vol. 29, pp. 26–30, 1999.
- [36] H. R. Reinhoudt, R. Troost, S. van Schalkwijk, A. D. van Langeveld, S. T. Sie, J. A. R. van Veen, and J. A. Moulijn, "Testing and characterisation of Pt/ASA for deep HDS reactions," *Fuel Process. Technol.*, vol. 61, pp. 117–131, Sep. 1999.
- [37] R. L. Irvine and D. M. Varraveto, "Adsorption process for removal of nitrogen and sulphur," *Petr. Tech. Quart.*, vol. 3, pp. 37–42, 1999.
- [38] A. B. S. H. Salem and H. S. Hamid, "Removal of sulfur compounds from naphtha solutions using solid adsorbents," *Chem. Eng. Technol.*, vol. 20, pp. 342–347, 1997.
- [39] G. Parkinson, "Gasoline minus MTBE," *Chem. Eng.*, vol. 8, pp. 45–46, 2000.
- [40] H. Chen, X. Zhou, H. Shang, C. Liu, J. Qiu, and F. Wei, "Study of dibenzothiophene adsorption over carbon nanotube supported CoMo HDS catalysts," *J. Nat. Gas Chem.*, vol. 13, pp. 209–217, 2004.
- [41] M. Seredych and T. J. Bandosz, "Adsorption of dibenzothiophenes on activated carbons with copper and iron deposited on their surfaces," *Fuel Process. Technol.*, vol. 91, pp. 693–701, 2010.

- [42] A. J. Hernández-Maldonado, G. Qi, and R. T. Yang, “Desulfurization of commercial fuels by π -complexation: Monolayer CuCl/ γ -Al₂O₃,” *Appl. Catal. B Environ.*, vol. 61, no. 3–4, pp. 212–218, Nov. 2005.
- [43] C. O. Ania and T. J. Bandoz, “Metal-loaded polystyrene-based activated carbons as dibenzothiophene removal media via reactive adsorption,” *Carbon N. Y.*, vol. 44, pp. 2404–2412, 2006.
- [44] Y. Yang, H. Lu, P. Ying, Z. Jiang, and C. Li, “Selective dibenzothiophene adsorption on modified activated carbons,” *Carbon N. Y.*, vol. 45, pp. 3042–3059, Dec. 2007.
- [45] X. Meng, W. de Jong, R. Pal, and A. H. M. Verkooijen, “In bed and downstream hot gas desulphurization during solid fuel gasification: A review,” *Fuel Process. Technol.*, vol. 91, pp. 964–981, Aug. 2010.
- [46] H. H. Kung, “Deactivation of methanol synthesis catalysts — A review,” *Catal. Today*, vol. 11, pp. 443–453, 1992.
- [47] H. Leibold, A. Hornung, and H. Seifert, “HTHP syngas cleaning concept of two stage biomass gasification for FT synthesis,” *Powder Tech.*, vol. 180, pp. 265–270, Jan. 2008.
- [48] F. Garca-Labiano, L. F. de Diego, and J. Adanez, “Effectiveness of natural, commercial, and modified calcium-based sorbents as H₂S removal agents at high temperatures,” *Environ. Sci. Technol.*, vol. 33, pp. 288–293, 1999.
- [49] A. M. Squires, R. A. Graff, and M. Pell, “Desulfurization of fuel with calcined dolomite. I. Introduction and first kinetic results,” *Chem. Eng. Prog. Symp.*, vol. 67, pp. 23–34, 1971.
- [50] R. H. Borgwardt and N. F. Roache, “Reaction of H₂S and sulphur with limestone particles,” *Ind. Eng. Chem. Process Des. Dev.*, vol. 23, pp. 742–748, 1984.

- [51] J. Abasian, A. Rehmat, D. Leppin, and D. D. Banerjee, "Desulphurization of fuels with calcium-based sorbents," *Fuel Process. Technol.*, vol. 25, pp. 1–15, 1990.
- [52] A. B. M. Heesink and W. P. M. Van Swaij, "The sulphidation of calcined limestone with hydrogen sulphide and carbonyl sulphide," *Chem. Eng. Sci.*, vol. 50, pp. 2983–2996, Sep. 1995.
- [53] K. P. Yrjas, C. A. P. Zevenhoven, and M. Hupa, "Hydrogen sulfide capture by limestone and dolomite at elevated pressure. 1. Sorbent performance," *Ind. Eng. Chem. Res.*, vol. 35, pp. 176–183, Jan. 1996.
- [54] J. Adanez, F. García-Labiano, L. F. de Diego, and V. Fierro, "Utilization of calcium acetate and calcium magnesium acetate for H₂S removal in coal gas cleaning at high temperatures," *Energy & Fuels*, vol. 13, pp. 440–448, 1999.
- [55] R. T. Yang and M. S. Shen, "Calcium silicates: A new class of highly regenerative sorbents for hot gas desulfurization," *AIChE J.*, vol. 25, pp. 811–819, 2004.
- [56] W. J. W. Bakker, F. Kapteijn, and J. A. Moulijn, "A high capacity manganese-based sorbent for regenerative high temperature desulfurization with direct sulfur production," *Chem. Eng. J.*, vol. 96, pp. 223–235, Dec. 2003.
- [57] R. Steudel and Y. Steudel, "Interaction of zinc oxide clusters with molecules related to the sulfur vulcanization of polyolefins ('rubber').," *Chem. - A Eur. J.*, vol. 12, no. 33, pp. 8589–8602, Nov. 2006.
- [58] J. A. Rodriguez, S. Chaturvedi, M. Kuhn, and J. Hrbek, "Reaction of H₂S and S₂ with metal/oxide surfaces: Band-gap size and chemical reactivity," *J. Phys. Chem. B*, vol. 102, pp. 5511–5519, 1998.

- [59] P. R. Westmoreland and D. P. Harrison, "Evaluation of candidate solids for high-temperature desulfurization of low-Btu gases," *Environ. Sci. Technol.*, vol. 10, pp. 659–661, 1976.
- [60] C. L. Carnes and K. J. Klabunde, "Unique Chemical Reactivities of Nanocrystalline Metal Oxides toward Hydrogen Sulfide," *Chem. Mater.*, vol. 14, no. 4, pp. 1806–1811, Apr. 2002.
- [61] R. Gupta, S. K. Gangwal, and S. C. Jain, "Development of zinc ferrite sorbents for desulfurization of hot coal gas in a fluid-bed reactor," *Energy Fuels*, vol. 6, pp. 21–27, 1992.
- [62] M. Pineda, J. L. G. Fierro, J. M. Palacios, C. Cilleruelo, E. García, and J. V. Ibarra, "Characterization of zinc oxide and zinc ferrite doped with Ti or Cu as sorbents for hot gas desulphurization," *Appl. Surf. Sci.*, vol. 119, pp. 1–10, 1997.
- [63] N. Ikenaga, Y. Ohgaito, H. Matsushima, and T. Suzuki, "Preparation of zinc ferrite in the presence of carbon material and its application to hot-gas cleaning," *Fuel*, vol. 83, pp. 661–669, Apr. 2004.
- [64] M. S. Liang, H. Y. Xu, and K. C. Xie, "Bench-scale testing of zinc ferrite sorbent for hot gas clean-up," *J. Nat. Gas Chem.*, vol. 16, pp. 204–209, 2007.
- [65] S. Lew, A. F. Sarofim, and M. Flytzani-Stephanopoulos, "Sulfidation of zinc titanate and zinc oxide solids," *Ind. Eng. Chem. Res.*, vol. 31, pp. 1980–1989, 1992.
- [66] W. F. Elseviers and H. Verelst, "Transition metal oxides for hot gas desulphurisation," *Fuel*, vol. 78, pp. 601–612, 1999.
- [67] J. A. Poston, "A reduction in the spalling of zinc titanate desulfurization sorbents through the addition of lanthanum oxide," *Ind. Eng. Chem. Res.*, vol. 35, pp. 875–882, Jan. 1996.

- [68] H. K. Jun, J. H. Koo, T. J. Lee, S. O. Ryu, C. K. Yi, C. K. Ryu, and J. C. Kim, "A study of Zn–Ti-based H₂S removal sorbents promoted with cobalt and nickel oxides," *Energy & Fuels*, vol. 18, pp. 41–48, 2004.
- [69] X. P. Bu, Y. J. Ying, C. Q. Zhang, and W. W. Peng, "Research improvement in Zn-based sorbent for hot gas desulfurization," *Powder Tech.*, vol. 180, pp. 253–258, Jan. 2008.
- [70] Y. J. Lee, N. K. Park, G. B. Han, S. O. Ryu, T. J. Lee, and C. H. Chang, "The preparation and desulfurization of nano-size ZnO by a matrix-assisted method for the removal of low concentration of sulfur compounds," *Curr. Appl. Phys.*, vol. 8, pp. 746–751, Oct. 2008.
- [71] T. Kyotani, H. Kawashima, A. Tomita, A. Palmer, and E. Furimsky, "Removal of H₂S from hot gas in the presence of Cu-containing sorbents," *Fuel*, vol. 68, pp. 74–79, Jan. 1989.
- [72] Z. J. Li and M. Flytzani-Stephanopoulos, "Cu–Cr–O and Cu–Ce–O Regenerable Oxide Sorbents for Hot Gas Desulfurization," *Ind. Eng. Chem. Res.*, vol. 36, pp. 187–196, Jan. 1997.
- [73] S. Yasyerli, G. Dogu, and I. Ar, "Activities of copper oxide and Cu–V and Cu–Mo mixed oxides for H₂S removal in the presence and absence of hydrogen and predictions of a deactivation model," *Ind. Eng. Chem. Res.*, vol. 40, pp. 5206–5214, Nov. 2001.
- [74] O. Karvan and H. Atakül, "Investigation of CuO/mesoporous SBA-15 sorbents for hot gas desulfurization," *Fuel Process. Technol.*, vol. 89, pp. 908–915, Sep. 2008.
- [75] Z. Ni, Y. Wang, T. Yu, and Z. Shen, "Raman spectroscopy and imaging of graphene," *Nano Res.*, vol. 1, no. 4, pp. 273–291, Apr. 2010.

- [76] N. Jung, A. C. Crowther, N. Kim, P. Kim, and L. Brus, “Raman enhancement on graphene: adsorbed and intercalated molecular species.,” *ACS Nano*, vol. 4, no. 11, pp. 7005–13, Nov. 2010.
- [77] R. Zan, U. Bangert, Q. Ramasse, and K. S. Novoselov, “Metal-Graphene Interaction Studied via Atomic Resolution Scanning Transmission Electron Microscopy,” *Nano Lett.*, vol. 11, pp. 1087–1092, Oct. 2011.
- [78] T. Zhou, F. Chen, K. Liu, H. Deng, Q. Zhang, J. Feng, and Q. Fu, “A simple and efficient method to prepare graphene by reduction of graphite oxide with sodium hydrosulfite.,” *Nanotechnology*, vol. 22, no. 4, p. 045704 (6pp), Jan. 2011.
- [79] K.-H. Liao, A. Mittal, S. Bose, C. Leighton, K. A. Mkhoyan, and C. W. Macosko, “Aqueous only route toward graphene from graphite oxide,” *ACS Nano*, vol. 5, no. 2, pp. 1253–1258, Feb. 2011.
- [80] S. M. Choi, M. H. Seo, H. J. Kim, and W. B. Kim, “Synthesis of surface functionalized graphene nanosheets with high Pt-loadings and their applications to methanol electrooxidation,” *Carbon N. Y.*, vol. 49, no. 3, pp. 904–909, Nov. 2010.
- [81] D. R. Dreyer, S. Park, C. W. Bielawski, and R. S. Ruoff, “The chemistry of graphene oxide,” *Chem. Soc. Rev.*, vol. 39, pp. 228–240, Jan. 2010.
- [82] a Ferrari, “Raman spectroscopy of graphene and graphite: Disorder, electron–phonon coupling, doping and nonadiabatic effects,” *Solid State Commun.*, vol. 143, pp. 47–57, Jul. 2007.
- [83] Y. Wang, W. Fan, G. Wang, and M. Ji, “New Insight into the Graphene Based Films Prepared from Carbon Fibers,” *Mater. Sci. Appl.*, vol. 2, pp. 834–838, 2011.

- [84] H. M. a. Hassan, V. Abdelsayed, A. E. R. S. Khder, K. M. AbouZeid, J. Turner, M. S. El-Shall, S. I. Al-Resayes, and A. A. El-Azhary, "Microwave synthesis of graphene sheets supporting metal nanocrystals in aqueous and organic media," *J. Mater. Chem.*, vol. 19, pp. 3832–3837, 2009.
- [85] J. Lee, K. S. Novoselov, and H. S. Shin, "Interaction between metal and graphene: Dependence on the layer number of graphene," *ACS Nano*, vol. 5, pp. 608–612, Jan. 2011.
- [86] Y. Zhu, S. Murali, W. Cai, X. Li, J. W. Suk, J. R. Potts, and R. S. Ruoff, "Graphene and graphene oxide: synthesis, properties, and applications.," *Adv. Mater.*, vol. 22, pp. 3906–3924, Sep. 2010.
- [87] S. Stankovich, D. a Dikin, G. H. B. Dommett, K. M. Kohlhaas, E. J. Zimney, E. a Stach, R. D. Piner, S. T. Nguyen, and R. S. Ruoff, "Graphene-based composite materials.," *Nature*, vol. 442, no. 7100, pp. 282–6, Jul. 2006.
- [88] R. Muszynski, B. Seger, and P. V Kamat, "Decorating Graphene Sheets with Gold Nanoparticles," *Society*, pp. 5263–5266, 2008.
- [89] G. Williams and P. V Kamat, "Graphene-semiconductor nanocomposites: excited-state interactions between ZnO nanoparticles and graphene oxide.," *Langmuir*, vol. 25, no. 24, pp. 13869–73, Dec. 2009.
- [90] O. Akhavan and E. Ghaderi, "Photocatalytic Reduction of Graphene Oxide Nanosheets on TiO₂ Thin Film for Photoinactivation of Bacteria in Solar Light Irradiation," *Ratio*, no. 50 mL, pp. 20214–20220, 2009.
- [91] L.-C. Chen, Y.-C. Ho, W.-S. Guo, C.-M. Huang, and T.-C. Pan, "Enhanced visible light-induced photoelectrocatalytic degradation of phenol by carbon nanotube-doped TiO₂ electrodes," *Electrochim. Acta*, vol. 54, no. 15, pp. 3884–3891, Jun. 2009.

- [92] C. Xu, X. Wang, J. Zhu, X. Yang, and L. Lu, "Deposition of Co₃O₄ nanoparticles onto exfoliated graphite oxide sheets," *J. Mater. Chem.*, vol. 18, pp. 5625–5629, 2008.
- [93] I. V Lightcap, T. H. Kosel, and P. V Kamat, "Anchoring semiconductor and metal nanoparticles on a two-dimensional catalyst mat. Storing and shuttling electrons with reduced graphene oxide.," *Nano Lett.*, vol. 10, no. 2, pp. 577–583, Feb. 2010.
- [94] B. Adhikari, A. Biswas, and A. Banerjee, "Graphene oxide-based hydrogels to make metal nanoparticle-containing reduced graphene oxide-based functional hybrid hydrogels.," *ACS Appl. Mater. Interfaces*, vol. 4, pp. 5472–5482, Oct. 2012.
- [95] X. Zhou, X. Huang, X. Qi, S. Wu, C. Xue, F. Y. C. Boey, Q. Yan, P. Chen, and H. Zhang, "In Situ Synthesis of Metal Nanoparticles on Single-Layer Graphene Oxide and Reduced Graphene Oxide Surfaces," *J. Phys. Chem. C*, vol. 113, no. 25, pp. 10842–10846, 2009.
- [96] S. Chen, J. Zhu, and X. Wang, "One-Step Synthesis of Graphene–Cobalt Hydroxide Nanocomposites and Their Electrochemical Properties," *J. Phys. Chem. C*, vol. 114, no. 27, pp. 11829–11834, Jul. 2010.
- [97] W. Zou, J. Zhu, Y. Sun, and X. Wang, "Depositing ZnO nanoparticles onto graphene in a polyol system," *Mater. Chem. Phys.*, vol. 125, no. 3, pp. 617–620, Feb. 2011.
- [98] H. Wang, L. Wang, C. Qu, Y. Su, S. Yu, W. Zheng, and Y. Liu, "Photovoltaic properties of graphene oxide sheets beaded with ZnO nanoparticles," *J. Solid State Chem.*, vol. 184, no. 4, pp. 881–887, Apr. 2011.
- [99] C. Gómez-Navarro, R. T. Weitz, A. M. Bittner, M. Scolari, A. Mews, M. Burghard, and K. Kern, "Electronic transport properties of individual chemically reduced graphene oxide sheets.," *Nano Lett.*, vol. 7, no. 11, pp. 3499–503, Nov. 2007.

- [100] X. Zhu, Y. Zhu, S. Murali, M. D. Stoller, and R. S. Ruoff, "Nanostructured reduced graphene oxide/Fe₂O₃ composite as a high-performance anode material for lithium ion batteries.," *ACS Nano*, vol. 5, no. 4, pp. 3333–3338, Apr. 2011.
- [101] S. Wang, S. P. Jiang, and X. Wang, "Microwave-assisted one-pot synthesis of metal/metal oxide nanoparticles on graphene and their electrochemical applications," *Electrochim. Acta*, vol. 56, pp. 3338–3344, Mar. 2011.
- [102] Y. Lin, D. W. Baggett, J.-W. Kim, E. J. Siochi, and J. W. Connell, "Instantaneous formation of metal and metal oxide nanoparticles on carbon nanotubes and graphene via solvent-free microwave heating.," *ACS Appl. Mater. Interfaces*, vol. 3, no. 5, pp. 1652–64, May 2011.
- [103] Q. Chen, L. Zhang, and G. Chen, "Facile preparation of graphene-copper nanoparticle composite by in situ chemical reduction for electrochemical sensing of carbohydrates.," *Anal. Chem.*, vol. 84, no. 1, pp. 171–178, Jan. 2012.
- [104] D. Li, M. B. Müller, S. Gilje, R. B. Kaner, and G. G. Wallace, "Processable aqueous dispersions of graphene nanosheets.," *Nat. Nanotechnol.*, vol. 3, no. 2, pp. 101–5, Mar. 2008.
- [105] E. A. Meulenkaamp, "Synthesis and Growth of ZnO Nanoparticles," vol. 5647, no. 98, pp. 5566–5572, 1998.
- [106] H. C. Schniepp, J.-L. Li, M. J. McAllister, H. Sai, M. Herrera-Alonso, D. H. Adamson, R. K. Prud'homme, R. Car, D. A. Saville, and I. A. Aksay, "Functionalized single graphene sheets derived from splitting graphite oxide," *J. Phys. Chem. B*, vol. 110, no. 17, pp. 8535–8539, May 2006.

- [107] Y. Chen, Z. Hu, Y. Chang, H. Wang, Z. Zhang, Y. Yang, and H. Wu, “Zinc Oxide/Reduced Graphene Oxide Composites and Electrochemical Capacitance Enhanced by Homogeneous Incorporation of Reduced Graphene Oxide Sheets in Zinc Oxide Matrix,” *J. Phys. Chem. C*, vol. 115, pp. 2563–2571, 2011.
- [108] M. Toupin, T. Brousse, and D. Belanger, “Charge storage mechanism of MnO₂ electrode used in aqueous electrochemical capacitor,” *Chem. Mater.*, vol. 16, pp. 3184–3190, 2004.
- [109] W. Sugimoto, H. Iwata, K. Yokoshima, Y. Murakami, and Y. Takasu, “Proton and electron conductivity in hydrous ruthenium oxides evaluated by electrochemical impedance spectroscopy: the origin of large capacitance,” *J. Phys. Chem. B*, vol. 109, no. 15, pp. 7330–8, Apr. 2005.
- [110] S.-S. Lo and D. Huang, “Morphological variation and Raman spectroscopy of ZnO hollow microspheres prepared by a chemical colloidal process,” *Langmuir*, vol. 26, no. 9, pp. 6762–6, May 2010.
- [111] M. Herrera-Alonso, A. a Abdala, M. J. McAllister, I. a Aksay, and R. K. Prud’homme, “Intercalation and stitching of graphite oxide with diaminoalkanes,” *Langmuir*, vol. 23, no. 21, pp. 10644–9, Oct. 2007.
- [112] C. Nethravathi and M. Rajamathi, “Chemically modified graphene sheets produced by the solvothermal reduction of colloidal dispersions of graphite oxide,” *Carbon N. Y.*, vol. 46, no. 14, pp. 1994–1998, Nov. 2008.
- [113] N. Lepot, M. K. Van Bael, H. Van den Rul, J. D’Haen, R. Peeters, D. Franco, and J. Mullens, “Synthesis of ZnO nanorods from aqueous solution,” *Mater. Lett.*, vol. 61, no. 13, pp. 2624–2627, May 2007.

- [114] B. Li, H. Cao, G. Yin, Y. Lu, and J. Yin, "Cu₂O@reduced graphene oxide composite for removal of contaminants from water and supercapacitors," *J. Mater. Chem.*, vol. 21, no. 29, p. 10645, 2011.
- [115] Y. Yu, L.-L. Ma, W.-Y. Huang, F.-P. Du, J. C. Yu, J.-G. Yu, J.-B. Wang, and P.-K. Wong, "Sonication assisted deposition of Cu₂O nanoparticles on multiwall carbon nanotubes with polyol process," *Carbon N. Y.*, vol. 43, no. 3, pp. 670–673, 2005.
- [116] Y. Li, W. Gao, L. Ci, C. Wang, and P. M. Ajayan, "Catalytic performance of Pt nanoparticles on reduced graphene oxide for methanol electro-oxidation," *Carbon N. Y.*, vol. 48, no. 4, pp. 1124–1130, Apr. 2010.
- [117] C.-C. Chien and K.-T. Jeng, "Effective preparation of carbon nanotube-supported Pt–Ru electrocatalysts," *Mater. Chem. Phys.*, vol. 99, no. 1, pp. 80–87, Sep. 2006.
- [118] Y. Matsuo, K. Hatase, and Y. Sugie, "Preparation and characterization of poly (vinyl alcohol) and Cu(OH)₂ -Poly (vinyl alcohol)-intercalated graphite oxides," *Chem. Mater.*, vol. 10, pp. 2266–2269, 1998.
- [119] A. B. Bourlinos, D. Gournis, D. Petridis, T. Szabo, A. Szeri, and I. Dekany, "Graphite oxide: Chemical reduction to graphite and surface modification with primary aliphatic amines and amino acids," *Langmuir*, vol. 19, pp. 6050–6055, 2003.
- [120] H.-K. Jeong, Y. P. Lee, R. J. W. E. Lahaye, M.-H. Park, K. H. An, I. J. Kim, C.-W. Yang, C. Y. Park, R. S. Ruoff, and Y. H. Lee, "Evidence of graphitic AB stacking order of graphite oxides," *J. Am. Chem. Soc.*, vol. 130, no. 4, pp. 1362–6, Jan. 2008.
- [121] C. Xu, X. Wang, L. Yang, and Y. Wu, "Fabrication of a graphene–cuprous oxide composite," *J. Solid State Chem.*, vol. 182, no. 9, pp. 2486–2490, Sep. 2009.

- [122] M. Seredych and T. J. Bandosz, "Effects of Surface Features on Adsorption of SO₂ on Graphite Oxide/Zr(OH)₄ Composites," *J. Phys. Chem. C*, vol. 114, pp. 14552–14560, 2010.
- [123] C. Petit, B. Levasseur, B. Mendoza, and T. J. Bandosz, "Reactive adsorption of acidic gases on MOF/graphite oxide composites," *Microporous Mesoporous Mater.*, vol. 154, pp. 107–112, May 2012.
- [124] B. Li, T. Liu, L. Hu, and Y. Wang, "A facile one-pot synthesis of Cu₂O/RGO nanocomposite for removal of organic pollutant," *J. Phys. Chem. Solids*, vol. 74, no. 4, pp. 635–640, Apr. 2013.
- [125] O. Mabayoje, M. Seredych, and T. J. Bandosz, "Cobalt (hydr)oxide/graphite oxide composites: Importance of surface chemical heterogeneity for reactive adsorption of hydrogen sulfide.," *J. Colloid Interface Sci.*, vol. 378, pp. 1–9, Jul. 2012.
- [126] H. S. Song, M. G. Park, S. J. Kwon, K. B. Yi, E. Croiset, Z. Chen, and S. C. Nam, "Hydrogen sulfide adsorption on nano-sized zinc oxide/reduced graphite oxide composite at ambient condition," *Appl. Surf. Sci.*, vol. 276, pp. 646–652, 2013.
- [127] J. F. Moulder, W. F. Stickle, P. E. Sobol, and K. D. Bomben, "Handbook of X-ray photoelectron spectroscopy," in *Perkin-Elmer Corp, Eden Prairie*, 1992.
- [128] M. Hilder, O. Winther-Jensen, B. Winther-Jensen, and D. R. MacFarlane, "Graphene/zinc nano-composites by electrochemical co-deposition," *Phys. Chem. Chem. Phys.*, vol. 14, pp. 14034–14040, Oct. 2012.
- [129] T. Yang, L. H. Liu, J. W. Liu, M. L. Chen, and J. H. Wang, "Cyanobacterium metallothionein decorated graphene oxide nanosheets for highly selective adsorption of ultra-trace cadmium," *J. Mater. Chem.*, vol. 22, pp. 21909–21916, 2012.

- [130] A. J. Hernández-Maldonado and R. T. Yang, “Desulfurization of commercial liquid fuels by selective adsorption via π -complexation with Cu(I)-Y zeolite,” *Ind. Eng. Chem. Res.*, vol. 42, pp. 3103–3110, 2003.
- [131] Y. Wang, R. Yang, and J. Heinzl, “Desulfurization of jet fuel by $\pi\pi$ -complexation adsorption with metal halides supported on MCM-41 and SBA-15 mesoporous materials,” *Chem. Eng. Sci.*, vol. 63, no. 2, pp. 356–365, Jan. 2008.
- [132] J. Björk, F. Hanke, C.-A. Palma, P. Samori, M. Cecchini, and M. Persson, “Adsorption of aromatic and anti-aromatic systems on graphene through π - π stacking,” *J. Phys. Chem. Lett.*, vol. 1, no. 23, pp. 3407–3412, Dec. 2010.
- [133] K. N. Kudin, B. Ozbas, H. C. Schniepp, R. K. Prud’homme, I. A. Aksay, and R. Car, “Raman spectra of graphite oxide and functionalized graphene sheets,” *Nano Lett.*, vol. 8, no. 1, pp. 36–41, Jan. 2008.
- [134] D. Long, W. Li, L. Ling, J. Miyawaki, I. Mochida, and S.-H. Yoon, “Preparation of nitrogen-doped graphene sheets by a combined chemical and hydrothermal reduction of graphene oxide,” *Langmuir*, vol. 26, no. 20, pp. 16096–16102, Oct. 2010.
- [135] S. Wakeland, R. Martinez, J. K. Grey, and C. C. Luhrs, “Production of graphene from graphite oxide using urea as expansion–reduction agent,” *Carbon N. Y.*, vol. 48, no. 12, pp. 3463–3470, Oct. 2010.
- [136] D. C. Marcano, D. V Kosynkin, J. M. Berlin, A. Sinitskii, Z. Sun, A. Slesarev, L. B. Alemany, W. Lu, and J. M. Tour, “Improved synthesis of graphene oxide,” *ACS Nano*, vol. 4, no. 8, pp. 4806–14, Aug. 2010.
- [137] J. Wu, S. Bai, X. Shen, and L. Jiang, “Preparation and characterization of graphene/CdS nanocomposites,” *Appl. Surf. Sci.*, vol. 257, no. 3, pp. 747–751, Nov. 2010.

- [138] G. Srinivas, Y. Zhu, R. Piner, N. Skipper, M. Ellerby, and R. Ruoff, "Synthesis of graphene-like nanosheets and their hydrogen adsorption capacity," *Carbon N. Y.*, vol. 48, no. 3, pp. 630–635, Mar. 2010.
- [139] J.-Z. Wang, C. Zhong, S.-L. Chou, and H.-K. Liu, "Flexible free-standing graphene-silicon composite film for lithium-ion batteries," *Electrochem. commun.*, vol. 12, pp. 1467–1470, Nov. 2010.
- [140] C. Hontoria-Lucas, "Study of oxygen-containing groups in a series of graphite oxides: Physical and chemical characterization," *Carbon N. Y.*, vol. 33, no. 11, pp. 1585–1592, 1995.
- [141] G. A. Zickler, B. Smarsly, N. Gierlinger, H. Peterlik, and O. Paris, "A reconsideration of the relationship between the crystallite size L_a of carbons determined by X-ray diffraction and Raman spectroscopy," *Carbon N. Y.*, vol. 44, no. 15, pp. 3239–3246, Dec. 2006.
- [142] M. Zhang, D. Lei, Z. Du, X. Yin, L. Chen, Q. Li, Y. Wang, and T. Wang, "Fast synthesis of SnO₂/graphene composites by reducing graphene oxide with stannous ions," *J. Mater. Chem.*, vol. 21, no. 6, pp. 1673–1676, 2011.
- [143] A. L. Higginbotham, D. V. Kosynkin, A. Sinitskii, Z. Sun, and J. M. Tour, "Lower-defect graphene oxide nanoribbons from multiwalled carbon nanotubes," *ACS Nano*, vol. 4, no. 4, pp. 2059–2069, 2010.
- [144] B. Saner, F. Dinç, and Y. Yürüm, "Utilization of multiple graphene nanosheets in fuel cells: 2. The effect of oxidation process on the characteristics of graphene nanosheets," *Fuel*, vol. 90, no. 8, pp. 2609–2616, Aug. 2011.

- [145] G. I. Titelman, V. Gelman, S. Bron, R. L. Khalfin, Y. Cohen, and H. Bianco-Peled, “Characteristics and microstructure of aqueous colloidal dispersions of graphite oxide,” *Carbon N. Y.*, vol. 43, no. 3, pp. 641–649, 2005.
- [146] Y. Liu, Y. Hu, M. Zhou, H. Qian, and X. Hu, “Microwave-assisted non-aqueous route to deposit well-dispersed ZnO nanocrystals on reduced graphene oxide sheets with improved photoactivity for the decolorization of dyes under visible light,” *Appl. Catal. B Environ.*, vol. 125, pp. 425–431, Aug. 2012.
- [147] N.-K. Park, Y. J. Lee, G. B. Han, S. O. Ryu, T. J. Lee, C. H. Chang, and G. Y. Han, “Synthesis of various zinc oxide nanostructures with zinc acetate and activated carbon by a matrix-assisted method,” *Colloids Surfaces A Physicochem. Eng. Asp.*, vol. 313–314, pp. 66–71, Feb. 2008.
- [148] Y. Yang and T. Liu, “Fabrication and characterization of graphene oxide/zinc oxide nanorods hybrid,” *Appl. Surf. Sci.*, vol. 257, no. 21, pp. 8950–8954, May 2011.
- [149] G. Liu, Z.-H. Huang, and F. Kang, “Preparation of ZnO/SiO₂ gel composites and their performance of H₂S removal at room temperature,” *J. Hazard. Mater.*, vol. 215–216, pp. 166–72, May 2012.
- [150] P. Dhage, A. Samokhvalov, D. Repala, E. C. Duin, and B. J. Tatarchuk, “Regenerable Fe-Mn-ZnO/SiO₂ sorbents for room temperature removal of H₂S from fuel reformates: Performance, active sites, operando studies,” *Phys. Chem. Chem. Phys.*, vol. 13, pp. 2179–2187, Feb. 2011.
- [151] D. Jiang, L. Su, L. Ma, N. Yao, X. Xu, H. Tang, and X. Li, “Cu–Zn–Al mixed metal oxides derived from hydroxycarbonate precursors for H₂S removal at low temperature,” *Appl. Surf. Sci.*, vol. 256, pp. 3216–3223, Mar. 2010.

- [152] A. Prakash, S. K. Misra, and D. Bahadur, "The role of reduced graphene oxide capping on defect induced ferromagnetism of ZnO nanorods," *Nanotechnology*, vol. 24, no. 9, p. 095705, Mar. 2013.
- [153] J. Xie, W.-T. Song, S.-Y. Liu, G. S. Cao, T. Zhu, and X. B. Zhao, "Self-assembly of ZnFe₂O₄/graphene hybrid and its application as high-performance anode material for Li-ion batteries," *New J. Chem.*, vol. 36, pp. 2236–2241, 2012.
- [154] S. Dubin, S. Gilje, K. Wang, V. C. Tung, K. Cha, A. S. Hall, J. Farrar, R. Varshneya, Y. Yang, and R. B. Kaner, "A one-step, solvothermal reduction method for producing reduced graphene oxide dispersions in organic solvents," *ACS Nano*, vol. 4, no. 7, pp. 3845–3852, Jul. 2010.
- [155] X.-P. Shen, A.-H. Yuan, Y.-M. Hu, Y. Jiang, Z. Xu, and Z. Hu, "Fabrication, characterization and field emission properties of large-scale uniform ZnO nanotube arrays," *Nanotechnology*, vol. 16, no. 10, pp. 2039–2043, Oct. 2005.
- [156] T. Lu, L. Pan, H. Li, G. Zhu, T. Lv, X. Liu, Z. Sun, T. Chen, and D. H. C. Chua, "Microwave-assisted synthesis of graphene–ZnO nanocomposite for electrochemical supercapacitors," *J. Alloys Compd.*, vol. 509, no. 18, pp. 5488–5492, May 2011.
- [157] P. Kundu, C. Nethravathi, P. a. Deshpande, M. Rajamathi, G. Madras, and N. Ravishankar, "Ultrafast Microwave-Assisted Route to Surfactant-Free Ultrafine Pt Nanoparticles on Graphene: Synergistic Co-reduction Mechanism and High Catalytic Activity," *Chem. Mater.*, vol. 23, no. 11, pp. 2772–2780, Jun. 2011.
- [158] T. Baird, P. J. Denny, R. Hoyle, F. Mcmonagle, and D. Stirling, "Modified Zinc Oxide Absorbents for Low-temperature Gas Desulfurisation," vol. 88, no. 22, pp. 3375–3382, 1992.

- [159] W. Bai, K. Yu, Q. Zhang, Y. Huang, Q. Wang, Z. Zhu, N. Dai, and Y. Sun, “Chemical solution-process method to synthesize ZnO nanorods with ultra-thin pinheads and ultra-thin nanobelts,” *Appl. Phys. A*, vol. 87, no. 4, pp. 755–759, Mar. 2007.
- [160] I. I. Novochinskii, C. Song, X. Ma, X. Liu, L. Shore, J. Lampert, and R. J. Farrauto, “Low-temperature H₂S removal from steam-containing gas mixtures with ZnO for fuel cell application. 1. ZnO particles and extrudates,” *Energy & Fuels*, vol. 18, no. 2, pp. 576–583, Mar. 2004.
- [161] S. Lew, A. F. Sarofim, and M. Flytzani-Stephanopoulos, “Sulfidation of zinc titanate and zinc oxide solids,” *Ind. Eng. Chem. Res.*, vol. 31, no. 8, pp. 1890–1899, Aug. 1992.
- [162] H. a. J. van Dijk, S. Walspurger, P. D. Cobden, R. W. van den Brink, and F. G. de Vos, “Testing of hydrotalcite-based sorbents for CO₂ and H₂S capture for use in sorption enhanced water gas shift,” *Int. J. Greenh. Gas Control*, vol. 5, no. 3, pp. 505–511, May 2011.
- [163] A. M. Palve and S. S. Garje, “A facile synthesis of ZnS nanocrystallites by pyrolysis of single molecule precursors, Zn (cinnamtscz)₂ and ZnCl₂ (cinnamtsczH)₂,” *Bull. Mater. Sci.*, vol. 34, pp. 667–671, 2011.
- [164] A. Cabral, R. G. Duarte, M. F. Montemor, M. L. Zheludkevich, and M. G. S. Ferreira, “Analytical characterisation and corrosion behaviour of bis-[triethoxysilylpropyl]tetrasulphide pre-treated AA2024-T3,” *Corros. Sci.*, vol. 47, pp. 869–881, Mar. 2005.
- [165] H. Ma, J. Han, Y. Fu, Y. Song, C. Yu, and X. Dong, “Synthesis of visible light responsive ZnO–ZnS/C photocatalyst by simple carbothermal reduction,” *Appl. Catal. B*, vol. 102, no. 3–4, pp. 417–423, Feb. 2011.

- [166] L. Fen, Y. Bo, Z. Jie, J. Anxi, S. Chunhong, K. Xiangji, and W. Xin, "Study on dsulfurization Efficiency and Products of Ce-Doped Nanosized ZnO Desulfurizer at Ambient Temperature," *J. Rare Earths*, vol. 25, pp. 306–310, 2007.
- [167] J. E. Thomas, W. M. Skinner, and R. S. C. Smart, "A comparison of the dissolution behavior of troilite with other iron(II) sulfides; implications of structure," *Geochim. Cosmochim. Acta*, vol. 67, pp. 831–843, 2003.
- [168] Z.-H. Huang, G. Liu, and F. Kang, "Glucose-promoted Zn-based metal-organic framework/graphene oxide composites for hydrogen sulfide removal.," *ACS Appl. Mater. Interfaces*, vol. 4, no. 9, pp. 4942–4947, Sep. 2012.
- [169] H. S. Song, M. G. Park, E. Croiset, Z. Chen, S. C. Nam, H.-J. Ryu, and K. B. Yi, "Effect of active Zinc Oxide dispersion on reduced graphite oxide for hydrogen sulfide adsorption at mid-temperature," *Appl. Surf. Sci.*, vol. 280, pp. 360–365, May 2013.
- [170] J. Lin, J. A. May, S. V. Didziulis, and E. I. Solomon, "Variable-energy photoelectron spectroscopic studies of H₂S chemisorption on Cu₂O and ZnO single-crystal surfaces: HS- bonding to Copper(I) and Zinc(II) sites related to catalytic poisoning," *J. Am. Chem. Soc.*, vol. 114, pp. 4718–4727, 1992.
- [171] C. X. Xu, X. W. Sun, X. H. Zhang, L. Ke, and S. J. Chua, "Photoluminescent properties of copper-doped zinc oxide nanowires," *Nanotechnology*, vol. 15, pp. 856–861, Jul. 2004.
- [172] K. G. Kanade, B. B. Kale, J.-O. Baeg, S. M. Lee, C. W. Lee, S.-J. Moon, and H. Chang, "Self-assembled aligned Cu doped ZnO nanoparticles for photocatalytic hydrogen production under visible light irradiation," *Mater. Chem. Phys.*, vol. 102, pp. 98–104, Mar. 2007.

- [173] E. Kester and B. Gillot, "Cation Distribution, Thermodynamic and Kinetics Considerations in Nanoscaled Copper Ferrite Spinel. New Experimental Approach By Xps and New Results Both in the Bulk and on the Grain Boundary," *J. Phys. Chem Solids*, vol. 59, pp. 1259–1269, Aug. 1998.
- [174] M. F. Al-Kuhaili, "Characterization of copper oxide thin films deposited by the thermal evaporation of cuprous oxide (Cu₂O)," *Vacuum*, vol. 82, pp. 623–629, Feb. 2008.
- [175] S. J. Yuan and S. O. Pehkonen, "Surface characterization and corrosion behavior of 70/30 Cu–Ni alloy in pristine and sulfide-containing simulated seawater," *Corros. Sci.*, vol. 49, no. 3, pp. 1276–1304, Mar. 2007.
- [176] S. Chaturvedi, J. A. Rodriguez, and J. Hrbek, "Reaction of S₂ with ZnO and Cu/ZnO surfaces: Photoemission and molecular orbital studies," *J. Phys. Chem. B*, vol. 101, pp. 10860–10869, 1997.
- [177] D. Tahir and S. Tougaard, "Electronic and optical properties of Cu, CuO and Cu₂O studied by electron spectroscopy.," *J. Phys. Condens. Matter*, vol. 24, no. 17, p. 175002, May 2012.
- [178] Z. Zhang and P. Wang, "Highly stable copper oxide composite as an effective photocathode for water splitting via a facile electrochemical synthesis strategy," *J. Mater. Chem.*, vol. 22, no. 6, pp. 2456–2464, 2012.
- [179] A. Prakash, S. K. Misra, and D. Bahadur, "The role of reduced graphene oxide capping on defect induced ferromagnetism of ZnO nanorods.," *Nanotechnology*, vol. 24, p. 095705, Mar. 2013.

- [180] F. S. Omar, H. N. Ming, S. M. Hafiz, and L. H. Ngee, "Microwave synthesis of Zinc oxide/reduced graphene oxide hybrid for adsorption-photocatalysis application," *Int. J. Photoenergy*, vol. 2014, pp. 1–8, 2014.
- [181] J. Wang, T. Tsuzuki, B. Tang, X. Hou, L. Sun, and X. Wang, "Reduced graphene oxide/ZnO composite: Reusable adsorbent for pollutant management," *ACS Appl. Mater. Interf.*, vol. 4, pp. 3084–3090, Jun. 2012.
- [182] S. Aksoy, Y. Caglar, S. Ilican, and M. Caglar, "Sol-gel derived Li-Mg co-doped ZnO films: Preparation and characterization via XRD, XPS, FESEM," *J. Alloy Compd.*, vol. 512, pp. 171–178, Jan. 2012.

Appendix I: Uncertainty Analysis and Confidential Interval
(Sample Calculations)

Some of H₂S adsorption breakthrough tests have been repeated; and from those repeated results, the average and standard deviations (STDEV) were calculated. The uncertainty (CONF) reported throughout the thesis are for a 95% confidence interval. Examples of uncertainty analysis calculation for ZnO and ZnO/rGO are given in Table I-1 below:

Table I.1: Repeated results for H₂S adsorption in different conditions

Material	Condition	Trial 1	Trial 2	Trial 3	Trial 4	Average	STDEV	CONF
ZnO	H ₂ S	152.1	155.2	154.7		154.0	1.7	1.9
	CO ₂ /H ₂ S	129.2	135.1			132.2	4.2	5.8
	H ₂ /H ₂ S	158.0	159.5	163.4		160.3	2.8	3.2
ZnO/rGO	H ₂ S	622.5	619.3	606.4	624.1	618.1	8.1	7.8
	CO ₂ /H ₂ S	536.4	529.1	541.9		535.7	6.5	7.3
	H ₂ /H ₂ S	742.1	748.4	769.2	777.8	759.4	16.9	16.5

An example for calculating the uncertainty is given below for the case of ZnO in H₂S:

$$\text{Average } (\mu): = \frac{152.1+155.2+154.7}{3} = 154.0 \frac{\text{min}}{\text{g ZnO}}$$

$$\begin{aligned} \text{Standard deviation } (\sigma): &= \sqrt{\text{avg}[(x_i - \mu)^2]} \\ &= \sqrt{\frac{(152.1 - 154)^2 + (155.2 - 154)^2 + (154.7 - 154)^2}{3}} \\ &= 1.7 \end{aligned}$$

$$\text{Confidence interval (95%): } \alpha = 0.95, \sigma = 1.7, n = 3$$

$$\begin{aligned} \text{- Margin of error} &= Z_{\alpha/2} * \sigma / (n)^{0.5} \text{ where } Z_{\alpha/2} = 1.96 \text{ (from Z-table)} \\ &= 1.96 * 1.7 / (3^{0.5}) = 1.923 \end{aligned}$$

→ The average with confidence interval = 154.0 ± 1.9

Appendix II: Crystal Size Calculation

Crystallite size and lattice parameters (a and c) for ZnO can be calculated based on XRD

data as below:

Table II: ZnO lattice parameter calculation

2θ (°)	radian	$\sin \theta$ (rad)	d spacing (Å)	h	k	l	a (Å)	c (Å)
31.8	0.277	0.274	2.814	1	0	0	3.255	
34.4	0.300	0.295	2.608	0	0	2		5.215
36.3	0.316	0.311	2.476	1	0	1		
47.5	0.415	0.403	1.911	1	0	2		
56.5	0.493	0.473	1.627	1	1	0	3.254	
56.5	0.493	0.473	1.628	1	0	3		
66.4	0.579	0.547	1.407	2	0	0		
68.0	0.593	0.559	1.378	1	1	2		
69.1	0.603	0.567	1.358	2	0	1		
72.6	0.633	0.592	1.302	0	0	4		5.207

- (100) at $2\theta = 31.8^\circ$

$$\rightarrow 31.8^\circ = 31.8 \times \frac{\pi}{180} = 0.277 \text{ rad}$$

$$\rightarrow d\text{-spacing} = \frac{\lambda (=1.5405)}{2 \times \sin \theta} = \frac{1.5405}{2 \cdot 0.277} = 2.814 \text{ Å}$$

$$\rightarrow a = \frac{1.5406}{\sqrt{3} \sin(0.277 \text{ rad}/2)} = 3.255 \text{ Å}$$

- (002) at $2\theta = 34.4^\circ$

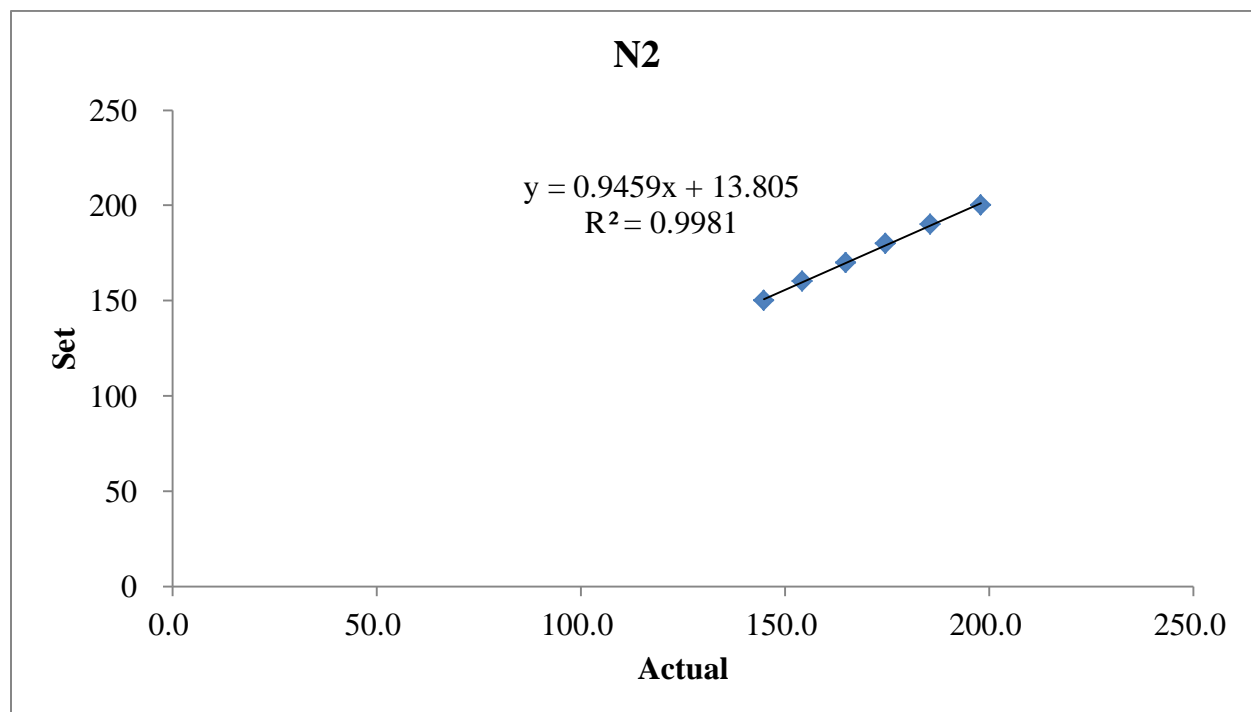
$$\rightarrow 34.4^\circ = 34.4 \times \frac{\pi}{180} = 0.300 \text{ rad}$$

$$\rightarrow d\text{-spacing} = \frac{\lambda (=1.5405)}{2 \times \sin \theta} = \frac{1.5405}{2 \cdot 0.3} = 2.608 \text{ Å}$$

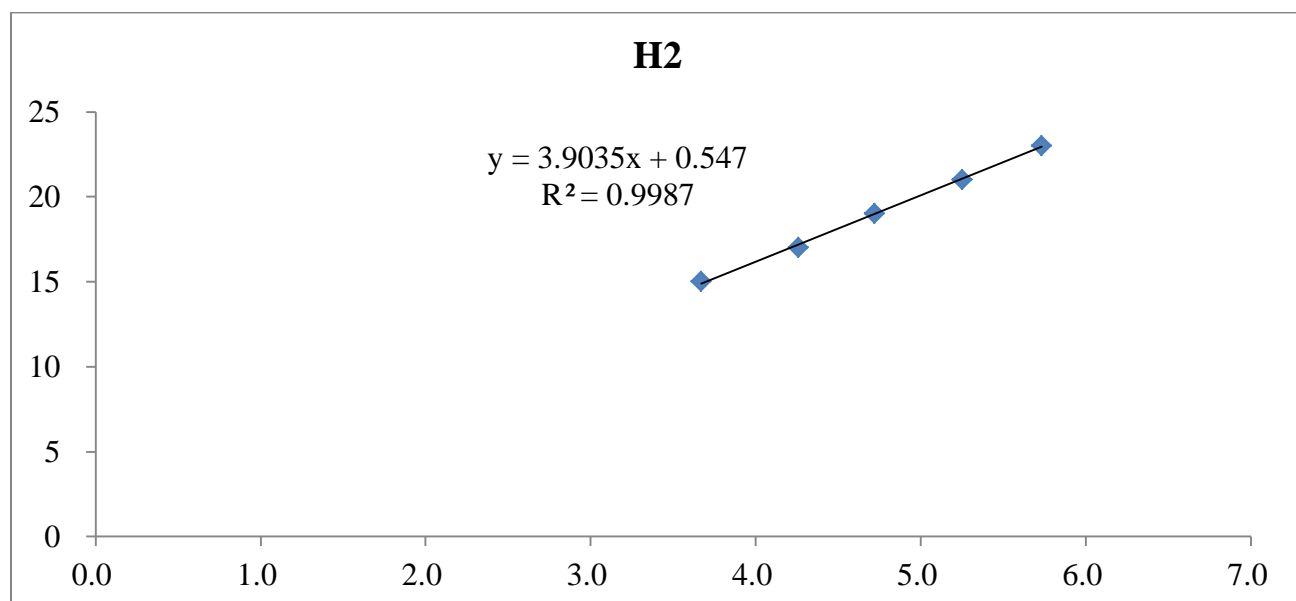
$$\rightarrow c = d\text{-spacing} \times 2 (= l) = 5.215 \text{ Å}$$

Appendix III: Mass Flow Controller Calibration

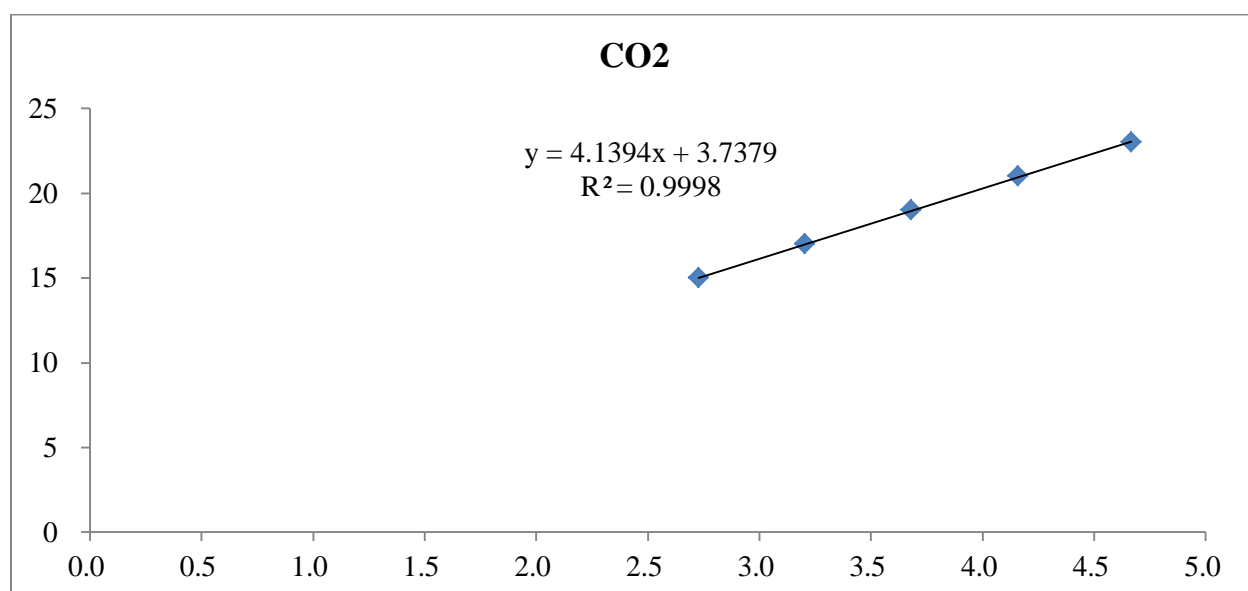
N ₂ (99mL)					
SET	#1	#2	Average	mL/sec	mL/min
150	41	41	41.0	2.4	144.9
160	38	39	38.5	2.6	154.3
170	36	36	36.0	2.8	165.0
180	34	34	34.0	2.9	174.7
190	32	32	32.0	3.1	185.6
200	30	30	30.0	3.3	198.0



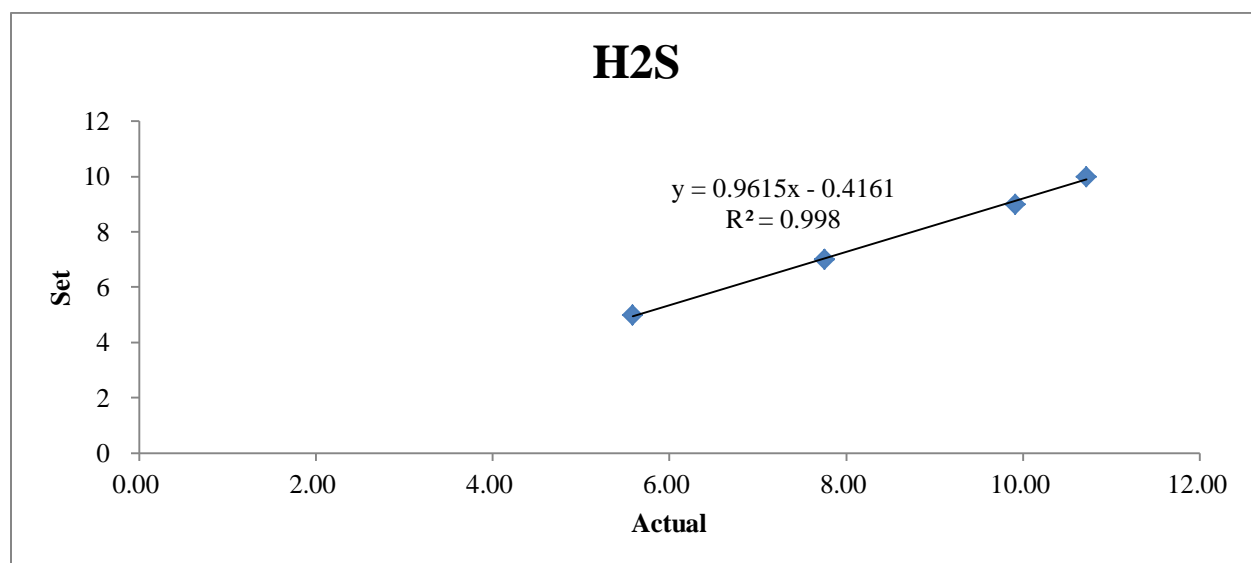
H₂ (1mL)								
	#1	#2	#3	#4	#5	Average	mL/sec	mL/min
15	16.35	16.34				16.3	0.061	3.7
17	14.19	13.83	14.08	14.18	14.15	14.1	0.071	4.3
19	12.44	12.62	12.66	12.98	12.83	12.7	0.079	4.7
21	11.41	11.17	11.53	11.57	11.46	11.4	0.088	5.3
23	10.43	10.39	10.45	10.45	10.6	10.5	0.096	5.7



CO ₂ (1mL)					
	#1	#2	Average	mL/sec	mL/min
15	22.21	21.8	22.0	0.045	2.7
17	18.42	19.02	18.7	0.053	3.2
19	16.28	16.33	16.3	0.061	3.7
21	14.36	14.5	14.4	0.069	4.2
23	12.74	12.98	12.9	0.078	4.7



H₂S (1mL)								
	#1	#2	#3	#4	#5	Average	mL/sec	mL/min
5	10.66	10.85	10.71	10.71	10.76	10.74	0.09	5.59
7	7.84	7.8	7.59	7.7	7.73	7.73	0.13	7.76
9	5.9	6.01	6.04	6.13	6.19	6.05	0.17	9.91
10	5.51	5.6	5.63	5.59	5.67	5.60	0.18	10.71



Appendix IV: Raw Data

1. DBT adsorption data

	Trial #1	Trial #2	Trial #3	Trial #4	Average
Graphite	0.2	0.13	0.14	0.21	0.17
GO-H	0.15	0.14	0.1	0.18	0.1425
GO-I	0.21	0.15	0.26	0.21	0.2075
GP-H	5.48	5.68	6.39	4.87	5.605
GP-I	10.59	9.87	11.01	10.53	10.5

** Unit: mg S adsorbed / g of adsorbent

2. H₂S adsorption data on ZnO and ZnO/rGO composite

2.1. H₂S adsorption on ZnO in H₂S/N₂ environment at 300°C

Trial #1 Sample weight 0.355 g

min	0	1	2	3	4	5	6	7	8	9	10
min/g of ads	0.0	2.8	5.6	8.5	11.3	14.1	16.9	19.7	22.5	25.4	28.2
H ₂ S (ppm)	0.0	0.0	0.0	0.0	0.0	0.0	0.0	0.0	0.0	0.0	0.0
min	11	12	13	14	15	16	17	18	19	20	21
min/g of ads	31.0	33.8	36.6	39.4	42.3	45.1	47.9	50.7	53.5	56.3	59.2
H ₂ S (ppm)	0.0	0.0	0.0	0.0	0.0	0.0	0.0	0.0	0.0	0.0	0.0
min	22	23	24	25	26	27	28	29	30	31	32
min/g of ads	62.0	64.8	67.6	70.4	73.2	76.1	78.9	81.7	84.5	87.3	90.1
H ₂ S (ppm)	0.0	0.0	0.0	0.0	0.0	0.0	0.0	0.0	0.0	0.0	0.0
min	33	34	35	36	37	38	39	40	41	42	43
min/g of ads	93.0	95.8	98.6	101.4	104.2	107.0	109.9	112.7	115.5	118.3	121.1
H ₂ S (ppm)	0.0	0.0	0.0	0.0	0.0	0.0	0.0	0.0	0.0	0.0	0.0
min	44	45	46	47	48	49	50	51	52	53	54
min/g of ads	123.9	126.8	129.6	132.4	135.2	138.0	140.8	143.7	146.5	149.3	152.1
H ₂ S (ppm)	0.0	0.0	0.0	0.0	0.0	0.0	0.0	0.0	0.0	0.0	0.8
min	55	56									
min/g of ads	154.9	157.7									
H ₂ S (ppm)	2.6	6.8									

Trial #2 Sample weight 0.348 g

min	0	1	2	3	4	5	6	7	8	9	10
min/g of ads	0.0	2.9	5.7	8.6	11.5	14.4	17.2	20.1	23.0	25.9	28.7
H2S (ppm)	0.0	0.0	0.0	0.0	0.0	0.0	0.0	0.0	0.0	0.0	0.0
min	11	12	13	14	15	16	17	18	19	20	21
min/g of ads	31.6	34.5	37.4	40.2	43.1	46.0	48.9	51.7	54.6	57.5	60.3
H2S (ppm)	0.0	0.0	0.0	0.0	0.0	0.0	0.0	0.0	0.0	0.0	0.0
min	22	23	24	25	26	27	28	29	30	31	32
min/g of ads	63.2	66.1	69.0	71.8	74.7	77.6	80.5	83.3	86.2	89.1	92.0
H2S (ppm)	0.0	0.0	0.0	0.0	0.0	0.0	0.0	0.0	0.0	0.0	0.0
min	33	34	35	36	37	38	39	40	41	42	43
min/g of ads	94.8	97.7	100.6	103.4	106.3	109.2	112.1	114.9	117.8	120.7	123.6
H2S (ppm)	0.0	0.0	0.0	0.0	0.0	0.0	0.0	0.0	0.0	0.0	0.0
min	44	45	46	47	48	49	50	51	52	53	54
min/g of ads	126.4	129.3	132.2	135.1	137.9	140.8	143.7	146.6	149.4	152.3	155.2
H2S (ppm)	0.0	0.0	0.0	0.0	0.0	0.0	0.0	0.0	0.0	0.0	0.2
min	55	56									
min/g of ads	158.0	160.9									
H2S (ppm)	3.8	9.2									

Trial #3 Sample weight 0.362 g

min	0	1	2	3	4	5	6	7	8	9	10
min/g of ads	0.0	2.8	5.5	8.3	11.0	13.8	16.6	19.3	22.1	24.9	27.6
H2S (ppm)	0.0	0.0	0.0	0.0	0.0	0.0	0.0	0.0	0.0	0.0	0.0
min	11	12	13	14	15	16	17	18	19	20	21
min/g of ads	30.4	33.1	35.9	38.7	41.4	44.2	47.0	49.7	52.5	55.2	58.0
H2S (ppm)	0.0	0.0	0.0	0.0	0.0	0.0	0.0	0.0	0.0	0.0	0.0
min	22	23	24	25	26	27	28	29	30	31	32
min/g of ads	60.8	63.5	66.3	69.1	71.8	74.6	77.3	80.1	82.9	85.6	88.4
H2S (ppm)	0.0	0.0	0.0	0.0	0.0	0.0	0.0	0.0	0.0	0.0	0.0
min	33	34	35	36	37	38	39	40	41	42	43
min/g of ads	91.2	93.9	96.7	99.4	102.2	105.0	107.7	110.5	113.3	116.0	118.8
H2S (ppm)	0.0	0.0	0.0	0.0	0.0	0.0	0.0	0.0	0.0	0.0	0.0
min	44	45	46	47	48	49	50	51	52	53	54
min/g of ads	121.5	124.3	127.1	129.8	132.6	135.4	138.1	140.9	143.6	146.4	149.2
H2S (ppm)	0.0	0.0	0.0	0.0	0.0	0.0	0.0	0.0	0.0	0.0	0.0
min	55	56	57								
min/g of ads	151.9	154.7	157.5								
H2S (ppm)	0.0	2.7	8.2								

2.2. H₂S adsorption on ZnO in H₂S/CO₂/N₂ environment at 300°C

Trial #1	Sample weight 0.356 g										
min	0	1	2	3	4	5	6	7	8	9	10
min/g of ads	0.0	2.8	5.6	8.4	11.2	14.0	16.9	19.7	22.5	25.3	28.1
H ₂ S (ppm)	0.0	0.0	0.0	0.0	0.0	0.0	0.0	0.0	0.0	0.0	0.0
min	11	12	13	14	15	16	17	18	19	20	21
min/g of ads	30.9	33.7	36.5	39.3	42.1	44.9	47.8	50.6	53.4	56.2	59.0
H ₂ S (ppm)	0.0	0.0	0.0	0.0	0.0	0.0	0.0	0.0	0.0	0.0	0.0
min	22	23	24	25	26	27	28	29	30	31	32
min/g of ads	61.8	64.6	67.4	70.2	73.0	75.8	78.7	81.5	84.3	87.1	89.9
H ₂ S (ppm)	0.0	0.0	0.0	0.0	0.0	0.0	0.0	0.0	0.0	0.0	0.0
min	33	34	35	36	37	38	39	40	41	42	43
min/g of ads	92.7	95.5	98.3	101.1	103.9	106.7	109.6	112.4	115.2	118.0	120.8
H ₂ S (ppm)	0.0	0.0	0.0	0.0	0.0	0.0	0.0	0.0	0.0	0.0	0.0
min	44	45	46	47	48						
min/g of ads	123.6	126.4	129.2	132.0	134.8						
H ₂ S (ppm)	0.0	0.0	1.9	3.6	9.1						

Trial #2 Sample weight 0.348 g

min	0	1	2	3	4	5	6	7	8	9	10
min/g of ads	0.0	2.9	5.7	8.6	11.5	14.4	17.2	20.1	23.0	25.9	28.7
H ₂ S (ppm)	0.0	0.0	0.0	0.0	0.0	0.0	0.0	0.0	0.0	0.0	0.0
min	11	12	13	14	15	16	17	18	19	20	21
min/g of ads	31.6	34.5	37.4	40.2	43.1	46.0	48.9	51.7	54.6	57.5	60.3
H ₂ S (ppm)	0.0	0.0	0.0	0.0	0.0	0.0	0.0	0.0	0.0	0.0	0.0
min	22	23	24	25	26	27	28	29	30	31	32
min/g of ads	63.2	66.1	69.0	71.8	74.7	77.6	80.5	83.3	86.2	89.1	92.0
H ₂ S (ppm)	0.0	0.0	0.0	0.0	0.0	0.0	0.0	0.0	0.0	0.0	0.0
min	33	34	35	36	37	38	39	40	41	42	43
min/g of ads	94.8	97.7	100.6	103.4	106.3	109.2	112.1	114.9	117.8	120.7	123.6
H ₂ S (ppm)	0.0	0.0	0.0	0.0	0.0	0.0	0.0	0.0	0.0	0.0	0.0
min	44	45	46	47	48	49	50				
min/g of ads	126.4	129.3	132.2	135.1	137.9	140.8	143.7				
H ₂ S (ppm)	0.0	0.0	0.0	2.8	5.1	7.2	9.8				

2.3. H₂S adsorption on ZnO in H₂S/H₂/N₂ environment at 300°C

Trial #1	Sample weight 0.348 g										
min	0	1	2	3	4	5	6	7	8	9	10
min/g of ads	0.0	2.9	5.7	8.6	11.5	14.4	17.2	20.1	23.0	25.9	28.7
H ₂ S (ppm)	0.0	0.0	0.0	0.0	0.0	0.0	0.0	0.0	0.0	0.0	0.0
min	11	12	13	14	15	16	17	18	19	20	21
min/g of ads	31.6	34.5	37.4	40.2	43.1	46.0	48.9	51.7	54.6	57.5	60.3
H ₂ S (ppm)	0.0	0.0	0.0	0.0	0.0	0.0	0.0	0.0	0.0	0.0	0.0
min	22	23	24	25	26	27	28	29	30	31	32
min/g of ads	63.2	66.1	69.0	71.8	74.7	77.6	80.5	83.3	86.2	89.1	92.0
H ₂ S (ppm)	0.0	0.0	0.0	0.0	0.0	0.0	0.0	0.0	0.0	0.0	0.0
min	33	34	35	36	37	38	39	40	41	42	43
min/g of ads	94.8	97.7	100.6	103.4	106.3	109.2	112.1	114.9	117.8	120.7	123.6
H ₂ S (ppm)	0.0	0.0	0.0	0.0	0.0	0.0	0.0	0.0	0.0	0.0	0.0
min	44	45	46	47	48	49	50	51	52	53	54
min/g of ads	126.4	129.3	132.2	135.1	137.9	140.8	143.7	146.6	149.4	152.3	155.2
H ₂ S (ppm)	0.0	0.0	0.0	0.0	0.0	0.0	0.0	0.0	0.0	0.0	0.0
min	55	56	57	58							
min/g of ads	158.0	160.9	163.8	166.7							
H ₂ S (ppm)	0.1	1.2	2.8	7.2							

Trial #2 Sample weight 0.351 g

min min/g of ads H2S (ppm)	0 0.0	1 2.8	2 5.7	3 8.5	4 11.4	5 14.2	6 17.1	7 19.9	8 22.8	9 25.6	10 28.5
min min/g of ads H2S (ppm)	11 31.3	12 34.2	13 37.0	14 39.9	15 42.7	16 45.6	17 48.4	18 51.3	19 54.1	20 57.0	21 59.8
min min/g of ads H2S (ppm)	22 62.7	23 65.5	24 68.4	25 71.2	26 74.1	27 76.9	28 79.8	29 82.6	30 85.5	31 88.3	32 91.2
min min/g of ads H2S (ppm)	33 94.0	34 96.9	35 99.7	36 102.6	37 105.4	38 108.3	39 111.1	40 114.0	41 116.8	42 119.7	43 122.5
min min/g of ads	44 125.4	45 128.2	46 131.1	47 133.9	48 136.8	49 139.6	50 142.5	51 145.3	52 148.1	53 151.0	54 153.8

H2S (ppm)	0.0	0.0	0.0	0.0	0.0	0.0	0.0	0.0	0.0	0.0	0.0
min	55	56	57	58	59						
min/g of ads	156.7	159.5	162.4	165.2	168.1						
H2S (ppm)	0.0	2.7	5.2	8.1	9.6						

Trial #3 Sample weight 0.355 g

min	0	1	2	3	4	5	6	7	8	9	10
min/g of ads	0.0	2.8	5.6	8.5	11.3	14.1	16.9	19.7	22.5	25.4	28.2
H2S (ppm)	0.0	0.0	0.0	0.0	0.0	0.0	0.0	0.0	0.0	0.0	0.0
min	11	12	13	14	15	16	17	18	19	20	21
min/g of ads	31.0	33.8	36.6	39.4	42.3	45.1	47.9	50.7	53.5	56.3	59.2
H2S (ppm)	0.0	0.0	0.0	0.0	0.0	0.0	0.0	0.0	0.0	0.0	0.0
min	22	23	24	25	26	27	28	29	30	31	32
min/g of ads	62.0	64.8	67.6	70.4	73.2	76.1	78.9	81.7	84.5	87.3	90.1
H2S (ppm)	0.0	0.0	0.0	0.0	0.0	0.0	0.0	0.0	0.0	0.0	0.0
min	33	34	35	36	37	38	39	40	41	42	43
min/g of ads	93.0	95.8	98.6	101.4	104.2	107.0	109.9	112.7	115.5	118.3	121.1
H2S (ppm)	0.0	0.0	0.0	0.0	0.0	0.0	0.0	0.0	0.0	0.0	0.0
min	44	45	46	47	48	49	50	51	52	53	54
min/g of ads	123.9	126.8	129.6	132.4	135.2	138.0	140.8	143.7	146.5	149.3	152.1
H2S (ppm)	0.0	0.0	0.0	0.0	0.0	0.0	0.0	0.0	0.0	0.0	0.0
min	55	56	57	58	59						
min/g of ads	154.9	157.7	160.6	163.4	166.2						
H2S (ppm)	0.0	0.0	0.0	2.8	7.1						

2.4. H₂S adsorption on ZnO/rGO in H₂S/ N₂ environment at 300°C

Trial #1	Sample weight 0.151 g										
min	0	1	2	3	4	5	6	7	8	9	10
min/g of ads	0.0	6.6	13.2	19.9	26.5	33.1	39.7	46.4	53.0	59.6	66.2
H ₂ S (ppm)	0.0	0.0	0.0	0.0	0.0	0.0	0.0	0.0	0.0	0.0	0.0
min	11	12	13	14	15	16	17	18	19	20	21
min/g of ads	72.8	79.5	86.1	92.7	99.3	106.0	112.6	119.2	125.8	132.5	139.1
H ₂ S (ppm)	0.0	0.0	0.0	0.0	0.0	0.0	0.0	0.0	0.0	0.0	0.0
min	22	23	24	25	26	27	28	29	30	31	32
min/g of ads	145.7	152.3	158.9	165.6	172.2	178.8	185.4	192.1	198.7	205.3	211.9
H ₂ S (ppm)	0.0	0.0	0.0	0.0	0.0	0.0	0.0	0.0	0.0	0.0	0.0
min	33	34	35	36	37	38	39	40	41	42	43
min/g of ads	218.5	225.2	231.8	238.4	245.0	251.7	258.3	264.9	271.5	278.1	284.8
H ₂ S (ppm)	0.0	0.0	0.0	0.0	0.0	0.0	0.0	0.0	0.0	0.0	0.0
min	44	45	46	47	48	49	50	51	52	53	54
min/g of ads	291.4	298.0	304.6	311.3	317.9	324.5	331.1	337.7	344.4	351.0	357.6
H ₂ S (ppm)	0.0	0.0	0.0	0.0	0.0	0.0	0.0	0.0	0.0	0.0	0.0
min	55	56	57	58	59	60	61	62	63	64	65
min/g of ads	364.2	370.9	377.5	384.1	390.7	397.4	404.0	410.6	417.2	423.8	430.5
H ₂ S (ppm)	0.0	0.0	0.0	0.0	0.0	0.0	0.0	0.0	0.0	0.0	0.0
min	66	67	68	69	70	71	72	73	74	75	76
min/g of ads	437.1	443.7	450.3	457.0	463.6	470.2	476.8	483.4	490.1	496.7	503.3
H ₂ S (ppm)	0.0	0.0	0.0	0.0	0.0	0.0	0.0	0.0	0.0	0.0	0.0
min	77	78	79	80	81	82	83	84	85	86	87

min/g of ads	509.9	516.6	523.2	529.8	536.4	543.0	549.7	556.3	562.9	569.5	576.2
H2S (ppm)	0.0	0.0	0.0	0.0	0.0	0.0	0.0	0.0	0.0	0.0	0.0
min	88	89	90	91	92	93	94	95	96	97	
min/g of ads	582.8	589.4	596.0	602.6	609.3	615.9	622.5	629.1	635.8	642.4	
H2S (ppm)	0.0	0.0	0.0	0.0	0.0	0.0	0.7	1.2	3.8	8.1	

Trial #2 Sample weight 0.155 g

min	0	1	2	3	4	5	6	7	8	9	10
min/g of ads	0.0	6.5	12.9	19.4	25.8	32.3	38.7	45.2	51.6	58.1	64.5
H2S (ppm)	0.0	0.0	0.0	0.0	0.0	0.0	0.0	0.0	0.0	0.0	0.0
min	11	12	13	14	15	16	17	18	19	20	21
min/g of ads	71.0	77.4	83.9	90.3	96.8	103.2	109.7	116.1	122.6	129.0	135.5
H2S (ppm)	0.0	0.0	0.0	0.0	0.0	0.0	0.0	0.0	0.0	0.0	0.0
min	22	23	24	25	26	27	28	29	30	31	32
min/g of ads	141.9	148.4	154.8	161.3	167.7	174.2	180.6	187.1	193.5	200.0	206.5
H2S (ppm)	0.0	0.0	0.0	0.0	0.0	0.0	0.0	0.0	0.0	0.0	0.0
min	33	34	35	36	37	38	39	40	41	42	43
min/g of ads	212.9	219.4	225.8	232.3	238.7	245.2	251.6	258.1	264.5	271.0	277.4
H2S (ppm)	0.0	0.0	0.0	0.0	0.0	0.0	0.0	0.0	0.0	0.0	0.0
min	44	45	46	47	48	49	50	51	52	53	54
min/g of ads	283.9	290.3	296.8	303.2	309.7	316.1	322.6	329.0	335.5	341.9	348.4
H2S (ppm)	0.0	0.0	0.0	0.0	0.0	0.0	0.0	0.0	0.0	0.0	0.0
min	55	56	57	58	59	60	61	62	63	64	65
min/g of ads	354.8	361.3	367.7	374.2	380.6	387.1	393.5	400.0	406.5	412.9	419.4
H2S (ppm)	0.0	0.0	0.0	0.0	0.0	0.0	0.0	0.0	0.0	0.0	0.0
min	66	67	68	69	70	71	72	73	74	75	76
min/g of ads	425.8	432.3	438.7	445.2	451.6	458.1	464.5	471.0	477.4	483.9	490.3
H2S (ppm)	0.0	0.0	0.0	0.0	0.0	0.0	0.0	0.0	0.0	0.0	0.0
min	77	78	79	80	81	82	83	84	85	86	87
min/g of ads	496.8	503.2	509.7	516.1	522.6	529.0	535.5	541.9	548.4	554.8	561.3

H2S (ppm)	0.0	0.0	0.0	0.0	0.0	0.0	0.0	0.0	0.0	0.0	0.0
min	88	89	90	91	92	93	94	95	96	97	98
min/g of ads	567.7	574.2	580.6	587.1	593.5	600.0	606.5	612.9	619.4	625.8	632.3
H2S (ppm)	0.0	0.0	0.0	0.0	0.0	0.0	0.0	0.0	0.9	5.2	7.3

Trial #3 Sample weight 0.155 g

min	0	1	2	3	4	5	6	7	8	9	10
min/g of ads	0.0	6.5	12.9	19.4	25.8	32.3	38.7	45.2	51.6	58.1	64.5
H2S (ppm)	0.0	0.0	0.0	0.0	0.0	0.0	0.0	0.0	0.0	0.0	0.0
min	11	12	13	14	15	16	17	18	19	20	21
min/g of ads	71.0	77.4	83.9	90.3	96.8	103.2	109.7	116.1	122.6	129.0	135.5
H2S (ppm)	0.0	0.0	0.0	0.0	0.0	0.0	0.0	0.0	0.0	0.0	0.0
min	22	23	24	25	26	27	28	29	30	31	32
min/g of ads	141.9	148.4	154.8	161.3	167.7	174.2	180.6	187.1	193.5	200.0	206.5
H2S (ppm)	0.0	0.0	0.0	0.0	0.0	0.0	0.0	0.0	0.0	0.0	0.0
min	33	34	35	36	37	38	39	40	41	42	43
min/g of ads	212.9	219.4	225.8	232.3	238.7	245.2	251.6	258.1	264.5	271.0	277.4
H2S (ppm)	0.0	0.0	0.0	0.0	0.0	0.0	0.0	0.0	0.0	0.0	0.0
min	44	45	46	47	48	49	50	51	52	53	54
min/g of ads	283.9	290.3	296.8	303.2	309.7	316.1	322.6	329.0	335.5	341.9	348.4
H2S (ppm)	0.0	0.0	0.0	0.0	0.0	0.0	0.0	0.0	0.0	0.0	0.0
min	55	56	57	58	59	60	61	62	63	64	65
min/g of ads	354.8	361.3	367.7	374.2	380.6	387.1	393.5	400.0	406.5	412.9	419.4
H2S (ppm)	0.0	0.0	0.0	0.0	0.0	0.0	0.0	0.0	0.0	0.0	0.0
min	66	67	68	69	70	71	72	73	74	75	76
min/g of ads	425.8	432.3	438.7	445.2	451.6	458.1	464.5	471.0	477.4	483.9	490.3
H2S (ppm)	0.0	0.0	0.0	0.0	0.0	0.0	0.0	0.0	0.0	0.0	0.0
min	77	78	79	80	81	82	83	84	85	86	87
min/g of ads	496.8	503.2	509.7	516.1	522.6	529.0	535.5	541.9	548.4	554.8	561.3

H2S (ppm)	0.0	0.0	0.0	0.0	0.0	0.0	0.0	0.0	0.0	0.0	0.0
min	88	89	90	91	92	93	94	95	96	97	
min/g of ads	567.7	574.2	580.6	587.1	593.5	600.0	606.5	612.9	619.4	625.8	
H2S (ppm)	0.0	0.0	0.0	0.0	0.0	0.0	0.1	0.4	4.1	6.3	

Trial #4 Sample weight 0.149 g

min	0	1	2	3	4	5	6	7	8	9	10
min/g of ads	0.0	6.7	13.4	20.1	26.8	33.6	40.3	47.0	53.7	60.4	67.1
H2S (ppm)	0.0	0.0	0.0	0.0	0.0	0.0	0.0	0.0	0.0	0.0	0.0
min	11	12	13	14	15	16	17	18	19	20	21
min/g of ads	73.8	80.5	87.2	94.0	100.7	107.4	114.1	120.8	127.5	134.2	140.9
H2S (ppm)	0.0	0.0	0.0	0.0	0.0	0.0	0.0	0.0	0.0	0.0	0.0
min	22	23	24	25	26	27	28	29	30	31	32
min/g of ads	147.7	154.4	161.1	167.8	174.5	181.2	187.9	194.6	201.3	208.1	214.8
H2S (ppm)	0.0	0.0	0.0	0.0	0.0	0.0	0.0	0.0	0.0	0.0	0.0
min	33	34	35	36	37	38	39	40	41	42	43
min/g of ads	221.5	228.2	234.9	241.6	248.3	255.0	261.7	268.5	275.2	281.9	288.6
H2S (ppm)	0.0	0.0	0.0	0.0	0.0	0.0	0.0	0.0	0.0	0.0	0.0
min	44	45	46	47	48	49	50	51	52	53	54
min/g of ads	295.3	302.0	308.7	315.4	322.1	328.9	335.6	342.3	349.0	355.7	362.4
H2S (ppm)	0.0	0.0	0.0	0.0	0.0	0.0	0.0	0.0	0.0	0.0	0.0
min	55	56	57	58	59	60	61	62	63	64	65
min/g of ads	369.1	375.8	382.6	389.3	396.0	402.7	409.4	416.1	422.8	429.5	436.2
H2S (ppm)	0.0	0.0	0.0	0.0	0.0	0.0	0.0	0.0	0.0	0.0	0.0
min	66	67	68	69	70	71	72	73	74	75	76
min/g of ads	443.0	449.7	456.4	463.1	469.8	476.5	483.2	489.9	496.6	503.4	510.1
H2S (ppm)	0.0	0.0	0.0	0.0	0.0	0.0	0.0	0.0	0.0	0.0	0.0
min	77	78	79	80	81	82	83	84	85	86	87
min/g of ads	516.8	523.5	530.2	536.9	543.6	550.3	557.0	563.8	570.5	577.2	583.9

H2S (ppm)	0.0	0.0	0.0	0.0	0.0	0.0	0.0	0.0	0.0	0.0	0.0
min	88	89	90	91	92	93	94	95			
min/g of ads	590.6	597.3	604.0	610.7	617.4	624.2	630.9	637.6			
H2S (ppm)	0.0	0.0	0.0	0.0	0.0	0.8	1.9	6.2			

2.5. H₂S adsorption on ZnO/rGO in H₂S/ CO₂/N₂ environment at 300°C

Trial #1	Sample weight 0.151 g										
min	0	1	2	3	4	5	6	7	8	9	10
min/g of ads	0.0	6.6	13.2	19.9	26.5	33.1	39.7	46.4	53.0	59.6	66.2
H ₂ S (ppm)	0.0	0.0	0.0	0.0	0.0	0.0	0.0	0.0	0.0	0.0	0.0
min	11	12	13	14	15	16	17	18	19	20	21
min/g of ads	72.8	79.5	86.1	92.7	99.3	106.0	112.6	119.2	125.8	132.5	139.1
H ₂ S (ppm)	0.0	0.0	0.0	0.0	0.0	0.0	0.0	0.0	0.0	0.0	0.0
min	22	23	24	25	26	27	28	29	30	31	32
min/g of ads	145.7	152.3	158.9	165.6	172.2	178.8	185.4	192.1	198.7	205.3	211.9
H ₂ S (ppm)	0.0	0.0	0.0	0.0	0.0	0.0	0.0	0.0	0.0	0.0	0.0
min	33	34	35	36	37	38	39	40	41	42	43
min/g of ads	218.5	225.2	231.8	238.4	245.0	251.7	258.3	264.9	271.5	278.1	284.8
H ₂ S (ppm)	0.0	0.0	0.0	0.0	0.0	0.0	0.0	0.0	0.0	0.0	0.0
min	44	45	46	47	48	49	50	51	52	53	54
min/g of ads	291.4	298.0	304.6	311.3	317.9	324.5	331.1	337.7	344.4	351.0	357.6
H ₂ S (ppm)	0.0	0.0	0.0	0.0	0.0	0.0	0.0	0.0	0.0	0.0	0.0
min	55	56	57	58	59	60	61	62	63	64	65
min/g of ads	364.2	370.9	377.5	384.1	390.7	397.4	404.0	410.6	417.2	423.8	430.5
H ₂ S (ppm)	0.0	0.0	0.0	0.0	0.0	0.0	0.0	0.0	0.0	0.0	0.0
min	66	67	68	69	70	71	72	73	74	75	76
min/g of ads	437.1	443.7	450.3	457.0	463.6	470.2	476.8	483.4	490.1	496.7	503.3
H ₂ S (ppm)	0.0	0.0	0.0	0.0	0.0	0.0	0.0	0.0	0.0	0.0	0.0
min	77	78	79	80	81	82	83				

min/g of ads	509.9	516.6	523.2	529.8	536.4	543.0	549.7				
H2S (ppm)	0.0	0.0	0.0	0.0	2.1	3.8	6.1				

Trial #2 Sample weight 0.155 g

min	0	1	2	3	4	5	6	7	8	9	10
min/g of ads	0.0	6.5	12.9	19.4	25.8	32.3	38.7	45.2	51.6	58.1	64.5
H2S (ppm)	0.0	0.0	0.0	0.0	0.0	0.0	0.0	0.0	0.0	0.0	0.0
min	11	12	13	14	15	16	17	18	19	20	21
min/g of ads	71.0	77.4	83.9	90.3	96.8	103.2	109.7	116.1	122.6	129.0	135.5
H2S (ppm)	0.0	0.0	0.0	0.0	0.0	0.0	0.0	0.0	0.0	0.0	0.0
min	22	23	24	25	26	27	28	29	30	31	32
min/g of ads	141.9	148.4	154.8	161.3	167.7	174.2	180.6	187.1	193.5	200.0	206.5
H2S (ppm)	0.0	0.0	0.0	0.0	0.0	0.0	0.0	0.0	0.0	0.0	0.0
min	33	34	35	36	37	38	39	40	41	42	43
min/g of ads	212.9	219.4	225.8	232.3	238.7	245.2	251.6	258.1	264.5	271.0	277.4
H2S (ppm)	0.0	0.0	0.0	0.0	0.0	0.0	0.0	0.0	0.0	0.0	0.0
min	44	45	46	47	48	49	50	51	52	53	54
min/g of ads	283.9	290.3	296.8	303.2	309.7	316.1	322.6	329.0	335.5	341.9	348.4
H2S (ppm)	0.0	0.0	0.0	0.0	0.0	0.0	0.0	0.0	0.0	0.0	0.0
min	55	56	57	58	59	60	61	62	63	64	65
min/g of ads	354.8	361.3	367.7	374.2	380.6	387.1	393.5	400.0	406.5	412.9	419.4
H2S (ppm)	0.0	0.0	0.0	0.0	0.0	0.0	0.0	0.0	0.0	0.0	0.0
min	66	67	68	69	70	71	72	73	74	75	76
min/g of ads	425.8	432.3	438.7	445.2	451.6	458.1	464.5	471.0	477.4	483.9	490.3
H2S (ppm)	0.0	0.0	0.0	0.0	0.0	0.0	0.0	0.0	0.0	0.0	0.0
min	77	78	79	80	81	82	83	84	85		
min/g of ads	496.8	503.2	509.7	516.1	522.6	529.0	535.5	541.9	548.4		

H2S (ppm)	0.0	0.0	0.0	0.0	0.0	0.3	3.9	6.9	8.1		
-----------	-----	-----	-----	-----	-----	-----	-----	-----	-----	--	--

Trial #3 Sample weight 0.155 g

min	0	1	2	3	4	5	6	7	8	9	10
min/g of ads	0.0	6.5	12.9	19.4	25.8	32.3	38.7	45.2	51.6	58.1	64.5
H2S (ppm)	0.0	0.0	0.0	0.0	0.0	0.0	0.0	0.0	0.0	0.0	0.0
min	11	12	13	14	15	16	17	18	19	20	21
min/g of ads	71.0	77.4	83.9	90.3	96.8	103.2	109.7	116.1	122.6	129.0	135.5
H2S (ppm)	0.0	0.0	0.0	0.0	0.0	0.0	0.0	0.0	0.0	0.0	0.0
min	22	23	24	25	26	27	28	29	30	31	32
min/g of ads	141.9	148.4	154.8	161.3	167.7	174.2	180.6	187.1	193.5	200.0	206.5
H2S (ppm)	0.0	0.0	0.0	0.0	0.0	0.0	0.0	0.0	0.0	0.0	0.0
min	33	34	35	36	37	38	39	40	41	42	43
min/g of ads	212.9	219.4	225.8	232.3	238.7	245.2	251.6	258.1	264.5	271.0	277.4
H2S (ppm)	0.0	0.0	0.0	0.0	0.0	0.0	0.0	0.0	0.0	0.0	0.0
min	44	45	46	47	48	49	50	51	52	53	54
min/g of ads	283.9	290.3	296.8	303.2	309.7	316.1	322.6	329.0	335.5	341.9	348.4
H2S (ppm)	0.0	0.0	0.0	0.0	0.0	0.0	0.0	0.0	0.0	0.0	0.0
min	55	56	57	58	59	60	61	62	63	64	65
min/g of ads	354.8	361.3	367.7	374.2	380.6	387.1	393.5	400.0	406.5	412.9	419.4
H2S (ppm)	0.0	0.0	0.0	0.0	0.0	0.0	0.0	0.0	0.0	0.0	0.0
min	66	67	68	69	70	71	72	73	74	75	76
min/g of ads	425.8	432.3	438.7	445.2	451.6	458.1	464.5	471.0	477.4	483.9	490.3
H2S (ppm)	0.0	0.0	0.0	0.0	0.0	0.0	0.0	0.0	0.0	0.0	0.0
min	77	78	79	80	81	82	83	84	85		
min/g of ads	496.8	503.2	509.7	516.1	522.6	529.0	535.5	541.9	548.4		

H2S (ppm)	0.0	0.0	0.0	0.0	0.0	0.0	0.0	2.6	8.1		
-----------	-----	-----	-----	-----	-----	-----	-----	-----	-----	--	--

2.6. H₂S adsorption on ZnO/rGO in H₂S/ H₂/N₂ environment at 300°C

Trial #1	Sample weight 0.151 g										
min	0	1	2	3	4	5	6	7	8	9	10
min/g of ads	0.0	6.3	12.6	18.9	25.2	31.4	37.7	44.0	50.3	56.6	62.9
H ₂ S (ppm)	0.0	0.0	0.0	0.0	0.0	0.0	0.0	0.0	0.0	0.0	0.0
min	11	12	13	14	15	16	17	18	19	20	21
min/g of ads	69.2	75.5	81.8	88.1	94.3	100.6	106.9	113.2	119.5	125.8	132.1
H ₂ S (ppm)	0.0	0.0	0.0	0.0	0.0	0.0	0.0	0.0	0.0	0.0	0.0
min	22	23	24	25	26	27	28	29	30	31	32
min/g of ads	138.4	144.7	150.9	157.2	163.5	169.8	176.1	182.4	188.7	195.0	201.3
H ₂ S (ppm)	0.0	0.0	0.0	0.0	0.0	0.0	0.0	0.0	0.0	0.0	0.0
min	33	34	35	36	37	38	39	40	41	42	43
min/g of ads	207.5	213.8	220.1	226.4	232.7	239.0	245.3	251.6	257.9	264.2	270.4
H ₂ S (ppm)	0.0	0.0	0.0	0.0	0.0	0.0	0.0	0.0	0.0	0.0	0.0
min	44	45	46	47	48	49	50	51	52	53	54
min/g of ads	276.7	283.0	289.3	295.6	301.9	308.2	314.5	320.8	327.0	333.3	339.6
H ₂ S (ppm)	0.0	0.0	0.0	0.0	0.0	0.0	0.0	0.0	0.0	0.0	0.0
min	55	56	57	58	59	60	61	62	63	64	65
min/g of ads	345.9	352.2	358.5	364.8	371.1	377.4	383.6	389.9	396.2	402.5	408.8
H ₂ S (ppm)	0.0	0.0	0.0	0.0	0.0	0.0	0.0	0.0	0.0	0.0	0.0
min	66	67	68	69	70	71	72	73	74	75	76
min/g of ads	415.1	421.4	427.7	434.0	440.3	446.5	452.8	459.1	465.4	471.7	478.0

H2S (ppm)	0.0	0.0	0.0	0.0	0.0	0.0	0.0	0.0	0.0	0.0	0.0
min	77	78	79	80	81	82	83	84	85	86	87
min/g of ads	484.3	490.6	496.9	503.1	509.4	515.7	522.0	528.3	534.6	540.9	547.2
H2S (ppm)	0.0	0.0	0.0	0.0	0.0	0.0	0.0	0.0	0.0	0.0	0.0
min	88	89	90	91	92	93	94	95	96	97	98
min/g of ads	553.5	559.7	566.0	572.3	578.6	584.9	591.2	597.5	603.8	610.1	616.4
H2S (ppm)	0.0	0.0	0.0	0.0	0.0	0.0	0.0	0.0	0.0	0.0	0.0
min	99	100	101	102	103	104	105	106	107	108	109
min/g of ads	622.6	628.9	635.2	641.5	647.8	654.1	660.4	666.7	673.0	679.2	685.5
H2S (ppm)	0.0	0.0	0.0	0.0	0.0	0.0	0.0	0.0	0.0	0.0	0.0
min	110	111	112	113	114	115	116	117	118	119	120
min/g of ads	691.8	698.1	704.4	710.7	717.0	723.3	729.6	735.8	742.1	748.4	754.7
H2S (ppm)	0.0	0.0	0.0	0.0	0.0	0.0	0.0	0.0	0.3	2.8	6.2
min	121										
min/g of ads	761.0										
H2S (ppm)	9.3										

Trial #2 Sample weight 0.151 g

min	0	1	2	3	4	5	6	7	8	9	10
min/g of ads	0.0	6.3	12.6	18.9	25.2	31.4	37.7	44.0	50.3	56.6	62.9
H2S (ppm)	0.0	0.0	0.0	0.0	0.0	0.0	0.0	0.0	0.0	0.0	0.0
min	11	12	13	14	15	16	17	18	19	20	21
min/g of ads	69.2	75.5	81.8	88.1	94.3	100.6	106.9	113.2	119.5	125.8	132.1
H2S (ppm)	0.0	0.0	0.0	0.0	0.0	0.0	0.0	0.0	0.0	0.0	0.0
min	22	23	24	25	26	27	28	29	30	31	32
min/g of ads	138.4	144.7	150.9	157.2	163.5	169.8	176.1	182.4	188.7	195.0	201.3
H2S (ppm)	0.0	0.0	0.0	0.0	0.0	0.0	0.0	0.0	0.0	0.0	0.0
min	33	34	35	36	37	38	39	40	41	42	43
min/g of ads	207.5	213.8	220.1	226.4	232.7	239.0	245.3	251.6	257.9	264.2	270.4
H2S (ppm)	0.0	0.0	0.0	0.0	0.0	0.0	0.0	0.0	0.0	0.0	0.0
min	44	45	46	47	48	49	50	51	52	53	54
min/g of ads	276.7	283.0	289.3	295.6	301.9	308.2	314.5	320.8	327.0	333.3	339.6
H2S (ppm)	0.0	0.0	0.0	0.0	0.0	0.0	0.0	0.0	0.0	0.0	0.0
min	55	56	57	58	59	60	61	62	63	64	65
min/g of ads	345.9	352.2	358.5	364.8	371.1	377.4	383.6	389.9	396.2	402.5	408.8
H2S (ppm)	0.0	0.0	0.0	0.0	0.0	0.0	0.0	0.0	0.0	0.0	0.0
min	66	67	68	69	70	71	72	73	74	75	76
min/g of ads	415.1	421.4	427.7	434.0	440.3	446.5	452.8	459.1	465.4	471.7	478.0
H2S (ppm)	0.0	0.0	0.0	0.0	0.0	0.0	0.0	0.0	0.0	0.0	0.0
min	77	78	79	80	81	82	83	84	85	86	87
min/g of ads	484.3	490.6	496.9	503.1	509.4	515.7	522.0	528.3	534.6	540.9	547.2

H2S (ppm)	0.0	0.0	0.0	0.0	0.0	0.0	0.0	0.0	0.0	0.0	0.0
min	88	89	90	91	92	93	94	95	96	97	98
min/g of ads	553.5	559.7	566.0	572.3	578.6	584.9	591.2	597.5	603.8	610.1	616.4
H2S (ppm)	0.0	0.0	0.0	0.0	0.0	0.0	0.0	0.0	0.0	0.0	0.0
min	99	100	101	102	103	104	105	106	107	108	109
min/g of ads	622.6	628.9	635.2	641.5	647.8	654.1	660.4	666.7	673.0	679.2	685.5
H2S (ppm)	0.0	0.0	0.0	0.0	0.0	0.0	0.0	0.0	0.0	0.0	0.0
min	110	111	112	113	114	115	116	117	118	119	120
min/g of ads	691.8	698.1	704.4	710.7	717.0	723.3	729.6	735.8	742.1	748.4	754.7
H2S (ppm)	0.0	0.0	0.0	0.0	0.0	0.0	0.0	0.0	0.0	2.1	7.2
min	121										
min/g of ads	761.0										
H2S (ppm)	9.6										

Trial #3 Sample weight 0.156 g

min	0	1	2	3	4	5	6	7	8	9	10
min/g of ads	0.0	6.4	12.8	19.2	25.6	32.1	38.5	44.9	51.3	57.7	64.1
H2S (ppm)	0.0	0.0	0.0	0.0	0.0	0.0	0.0	0.0	0.0	0.0	0.0
min	11	12	13	14	15	16	17	18	19	20	21
min/g of ads	70.5	76.9	83.3	89.7	96.2	102.6	109.0	115.4	121.8	128.2	134.6
H2S (ppm)	0.0	0.0	0.0	0.0	0.0	0.0	0.0	0.0	0.0	0.0	0.0
min	22	23	24	25	26	27	28	29	30	31	32
min/g of ads	141.0	147.4	153.8	160.3	166.7	173.1	179.5	185.9	192.3	198.7	205.1
H2S (ppm)	0.0	0.0	0.0	0.0	0.0	0.0	0.0	0.0	0.0	0.0	0.0
min	33	34	35	36	37	38	39	40	41	42	43
min/g of ads	211.5	217.9	224.4	230.8	237.2	243.6	250.0	256.4	262.8	269.2	275.6
H2S (ppm)	0.0	0.0	0.0	0.0	0.0	0.0	0.0	0.0	0.0	0.0	0.0
min	44	45	46	47	48	49	50	51	52	53	54
min/g of ads	282.1	288.5	294.9	301.3	307.7	314.1	320.5	326.9	333.3	339.7	346.2
H2S (ppm)	0.0	0.0	0.0	0.0	0.0	0.0	0.0	0.0	0.0	0.0	0.0
min	55	56	57	58	59	60	61	62	63	64	65
min/g of ads	352.6	359.0	365.4	371.8	378.2	384.6	391.0	397.4	403.8	410.3	416.7
H2S (ppm)	0.0	0.0	0.0	0.0	0.0	0.0	0.0	0.0	0.0	0.0	0.0
min	66	67	68	69	70	71	72	73	74	75	76
min/g of ads	423.1	429.5	435.9	442.3	448.7	455.1	461.5	467.9	474.4	480.8	487.2
H2S (ppm)	0.0	0.0	0.0	0.0	0.0	0.0	0.0	0.0	0.0	0.0	0.0
min	77	78	79	80	81	82	83	84	85	86	87
min/g of ads	493.6	500.0	506.4	512.8	519.2	525.6	532.1	538.5	544.9	551.3	557.7

H2S (ppm)	0.0	0.0	0.0	0.0	0.0	0.0	0.0	0.0	0.0	0.0	0.0
min	88	89	90	91	92	93	94	95	96	97	98
min/g of ads	564.1	570.5	576.9	583.3	589.7	596.2	602.6	609.0	615.4	621.8	628.2
H2S (ppm)	0.0	0.0	0.0	0.0	0.0	0.0	0.0	0.0	0.0	0.0	0.0
min	99	100	101	102	103	104	105	106	107	108	109
min/g of ads	634.6	641.0	647.4	653.8	660.3	666.7	673.1	679.5	685.9	692.3	698.7
H2S (ppm)	0.0	0.0	0.0	0.0	0.0	0.0	0.0	0.0	0.0	0.0	0.0
min	110	111	112	113	114	115	116	117	118	119	120
min/g of ads	705.1	711.5	717.9	724.4	730.8	737.2	743.6	750.0	756.4	762.8	769.2
H2S (ppm)	0.0	0.0	0.0	0.0	0.0	0.0	0.0	0.0	0.0	0.0	1.1
min	121	122									
min/g of ads	775.6	782.1									
H2S (ppm)	3.6	7.1									

Trial #4 Sample weight 0.153 g

min	0	1	2	3	4	5	6	7	8	9	10
min/g of ads	0.0	6.5	13.1	19.6	26.1	32.7	39.2	45.8	52.3	58.8	65.4
H2S (ppm)	0.0	0.0	0.0	0.0	0.0	0.0	0.0	0.0	0.0	0.0	0.0
min	11	12	13	14	15	16	17	18	19	20	21
min/g of ads	71.9	78.4	85.0	91.5	98.0	104.6	111.1	117.6	124.2	130.7	137.3
H2S (ppm)	0.0	0.0	0.0	0.0	0.0	0.0	0.0	0.0	0.0	0.0	0.0
min	22	23	24	25	26	27	28	29	30	31	32
min/g of ads	143.8	150.3	156.9	163.4	169.9	176.5	183.0	189.5	196.1	202.6	209.2
H2S (ppm)	0.0	0.0	0.0	0.0	0.0	0.0	0.0	0.0	0.0	0.0	0.0
min	33	34	35	36	37	38	39	40	41	42	43
min/g of ads	215.7	222.2	228.8	235.3	241.8	248.4	254.9	261.4	268.0	274.5	281.0
H2S (ppm)	0.0	0.0	0.0	0.0	0.0	0.0	0.0	0.0	0.0	0.0	0.0
min	44	45	46	47	48	49	50	51	52	53	54
min/g of ads	287.6	294.1	300.7	307.2	313.7	320.3	326.8	333.3	339.9	346.4	352.9
H2S (ppm)	0.0	0.0	0.0	0.0	0.0	0.0	0.0	0.0	0.0	0.0	0.0
min	55	56	57	58	59	60	61	62	63	64	65
min/g of ads	359.5	366.0	372.5	379.1	385.6	392.2	398.7	405.2	411.8	418.3	424.8
H2S (ppm)	0.0	0.0	0.0	0.0	0.0	0.0	0.0	0.0	0.0	0.0	0.0
min	66	67	68	69	70	71	72	73	74	75	76
min/g of ads	431.4	437.9	444.4	451.0	457.5	464.1	470.6	477.1	483.7	490.2	496.7
H2S (ppm)	0.0	0.0	0.0	0.0	0.0	0.0	0.0	0.0	0.0	0.0	0.0
min	77	78	79	80	81	82	83	84	85	86	87
min/g of ads	503.3	509.8	516.3	522.9	529.4	535.9	542.5	549.0	555.6	562.1	568.6

H2S (ppm)	0.0	0.0	0.0	0.0	0.0	0.0	0.0	0.0	0.0	0.0	0.0
min	88	89	90	91	92	93	94	95	96	97	98
min/g of ads	575.2	581.7	588.2	594.8	601.3	607.8	614.4	620.9	627.5	634.0	640.5
H2S (ppm)	0.0	0.0	0.0	0.0	0.0	0.0	0.0	0.0	0.0	0.0	0.0
min	99	100	101	102	103	104	105	106	107	108	109
min/g of ads	647.1	653.6	660.1	666.7	673.2	679.7	686.3	692.8	699.3	705.9	712.4
H2S (ppm)	0.0	0.0	0.0	0.0	0.0	0.0	0.0	0.0	0.0	0.0	0.0
min	110	111	112	113	114	115	116	117	118	119	120
min/g of ads	719.0	725.5	732.0	738.6	745.1	751.6	758.2	764.7	771.2	777.8	784.3
H2S (ppm)	0.0	0.0	0.0	0.0	0.0	0.0	0.0	0.0	0.0	2.3	6.2
min	121										
min/g of ads	790.8										
H2S (ppm)	8.1										

2.7. Regeneration ability on ZnO

** Regeneration at 600°C in N₂ environment for 1 hr (sample weight: 0.494g)

min	min/g ads	Fresh	1st	2nd	3rd	4th
0	0.0	0	0	0	0	0
1	2.0	0	0	0	0	0
2	4.0	0	0	0	0	0
3	6.1	0	0	0	0	0
4	8.1	0	0	0	0	0
5	10.1	0	0	0	0	0
6	12.1	0	0	0	0	0
7	14.2	0	0	0	0	0
8	16.2	0	0	0	0	0
9	18.2	0	0	0	0	0
10	20.2	0	0	0	0	0
11	22.3	0	0	0	0	0
12	24.3	0	0	0	0.14	0
13	26.3	0	0	0	0.39	0.16
14	28.3	0	0	0	0.73	0.35
15	30.4	0	0	0.18	1.17	0.62
16	32.4	0	0	0.42	1.73	0.91
17	34.4	0	0	0.76	2.38	1.26
18	36.4	0	0	1.12	3.09	1.62
19	38.5	0	0	1.53	3.73	2.02
20	40.5	0	0	2.00	4.13	2.48
21	42.5	0	0	2.53	4.24	2.95
22	44.5	0	0	3.10		3.50
23	46.6	0	0	3.72		4.32
24	48.6	0	0	4.31		
25	50.6	0	0	4.67		
26	52.6	0	0			
27	54.7	0	0			
28	56.7	0	0			

29	58.7	0	0
30	60.7	0	0
31	62.8	0	0
32	64.8	0	0
33	66.8	0	0
34	68.8	0	0
35	70.9	0	0
36	72.9	0	0
37	74.9	0	0
38	76.9	0	0
39	78.9	0	0
40	81.0	0	0
41	83.0	0	0
42	85.0	0	0
43	87.0	0	0.40
44	89.1	0	1.61
45	91.1	0	3.67
46	93.1	0	6.92
47	95.1	0	
48	97.2	0	
49	99.2	0	
50	101.2	0	
51	103.2	0	
52	105.3	0	
53	107.3	0	
54	109.3	0	
55	111.3	0	
56	113.4	0	
57	115.4	0	
58	117.4	0	
59	119.4	0	
60	121.5	0	
61	123.5	0	

62	125.5	0
63	127.5	0
64	129.6	0
65	131.6	0
66	133.6	0
67	135.6	0
68	137.7	0
69	139.7	0
70	141.7	0
71	143.7	0
72	145.7	0
73	147.8	0.18
74	149.8	0.30
75	151.8	0.47
76	153.8	0.68
77	155.9	0.93
78	157.9	1.24
79	159.9	1.64
80	161.9	2.11
81	164.0	2.68
82	166.0	3.38
83	168.0	4.24
84	170.0	5.24
85	172.1	6.16

2.8. Regeneration ability on ZnO/rGO

** Regeneration at 600°C in N₂ environment for 1 hr (sample weight: 0.060g)

min	min/g ads	Fresh	1st	2nd	3rd	4th	5th	6th	7th	8th
0	0.0	0	0	0	0	0	0	0	0	0
1	16.8	0	0	0	0	0	0	0	0	0
2	33.5	0	0	0	0	0	0	0	0	0
3	50.3	0	0	0	0	0	0	0	0	0
4	67.0	0	0	0	0	0	0	0	0	0
5	83.8	0	0	0	0	0	0	0	0	0
6	100.5	0	0	0	0	0	0	0	0	0
7	117.3	0	0	0	0	0	0	0	0	0
8	134.0	0	0	0	0	0	0	0	0	0
9	150.8	0	0	0	0	0	0	0	0	0
10	167.5	0	0	0	0	0	0	0	0	0
11	184.3	0	0	0	0	0	0	0	0	0
12	201.0	0	0	0	0	0	0	0	0	0
13	217.8	0	0	0	0	0	0	0	0	0
14	234.5	0	0	0	0	0	0	0	0	0
15	251.3	0	0	0	0	0	0	0	0	0
16	268.0	0	0	0	0	0	0	0	0	0
17	284.8	0	0	0	0	0	0	0	0	0
18	301.5	0	0	0	0	0	0	0	0	0
19	318.3	0	0	0	0	0	0	0	0	0
20	335.0	0	0	0	0	0	0	0	0	0
21	351.8	0	0	0	0	0	0	0	0	0
22	368.5	0	0	0	0	0	0	0	0	0
23	385.3	0	0	0	0	0	0	0	0	0
24	402.0	0	0	0	0	0	0	0	0	0
25	418.8	0	0	0.12	0	0	0	0	3.15	0
26	435.5	0	1.24	14.47	0.33	0	1.75	10.09	29.44	2.72
27	452.3	0	27.68		20.95	5.66	20.24	37.14		21.66
28	469.0	0								

29	485.8	0
30	502.5	0
31	519.3	0
32	536.0	0
33	552.8	0
34	569.5	0
35	586.3	0
36	603.0	0
37	619.8	0
38	636.5	0
39	653.3	0
40	670.0	0
41	686.8	0
42	703.5	0
43	720.3	0
44	737.0	0
45	753.8	0
46	770.5	0
47	787.3	0.04
48	804.0	0.33
49	820.8	2.17
50	837.5	8.21
51	854.3	17.69